Field-resolved infrared spectroscopy based on thulium fiber laser technology

Daniel Marco Bausch
geb. Gerz

SIGILL. UNIVERSITAT. LUDOVIC. MAXIM.

München 2024

Field-resolved infrared spectroscopy based on thulium fiber laser technology

Daniel Marco Bausch
geb. Gerz

Dissertation
der Fakultät für Physik
der Ludwig-Maximilians-Universität
München

vorgelegt von
Daniel Marco Bausch
geb. Gerz
aus Heidelberg

München, den 8. November 2022

Erstgutachter: Prof. Dr. Ferenz Krausz
Zweitgutachter: Prof. Dr. Jens Limpert
Tag der mündlichen Prüfung: 2.5.2023

Contents

List of Figures **vii**

List of Tables **ix**

Acronyms **xiv**

Abstract **xv**

Zusammenfassung **xvii**

List of Publications **xix**

1 Introduction and Motivation **1**
- 1.1 State of the art MIR spectroscopy . . . 2
- 1.2 Structure of the thesis . . . 4

2 Field-resolved spectroscopy of molecular vibrations **5**
- 2.1 Theoretical background . . . 5
  - 2.1.1 Linear optics . . . 5
  - 2.1.2 Pertubative nonlinear optics . . . 8
- 2.2 Electro-optic sampling . . . 13
- 2.3 Light-matter interaction . . . 17
  - 2.3.1 Ro-vibrational absorption lines . . . 17
  - 2.3.2 Molecular response . . . 19

3 Bright source of coherent, few-cycle infrared pulses **23**
- 3.1 CEP stable femtosecond frontend . . . 23
  - 3.1.1 High-power frequency comb at 2 μm wavelength emitted by a Tm-doped fiber laser system . . . 23
  - 3.1.2 Pulse picker and spectrum of Raman shift . . . 30
  - 3.1.3 Pulse characterization with frequency-resolved optical gating . . . 32
  - 3.1.4 Relative intensity noise in the chain . . . 34
- 3.2 Thulium-fiber laser based mid-infrared generation and electro-optic sampling 36

3.2.1 Watt-scale 50 MHz source of single-cycle waveform-stable pulses in the molecular fingerprint region . . . 36
3.2.2 Multi-octave spanning, Watt-level ultrafast mid-infrared source . . 43
3.3 Intra-pulse difference frequency generation . . . 55
3.3.1 Phase matching and nonlinear crystals . . . 56
3.3.2 IPDFG with gallium selenide . . . 57
3.4 Long-term stability . . . 62
3.4.1 Water temperature stabilization . . . 62
3.4.2 Fiber considerations . . . 66
3.5 Dispersion control in the MIR spectral region . . . 70
3.5.1 Mid-infrared long-pass filter for high-power applications based on grating diffraction . . . 73

4 Sensitive electric-field-resolved detection of infrared waves 81
4.1 Experimental prerequisites . . . 81
4.2 Field-resolved spectroscopy approaching ultimate detection sensitivity . . . 84
4.2.1 Abstract . . . 84
4.2.2 Main text . . . 84
4.2.3 Methods . . . 90
4.2.4 Supplementary information . . . 95
4.2.5 Extended data . . . 97

5 Applications - an Outlook 105
5.1 Gas-phase EOS . . . 105
5.1.1 Energy transfer and spectral lines . . . 105
5.1.2 Measurement challenges . . . 110
5.1.3 Cavity-enhanced field-resolved spectroscopy . . . 114
5.2 Toward high-throughput flow cytometry . . . 117
5.2.1 Fast scan . . . 118
5.2.2 Performance . . . 119

A Data archiving 143

Acknowledgements 145

List of Figures

2.1 Schematic of a mode-locked laser 6
2.2 Illustration of second-order nonlinear processes 9
2.3 Concept of birefringent phase matching 11
2.4 Illustration of self-phase modulation 13
2.5 EOS as a two-step process 15
2.6 EOS instrument response dependence on gate pulse duration 15
2.7 Absorption line profiles of gases 19
2.8 Molecular response of methanol in the time and frequency domain 22

3.1 Schematic of the setup for the frequency comb demonstration 25
3.2 Simulation self-compressed pulse with spectrum 26
3.3 FROG retrieval of pulse 27
3.4 Measured RF-signals of the f-2f interferometer 28
3.5 Measurements of the CEP noise 29
3.6 Pulse picker schematic and DC drift 31
3.7 Seed spectra and associated power spectral density. 32
3.8 Spectral response of spectrometers used in FROG 33
3.9 RIN in the chain 35
3.10 Schematic of the Tm:fibre-based CPA frontend for first EOS 38
3.11 FROGs of the gate and driving pulse used in first EOS measurements . . . 39
3.12 Setup of the IPDFG and EOS 40
3.13 Measured and compressed EOS trace 41
3.14 Photon brilliance of the MIR spectrum 42
3.15 Schematic layout of the fiber CPA and three frequency conversion channels 46
3.16 Characterization of the LMA15 fiber 48
3.17 Characterization of the ZBLAN fiber 51
3.18 Measured supercontinuum spectrum generated in a ZBLAN fiber 52
3.19 Characterization of the LPF40 fiber 53
3.20 Impact of IPDFG on the driving pulse spectrum 54
3.21 Brilliance and PSD of the 3-channel source 56
3.22 Typical MIR absorption spectra of gas phase and biological samples 57
3.23 Phase matching in GaSe 58
3.24 Spectra from IPDFG in GaSe 60

3.25 Pictures of damaged GaSe crystals 61
3.26 Impact of chiller water temperature on MIR power 63
3.27 Impact test of abrupt change in chiller temperature 64
3.28 Water temperature stabilization - schematic and results 65
3.29 Optimized MIR power stability 65
3.30 Generated MIR power and RIN vs. driving pulse power 66
3.31 Simulated pulse propagation through the LMA15 PCF 67
3.32 Point of best self-compression for different LMA15 PCF lengths 69
3.33 PCF integration into setup 70
3.34 Material dispersion in the MIR spectral range 72
3.35 Dispersive mirrors in the MIR spectral range 73
3.36 Concept of a grating as a long-pass filter 75
3.37 Grating diffraction efficiencies - simulated and measured 77
3.38 Long-pass filter performance for different settings 78
3.39 Thermal stability of gratings 79

4.1 Shot-noise of heterodyne detection 82
4.2 FROG of gate pulse used for the sensitive EOS 83
4.3 Schematic of the sensitive EOS setup 86
4.4 Characterization of detection sensitivity and dynamic range 87
4.5 Field-resolved spectroscopy of methanol 89
4.6 Broadband spectroscopy of a mixture of methanol, acetylene and methane 90
4.7 Detailed schematic of the optical setup used for sensitive EOS 97
4.8 Estimated MIR electric field and EOS IRF for thin GaSe crystal 98
4.9 Temporal gate functions for two detection crystal thicknesses 99
4.10 Determination of the spectrally-resolved detection efficiency 99
4.11 Comparison of the detection efficiency for two different GaSe thicknesses . 100
4.12 Spectrogram of the MIR waveform 100
4.13 Gas handling setup 101
4.14 SDNR of methanol samples measured at different average MIR powers . . 101
4.15 Comparison of the methanol absorbance from FRS and FTIR 101
4.16 Simulated SDNR versus methanol concentration 102

5.1 Energy transfer of few-cycle excitation 107
5.2 Impact of temperature and pressure on energy transfer for gases 108
5.3 Simulated electric field envelopes of methanol for varying line widths . . . 109
5.4 LOD of methanol concentration versus total integration time 111
5.5 Measured EOS trace of methanol for a delay of up to 550 ps 113
5.6 Concentration dynamic range of methanol with an FTIR spectrometer . . 114
5.7 EOS of enhancement cavity outputs 115
5.8 Typical Raman and FRS spectra of cells 118
5.9 Sonotrode setup for rapid scanning 119
5.10 Example data recorded with the rapid scan 120

5.11 Allan deviation in time and frequency domain for rapid scan 121
5.12 Intensity dynamic range for the slow and rapid scan technique 122

List of Tables

3.1 Retrievals utilizing the home-made FROG setup 34
3.2 Provided Sellmeier coefficients for ZBLAN fiber 50
3.3 Nonlinear crystals with key characteristics for IPDFG 57

4.1 Dynamic range comparison for state-of-the-art broadband vibrational spectroscopies 102
4.2 State-of-the-art EOS detection efficiency and sensitivity 103
4.3 Comparison of the various efficiency values for two different thicknesses of GaSe crystals 103
4.4 Comparison of state-of-the-art broadband infrared spectroscopy experiments 104

Acronyms

AGS silver gallium sulfide.

AGSE silver gallium selenide.

BaF_2 barium fluoride.

BBO beta-barium borate.

CARS coherent anti-Stokes Raman scattering spectroscopy.

CCD charge-coupled device.

CEO carrier-envelope offset.

CEP carrier-envelope phase.

CET coherent energy transfer.

CFBG chirped fiber Bragg grating.

CPA chirped pulse amplifier.

CSP cadmium silicon phosphide.

CW continuous wave.

DC direct current.

DFG difference-frequency generation.

DM dispersive mirror.

DO diffraction order.

EOS electro-optic sampling.

Er erbium.

ErFO erbium:fiber based modelocked oscillator.

FM figure of merit.

FROG frequency-resolved optical gating.

FRS field-resolved spectroscopy.

fsEC femtosecond enhancement cavity.

FTIR Fourier-transform infrared.

FWHM full-width-at-half-maxima.

GaSe gallium selenide.

GD group delay.

GDD group-delay dispersion.

GDV group-delay velocity.

Ge germanium.

GVD group-velocity dispersion.

HAPI HITRAN application programming interface.

HITRAN high-resolution transmission molecular absorption database.

HNLF highly-nonlinear fiber.

HWHM half-width-at-half-maxima.

HWP half waveplate.

InGaAs indium gallium arsenide.

IPDFG intra-pulse difference-frequency generation.

IR infrared.

LIDT laser-induced damage threshold.

$LiNbO_3$ lithium niobate.

LMA large mode area.

LOD limit of detection.

LPF large pitch fiber.

LPF long-pass filter.

MFD mode-field diameter.

MIR mid-infrared.

NA numerical aperture.

NIR near-infrared.

OOF optimum offset frequency.

OPA optical parametric amplification.

OR optical rectification.

PCF photonic-crystal fiber.

PID proportional–integral–derivative.

PNNL Pacific Northwest National Laboratory.

ppb parts-per-billion.

ppt parts-per-trillion.

PSD power spectral density.

QCL quantum cascade laser.

QWP quarter waveplate.

RBW resolution bandwidth.

RF radio frequency.

RIN relative intensity noise.

RMS root mean square.

SCG supercontinuum generation.

SDNR time-dependent EOS-signal-to-detection-noise ratio.

SFG sum-frequency generation.

SHG second harmonic generation.

Si silicon.

SiO_2 silicon oxide.

SNR signal-to-noise ratio.

SPM self-phase modulation.

SRS stimulated Raman spectroscopy.

TE transverse electric.

Tm thulium.

TM transverse magnetic.

TmFCPA Tm-doped fiber chirped-pulse amplification system.

TOD third order dispersion.

WP Wollaston prism.

Yb ytterbium.

ZBLAN ZBLAN fluoride glass.

ZGP zinc germanium phosphide.

ZnSe zinc selenide.

Abstract

In recent years, developments in novel brilliant and coherent light sources were made in the mid-infrared (MIR) molecular fingerprint region (2.5-20 μm or 500-4000 cm^{-1}). This advance enabled new spectroscopic techniques and applications such as frequency comb spectroscopy and field-resolved infrared spectroscopy (FRS). Research efforts at our institute focus on the development of FRS technology, utilizing nonlinear optical processes for the generation and detection of MIR waveforms, as well as for studies of biological samples. Advances in thulium fiber laser technology have facilitated access to femtosecond pulses at a central wavelength around 2 μm. This is roughly twice as long as that of the frontends' driving the first-generation FRS instrumentation. The corresponding lower photon energy enables the usage of highly nonlinear non-oxide crystals for efficient frequency conversions, benefiting both the generation and the detection of ultra-broadband MIR signals.

This work presents the development and benchmarking of the first FRS instrument based on thulium-fiber technology. A commercial Er-fiber oscillator with control over its carrier-envelope offset frequency was used as a seed oscillator. Solid-core photonic crystal fibers enabled a compact and simple pulse compression scheme yielding pulse durations down to 11 fs and peak powers up to 14 MW at multi-megahertz repetition rates. Investigations showed that the frequency comb properties of the oscillator can be transferred to the compressed pulses. This allowed a demonstration of a phase stability of $<$30 mrad in the RF-band spanning 10 Hz to 1 MHz with an average power per comb-line of $>$1 μW.

The compressed pulses were focused onto a GaSe crystal, yielding waveform-stable long-wave MIR pulses with durations down to 43 fs and a spectral coverage of between 6 μm and 18 μm at the -30 dB intensity level. This intra-pulse difference frequency generation step reached a conversion efficiency of 2 % and yielded an average power of 0.5 W. A novel long-pass filter based on grating diffraction for dispersion-free separation of the powerful driving pulse from the MIR pulses was developed and characterized.

Field-resolved detection was implemented via electro-optic sampling (EOS) employing the compressed 2-μm pulses for variably-delayed temporal gating. The signal strength in the EOS detection benefits from the high average power (4 W) of the gate pulse train and from the usage of a thick (541 μm) GaSe crystal. After spectral filtering, a heterodyne detection with a noise floor of only a factor of 2 above shot noise was realized with low-noise InGaAs diodes. This combination allowed the demonstration of an unprecedented intensity dynamic range of more than 14 orders of magnitude in a broadband setting (8-14 μm) at a spectral resolution of 15 cm^{-1} and within a measurement time of 1 s. The corresponding measurable electric field strengths of the MIR pulse span from a few mV/cm up to the MV/cm range. Both the sensitivity (that is, the limit of detection) and the dynamic range of this detection performance are unprecedented for electric-field-resolved optical metrology.

The high linearity of this detection enabled quantitative spectroscopy of gaseous methanol samples, revealing a sub-ppb limit of detection for methanol in a 45-cm-long gas cell at a resolution of $3.1\,\mathrm{cm}^{-1}$, within 160 s effective measurement time. This corresponds to an improvement of more than one order of magnitude in detectable concentration as compared to current state-of-the-art broadband MIR absorption spectroscopy, when accounting for integration time, interaction length and resolution.

Finally, the potential of a combination of this sensitive field-resolved detection with a newly-implemented rapid scanning unit with a time resolution of $26\,\mu$s per single scan is examined for the application of high-throughput flow cytometry.

Zusammenfassung

In den letzten Jahren wurden neuartige brillante und kohärente Lichtquellen im molekularer Fingerabdruckbereich (2.5-20 μm oder 500-4000 cm^{-1}) des mittleren Infrarots (MIR) entwickelt. Diese ermöglichten neue spektroskopische Techniken und Anwendungen wie die Frequenzkamm-Spektroskopie und die feldaufgelöste Infrarot-Spektroskopie (*field-resolved spectrsocopy*, FRS). Die Forschungsarbeiten an unserem Institut konzentrieren sich auf die Entwicklung der FRS-Technologie. Diese verwendet nichtlineare optische Prozesse zur Erzeugung und Detektion von MIR-Wellenformen, sowie zur Untersuchung biologischer Proben. Fortschritte in der Thulium-Faserlaser Technologie haben den Zugang zu Femtosekundenpulsen mit einer Zentralwellenlänge von etwa 2 μm ermöglicht, die somit etwa doppelt so lang ist wie die der Quellen der FRS-Instrumente der ersten Generation. Die entsprechend niedrigere Photonenenergie ermöglicht den Einsatz einer breiteren Auswahl besonders nichtlinearer Kristalle (mit kleinerer Bandlücke) für eine effiziente Frequenzumwandlung. Dieses kommt sowohl der Erzeugung als auch der Detektion von breitbandigen MIR-Signalen zugute.

In dieser Arbeit werden die Entwicklung und die Charakterisierung des ersten FRS-Instruments, welches auf Thulium-Fasertechnologie basiert, vorgestellt. Als Seedlaser wurde ein kommerzieller Er:Faser-Oszillator mit Kontrolle über die Versatzfrequenz der Träger-Einhüllenden verwendet. Photonische Kristallfasern mit Glaskern ermöglichten einen kompakten und einfachen Pulskompressionsaufbau, der Pulsdauern von bis zu 11 fs und Spitzenleistungen von bis zu 14 MW bei Wiederholungsraten von mehreren Megahertz ermöglicht. Untersuchungen zeigten, dass die Frequenzkamm-Eigenschaften des Oszillators auf die komprimierten Pulse übertragen werden. Es konnte eine Phasenstabilität von $<$30 mrad, im Hochfrequenz-Band von 10 Hz bis 1 MHz, mit einer durchschnittlichen Leistung pro Kammlinie von $>$1 μW nachgewiesen werden.

Die komprimierten Pulse wurden auf einen GaSe-Kristall fokussiert und ergaben wellenformstabile, langwellige MIR-Pulse mit einer Dauer von bis zu 43 fs bei einer spektralen Abdeckung von 6-18 μm (mit einer Intensität über -30 dB). Dieser Schritt der Intrapuls-Differenzfrequenzerzeugung erreichte eine Umwandlungseffizienz von 2 % und lieferte eine durchschnittliche Leistung von 0.5 W. Ein neuartiger Langpassfilter auf der Basis von Gitterbeugung zur dispersionsfreien Trennung des starken Treiberpulses von den MIR-Pulsen wurde entwickelt und charakterisiert.

Die feldaufgelöste Detektion wurde mittels elektro-optischer Abtastung (*electro-optic sampling*, EOS) unter Verwendung der komprimierten 2-*μm*-Pulse für ein variabel verzö-

gertes zeitliches Abtasten realisiert. Die Signalstärke von EOS profitiert von der hohen mittleren Leistung (4 W) des Abtastpulszugs und von der Verwendung eines 541 μm dicken GaSe-Kristalls. Nach der spektralen Filterung wurde mit rauscharmen InGaAs-Dioden eine heterodyne Detektion mit einem Rauschniveau von nur einem Faktor 2 über dem Schrotrauschen realisiert. Diese Kombination ermöglichte die Demonstration eines noch nie da gewesenen Intensitätsdynamikbereichs von mehr als 14 Größenordnungen in einer breitbandigen spektralen Abdeckung (8-14 μm) mit einer spektralen Auflösung von 15 cm^{-1} und einer Messzeit von 1 s. Die entsprechenden messbaren elektrischen Feldstärken des MIR-Pulses reichen von wenigen mV/cm bis in den MV/cm Bereich. Sowohl die Empfindlichkeit (d.h. die Nachweisgrenze) als auch der dynamische Bereich dieser Detektion waren für die feldaufgelöste optische Metrologie bislang unerreicht.

Die hohe Linearität dieser Detektion ermöglichte die quantitative Spektroskopie gasförmigen Methanols, wobei eine Sub-ppb-Nachweisgrenze in einer 45 cm langen Gaszelle bei einer Auflösung von 3.1 cm^{-1} innerhalb von 160 s effektiver Messzeit ermittelt wurde. Dies entspricht einer Verbesserung der nachweisbaren Konzentration um mehr als eine Größenordnung im Vergleich zum aktuellen Stand der Technik von breitbandigen MIR-Absorptionsspektroskopien, wenn man Integrationszeit, Länge der Gaszelle und spektrale Auflösung berücksichtigt.

Zuletzt wird das Potenzial einer Kombination dieser empfindlichen feldaufgelösten Detektion mit einer neu implementierten schnellen Abtastung, die eine zeitliche Auflösung von 26 μs pro Spur erreicht, für die Anwendung der Durchflusszytometrie mit hohem Durchsatz behandelt.

List of Publications

Journal publications:

- C. Gaida, T. Heuermann, M. Gebhardt, E. Shestaev, T.P. Butler, D.Gerz, N. Lilienfein, P. Sulzer, M. Fischer, R. Holzwarth, A. Leitenstorfer, I. Pupeza, J. Limpert, *High-power frequency comb at* $2\,\mu$m *wavelength emitted by a Tm-doped fiber laser system*, Optics Letters, vol. 43, no. 21, p. 5178, (2018).

- T. P. Butler, D. Gerz, C. Hofer, J. Xu, C. Gaida, T. Heuermann, M. Gebhardt, L. Vamos, W.Schweinberger, J. A. Gessner, T. Siefke, M. Heusinger, U. Zeitner, A. Apolonskiy, N. Karpowicz, J.Limpert, F. Krausz, I. Pupeza, *Watt-scale 50-MHz source of single cycle waveform-stable pulses in the molecular fingerprint region*, Optics Letters, vol. 44, no. 7, p. 1730 (2019).

- D. Gerz, W. Schweinberger, T.P. Butler, T. Siefke, M. Heusinger, T. Amotchkina, V. Pervak, U. Zeitner, I. Pupeza, *Mid-infrared long-pass filter for high-power applications based on grating diffraction*, Optics Letters, vol. 44, no. 12, p. 2014 (2019).

- T. Amotchkina, M. Trubetskov, S.A. Hussain, D. Hahner, D. Gerz, M. Huber, W. Schweinberger, I. Pupeza, F. Krausz, V. Pervak, *Broadband dispersive* Ge/YbF_3 *mirrors for mid-infrared spectral range*, Optics Letters, vol.44, no. 21, p. 5210 (2019).

- T. P. Butler, N. Lilienfein, J. Xu, N. Nagl, C. Hofer, D. Gerz, K. F. Mak, C. Gaida, T. Heuermann, M. Gebhardt, J. Limpert, F. Krausz, I. Pupeza, *Multi-octave spanning, Watt-level ultrafast mid-infrared source*, Journal of Physics: Photonics, vol. 1, no. 4, p. 044006 (2019).

- P. Sulzer[1], M. Högner[1], A. Raab, L. Fürst, E. Fill, D. Gerz, C. Hofer, L. Voronina, I. Pupeza,*Cavity-enhanced field-resolved spectroscopy*, Nature Photonics, vol.16, no. 10, p. 692 (2022).

- C. Hofer[1], D. Gerz[1], L. Fürst, M. Högner, T. P. Butler, M. Gebhardt, T. Heuermann, C. Gaida, K.S. Maiti, M. Huber, E. Fill, J. Limpert, F. Krausz and I. Pupeza, *Sensitive electric-field-resolved detection of infrared waves*, manuscript submitted to Nature (2022).

---

[1] These author contributed equally

Chapter 1

Introduction and Motivation

The molecular composition of biological systems and its changes are reflected by the physiological state and its transformation. Therefore, the ability to simultaneously observe the changes in concentrations of a variety of molecules in biological systems is highly desirable for applications in biology and medicine. Advances in sensitivity, acquisition speed, reliability and the ability to simultaneously probe multiple molecular species relevant to biological processes or a phenotype are likely to bring about breakthroughs in medical applications such as early disease diagnosis, low-abundance tumor cell detection, online monitoring of breath, direct monitoring of therapy response and others. However, the large variety of molecular species and their vastly different concentration ranges occurring in biological systems pose a major challenge to quantitative and multivariate detection. For instance, human blood plasma contains more than 1000 different proteins covering 10 orders of magnitude in concentration [1], and human breath is estimated to contain over 3000 volatile organic compounds [2].

Optical interrogation of molecular vibrations affords the advantage of highly multivariate and simultaneous probing while permitting non-destructive measurements of samples in their native state. The (broadband) optical response of the sample contains contributions from all molecular components having Raman or infrared (IR) active vibrations [3], spectrally located at the respective vibrational eigenfrequencies. While the temporal and spectral overlap of these contributions challenges quantitative identification of individual molecular species in complex mixtures [4, 5], these measurements yield highly sample-specific global vibrational fingerprints, rich in information on molecular abundance and conformation.

A huge variety of vibrational molecular modes and overtones are found in the so-called molecular fingerprint region spanning the near-IR (NIR) to the mid-IR (MIR) spectral region (2-20 μm). IR spectroscopies directly probe these modes and, compared to other optical spectroscopies, profit from large absorption cross-sections [6, 7]. However, technological limitations of available broadband IR radiation sources and detectors have long been a severe constraint to the applicability of IR vibrational spectroscopy and microscopy to real-world biomedical applications, in particular in the context of the strong and broadband absorption of liquid water molecules.

1.1 State of the art MIR spectroscopy

For the past few decades, the gold-standard method in MIR absorption spectroscopy has been Fourier-transform infrared (FTIR) spectroscopy [6]. Here, a thermal-radiation beam is split into two arms of an interferometer (e.g., a Michelson interferometer) and an interferogram is recorded by varying the mutual delay in the two arms. The Fourier transform of the resulting interferogram corresponds to the power spectrum of the incident light. FTIR spectrometers benefit from this compact, robust, low-cost, broadband and flexible setup that also facilitates mobile operation. More advanced applications include asymmetric (dispersive) FTIR spectroscopy providing the complex refractive index of a sample, and time-resolved FTIR difference spectroscopy [4, 5, 8, 9]. However, performance advances of FTIR technology in terms of sensitivity and detection dynamic range have been approaching a plateau in the past few decades. One major impediment stems from the use of spatially and temporally incoherent thermal radiation sources, limiting the brightness and the propagation path length. Other limitations arise from IR detectors usually having modest detectivity and linear dynamic range [10], as well as from technical and thermal-background noise.

Synchrotron facilities offer ultra-broadband coherent radiation with a high brightness, albeit at the disadvantages of high cost, low availability and facility-scale size [8, 11, 12]. The recent development of quantum cascade lasers (QCL), generating brilliant, coherent MIR radiation in a table-top configuration, has opened up a new chapter in broadband IR vibrational fingerprinting [13–16]. The often narrowband ($<1\,\mathrm{cm}^{-1}$) but broadly tunable ($>100\,\mathrm{cm}^{-1}$) watt-level QCLs have enabled for example the first transmission measurements with path lengths of several tens of μm in water, thus permitting transmission measurements of living organisms [17–19]. Another example is single-species trace-gas detection, that benefits from the high spectral resolution derived from the narrowband linewidth of the laser. For single-line trace-gas detection, sensitivities in the lower ppb range have been demonstrated [20]. Limitations of IR detectors in direct measurements (that is, of the IR radiation *itself*) can be mitigated by indirect detection (that is, of an *effect* of the radiation). For instance, optoacoustic spectroscopy [21] has enabled label-free metabolic imaging in living cells with (sub-)mM sensitivity [22].

The main property underlying such innovative applications with these semiconductor lasers is their spectral and spatial coherence. For IR vibrational spectroscopy, the most commonly used coherent light sources are mode-locked lasers that have a fixed phase relation between the optical modes of a resonant gain cavity and, thus, these lasers can produce trains of broadband and short optical pulses. Each optical frequency mode f_N can be described as the sum of two radio frequencies, the pulse repetition frequency f_r multiplied by an integer N and an overall offset frequency f_0 specifying the pulse-to-pulse evolution of the waveform with respect to the intensity envelope ($f_N = f_0 + N f_r$) [23]. A precise control of f_0 and N allows to map the optical frequencies to radio frequencies, providing a high-precision technique for comparing and measuring optical frequencies. These so-called frequency-comb techniques afford highest spectral resolution [24–27] and are consequently well suited for sensitive, quantitative detection of gaseous media with linear [28] as well as with multidimensional coherent spectroscopy [29].

The extension of usable optical gain media in the molecular fingerprint spectral region has been one focus in laser development over the last decades. Recently QCL technology has shown rapid advances towards room-temperature, broadband, modelocked operation [30, 31] and (dual-)frequency-comb realizations [32, 33] highlighting their current potential. Gain media doped with holmium [34, 35], thulium [36] or chromium [37] have enabled the generation of femtosecond pulses with watt-level powers in the spectral region between 1.9 and 2.5 μm. Although a direct, complete coverage of the molecular fingerprint region with these mode-locked sources is still to be demonstrated, the attainable high peak powers afford efficient spectral broadening via nonlinear optical processes. For this purpose, one of the most widely used techniques is supercontinuum generation (SCG), predominantly caused by self-phase modulation, which broadens the spectrum of the incident light [38–40]. In order to reach sufficient peak power, the light is either tightly focused into a bulk material or confined in optical waveguides, such as photonic crystal fibers or ZBLAN fibers.

For the generation of longer wavelengths, other nonlinear parametric processes such as optical parametric oscillation [41], parametric amplification [42] and difference frequency generation (DFG) [43] are more favorable. Here, energy is distributed from high-energy photons to lower-energy photons while the efficiency of this process is strongly impacted by the phase matching of the nonlinear crystal. One process known as optical rectification or intra-pulse DFG (IPDFG) has distinguished itself as a simple, in-line method for the generation of passively stable waveforms, i.e. trains of pulses with constant phase between the optical carrier and their intensity envelope. Super-octave spanning spectra with tens-of-mW MIR average power have been achieved with these sources, rivaling the powers of QCL and attaining brilliances exceeding those of IR beamlines at 3^{rd}-generation synchrotrons by up to a few orders of magnitude [44–48].

The waveform stability enables multi-shot sampling measurements of the electric field and were first realized in the lower-THz range by making use of optical rectification or photoconductive sampling [49, 50]. In the time domain, this permits the study of light-matter interactions on the level of individual oscillations of the electric field. Here, this class of techniques are referred to as field-resolved spectroscopy (FRS). For such measurements electro-optic sampling (EOS) is a well-established technique for broadband spectroscopy in the few-THz spectral region.

EOS is often described with the Pockels effect [51]. The change of birefringence induced by the electric field of the long-wavelength test wave rotates the polarization of a gate pulse and is recorded for varying time delays between the two. The resulting EOS trace corresponds to the electric field convoluted with the instrument response function.

However, for MIR waveforms not all spectral components of the implicitly broadband gate pulse are evenly rotated and the technique is better described as a two-step process [52, 53]. In a first step, the two participating fields are mixed in a parametric nonlinear process such as sum-frequency generation (SFG) and/or difference frequency generation (DFG). In a second step, the spectrally overlapping portion of the unconverted gate field is used as a local oscillator for balanced heterodyne detection.

In FRS, the direct access to the electric field results in the conceptual advantage of recording the information of the coherently emitted, ensemble-integrated electric field of the optical response trailing behind the excitation. Directly measuring a signal proportional to the electric field relaxes the dynamic-range requirements of the detection and makes FRS well suited for strongly absorbing samples [54], e.g. intact biological systems such as living plant leaves, enabling live monitoring of their metabolism [55]. The temporal gating via nonlinear frequency upconversion in EOS renders FRS robust against noise from the thermal background radiation and technical noise of the MIR source. Another advantage of EOS is the detection in the spectral region of the probe pulse permitting the use of low-noise, high-dynamic-range detectors operating at room temperature, e.g., based on silicon (Si) or indium gallium arsenide (InGaAs). These benefits enabled FRS to improve the limit of detection of the concentration in aqueous samples by more than one order of magnitude compared to research-grade FTIR spectrometers [55]. Furthermore, the combination of FRS with frequency-comb technology shows high potential for sensitive, high-resolution gas spectroscopy[27].

1.2 Structure of the thesis

In this work, results from developing and benchmarking a new generation of FRS instrumentation, in particular harnessing recent advances in thulium-doped fiber technology are presented. The main objectives were to achieve (i) a broader spectral coverage, ideally of the entire molecular fingerprint region, while maintaining high average powers (ii) a higher sensitivity compared to the first generation of FRS spectrometers, ideally close to the ultimate limit of detecting all photons in the time-gated window and (iii) to demonstrate this new regime of broad bandwidth and high sensitivity in proof-of-principle FRS measurements.

Chapter 2 elaborates on the theoretical **background** of the involved nonlinear processes, the details of electro-optic sampling and the origin of time-domain signals in vibrational spectroscopy on the level of the electric field.

Chapter 3 details the individual components of the **source**. First, the frequency-comb capabilities at the driving wavelength, the pulse retrieval and the noise propagation through the system are discussed, followed by the generation of waveform-stable MIR pulses and their dispersion control.

Chapter 4 investigates the sensitivity limits of **EOS detection** and the application on gaseous samples.

Chapter 5 summarizes examples for **applications** harnessing the advantages of FRS. Specifically, multi-species gas spectroscopy with an unprecedented dynamic range of detectable concentrations, and first developments toward high-throughput flow cytometry are discussed.

Chapter 2

Field-resolved spectroscopy of molecular vibrations

2.1 Theoretical background

In this chapter, the basic theory of the most relevant optical processes for this thesis is presented. First, linear optics are described in the context of ultrafast pulses and frequency combs. The high peak intensities of femtosecond pulses make nonlinear processes accessible and the most relevant are described. Subsequently, the detection technique of electro-optic sampling is discussed. The last section deals with molecular vibrations and their optical interrogation, with a particular emphasis on the case of gaseous media.

2.1.1 Linear optics

Since the first demonstration of **l**ight **a**mplification by **s**timulated **e**mission of **r**adiation (laser) in 1960 by Theodore H. Maiman [56] the laser as a source for coherent radiation has been widely developed. One of the major research directions has been to confine coherent light to trains of (ultra-)short pulses in a mode-locked laser, see Figure 2.1. Such a laser consists of an optical cavity where light waves interfere and thus only resonant modes f_n form. A gain medium placed inside the optical cavity leads to amplification of the longitudinal modes that have a spectral overlap with the emission spectrum. The dynamics of such an optical cavity can be described by the Haus master equation [57], which considers the losses, gain and dispersion of the modes. For a given optical spectrum, the shortest pulse duration is achieved when all longitudinal modes are temporally aligned with respect to an electric-field maximum. Such a pulse is called transform-limited and for a given pulse shape the time-bandwidth product is a constant. For instance, for a Gaussian pulse the product of the full-width-at-half-maxima (FWHM) of the temporal and spectral intensities is 0.441.

A mode-locked laser provides a fixed phase relation between all the longitudinal modes in the cavity and can thus deliver trains of pulses. Mode-locking in the time-domain picture can be achieved by introducing a time-dependent loss which is larger for continuous wave

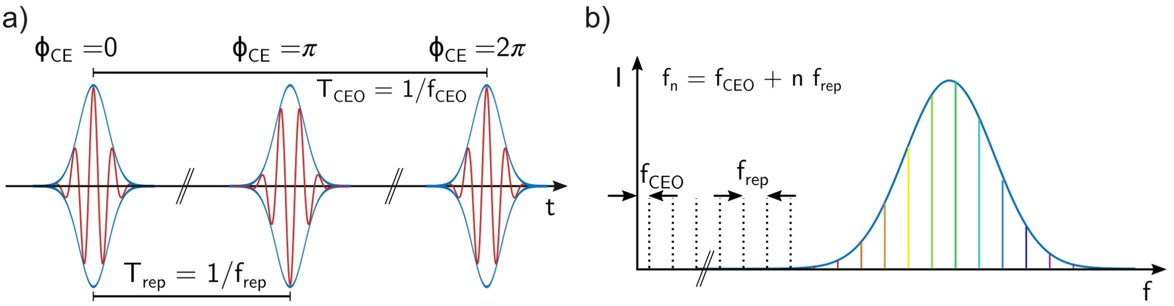

Figure 2.1: Pulse train of a mode-locked laser in the a) frequency domain and b) time domain.

(CW) radiation compared to pulsed light. There exist various mode-locking techniques such as active mode locking via electro-optic modulation or passive mode locking with saturable absorbers [58] e.g. implemented employing the nonlinear Kerr effect [59].

In Figure 2.1 a) a pulse train in the time domain with its electric field in red and its envelope in blue are shown. The round trip time in the optical cavity corresponds to the time between consecutive pulses T_{rep} and the inverse of the round trip time, the repetition rate f_{rep}, corresponds to the spacing of the equidistant spaced modes. The carrier-envelope phase ϕ_{CE} can be defined for simple pulses as the phase of the electric-field with respect to the maximum of the envelope. The change of the ϕ_{CE} for consecutive pulses $\Delta\Phi_{CE}$ leads to a carrier-envelope offset (CEO) frequency $f_{CEO} = \phi_{CE} f_{rep}/(2\pi)$. In the frequency domain f_{CEO} leads to an offset of the comb from zero so that all modes can be described as:

$$f_n = f_{CEO} + n \cdot f_{rep} \tag{2.1}$$

For all consecutive pulses the envelope remains the same and in case f_{CEO} equals to zero this holds also true for the electric field and the pulse train is called are waveform stable.

A practical way to describe a single laser pulse in the frequency domain is the complex electric field:

$$\tilde{E}_\omega(\omega) = A(\omega)e^{-i\varphi(\omega)} + c.c. \tag{2.2}$$

defined for positive and negative frequencies with the spectral amplitude $A(\omega) = A(-\omega)$ and spectral phase $\varphi(\omega) = -\varphi(-\omega)$. The real valued time-domain electric field $E(t)$ can be obtained via a Fourier transformation

$$E(t) = \mathcal{F}\left\{\tilde{E}_\omega(\omega)\right\} = \frac{1}{\sqrt{2\pi}} \int_{-\infty}^{\infty} \tilde{E}_\omega(\omega)e^{-i\omega t}\, d\omega. \tag{2.3}$$

Mode locked lasers allow the generation of transform-limited pulses and their time domain electric field with its envelope A(t) can be described as [23]:

$$E(t) = Re\left(A(t)e^{-i\omega_c t}\right) = Re\left(\sum_n A_n e^{-i(\omega_c + 2\pi n f_{rep} + \varphi_n)}\right), \tag{2.4}$$

where A_n are the Fourier components of A(t) and the carrier frequency ω_c.

Molecular samples, such as gases or solids, are made up of atoms consisting of a positive charge surrounded by a cloud of negatively charged electrons. When applied, the electric field of a laser pulse acts on these charges with opposite forces and separates them as well as orientates existing dipoles. Assuming a linear material response, this induced electric dipole moment leads to a polarization P(t) of the material

$$P(t) = \epsilon_0 \chi(t) * E(t) \tag{2.5}$$

where ϵ_0 is the permittivity of free space, χ is the linear susceptibility of the material. The convolution is required in the time domain to account for non-instantaneous effects, while in the frequency domain this corresponds to a multiplication and a frequency dependent χ. The description of the light propagation in a material often uses the complex refractive index $\tilde{n}(\omega)$, which relates to the susceptibility via

$$\tilde{n}(\omega) = \sqrt{1 + \chi(\omega)} = n(\omega) - i\kappa(\omega), \tag{2.6}$$

where $n(\omega)$ is commonly described as refractive index and $\kappa(\omega)$ as the extinction coefficient. With the wavenumber $\tilde{k}(\omega) = \frac{\tilde{n}(\omega)\omega}{c}$ and the speed of light in vacuum c, the propagation of a laser pulse with an electric field $\tilde{E}_{in}(\omega)$ along the z-axis (assuming plane waves) in a linear medium is described by:

$$\tilde{E}_{out}(\omega) = \tilde{E}_{in}(\omega) e^{-i\tilde{k}(\omega)z} = \tilde{E}_{in}(\omega) e^{-in(\omega)\frac{\omega}{c}z} e^{-\kappa(\omega)\frac{\omega}{c}z}. \tag{2.7}$$

The last exponential describes the attenuation caused by absorption while the first exponential accounts for the spectral phase $\varphi(\omega) = n(\omega)\frac{\omega}{c}z$ caused by the linear dispersion of the medium. Often $\varphi(\omega)$ is expanded in a Taylor series around ω_c

$$\varphi(\omega) = \sum_{n=0}^{\infty} \frac{(\omega - \omega_c)^n}{n!} \underbrace{\frac{\partial^n}{\partial \omega^n} \varphi(\omega)}_{=D_n(\omega)}. \tag{2.8}$$

The dispersion coefficients D$_n(\omega)$ corresponding to the n$^t h$ derivative with respect to ω are useful quantities with the following meaning:

- **D**$_0$: corresponds to an overall phase accumulation and can change ϕ_{CE}
- **D**$_1$: is termed group delay (GD) and results in a time shift of the pulse envelope after the sample compared to a pulse traveling through free space.
- **D**$_2$: is called group delay dispersion (GDD) as it encompasses the linear dispersion of the GD. It changes the pulse envelope by inducing a linear shift of the instantaneous frequency $\omega(t) = \partial\varphi(t)/\partial t$ and is given in units of fs^2. A value intrinsic to the material is the group velocity dispersion (GVD) which is often normalized to the propagation of light for a length z (often 1 mm): $GDD = GVD \cdot z$.
- **D**$_3$: the third order dispersion (TOD) coefficient and higher dispersion coefficients often lead to a more complex distribution of the instantaneous frequency.

2.1.2 Pertubative nonlinear optics

In linear optics, the electric field oscillations lead to small-amplitude oscillating motions of the local charges (e.g., electrons, nuclei, quasi-particles), which then re-emit light as oscillating dipoles. This motion can be described with a driven harmonic oscillator model, where oscillating particles are trapped in a parabolic, that is, harmonic potential. The high intensities that can be reached by temporal confinement of coherent light in ultrashort pulses opens the door to the field of nonlinear optics, where this harmonic approximation loses its validity. In order to account for anharmonic potentials the susceptibility in Equation 2.5 is expanded in a Volterra series [60]:

$$
\begin{aligned}
P &= P^{(1)} + P^{(2)} + P^{(3)} + ... \\
&= \epsilon_0 \int\limits_{t_1<t} \chi^{(1)}(t_1) E(t-t_1)\ dt_1 + \epsilon_0 \iint\limits_{t_1,t_2<t} \chi^{(2)}(t_1,t_2) E(t-t_1) E(t-t_2)\ dt_1 dt_2 \\
&+ \epsilon_0 \iiint\limits_{t_1,t_2,t_3<t} \chi^{(3)}(t_1,t_2,t_3) E(t-t_1) E(t-t_2) E(t-t_3)\ dt_1 dt_2 dt_3 + ... \qquad (2.9) \\
&\overset{inst.\ \chi}{\widehat{=}} \epsilon_0 \left[\chi^{(1)} E + \chi^{(2)} E^2 + \chi^{(3)} E^3 + ...\right]. \qquad (2.10)
\end{aligned}
$$

Here, the tensors $\chi^{(1)}$,$\chi^{(2)}$ and $\chi^{(3)}$ denote the first, second and third order susceptibilities, respectively, with typical values on the order of: $\chi^{(1)} \approx 1$, $\chi^{(2)} \approx 1 \times 10^{-12}\,\mathrm{m/V}$ and $\chi^{(3)} \approx 1 \times 10^{-24}\,\mathrm{m^2/V^2}$ [61]. Importantly, for nonlinear polarizations, i.e., susceptibilities of order 2 and higher, the frequency-domain representation of the multi-dimensional convolution in eq.(2.9) is a multi-dimensional convolution. This is in contrast to the linear case, where the time-domain convolution becomes a multiplication in the frequency domain, and conceptually complicates the retrieval of higher-order susceptibilities in nonlinear spectroscopy. For simplification an instantaneous material response is assumed, leading to the Taylor series in Equation 2.10.

Second order processes

In order to illustrate the impact of the second order nonlinear contributions of the electrical field on the polarization, let us consider two monochromatic, superimposed planar waves:

$$
E(t) = \frac{1}{2}\left[E_1 e^{i(\omega_1 t)} + E_2 e^{i(\omega_2 t)} + c.c.\right] \tag{2.11}
$$

The polarization arising from the second-order susceptibility $\chi^{(2)}$ is

$$
\begin{aligned}
P^{(2)}(t) = \epsilon_0 \chi^{(2)} E^2(t) = \frac{\epsilon_0}{4}\chi^{(2)} \Big\{ & E_1^2 e^{i2(\omega_1 t)} + E_2^2 e^{i2(\omega_2 t)} && (SHG) \qquad (2.12) \\
& + 2E_1 E_2 e^{i((\omega_1+\omega_2)t)} && (SFG) \\
& + 2E_1 E_2^* e^{i((\omega_1-\omega_2)t)} && (DFG) \\
& + E_1 E_1^* + E_2^* E_2 && (OR) \\
& + c.c. \quad \Big\}.
\end{aligned}
$$

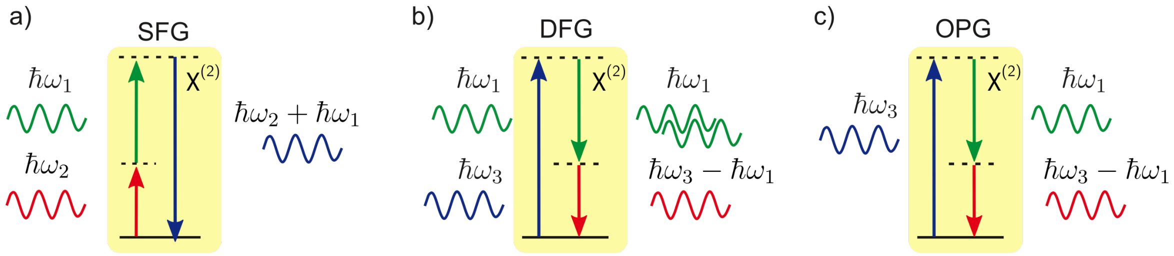

Figure 2.2: Illustration of second-order nonlinear processes in level diagram and photon picture. a) sum frequency generation, b) difference frequency generation, c) optical parametric generation.

The processes leading to the new frequencies are:

- In sum frequency generation (SFG) the electric field oscillates at $\omega_1 + \omega_2$.
- Second harmonic generation (SHG) is the degenerate case of SFG and the field oscillates at double the frequency.
- Difference frequency generation (DFG) is employed to generate long wavelength radiation as the resulting electric field oscillates at $|\omega_1 - \omega_2|$.
- In optical rectification (OR) static fields proportional to $|E_1|^2$ and $|E_2|^2$ emerge. This is the extreme case of DFG, where $\omega_1 \approx \omega_2$. For a temporally confined laser pulse optical rectification results in a time signal corresponding to the intensity envelope [62].

In Figure 2.2 second-order processes are shown in an energy level scheme, where a virtual level (dashed line) in a $\chi^{(2)}$ nonlinear medium acts as the intermediary state. In all cases the energy is conserved $\sum_i \hbar\omega_i = 0$. In SFG the two incident photons combine into a single emitted one, while in DFG the energy of the higher-frequency photon (pump) is transferred into a duplicated, lower-energy photon (signal), and an additional photon (idler) at the different frequency is generated. In the case the optical gain of a weak signal beam is employed for amplification the process is called optical parametric amplification (OPA). Another second order nonlinear process often employed to generate long-wavelength radiation is optical parametric generation (also known as spontaneous parametric down-conversion), which corresponds to OPA where the initial signal photon arises due to vacuum fluctuations.

Efficiency considerations

Although these nonlinear processes can occur at the same time, their efficiency can vastly differ and often only one process dominates. Let us consider the SFG process for two planar, monochromatic waves (indices 1 and 2) with frequency ω_i propagating along the z-direction of a nonlinear crystal with length L. Assuming no significant conversion efficiency, the incident beam intensities I_i remain constant. Solving the coupled wave equations for the resulting intensity of the SFG beam (index 3) I_3 by utilizing the slowly varying amplitude approximation yields [61]:

$$I_3 = \frac{8 d_{eff}^2 \omega_3^2 I_1 I_2}{n_1 n_2 n_3 \epsilon_0 c^2} L^2 \mathrm{sinc}^2 \left(\frac{\Delta k L}{2} \right). \tag{2.13}$$

Here, d_{eff} denotes the effective nonlinear coefficient, n_i the respective refractive index and Δk the momentum mismatch, elucidated in the following. This parametric process not only needs to obey energy conservation ($\omega_3 = \omega_1 + \omega_2$), but also momentum conservation $\hbar k_1 + \hbar k_2 - \hbar k_3 = 0$, where k_i is the wavevector $k_i = 2\pi/\lambda_i$. The uncertainty principle permits this process to happen for short distances even when momentum conservation is not perfectly fulfilled, but this drastically reduces the efficiency of the process. The last term in Equation 2.13 accounts for the momentum mismatch. At $L = 1/\Delta k$ I_3 reaches its maximum and after the coherence length $L_c = 2/\Delta k$ I_3 decays back to zero. The smaller the momentum mismatch the larger the maxima can get, see Figure2.3 a). This behavior can also be explained by newly generated frequencies running out of phase with respect to the driving frequencies. This leads to destructive interference of newly generated frequencies upon propagation through the crystal instead of a coherent built-up.

Perfect phase matching of an SHG process with $\omega_1 = \omega_2$ and due to energy conservation also $\omega_3 = 2\omega_1$ requires:

$$\frac{n_1 \omega_1}{c} + \frac{n_2 \omega_2}{c} = \frac{n_3 \omega_3}{c} \;\Rightarrow\; n(\omega_1) \overset{!}{=} n(2\omega_1). \tag{2.14}$$

In isotropic materials, even far from absorption lines, the refractive index is frequency dependent and the condition of Equation 2.14 can in general not be fulfilled.

This problem can be solved by employing a birefringent material with its angle- and polarization-dependent refractive index. In Figure 2.3 b) the geometry of the interaction is depicted and in c) the refractive index of beta barium borate (BBO), a negative uniaxial crystal, is shown or several incident angles θ. For an uniaxial crystal the refractive index of the ordinary polarization, which is orthogonal to the optical axis (z-axis), is a constant n_o. The effective refractive index of the extraordinary polarization $n_e(\theta)$ is a projection onto the index ellipsoid with the semi-axis n_o, n_{extra} and can be calculated according to [63]:

$$\frac{1}{n_e(\theta)^2} = \frac{\sin^2(\theta)}{n_{extra}^2} + \frac{\cos^2(\theta)}{n_o^2}. \tag{2.15}$$

Depending on the birefringence and the appropriate choice of incidence angle and the polarization of the interacting beams, the phase matching condition can be fulfilled. For example, light with a wavelength of $2\,\mu$m can be phase matched for SHG in a BBO crystal with θ angles of 21° and 30.9°, indicated in Figure 2.3 c) respectively. Phase matching with the two lower-frequency beams having the same polarization is referred to as type I (here at $\theta = 21°$) and for orthogonal polarizations type II (here at $\theta = 30.9°$).

In the case of perfect phase matching, the resulting SFG intensity is proportional to the incident intensities I_1 and I_2 and to the square of the crystal thickness. In practice, usable

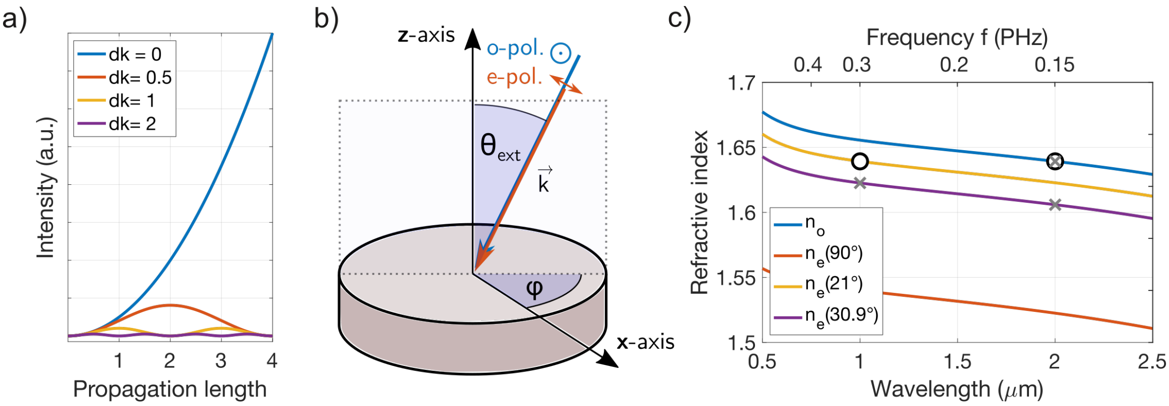

Figure 2.3: Phasematching. a) Intensity for different phase mismatches. b) Geometry of uniaxial birefringent crystal with Θ_{ext} as the external incident angle of a ordinary polarized beam (blue) and extraordinary polarization (red). c) Refractive index of BBO calculated from the Sellmeier coefficients from [66]. Phase matching for SHG indicated by circles for type I and crosses for type II.

intensities are limited by the laser-induced damage threshold (LIDT), which is dependent on the crystal type and the laser parameters, such as wavelength, pulse duration, repetition rate, intensity, fluence. Exceeding the LIDT results in irreversible damage of the crystal via various damaging mechanisms, such as (multi-)photon absorption leading to thermal stress or impact ionization [64, 65]. The parameters in Equation 2.13 related to the type of nonlinear crystal $\frac{d_{eff}^2}{n_1 n_2 n_3}$ are often taken as a figure of merit for the nonlinear crystal. For high conversion efficiencies Equation 2.13 becomes invalid, as the incident intensities deplete when propagating through the crystal and back conversion of I_3 into I_1 and I_2 through DFG occurs.

So far, we implicitly assumed perfect temporal and spatial overlap between the interacting monochromatic optical waves. More considerations are necessary for laser pulses with their finite spatial and temporal profiles and broad spectral bandwidths.

The envelope of a pulse travels with the group velocity $v_g = \partial\omega_i/\partial k$, which relates inversely to the group delay $GD = z/v_g$. Due to material dispersion, the group velocity is frequency dependent and the pulses temporally separate, thus limiting the effective interaction length in a nonlinear crystal. A measure for this separation for pulses with a FWHM of τ is the pulse splitting length ℓ defined as:

$$\ell = \left| \frac{\tau}{\frac{1}{v_g 1} - \frac{1}{v_g 2}} \right| . \tag{2.16}$$

Another impact of the crystal thickness needing consideration is the efficiency-bandwidth trade-off. In case two pulses interact and the carrier frequencies are phase matched, the broad spectral bandwidth still allows for mixing of other spectral parts of the pulses with $\Delta k \neq 0$. This can generate a broader spectral bandwidth. Increasing the crystal thickness results in higher efficiencies for perfectly phase-matched processes, while the momentum mismatch limits the efficiency of processes with $\Delta k \neq 0$ thus reducing the bandwidth.

Several other effects such as pulse broadening due to dispersion, spatial walk-off, finite Rayleigh length of the focused beams need to be considered when designing nonlinear conversion setups [67].

Intensity dependent refractive index

In centrosymmetric materials, $\chi^{(2)}$ is equal to zero and the lowest-order nonlinear susceptibility occurring - in fact, in all materials - for sufficiently high intensities is of the third order. An effective susceptibility χ^{eff} can then be defined from the polarization as:

$$P(\omega) = P^{(1)}(\omega) + P^{(3)}(\omega) = \epsilon_0 \underbrace{\left(\chi^{(0)} + \frac{3}{4}\chi^{(3)}|E(\omega)|^2\right)}_{=\chi^{eff}(E)} E(\omega) \tag{2.17}$$

where the factor 3/4 stems from considering all third order interactions and their permutations, as well as some simplifications [61]. With $|E(\omega)|^2 = 2I/(\epsilon_0 n_0 c)$, the refractive index becomes intensity dependent:

$$\begin{aligned} n(I) &= \sqrt{1+\chi^{eff}(E)} = n_0\sqrt{1+\frac{3\chi^{(3)}}{4n_0^2}|E(\omega)|^2} \approx n_0 + \frac{3\chi^{(3)}}{8n_0}|E(\omega)|^2 \\ &= n_0 + \frac{3}{4}\frac{\chi^{(3)}}{\epsilon_0 n_0^2 c} I = n_0 + n_2 I. \end{aligned} \tag{2.18}$$

Here n_0 denotes the linear and n_2 the nonlinear refractive index. This intensity dependence of the refractive index is known as optical Kerr effect and results for a spatially and temporally confined laser pulse in two major effects: self-phase modulation (SPM) and self-focusing.

Self-phase modulation occurs due to the temporal intensity variation changing the phase $\varphi(t)$ of a laser pulse propagation through a nonlinear medium of thickness L:

$$\varphi(t) = \omega_c t - \frac{2\pi}{\lambda_c} n(I) L \tag{2.19}$$

As a result of the phase change the instantaneous frequency $\omega(t)$ changes:

$$\omega(t) = \frac{d\varphi(t)}{dt} = \omega_c - \frac{2\pi}{\lambda_0}\frac{dn(I)}{dt}L = \omega_c\left(1 - \frac{n_2}{c}\frac{dI(t)}{dt}L\right). \tag{2.20}$$

This change in instantaneous frequency results in the generation of new frequency components, shown in Figure 2.4. For the shown Gaussian pulse the newly generated higher frequency components arrive earlier while the lower frequency components trail behind, resulting in a positive chirp.

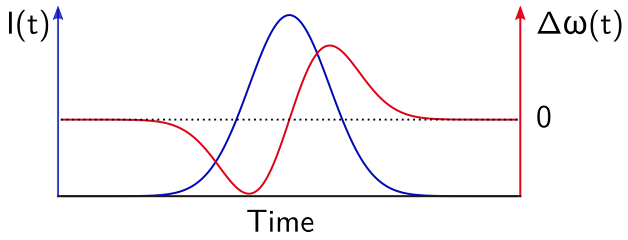

Figure 2.4: Illustration of self-phase modulation in medium with $\chi^{(3)} > 0$ and the intensity profile of a Gaussian laser pulse in blue and the change of the instantaneous frequency in red.

Self-focusing can occur in media with $n_2 > 0$ where higher intensities lead to a higher refractive index. For beam profiles such as a Gaussian mode, the spatial refractive index variation resembles a convex lens, thus causing a focusing effect. Diffraction effects lead to a divergence of the beam and these two effects cancel each other out at the critical power P_{cr}:

$$P_{cr} = \frac{0.61^2 \pi \lambda^2}{8 n_0 n_2}, \tag{2.21}$$

where $\lambda = 2\pi c/\omega$ is the wavelength. Remarkably, P_{cr} is independent of the initial beam diameter. Therefore self-focusing only occurs when the laser power exceeds P_{cr} and leads to a focus within the material during further propagation. This leads to the beam breaking up into several filaments in case the high intensities haven't resulted in prior optical damage of the material.

2.2 Electro-optic sampling

One well-established technique for measuring IR and THz waveforms is electro-optic sampling (EOS). For the few-THz spectral region, the following model lends itself for the explanation of EOS: the field strength of a test waveform E_{MIR} modulates the birefringence of an electro-optic crystal via the Pockels effect. An ellipsometry detection is set up such that this modulation is read out with sub-cycle temporal resolution by a by a delay-varied visible/near-infrared "gate" pulse, probing the momentary birefringence. Scanning the gate pulse over the test waveform yields the EOS trace. In the case of a test wave in the far infrared with a carrier frequency Ω and a NIR gate pulse with a much higher carrier frequency ω the electric field during the interaction can be assumed to be constant. Thus, the recorded EOS trace is proportional to the electric field of the test wave [68].

For test waves in the mid-infrared spectral region, the carrier frequencies Ω and ω are usually much closer and a frequency domain picture is more appropriate to describe the EOS process [52]. Here, in a first step the nonlinear interaction between the co-propagating test wave and the gate pulse in a nonlinear crystal results in SFG and DFG frequency components on the polarization axis orthogonal to that of the gate pulse. In a second step, the spatially and temporally overlapping frequency components interfere, resulting in a changed polarization state which is then detected for varying delays between the gate pulse and the test wave. In the following, equations for the magnitude of the EOS signal will be derived, in analogy to [52].

The second-order nonlinear processes of SFG and DFG between the electric field of the gate pulse $E_g(\omega_2)$ and the test wave $E_{MIR}(\Omega)$ results in the generation of frequencies $\omega_3 = \omega_2 + \omega_1$ and $\omega_4 = \omega_2 - \omega_1$, respectively. The nonlinear polarization as described in the previous section is given by :

$$P^{(2)}(\omega_3) = \epsilon_0 \chi^{(2)}(\omega_3) E_{MIR}(\Omega) E_g(\omega_2)$$
$$P^{(2)}(\omega_4) = \epsilon_0 \chi^{(2)}(\omega_4) E_{MIR}(\Omega) E_g^*(\omega_2)$$

and the resulting electric field after propagation in a nonlinear medium can then given by [52]:

$$E^{(2)}(\omega) = -i \int_{-\infty}^{\infty} f(\Omega) E_{MIR}(\Omega) E_g^*(\omega - \Omega) d\Omega. \tag{2.22}$$

Here, $f(\Omega)$ is a spectral response function containing the phase mismatch factor, the frequency dependent $\chi^{(2)}$ and other propagation effects. For a frequency ω within the spectral coverage of the gate-pulse contributions of the SFG and DFG processes can be found at the same frequency via $\omega_2 = \omega - \Omega$ and $\omega_2 = \omega + \Omega$, respectively. In the typical EOS geometry, the second-order nonlinear process is phase-matched for linearly polarized E_{MIR} and E_g on orthogonal axis and the resulting $E^{(2)}$ being on the same axis with E_{MIR}, see Figure 2.5. In order for interference between the spectrally overlapping E_g and $E^{(2)}$ to occur, they must be projected onto the same polarization axis. This is often achieved by employing a quarter-wave plate at 45° rotating the linearly polarized fields into circularly polarized ones. A subsequent Wollaston prism projects the light onto orthogonal axes, which are then detected by the two photodiodes of a balanced detector. The photocurrents of the two diodes are subtracted to yield the differential current ΔI. The phase shift $\Delta\varphi$ between the local oscillator derived from the gate pule and $E^{(2)}$ in this heterodyne detection can be defined as [53]:

$$\Delta\varphi = \frac{\pi}{2} + \varphi_0 \pm \Omega\tau \tag{2.23}$$

Here, τ is the relative delay between the gate pulse and the test wave and φ_0 corresponds to the delay independent phase shift arising for example due to the birefringence of the nonlinear crystal. The detected photocurrent at the balanced detector $\Delta I(\tau)$ can be described as [52]:

$$\Delta I(\tau) \propto \int_{-\infty}^{\infty} f(\Omega) e^{i\Omega\tau} \int_{-\infty}^{\infty} E_{MIR}(\Omega) E_g^*(\omega - \Omega) E_g(\omega) d\omega d\Omega \tag{2.24}$$

$$= \int_{-\infty}^{\infty} f(\Omega) E_{MIR}(\Omega) e^{i\Omega\tau} C(\Omega) d\Omega \tag{2.25}$$

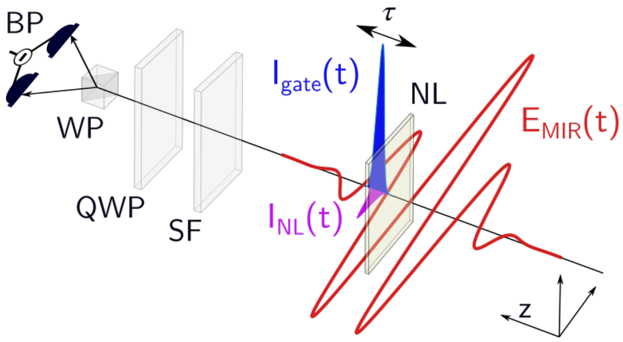

Figure 2.5: Schematic of the EOS as a two-step process. A MIR pulse ($E_{MIR}(t)$, electric field in red) and a variably delayed gate pulse ($I_{gate}(t)$ intensity envelope in blue) propagate along the z-axis and overlap in a nonlinear crystal (NL). The result of the nonlinear interaction ($I_{NL}(t)$, intensity envelope in purple), is polarized orthogonal to $I_{gate}(t)$. A quarter-waveplate (QWP) is placed such that a linear polarized gate pulse becomes circular polarized upon transmission. A Wollaston prism (WP) splits the beam onto its orthogonal polarizations, which are then sent onto balanced photodiodes (BP). $I_{NL}(t)$ results in a polarization rotation before the QWP and therefore into elliptical light after the QWP. The imbalance on the photocurrents is proportional to the poalrization rotation. Often only the spectral overlap between $I_{gate}(t)$ and $I_{NL}(t)$ is cut-out with a spectral filter (SF) to tailor the instruments response function and reduce noise from spectral regions not contributing to the heterodyne detection.

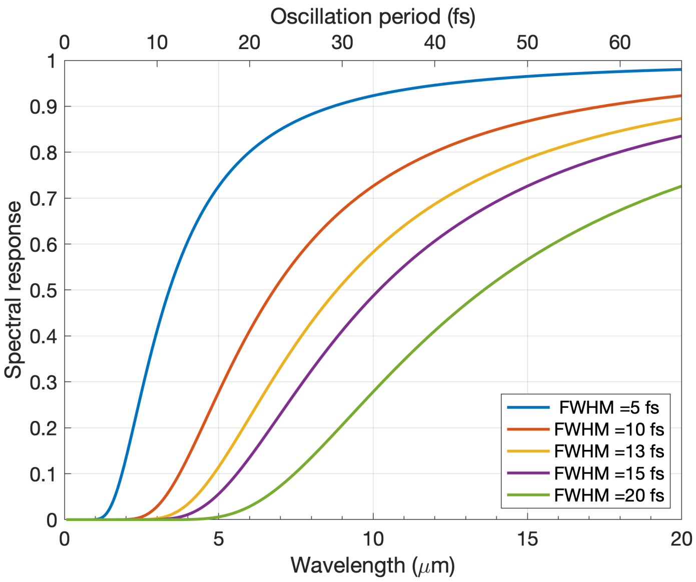

Figure 2.6: The absolute value of the Fourier transforms of the intensity envelopes of Gaussian pulses with various FWHM pulse durations are shown. Test-wave wavelengths (lower x-axis) or oscillation periods (top x-axis) for which this real-valued function is $\gg 0$ can be resolved via EOS.

The last term corresponds to the autocorrelation of the gate pulse spectrum, which corresponds to a multiplication of the Fourier transform of the intensity envelope of the gate pulse. In Figure 2.6, the spectral response of the intensity envelope is shown, elucidating the need of a gate pulse duration shorter than half a cycle of the test wave for sensitive detection. The EOS signal strength is thus proportional to field strength of the test wave E_{MIR} and the intensity of the gate pulse $I_g \propto E_g^* E_g$. The test wave can be retrieved via a division in the frequency domain for the case that the instrument response function $R(\Omega) = f(\Omega)C(\Omega)$ is precisely known. It can be obtained, e.g. via numerical simulation.

Noise contributions in heterodyne detection

The heterodyne detection step in EOS allows not only a phase-sensitive measurement but introduces a gain for the detection of a weak amplitude $E^{(2)}(\omega)$ by multiplying it with the local oscillator amplitude $E_g(\omega)$. A powerful local oscillator allows to lift the signal strength above other noise sources such as the dark current of the photodiode. But the local oscillator also introduces noise. One noise contribution is its relative intensity noise is proportional to its power and is correlated in both polarization axes and thus ideally canceled by the balanced detection of the ellipsometer [69]. The other noise contribution, the shot-noise, stems from the quantum nature of light. The measured light consists of an integer number of photons N following a Poissonian distribution with width $\sqrt{N}$ and an expectation value corresponding to the power of N photons with wavelength λ. The shot-noise strength increases, like the signal strength with the square root of the local oscillator power. In the case of a shot noise limited detection the signal-to-noise ratio (SNR) of the detected signal scales linearly with E_g and E_{MIR} and a single photon of the $E^{(2)}(\omega)$ field results in a SNR of 1. The shot-noise in the frequency domain can be calculated as follows:

The single-sided power spectral density s_q of a beam with wavelength λ and power P is frequency-independent (i.e., white) noise [70]:

$$s_q = \sqrt{\frac{2 \times hc}{P\lambda}}. \tag{2.26}$$

In case of a balanced detection, the white noise on both diodes is added, thus increasing it by a factor of $\sqrt{2}$. Furthermore, the power is split equally onto the diodes (P/2 per diode). Reflection and transmission losses of mirrors and optics as well as the imperfect quantum efficiency of the photodiodes lead to an effective reduction of the power by a factor of ν. With these considerations, the shot-noise dominated noise floor of a balanced detection is:

$$s_q = \sqrt{\frac{8 \times hc}{\nu P\lambda}} = 3.2 \times 10^{-8} Hz^{-0.5} \sqrt{\frac{1\,\mathrm{mW}}{\nu P}} \sqrt{\frac{1550\,\mathrm{nm}}{\lambda}} \tag{2.27}$$

Other common noise contributions in EOS detection include timing jitter, the uncertainty of the relative delay τ, and noise related to the test wave. Due to the fact that EOS detection is a multi-shot technique where the delay is scanned the test wave needs to be waveform stable, meaning that the CEP phase must remain constant during the measurement time.

2.3 Light-matter interaction

There are several types of interaction of electromagnetic waves with matter, such as absorption and emission, which are direct consequences of energy state transitions in the material. Among the plethora of existing energy states in matter, including nuclear spin states, rotational states, vibrational states and electronic states, in the following discussion we focus on the rotational (ro)-vibrational transitions of molecules in the gas phase. These transitions can be directly probed by photons of the same energy as long as they obey the corresponding selection rules. The molecule-specific transitions allow for the identification of molecules. The spectral region of the fundamental ro-vibrational modes lies within the MIR spectral range and is often referred to as the "molecular fingerprint region".

2.3.1 Ro-vibrational absorption lines

Ro-vibrational absorption lines originate from energy transitions between vibrational and rotational states of a molecule. In spectroscopy, the energy of the transition is often given in wavenumbers $\tilde{\nu} = \frac{E}{hc}$. The rotational energy E_{rot} of a linear diatomic molecule is dependent on the rotational quantum number J and the rotational constant B. In the rigid-rotor approximation, it is given by [71]:

$$E_{rot} = hcBJ(J+1). \tag{2.28}$$

The wavenumbers of the vibrational-rotational transition are then

$$\tilde{\nu} = \tilde{\nu}_{vib} + B''J''(J''+1) - B'J'(J'+1), \tag{2.29}$$

where $\tilde{\nu}_{vib}$ corresponds to the wavenumber of the vibrational transition and the quantum numbers with one and two primes correspond to the initial and final state, respectively. In this approximation, the molecular potential is a harmonic potential and all the transition lines are equidistant. Angular momentum conservation results in the change of J by only 1 from interaction with a photon and, thus, in the formation of the R-branch $\Delta J = +1$ and the P-branch $\Delta J = -1$. For vibrations in polyatomic molecules, where the vibration induces a dipole moment perpendicular to the molecular axis, the transition $\Delta J = 0$ is also allowed and forms the Q-branch.

In order to describe the likelihood rather than only the possibility of a transition, the spectral line intensity S_{ij} is used. The spectral line intensity between two rotational-vibrational states is dependent on the Einstein coefficient for spontaneous emission, the energy levels involved, and the temperature. The latter two can be used to calculate the probability to find a molecule in the initial state of the transition for an environment in thermal equilibrium.

The rotational constant is often of the same order of magnitude as the available energy at room temperature k_BT, leading to the population of higher rotational energy states at T>0. This leads to the characteristic form of the P- and R-branch, see Figure(2.7). Due to $\tilde{\nu}_{vib} \gg \frac{k_BT}{hc}$ at room temperature, in molecules in thermal equilibrium typically only the vibrational ground state is populated and, thus, the fundamental transition $\Delta\nu = +1$ has the highest probability. The frequency (i.e. the energy) of vibrational transitions with $|\Delta\nu| > 1$ are called overtones. Direct overtone transitions are only allowed due to the anharmonicity of the potential, which is usually weak. Consequently, overtones have much weaker Einstein coefficients and spectral line intensities.

Heisenberg's uncertainty principle links the energy uncertainty and the lifetime of an excited state. Spectral lines are never strictly monochromatic as this would require an infinitely narrow energy level. The temporal decay due to spontaneous emission, with the decay constant T results in the frequency domain in a Lorentzian line profile with the natural linewidth $\delta\nu = 1/(\pi c T)$ [72]. Among many other broadening mechanisms for spectral lines, the most prominent ones in gas spectroscopy are thermal Doppler and impact pressure broadening.

- Pressure broadening stems from the collisions of the molecules reducing the lifetime of the excited states and, thus, in a broader linewidth. All the molecules experience the same average rate of collision and the broadening is thus homogeneous and results in a Lorentzian lineshape. The half-width-at-half-maxima (HWHM) of the Lorentzian lineshape γ increases linearly with the pressure p of the environment. At standard pressure (that is 1013 mbar) this broadening is the dominant line broadening mechanism and results in typical values for the HWHM between 0.1 and 0.4 cm^{-1}. The environment of the molecules can also change the energy-level structure resulting in a pressure (density of environment) dependent shift δ of the center wavenumber.

- Doppler broadening occurs due to the Doppler effect, where the velocity of the molecule relative to the incident light results in a shifted light frequency in the frame of the molecule. This broadening is inhomogenous as it is different for separate molecules with their individual velocity. The velocity of the molecules in thermal equilibrium follow the Maxwell-Boltzmann distribution and results in a Gaussian line shape. In low-pressure (<1 mbar) environments Doppler broadening dominates. The Gaussian HWHM α_D is proportional to $\sqrt{T/m}$, where T is the temperature and m the mass of one molecule. At room temperature α_D is on the order of 10^{-3} cm^{-1}.

In order to account for both broadening mechanisms, the commonly used line profile is the Voigt profile, a convolution of the Gaussian and Lorentzian line shapes. The normalized line shapes are shown in Figure(2.7) and the their functions can be written as [73]:

$$f_{Lorentzian}(\nu;\nu_{ij},T,p) = \frac{1}{\pi}\frac{\gamma(p,T)}{\gamma(p,T)^2 + [\nu - (\nu_{ij} + \delta(p))]^2} \tag{2.30}$$

$$f_{Gaussian}(\nu;\nu_{ij},T) = \sqrt{\frac{\ln(2)}{\pi\alpha_D^2}}\exp\left(-\frac{(\nu-\nu_{ij})^2\ln(2)}{\alpha_D^2}\right) \tag{2.31}$$

$$f_{Voigt}(\nu;\nu_{ij},T,p) = \int_{-\infty}^{\infty} f_{Lorentzian}(\nu;\nu_{ij},T,p) f_{Gaussian}(\nu - n;\nu_{ij},T)dn. \tag{2.32}$$

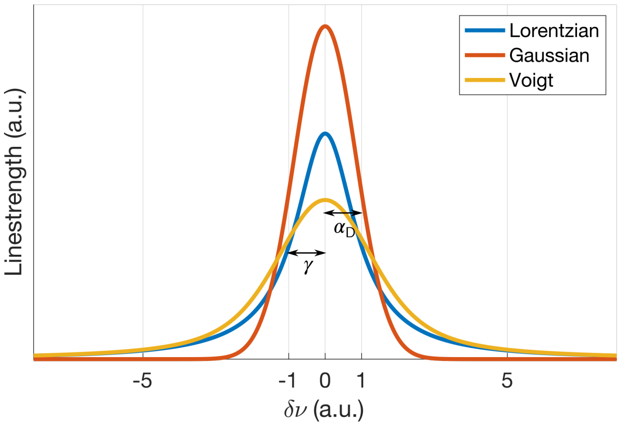

Figure 2.7: Common line profiles plotted versus their detuning $\delta\nu$ from the transition wavenumber and with areas normalized to one. α_D and γ correspond to the half width at half maxima of the Gaussian and Lorentzian profiles, respectively.

The absorbance at wavenumber ν of a homogeneous gas with path length ℓ and molar concentration c is then the sum of all contributing absorption lines weighted by their line strength:

$$A(\nu) = \sum_{ij} S_{ij}(T) f(\nu, \nu_{ij}, T, p) c\ell = \epsilon \ell c. \tag{2.33}$$

The last equivalence corresponds to the Beer-Lambert law with the molar attenuation coefficient ϵ.

2.3.2 Molecular response

Frequency domain

The Beer-Lambert law can be directly derived from classical electromagnetic theory, which is shown in the following in analogy to [74]. The electric field of light waves induce a polarization P in a medium and can be described in the frequency domain (in analogy to Equation 2.5)

$$P = \varepsilon_0 \chi E = \varepsilon_0(\varepsilon_r - 1)E \quad \Rightarrow \quad \varepsilon_r = 1 + \frac{P}{\varepsilon_0 E}. \tag{2.34}$$

Here, the second equation is rearranged for the relative permittivity ε_r. On the macroscopic level the polarization is directly proportional to the particle density N and their individual dipole moment p. Inserting this relation yields

$$\varepsilon_r = 1 + \frac{Np}{\varepsilon_0 E} = 1 + c\frac{N_A \alpha}{\varepsilon_0}. \tag{2.35}$$

The second equality is based on the relations $N = N_A c$, with the molar concentration c and the Avogadro constant N_A, as well as $p = \alpha E$ with the polarizability α. For homogeneous, isotropic, non-magnetic materials the relative permittivity relates to the complex refractive index via $\tilde{n}^2 = \varepsilon_r$. The refractive index then becomes (compare Equation 2.6):

$$\tilde{n} = \sqrt{1 + c\frac{N_A \alpha}{\varepsilon_0}}. \tag{2.36}$$

For gases in small concentrations the refractive index is close to unity, allowing the approximation $\sqrt{1+x} \approx 1 + x/2$. The complex part of the refractive index κ corresponds to the extinction coefficient and with the complex part of the polarizability α'' it can be written as:

$$\kappa \approx c\frac{N_A \alpha''}{2\varepsilon_0}. \tag{2.37}$$

Using Equation 2.7 one can find the Beer-Lambert law:

$$A = -\log_{10}(T) = -\log_{10}\left(\frac{I_{in}\exp(-\kappa 4\pi\nu\ell)}{I_{in}}\right) = \underbrace{\frac{2\pi\log_{10}(e) N_A \alpha''\nu}{\varepsilon_0}}_{=\epsilon}\ell c = \epsilon\ell c. \tag{2.38}$$

The linear dependence of the absorbance on the concentration is therefore only an approximation for small concentrations where $\chi \ll 1$. Furthermore, effects like scattering, optical gain or interaction between molecules are assumed to be be negligible. In gases this mostly holds true, but it deviates for higher concentrations. For instance, pressure broadening depends on the interacting molecular species thus resulting in different broadening factors.

Time domain

The ultrafast, resonant excitation of vibrational states leads to a distinct molecular response in the time domain, see Figure 2.8 for the molecular response of the C-O stretch of methanol. Laubereau and Kaiser [72] derived the formalism used in the following discussion for vibrational dynamics from semi-classical electromagnetic theory, where light is treated as a classical electromagnetic field and the sample as a two-level quantum-mechanical system.

The amplitude envelopes of the electric fields propagating along the z-axis are denoted by $A(z,t)$ and $A_0(t) = A(0,t)$ is the incident field before propagation through the material. The light is attenuated by $\exp(-(\alpha_1 + \alpha_2)z)$, where α_1 corresponds to the non-resonant attenuation and α_2 to the resonantly absorbed light. The amplitude of the propagating light can then be described by [72]:

$$A(z,t) = A_0(t)\exp\left(-\frac{\alpha_1 z}{2}\right) - \frac{\alpha_2 z}{T_2}\exp\left(-\frac{t - t_{max}}{T_2}\right)\underbrace{\frac{\sqrt{J_1(\varepsilon)}}{\sqrt{\varepsilon}}}_{\overset{\varepsilon\to 0}{\approx} 1/2}\int_{-\infty}^{t} A_0(t')\exp\left(-\frac{\alpha_1 z}{2}\right)dt'. \tag{2.39}$$

Where t_{max} corresponds to the time of maximum $A_0(t)$, T_2 is the lifetime of the excited state, J_1 is the Bessel function of the first order and $\varepsilon = \frac{2\alpha_z(t-t_{max})}{T_2}$. The non-resonant attenuation leads to an instanstaneous response and the resulting amplitude will be referred to as $A_{inst}(z,t) = A_0(t)\exp(-\alpha_1 z/2)$. The second term contains the resonant part of the molecular response. The minus sign corresponds to a π phase delay of the coherently emitted light by the vibrating molecules with respect to the excitation field, leading to a dip in the molecular response, see Figure 2.8b). In the case of a small depletion of the excitation $\alpha_2 z \ll 1$, the fraction with the Bessel function approaches a constant. For a frequency detuning $\Delta\omega = \omega_0 - \omega$ of the carrier frequency ω of the excitation from the resonance frequency ω_0 of the absorption an additional term $\exp(-i\Delta\omega t)$ leading to oscillations must be introduced. Equation 2.39 can then be rewritten [75] as

$$A(z,t) = A_{inst}(z,t) - \frac{\alpha_2 z}{2T_2}\Theta(t - t_{max})\exp\left(-(t - t_{max})(T_2^{-1} - i\Delta\omega)\right)\int_{-\infty}^{t} A_{inst}(z,t')dt', \tag{2.40}$$

with the Heaviside step function Θ. Here, the resonant molecular response ($\Delta\omega = 0$) decays exponentially $exp(-t/T_2)$. The amplitude is linearly proportional to the attenuation coefficient α_2. Employing the small concentration approximation in the Beer-Lambert law (Equation 2.37) this also implies that the amplitude of the resonant coherent response is proportional to the number of excited molecules.

In the case of an excitation much shorter than the time constant of the decay T_2 the excitation (first term of Equation 2.40) and the resonant molecular response (second term of Equation 2.40) overlap only for small t. For large t, the excitation has decayed and only contributions of the molecular response remain. This characteristic can be taken advantage of with regards to sensitivity in time-domain spectroscopies, e.g. in upconversion [75, 76] and in EOS [55]. Furthermore, the separation in time makes the detection sensitivity robust against excitation noise. Note that such a separation can also be implemented in space by interferometric subtraction [77, 78].

For a broadband excitation and a sample with multiple absorption features the time domain response constitutes of the interference of all the excited oscillators. In Figure 2.8 the molecular response of a typical gas sample with its Q-,P- and R-branch is depicted. The strong, single peaked Q-branch leads to an initial exponential decay of the molecular response after excitation (panel b)). The nearly equidistant ($1/T_{equ}$) absorption lines of the R- and P-branches lead to constructive interference after T_{equ} manifesting itself as ringing in the time domain. The anharmonicity of the potential (deviation from the rigid-rotor approximation) leads to increasing distances between the absorption lines and a smearing out of ringing, see the spectrogram in panel d).

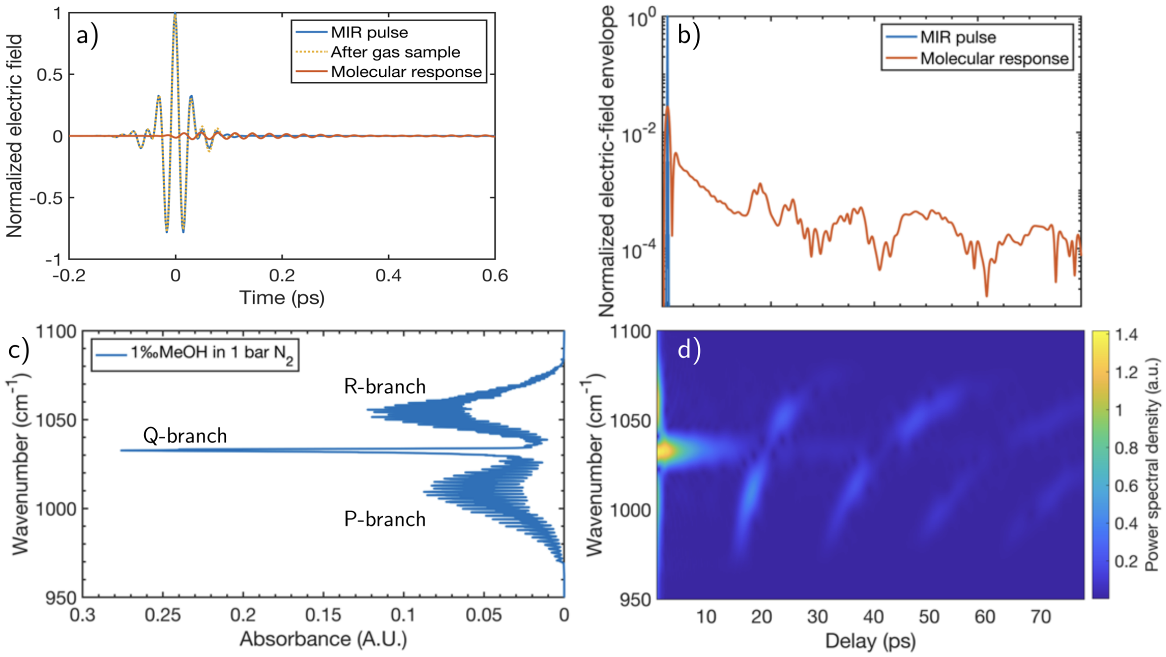

Figure 2.8: Resonant molecular response of methanol around its absorption lines of the C-O stretch with line data taken from the high-resolution transmission molecular absorption database (HITRAN) [73, 79]. a) Electric field of a MIR pulse before and after a 45 cm long gas cell filled with methanol at a 0.1 % concentration in 1 bar nitrogen. In red the subtracted fields are shown and constitute the impact of the molecular response. b) Logarithmic representations of the electric-field envelopes. c) Absorption lines of the C-O stretch. d) Spectrogram of the molecular response using 1 ps time windows.

Chapter 3

Bright source of coherent, few-cycle infrared pulses

This chapter presents several aspects of the development an FRS instrument based on a thulium fiber laser and starts with some details of the frontend and the demonstrated CEP stability in section 3.1. The first demonstration of the field-resolved detection with this system is presented in section 3.2.1. Followed in section 3.2.2 by a more detailed investigation of the self-compression in PCFs and the approach of supercontinuum generation to spectrally cover the entire molecular fingerprint region. The generation of waveform-stable MIR pulses in GaSe via IPDFG is discussed in section 3.3. The long-term stability of the MIR power and the choice of a working point for the self-compression in the PCFs is discussed in section 3.4. Furthermore, the time-domain aspect of the detection scheme warrants consideration of the spectral phase and the dispersion management in the MIR spectral region is discussed in section 3.5.

3.1 CEP stable femtosecond frontend

3.1.1 High-power frequency comb at $2\,\mu$m wavelength emitted by a Tm-doped fiber laser system

This section is identical[1] in wording and figures to the paper with the title "High-power frequency comb at $2\,\mu$m wavelength emitted by a Tm-doped fiber laser system" published in Optics Letters, vol. 43, no. 21, p. 5178, 2018 [80]. As one of the authors[2] I performed the characterization of the f-2f setup and built the FROG setup for pulse characterization.

---

[1] only the numbers of the references, figures and tables are changed for consistency throughout the thesis

[2] authors: Christian Gaida, Tobias Heuermann, Martin Gebhardt, Evgeny Shestaev, Thomas Patrick Butler, Daniel Gerz, Nikolai Lilienfein, Philipp Sulzer, Marc Fischer, Ronald Holzwarth, Alfred Leitenstorfer, Ioachim Pupeza, Jens Limpert

A detailed author contribution is found here[3].

Abstract

We report on the generation of a high-power frequency comb in the 2 μm wavelength regime featuring high amplitude and phase stability with unprecedented laser parameters, combining 60 W of average power with <30 fs pulse duration. The key components of the system are a mode-locked Er :fiber laser, a coherence-preserving nonlinear broadening stage, and a high-power Tm-doped fiber chirped-pulse amplifier with subsequent nonlinear self-compression of the pulses. Phase locking of the system resulted in a phase noise of less than 320 mrad measured within the 10 Hz-30 MHz band and 30 mrad in the band from 10 Hz to 1 MHz.

Main text

Optical frequency combs are of indispensable relevance for precision metrology [81], spectroscopy [82, 83], atto-science [84], and related application fields that are constantly explored [85–87]. In parallel, the requirements on optical frequency combs for next generation applications are ever-growing and comprise of wide spectral bandwidth, high power per comb-line, low phase noise and at the same time, high stability, compactness, and environmental robustness. Among the most prominent, robust, and compact sources for optical frequency combs are modelocked Er-doped fiber lasers, which typically cover a spectral region centered at 1.55 μm [88]. Highly nonlinear fibers (HNLF) are often employed for spectral broadening to the whole transparency range of silica fibers (350-2400 nm), but careful attention must be paid to the degradation of spectral coherence and gain of excessive amplitude noise due to the nonlinear processes involved [89, 90]. Power scaling of Er-fiber-laser-based frequency combs has so far remained relatively challenging [91] and promising alternatives are found with Yb-doped gain media in the 1 μm wavelength regime providing 10-100 W average power levels [92, 93].

Frequency combs at around 2 μm wavelength are currently of tremendous interest for next-generation spectroscopy targeting sensitive detection of certain gases (e.g., CO_2, NH_3) [94, 95] and/or to further extend the wavelength coverage of frequency combs to the molecular fingerprint region (3-20 μm) via parametric downconversion in nonlinear crystals [28, 96]. With only very few exceptions [44, 97], nonlinear crystals with high transmission in the mid-IR (>5 μm) are opaque at around 1 μm wavelength or high-power operation is severely limited by multiphoton absorption, exactly where the most powerful driving lasers operate [98]. It is for that reason that the development of powerful laser sources at wavelengths >1.5 μm are in urgent demand by a large community, which targets next-generation metrology and spectroscopy and relies on powerful frequency combs in the mid-IR. Access to the 2 μm wavelength regime by direct laser emission is possible through thulium- or

---

[3] Author contributions: Conceptualization: IP; Frequency shift: PS; f-2f: TPB, DG, MF, RH; Data curation: CG, TH, MG; Analysis: CG, TH, MG, ES; Initial writing: CG; Supervision: IP, JL, AL ; Review and editing: all authors.

holmium doped gain media. Such lasers have recently attained 100 W-class average power in ultrafast operation [36, 46, 99], but frequency combs have so far not been realized with average powers beyond the few-W-level [100]. In this work, we present a frequency comb emitted by a Tm-doped fiber chirped-pulse amplification system (TmFCPA) with an unprecedented average output power of 60 W at 100 MHz pulse repetition rate and <30 fs pulse duration, featuring low relative intensity and phase noise.

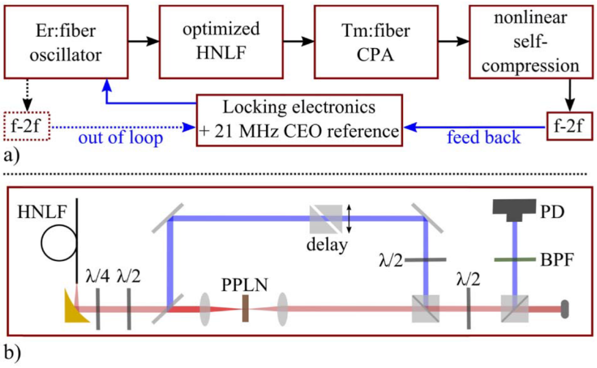

Figure 3.1: (a) Schematic of the experimental setup comprising an Er :fiber based mode-locked oscillator (ErFO), a highly-nonlinear fiber (HNLF) for coherent spectral broadening to seed the TmFCPA and a nonlinear self-compression stage. A home-built f-2f interferometer provides a beat-note signal, which can be fed back to the ErFO phase locking electronics (feed-back loop). Alternatively, a separate f-2f interferometer can be used to solely phase-lock the ErFO. (b) Setup of the home-built f-2f interferometer. PPLN, periodically poled lithium niobate; BPF, bandpass filter; PD, photodiode.

The experimental setup is schematically depicted in Figure 3.1(a) and is comprised of a modelocked Er:fiber oscillator/amplifier (ErFO) (Menlo Systems C-Fiber High Power), a nonlinear broadening stage utilizing a HNLF, a TmFCPA, and a nonlinear solid-core fiber self-compression stage. The seed ErFO provides pulses at 100 MHz repetition rate with a central wavelength of 1.55 μm and allows control over the carrier-envelope offset frequency (CEO) as well as stabilization of the pulse repetition frequency. An integrated f-2f interferometer is used to lock the ErFO CEO frequency to a flexible master frequency. The output of the ErFO is coupled to a germano-silicate fiber assembly with a core diameter of 4 μm and a length of 7 mm. The short fiber length is beneficial for preserving the coherence of the spectrally broadened output, which extends from 1500 to 2000 nm (−20 dB bandwidth). The pulses are subsequently coupled to an all-fiber pulse stretcher that includes a chirped fiber Bragg grating (CFBG) with a spectral hard-cut of 55 nm (−20 dB bandwidth) centered at 1960 nm. The stretched pulses have a duration of 550 ps (FWHM) and are amplified in a cladding-pumped thulium-doped step index fiber, boosting the average power from 0.05 to 300 mW. The main amplifier is a single-mode, double-clad, Tm-doped photonic crystal fiber with a 3 m length and 36 μm mode-field diameter (MFD). Co-pumping the fiber with 280 W at 793 nm wavelength allows for 90 W of average output power. The amplified pulses are compressed to 250 fs duration in a Treacy compressor with

78 % total efficiency (70 W compressed output power). The high-average-power sections of the system are operated in vacuum to avoid detrimental water absorption effects in the atmosphere [101]. The pulse duration is further reduced by incorporating a large pitch fiber [102] with 56 μm MFD and 5.6 cm length as nonlinear self-compression stage.

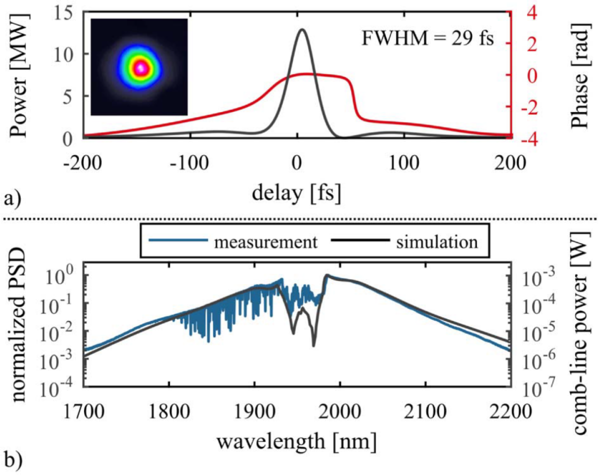

Figure 3.2: (a) Simulated pulse and (b) simulated and measured spectra after the nonlinear self-compression fiber output. The measured spectrum shows water absorption features due to transmission through air to the spectrometer. The inset shows the measured beam profile after the nonlinear compression at 60 W of average power.

This self-compression scheme is explained in detail in Ref. [99] and exploits the intrinsic anomalous dispersion of fused silica above 1.3 μm wavelength, which counteracts the positive chirp induced by self-phase modulation. Taking advantage of self-compression of the pulse during its nonlinear broadening requires the optimization of the setup with respect to the pulse peak power, mode-field diameter (MFD), fiber length, and dispersion [99, 103]. In order to determine the optimum fiber length of 5.6 cm, we simulated the pulse evolution for a MFD of 56 μm incorporating the laser parameters of the TmFCPA. The simulation is based on solving the non-linear Schrödinger equation including higher-order dispersion, intrapulse Raman scattering, and self-steepening [104]. Figure 3.2 shows the simulation result for circular polarization predicting a peak power of 14 MW and a pulse duration of 29 fs, corresponding to 600 nJ pulse energy. The resulting power per comb-line is >1 μW in the spectral range 1700-2200 nm.

The spectrum and frequency-resolved optical gating (FROG) spectrogram of the pulse were measured in air after transmission through a 2 mm potassium bromide (KBr) window with a homemade FROG device. Figure 3.3 compares the retrieved FROG pulse and spectrum to the simulation, which in this case accounts for the transmission of the pulse through the KBr window. Both the measured spectrum and the FROG retrieval show excellent agreement with the simulated pulse.

The carrier-envelope phase stability of the compressed output is characterized by generating a beat note in a home-built f-2f interferometer optimized for input pulses at around

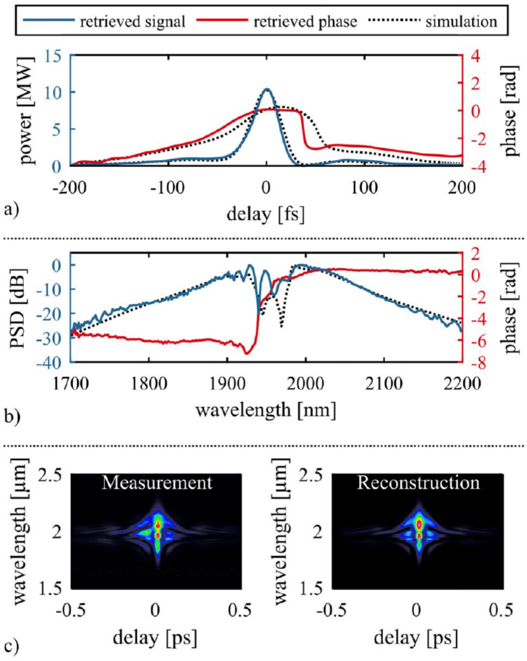

Figure 3.3: Retrieved SHG-FROG showing (a) temporal and (b) spectral intensity and phase measured after 2 mm KBr window and comparison to the simulation. (c) Measured and reconstructed FROG-Traces.

2 μm wavelength, which is schematically depicted in Figure 3.1(b). A 4 % fused-silica Fresnel-reflection of the high power output is sent to the f-2f interferometer setup, which includes a fused-silica HNLF with a core diameter of 4 μm, zero dispersion wavelength of 1560 nm and 8 cm length. The power level to the HNLF is further reduced with a pinhole. The HNLF-output contains a dispersive wave centered at 980 nm wavelength, which is separated from the remaining long wavelength output with a dichroic mirror and sent to the first interferometer arm which additionally contains two fused silica wedges for fine tuning of the temporal delay. The long wavelength part of the spectrum is focused into a periodically poled lithium niobate crystal for second harmonic generation (SHG). The dispersive wave and the SHG signal are combined in a polarizing beam splitter and brought to interference in a second polarizing beam splitter. A 10 nm optical bandpass filter centered at 980 nm supresses non-overlapping spectral components of the two beams. An amplified InGaAs photo-diode (Thorlabs PDA05CF2) is used for characterizing the RF spectrum.

In a first step, the ErFO is phase-locked utilizing the beatnote of the integrated f-2f interferometer while the rest of the system is operated "free-running". The home-built f-2f interferometer is optimized to measure a high contrast beatnote after the nonlinear compression stage for <30 fs pulses at 60 W of average output power. Critical optimization parameters for obtaining the highest possible beatnote contrast are good spatial, temporal and spectral overlap of the interfering pulses. With a resolution bandwidth (RBW) of 300 kHz, a beatnote with 28 dB signal to noise ratio (SNR) is obtained [Figure 3.4(a)]. A detailed scan at 50 Hz RBW reveals a SNR of the beatnote exceeding 50 dB [Figure 3.4(b)]. The obtained RF signal from the home-built f-2f interferometer is electronically filtered with a low-pass filter in order to obtain the maximum information on the phase stability up to 30 MHz. For "in-loop" phase stabilization of the entire system to the CEO-frequency of 21 MHz, the ErFO was locked to the signal provided by the f-to-2f interferometer at the CPA output.

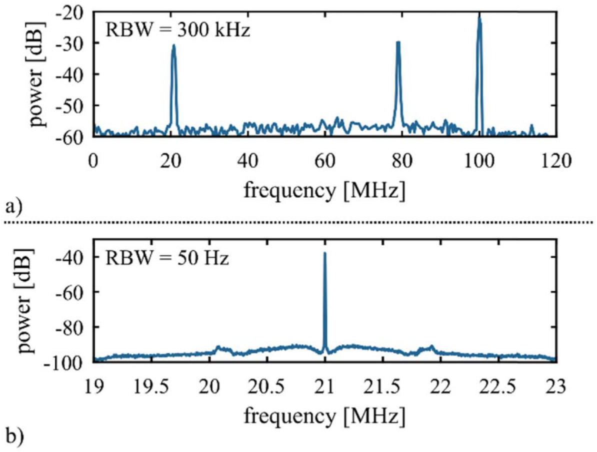

Figure 3.4: Measured RF-signals of the f-2f interferometer after the nonlinear compression stage at 60 W of average output power with a resolution bandwidth (RBW) (a) of 300 kHz and (b) of 50 Hz.

The phase stability of the system is analyzed in two steps. At first, the phase stability of the actively phase-locked ErFO is determined. Figure 3.5(a) shows the power spectral density (PSD) and integrated phase noise of the ErFO, which is obtained from the RF-spectrum of the integrated f-2f interferometer. The phase stability is <100 mrad for an RF-span of 10 Hz-30 MHz and the most noise is accumulated between 100 kHz and 30 MHz with the upper limit due to the lowpass characteristics of our measurement setup. In a second step, the beatnote generated by the home-built f-2f interferometer is sent to the locking electronics for in-loop stabilization of the entire system while the system delivers 30-fs pulses and 60 W of average power. Figure 3.5(b) (top) visualizes the power spectral density (PSD) and integrated phase noise revealing a phase stability of 320 mrad within a 10 Hz-30 MHz frequency range. Similar to the observation of the phase noise measurement of the ErFO alone, most noise contributions are accumulated at frequencies between 100 kHz and 30 MHz. Several conclusions can be drawn from this observation. Relatively slow phase instabilities at frequencies <100 kHz, that are added by the system components after the ErFO, can be sufficiently corrected by the locking mechanism during in-loop operation. The higher frequency noise >100 kHz is already weakly present at the ErFO and is obviously enhanced in the subsequent parts of the system. In order to investigate the source of the high-frequency noise, we have additionally measured the amplitude noise of the high-power nonlinearly compressed output. The result is depicted in Figure 3.5(b) (bottom) revealing a total relative intensity noise (RIN) of less than 0.5 %. Amplitude noise contributions are found at low frequencies <100 Hz, which are likely caused by slow beam fluctuations or vibrations in the TmFCPA. Interestingly, the main noise contribution is detected at frequencies >10 MHz MHz. The presence of high frequency amplitude noise obviously impacts the phase noise measurement in the f-2f interferometer. We have verified this in two different ways. First, we block either arm of the f-2f interferometer and found that the high-frequency noise, although weaker than before, was still detected. Second, we detuned the delay in the f-2f interferometer until the beat note disappeared completely, which resulted in a remaining broad noise floor. From this it is possible to estimate the total contribution of amplitude noise that contributes to the measured integrated phase noise value of 320 mrad, which is on the order of 20 %-30 %. It is important to note that the power of the broad noise floor significantly increased when optimizing the delay of the f-2f interferometer for highest beatnote contrast, which clearly indicates that the broad high frequency noise exists both as phase and amplitude fluctuations.

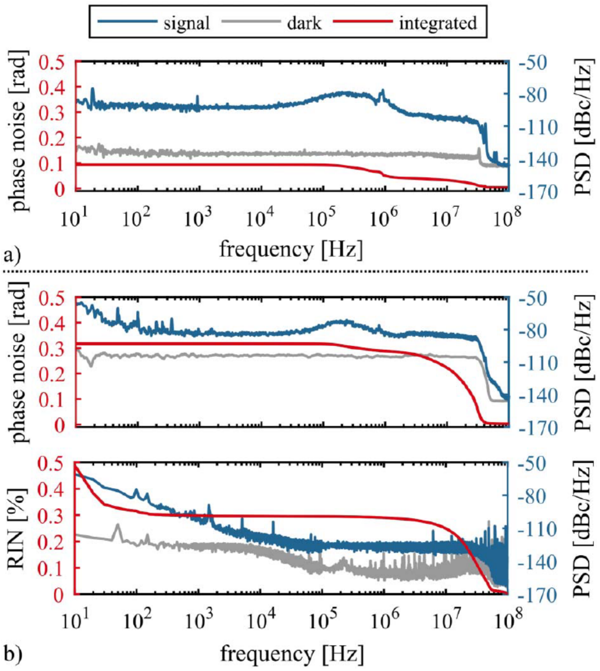

Figure 3.5: Measurement of the carrier-envelope phase noise of (a) the oscillator only. (b) The entire system in loop (top) and the amplitude noise spectrum (bottom) at 60 W of average output power.

Although it is difficult to conclusively identify the origin of the white-noise-like phase and amplitude instability, several possibilities can be named. Other studies have previously observed that quantum noise in nonlinear processes (e.g., modulation instability) can lead to white-noise-like fluctuations of phase and amplitude [89, 90]. Additionally, if amplitude noise is present prior to nonlinear processes, a coupling to phase noise can be expected [89, 90, 104]. As a consequence, white-noise-like instability contributions are accumulated in the nonlinear broadening stage prior to the TmFCPA or at the high-power nonlinear self-compression after the TmFCPA or even in the HNLF utilized in the f-2f interferometer. In fact, we have observed that reducing the HNLF length in the broadening stage after the ErFO prior to the TmFCPA helped to reduce the white noise contribution, which is equivalent to minimizing the loss of coherence during the nonlinear broadening process. Further improvements could be achieved by optimizing the system prior to this broadening stage with respect to amplitude noise and shortest possible pulse duration. These approaches have been extensively discussed in Refs. [90, 105]. Another promising possibility is to avoid nonlinear processes whenever possible, e.g., by utilizing the direct emission of a phase-lockable thulium-doped fiber oscillator [106]. Moreover, we have observed a slight degradation of 2-3 dB of the beatnote contrast at 300 kHz RBW from the f-2f interferometer when operating at the final system output parameters (<30 fs, 60 W) as compared to slightly lower power values/slightly longer pulses. We expect that further improvements of the system stability in terms of amplitude noise can lead to even higher phase stability in the future.

The laser system presented in this Letter provides a frequency comb with broad spectral coverage (1700-2200 nm), ultrashort pulse duration (<30 fs), and high average power (>60 W). In comparison to conventional characterization of phase stability published elsewhere [100], the system provides <30 mrad and <0.2 % RIN in an RF-band spanning 10 Hz-1 MHz, which is a remarkable result considering the high power per combline of >1 μW. In the course of our study, we have unveiled the necessity to expand the noise characterization to the high frequency realm for fiber-based sources that involve nonlinear processes. We have optimized the system with regard to phase and amplitude noise by following known approaches [89, 90, 104] and have demonstrated a high phase stability of 320 mrad and low RIN <0.5 % in an RF-band spanning 10 Hz–30 MHz. The presented laser is an ideal laser source for metrology and spectroscopy with unprecedented acquisition time and sensitivity in the 2 μm wavelength regime. Furthermore, this source can be utilized for parametric mid- IR generation paving the way for powerful frequency combs in the molecular fingerprint region (2-20 μm).

3.1.2 Pulse picker and spectrum of Raman shift

In the rest of the thesis the spectral shift from 1550 nm to 1965 nm was performed in a custom-made, all-fiber setup from Menlo Systems GmbH. This all-fiber setup circumvents losses and noise introduced by free-space propagation and coupling into the fiber of the TmFCPA. Measurements of the CEP after the TmFCPA using this seed revealed a broadband higher frequency noise (>100 kHz) that was stronger than shown in Figure 3.5. Tests for finding the origin of this source narrowed it down to the amplifier and spectral shift. Similar to the findings with the other seed, instabilities in the nonlinear shift seem to be the most likely source.

This setup also includes a pulse picker, which divides the 100 MHz repetition rate of the oscillator by an integer. A reduced repetition rate allows to operate the laser system at lower average power, but at the same pulse energy. Using the same pulse energy and shape results in the same peak intensities, which is important for the subsequent nonlinear processes. Effects dependent on the average power, such as thermal lensing alignment or heating of absorbing optics in damage analysis, can thus be directly tested for. Furthermore, the total output power of the laser system is limited by the average power of the employed pump diode and limits of the peak power set by the self-focusing limit. Reducing the repetition rate allows to scale the pulse energies up to the damage thresholds of the optical components.

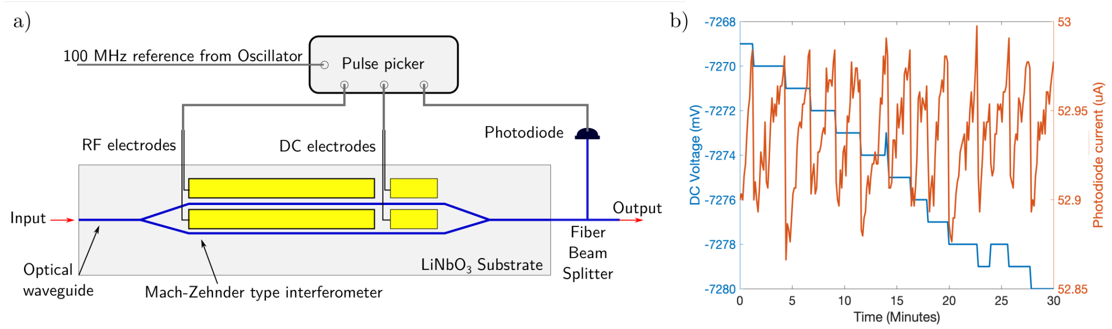

Figure 3.6: Pulse picker. a) Schematic of the LiNbO$_3$-based Mach-Zehnder Modulator. b) Typical compensation for DC-drift with the photodiode current as feedback.

The pulse picker is based on a Mach-Zehnder Modulator and depicted in Figure 3.6 a). The pulse propagates in an optical waveguide made from LiNbO$_3$ and shaped like a Mach-Zehnder-type interferometer. At one of the arms, electric fields can be applied through the RF and DC electrodes. The strength of the applied electric field results in a proportional change in the refractive index through the linear electro-optic effect (also known as Pockels-effect). Thus, the optical pathlength difference of the two interferometer arms can be adjusted to result in either destructive or constructive interference. The input pulse train can thus "be thinned out" by periodically switching between constructive and destructive interference via the voltage of the electrodes.

The device-specific required voltage to change between destructive and constructive interference was determined to be 1669 mV and can be applied within nanoseconds to the RF electrodes. The timing of the applied boxcar-shaped RF voltage is triggered by a 100-MHz reference derived from the repetition rate of the oscillator. With an RF voltage set to zero, the DC voltage is used to set the path-length difference to the most effective destructive interference, by minimizing the intensity of light impinging on a subsequent photodiode.

The required DC voltage suffers from drifts due to environmental changes, such as temperature, humidity and static electrical charge accumulation [107, 108]. The photocurrent of a photodiode after the interferometer acts as a feedback signal for the stabilization via locking electronics. The compensated drift is shown in Figure 3.6 b), where the DC voltage is regulated in 1-mV steps to lock the approximately linear drift of the photodiode current to an average current of 52.92 μA. The pulse picker can apply a maximal DC amplitude of 10 V and this limit is reached typically after a few days. Afterwards, the DC voltage is set to the next minimum of the photocurrent within the applicable range, typically around 6668 mV away, which corresponds to four times the RF amplitude value.

The pulses exciting the pulse picker are amplified and send through an HNLF for generating light in the desired spectral region of 1950-2000 nm via a Raman shift. A chirped fiber Bragg grating (CFBG) with a hard cut-off centered at 1960 nm with a width of 55 nm then elongates the pulse to around 550 ps and the reflection is used as a seed pulse for the consecutive two-stage CPA based on thulium-fiber technology. In Figure 3.7 a) the spectra of pulses transmitted through the CFBG together with the cut-off are shown. By tuning the current of the pumpdiode used in the amplifier, the pulse energy in the HNLF and thus the Raman shift can be tweaked.

Figure 3.7 b) shows the power spectral density (PSD) for different current settings. Even without a major change of the spectrum shown in a) the PSD can change by more than one order of magnitude for frequencies above 10 kHz. This indicates that the spectral shift is very sensitive to the pulse energy and requires careful optimization with respect to noise.

The combination of a pulse picker with a nonlinear shift and subsequent spectral filtering allows a high degree of suppression of unwanted pulses. For the reason that small pulse energies after destructive interference result are too small to shift the spectrum in the HNLF to the cut-off region of the CFBG.

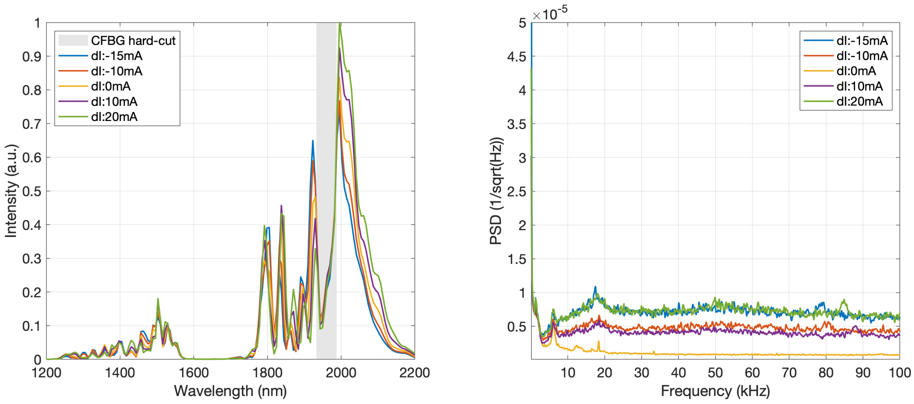

Figure 3.7: Seed spectra and associated power spectral density. Left: The result of the Raman shift of the oscillator pulses centered at 1550 nm and the hard cut-off from the CFBG. The energy of the pulses going to the HNLF for the Raman shift is tuned by adjusting the pump current of the prior fiber amplifier around 533 mA. Right: Associated power spectral density of the reflection of the CFBG.

3.1.3 Pulse characterization with frequency-resolved optical gating

The characterization of ultrashort pulses is essential for their utilization and optimization. Modern electronic oscilloscopes and photodiodes are able to access pulse durations on time scales of picoseconds. For optical pulses with durations on the femtosecond time scale the most common approaches utilize nonlinear processes. The simplest device is the intensity autocorrelator, where a pulse is split into two identical copies, which are then focused and overlapped in a nonlinear crystal with a $\chi^{(2)}$ nonlinearity. The delay between the two pulses is scanned and the intensity of the beam emerging from the nonlinear process (often SHG) is measured with a photodiode. In a non-collinear geometry, the SHG beam stemming from the interaction of the two copies emerges in a different direction due to momentum conservation and can be spatially isolated with a hard aperture. This autocorrelation signal corresponds to a convolution of the intensity envelope of the pulse with itself. Assuming a certain pulse shape, the pulse duration as the only remaining free parameter can be obtained by dividing with the appropriate deconvolution factor, e.g. $\sqrt{2}$ for a Gaussian and 1.54 for a sech^2 pulse shape.

Here, the intensity autocorrelation was used for routine checks of the pulse duration after the CPA, as it is particularly well suited for monitoring purposes. However, it cannot provide the shape of an unknown pulse because it does not provide its spectral phase information. Several methods have been developed for the characterization of the spectral phase, such as frequency-resolved optical gating (FROG)[109], spectral phase interferometry for direct electric-field reconstruction (SPIDER) and dispersive scans (d-scan)[110]. These methods have in common that they extend the measurement of the result of the nonlinear process to the spectral domain. In the following, the SHG-FROG setup built for the characterization of the NIR pulses is described.

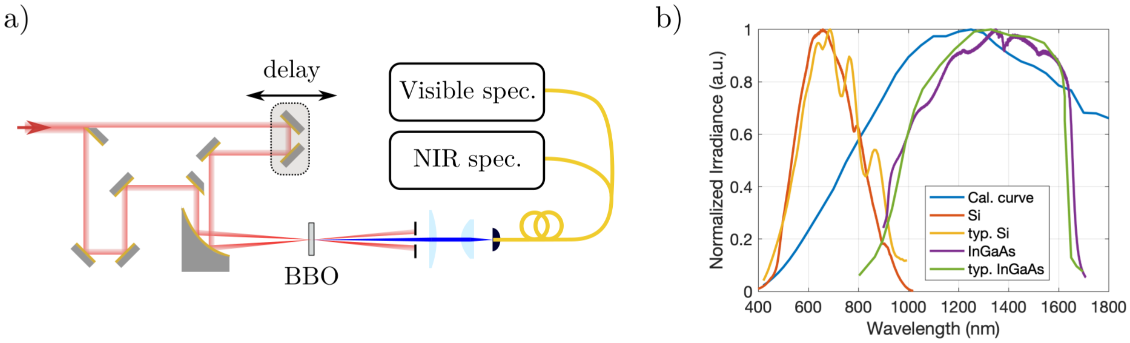

Figure 3.8: Spectral response of grating spectrometer with typical sensor materials. In blue, the theoretical irradiance of a calibration lamp (Ocean Optics, HL-3, HL-CAL-EXT) and in red and purple the results of the spectrometers used for the FROG (red: FLAME-S-VIS-NIR-ES, purple: NQ51B05551). In order to obtain the actual intensity from the spectrometer measurement a calibration factor for each wavelength is required, which was obtained by division of the expected (blue curve) by the measured irradiance.

The schematic of the built SHG FROG is shown in Figure 3.8 a). Compared to the previously described autocorrelator measuring the intensity, here a spectrum of the SHG beam is measured for each delay, resulting in a so-called FROG trace. For the setup, dispersion o transmissive optics were avoided as far as possible in order to retain the fidelity of the input pulse. Instead of a beam splitter a D-shaped mirror was used for splitting the pulse into two copies and a 2"- focal-length parabolic mirror was employed for focusing onto the nonlinear crystal. The phase matching bandwidth in the nonlinear crystal can be a limit for the shortest measurable pulse duration. Here, a 10-μm and a 20-μm thick Beta Barium Borate (BBO) crystal ($\theta = 23°$) were tested for pulses with durations above 10 fs. No significant difference in the spectral shape of the SHG beam were identified and the 20-μm thick crystal was employed because of the stronger signal (the SHG signal strength increases with the square of the crystal thickness in the non-depletion regime, see Equation 2.13).

The SHG spectrum of a pulse with a center wavelength of 2 μm is centered around 1 μm in case of a sufficiently broad phase matching bandwidth. The spectral response of the most commonly used sensor materials silicon and InGaAs typically drops significantly in this spectral region, see Figure 3.8 b). In order to measure the whole SHG spectrum, two spectrometers were used simultaneously at each delay. The spectrometers were calibrated using a fiber-coupled halogen calibration light source. In order to merge the two FROG traces all spectral components below 935 nm were taken from the silicon spectrometer and longer wavelengths were taken from the InGaAs spectrometer. In order to account for the different integration time and spectral response, a weighted correction factor was determined in the spectral overlap region 930-940 nm.

An SHG FROG trace is theoretically symmetric around the center delay and this requirement allows consistency checks during alignment. This symmetry also results in an ambiguity of the time direction. An additional measurement, where the pulse was dispersed by propagating through a known material (e.g. 5 mm fused silica), can help to resolve this ambiguity. The FROG traces and retrieved pulses used in this thesis are listed in table 3.1.

Pulse	Location
LPF40, 60 mm long	sec. 3.1.1, Figure 3.3
LMA15, 23 mm long	sec. 3.2.2, Figure 3.16
LPF40, 62 mm long	sec. 3.2.2, Figure 3.19
LMA15, 23 mm long	Figure 4.2

Table 3.1: Retrievals utilizing the discussed FROG setup.

3.1.4 Relative intensity noise in the chain

A high signal-to-noise ratio in spectroscopic measurements can be crucial in gaining sufficient information for answering a question in spectroscopy. The relative intensity noise (RIN) of the employed light can be a limiting factor. Here, a laser system encompassing various non-linear processes and amplification steps (see Figure 3.15) raises the question, where noise originates and how it propagates.

Figure 3.9 shows the RF power spectral density (PSD) measured at different points of the chain with an analog dynamic signal analyzer (Stanford Research, SR780) over its full frequency range spanning from 0.1 Hz to 102 kHz. The noise around 10 kHz is especially relevant for the experiments in this thesis, as it employs lock-in detection in the range of 10 kHz and higher frequency noise is averaged out.

The PSD of the oscillator follows a 1/f curve until it reaches a floor at around 100 Hz. After the pulse-picker and the soliton shift from 1.55 μm to 2 μm, the noise increases but keeps the general shape.

The PSD of the CPA is lower than that of the soliton around 1 kHz, which can be due to the nonlinear spectral shift. For frequencies above 3 kHz the spectral shift can introduce broadband noise, compare Figure 3.7. The CPA contains the first free-space propagation beam path between the pre-amplifier and the main amplifier, as well as the subsequent grating compressor. Significant and narrowband noise components are found between 50 Hz and 1.5 kHz, a frequency region which is rich in mechanical vibrations. Mechanical vibrations can impact the coupling efficiency into the main amplifier fiber and thus mechanical noise can couple onto intensity noise. A similar effect can happen if the beam clips at one optic or spatially dependent losses in general, e.g., due to dirt or damages. The RIN after the PCF increases to 0.7 %, and again mainly due to coupling of mechanical vibrations in the 50 Hz to 1.5 kHz frequency region and to drifts for lower frequencies, e.g., beam pointing changes due to thermal heating. For frequencies below 1 Hz only a few averages exist, which are highly dependent on slow drifts. This could be a reason why the PSD of the CPA lays above that of the PCF.

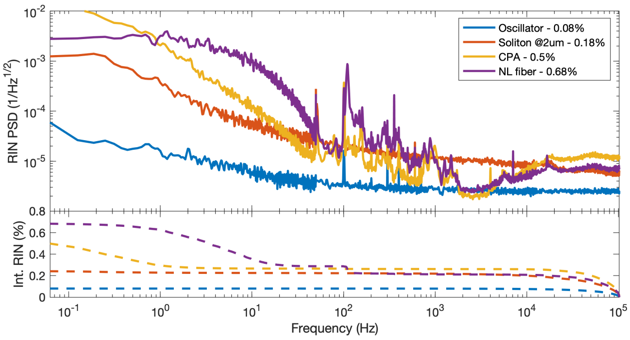

Figure 3.9: Relative intensity noise in the frequency range from 0.1 Hz to SI102kHz measured at different points in the laser system. The integrated RIN for each curve is shown in the bottom panel and the value given in the legend.

3.2 Thulium-fiber laser based mid-infrared generation and electro-optic sampling

3.2.1 Watt-scale 50 MHz source of single-cycle waveform-stable pulses in the molecular fingerprint region

This section is identical[4] in wording and figures to the paper with the title "Watt-scale 50 MHz source of single-cycle waveform-stable pulses in the molecular fingerprint region" published in Optics Letters, vol. 44, no. 7, p. 1730 in 2019 [111]. As one of the leading authors[5] together with Thomas Butler and Christina Hofer built the experimental setup for IPDFG and EOS and performed the measurements. Together we wrote the initial manuscript. A detailed author contribution is found here[6].

Abstract

We report a coherent mid-infrared (MIR) source with a combination of broad spectral coverage (6-18 μm), high repetition rate (50 MHz), and high average power (0.5 W). The waveform-stable pulses emerge via intrapulse difference frequency generation (IPDFG) in a GaSe crystal, driven by a 30-W-average-power train of 32-fs pulses spectrally centered at 2 μm, delivered by a fiber-laser system. Electro-optic sampling (EOS) of the waveform-stable MIR waveforms reveals their single-cycle nature, confirming the excellent phase matching both of IPDFG and of EOS with 2-μm pulses in GaSe.

Main text

Coherent mid-infrared (MIR) light sources have shown promise in the study of a wide range of resonant light–matter interactions, most notably in the study of ro-vibrational molecular transitions and dynamics [3], as well as the investigation of low-energy phonon dynamics [112], charge transport in semiconductors [113], and non-linear and high-field interactions [114]. As such, the development of both suitable light sources and appropriate detection techniques is an important step toward the improvement of the sensitivity and precision of measurements, especially in applications such as biomedical diagnostics

---

[4] only the numbers of the references, figures and tables are changed for consistency throughout the thesis

[5] authors: Thomas Patrick Butler, Daniel Gerz, Christina Hofer, Jia Xu, Christian Gaida, Tobias Heuermann, Martin Gebhardt, Lenard Vamos, Wolfgang Schweinberger, Julia Gessner, Thomas Siefke, Martin Heusinger, Uwe Zeitner, Alexander Apolonski, Nicholas Karpowicz, Jens Limpert, Ferenc Krausz, Ioachim Pupeza

[6] Author contributions: The experimental data acquisition, analysis, presentation and initial drawing of the manuscript were performed by TPB, DG and CH. The front-end and self-compression scheme came from CG, TH, MG, JL. The dispersion-free long-pass filters were manufactured by TS, MH, UZ. Experimental support for EOS came from JX, LV, WS, JG. The concept stems from AA, NK, FK, IP and the experiment was supervised by NK, JL, FK, IP. All authors reviewed and edited the manuscript and its revisions.

[115] and chemical/trace gas monitoring [28, 91]. Recent advances in near-infrared (NIR) femtosecond laser technology have provided a viable route towards table–top broadband ultrafast MIR sources via nonlinear processes such as parametric amplification or difference frequency generation (DFG) [28, 44, 46, 47, 91, 116, 117]. In particular, the frequency down-conversion technique of intra-pulse DFG (IPDFG) has emerged as a relatively simple way to create MIR pulse trains that combine several properties highly desirable for molecular spectroscopy [44, 46, 47, 91]. IPDFG , which generates a MIR idler signal through phase matched mixing of spectral components within a broadband driving pulse, ensures a passively waveform-stable output. This enables electro-optic sampling (EOS) to detect the generated electric field, transfer the detection to the NIR spectral region where low-noise semiconductor photodetectors offer increased performance over cooled MIR detectors [10] used in conventional Fourier transform infrared (FTIR) spectroscopy, and allows for ultra-sensitive [118] and broadband [87, 119] detection across the entire molecular fingerprint region.

The major limitation of IPDFG-based MIR sources so far has been the severe trade-off between bandwidth and efficiency in the nonlinear conversion process. Similarly, where high field-strengths are desirable, drivers are typically limited to kHz repetition rates [17]. In multi-MHz repetition rate systems, NIR-to-MIR conversion efficiencies on the order of 0.1 % have been demonstrated for 1-1μm [44], 1.5-μm [91], and 2-μm [46] sources. Very recently, IPDFG at a 1.25-MHz repetition rate with a conversion efficiency of 1.8 % driven by 2-μm, 16-fs pulses, generating a spectrum from 7.3 to 16.5 μm (at -10 dB) and a record power of 470 mW was reported [47]. Driving pulses at 2-μm can offer increased powers due to a lower quantum defect and lower photon energy, enabling the use of smaller-bandgap crystals with higher nonlinear coefficients [120]. At the same time, longer driving wavelengths increase the phase matched bandwidth by improving the group velocity matching between NIR and MIR pulses [116]. While the previous results were obtained with high driving pulse energies (24 μJ), they show the existence of favorable phase matching conditions for high-efficiency, broad-bandwidth IPDFG using GaSe as a nonlinear medium. These results show the possibility to achieve high-conversion efficiency and broad phase-matching via IPDFG using GaSe as a nonlinear medium, albeit using a large pulse energy and 1.25-MHz repetition rate. Here, we further investigate the suitability of 2-μm driven IPDFG to assess whether this conversion efficiency can be maintained at the high repetition rates typically needed for frequency-comb spectroscopy [28, 91] and also characterize the temporal profile of the MIR pulse, which is essential for field-resolved spectroscopy [55, 121].

In this Letter, we present a source which combines a watt-scale average power (0.5 W), super-octave bandwidth (6-18 μm), single-cycle pulse duration (43 fs), waveform stability, and high repetition rate (50 MHz). Our novel MIR source is based on 2-μm fiber laser technology, enabling both generation and field-sensitive detection of phase-stable MIR pulses. These MIR transients, generated via IPDFG of 30-W average power, 32-fs pulses in a GaSe crystal, have been characterized using EOS with few-cycle, watt-level 2-μm sampling pulses. Compression of the field to a single-cycle duration has been demonstrated, with the possibility to generate absolute field strengths in excess of 1 MV/cm at a 50-MHz rate. Compared to current state-of-the-art broadband MIR sources, our table–top system provides a significantly higher spectral brilliance across its entire bandwidth than current 3rd-generation facility-scale synchrotron sources [122], while maintaining a high degree of temporal and spatial coherence and close to bandwidth limited temporal compression.

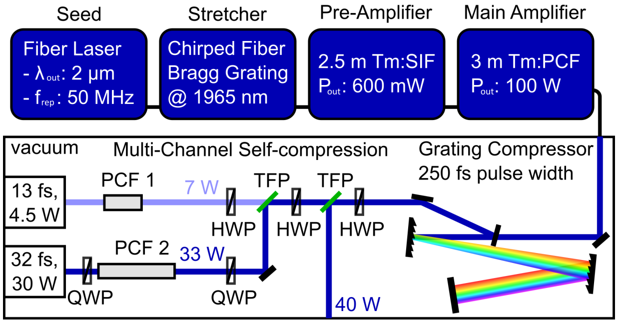

Figure 3.10: Experimental schematic of the Tm:fibre-based CPA frontend. SIF: step index fiber; HWP: half wave plate; TFP: thin film polarizer; QWP: quarter wave plate; PCF 1: 13-μm MFD; PCF 2: 56-13-μm MFD.

The experimental setup of the 2-μm femtosecond frontend is shown in Figure 3.10. The amplifier chain was seeded by a train of 50-MHz pulses from a fiber laser. This commercial source (Menlo C-Fiber) generated 2-μm pulses from a 1550-nm Er:fiber seed oscillator which was amplified and Raman shifted in a subsequent nonlinear fiber. Stretched pulses with a center wavelength of 1965 nm were subsequently amplified in two thulium-doped fibers boosting the average power of the pulse train to a maximum of 100 W [80]. Due to absorption by ambient water vapor, the entire high-power free-space beam path was housed in vacuum chambers at a pressure of $<$1 mbar, avoiding thermal lensing and preserving the beam quality [101]. At an output power of 40 W, the compressed 250-fs pulse train from the CPA was split between 2 channels, and further compressed nonlinearly in photonic crystal fibers (PCF) [99]. To achieve the high-average-power driving pulses required for efficient IPDFG , the first channel was compressed to 32-fs full width at half-intensity maximum (FWHM) using a 56-μm mode-field diameter (MFD) solid-core silica PCF with a length of 5.6 cm. The self-compressed pulse width of 32-fs FWHM was measured with a home-built second-harmonic-generation frequency-resolved optical gating (SHG -FROG) instrument utilizing a 10-μm thick BBO crystal, see Figures 3.11(a)–3.11(c). For accurate temporal measurement of MIR waveforms, a second fiber self-compression stage was implemented in parallel for use as the EOS sampling pulse train. In this case, a smaller core PCF fiber (13-μm MFD and 2.3 cm long) was used to spectrally broaden the CPA driving pulses to a width of 700 nm at -20 dB with $>$60 % efficiency while simultaneously temporally compressing the pulse to 2 optical cycles (13-fs FWHM), see Figures 3.11(d)–3.11(f).

Figure 3.12 presents a schematic layout of the IPDFG and EOS setup. The 32-fs p-polarized pulse train was focused to a 162- μm $1/e^2$-intensity spot diameter inside a 1-mm-thick GaSe crystal. Type-I phase matching was used with an external crystal angle of 38 degrees [47]. The resulting MIR light was measured with a wire-grid polarizer to

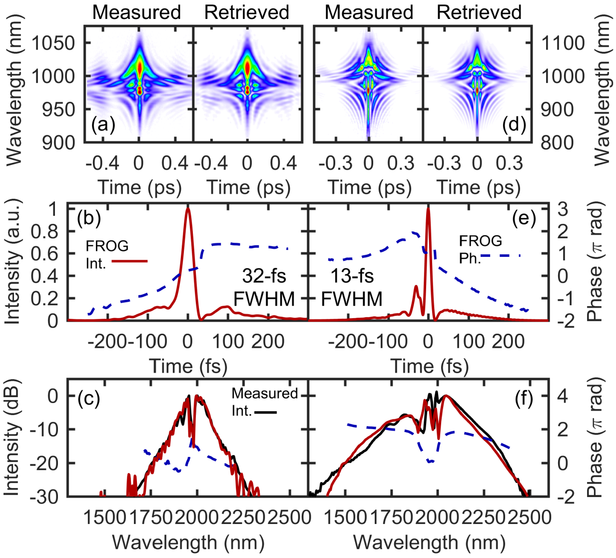

Figure 3.11: (a)Measured [left] and retrieved [right] FROG spectrograms of the longer pulse PCF compression channel. (b) Retrieved FROG temporal intensity and phase. (c) Retrieved FROG spectral intensity and phase, compared to independently measured spectrum obtained using a NIR grating spectrometer. (d–f) shows the same information as (a–c), this time measured for the shorter pulse PCF channel.

be s-polarized and was collimated using a gold-coated off-axis parabola. Separation of the collinearly propagating MIR and driving signals was achieved by using custom-fabricated gold-coated silicon diffraction gratings [123]. These gratings were designed to have a high diffraction efficiency at 2 μm, while retaining a large zeroth-order reflection coefficient for the MIR wavelengths. Three gratings were used in series in order to suppress the power of the driving pulses by 30 dB. Compared to other coated or transmissive filtering optics, diffraction gratings offer an exceptional thermal stability and impart no chromatic dispersion on the propagating MIR pulses. A reflective ZnSe wire-grid polarizer was used to combine the MIR pulses with the 2-μm sampling pulses in an orthogonal polarization state. Use of a reflective beamsplitter and recombiner meant that no transmissive elements were present in the MIR beam path, enabling a direct measurement of the MIR pulse as it exits the IPDFG crystal. After undergoing mixing in the GaSe crystal, at least 498 mW of MIR power was generated after the exit face of the crystal, estimated by accounting for the loss from subsequent mirrors and optics. Considering the power lost due to reflection from the front face of the crystal, a total NIR-to-MIR conversion efficiency of 2.0 % was achieved with a peak intensity at the focus of 75 GW/cm^2.

For lock-in detection of the electric field of the broadband MIR transients, the beam was mechanically chopped at a frequency of 7 kHz. The short p-polarized probe was combined with the MIR pulse train by transmission through a ZnSe wire grid polarizer. Dispersion of the probe pulse was compensated using bulk fused silica and sapphire plates, ensuring a 20-fs FWHM pulse, which was spatially overlapped with the MIR beam and focused into

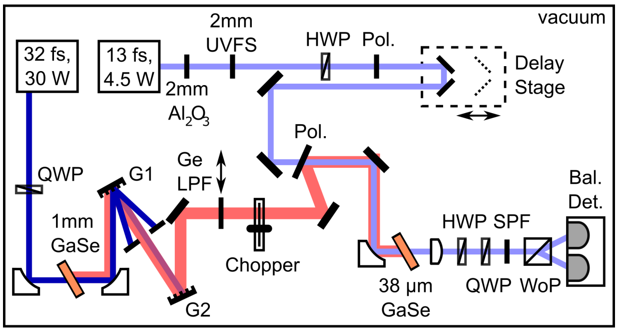

Figure 3.12: Experimental setup of the IPDFG and EOS. G1, G2 are gold-coated silicon beamsplitter gratings. Ge LPF: coated 1-mm Ge longpass filter with 4.5 μm cut-on. Pol.: wire grid polarizer; UVFS: UV fused silica; SPF: shortpass filter 1550 nm. WoP: Wollaston prism; Bal. Det.: balanced InGaAs photodetector.

a 38-μm thick GaSe crystal. Sum-frequency generation (SFG) of the two pulses results in an effective polarization rotation of the probe pulse, which is directly proportional to the MIR electric field [52]. Scanning of the probe pulse delay allows for detection of the MIR field. The thin detection crystal ensured good phase matching across the entire MIR spectrum. The measured EOS trace of the MIR pulse is shown in Figure 3.13(a). While a clear chirp of the waveform can be observed due to the dispersion-free nature of the beampath, it is inferred that this chirp is intrinsic to either the MIR wave passing through the nonlinear generation crystal or to the response of EOS detection. Numerical modelling of the EOS detection allows for retrieval of the input MIR electric field through independent calculation of the EOS instrument response function [119]. The retrieved field, also shown in Figure 3.13(a), excludes the latter as the source of the chirp. Figure 3.13(b) compares the spectrum of the measured EOS trace to the retrieved EOS input spectrum as well as the independently measured spectrum captured with an FTIR spectrometer. The good agreement of the two spectra validates the calculation of the EOS response. Comparison of the EOS and FTIR spectra shows that phase matching in the EOS detection process slightly suppresses the signal at longer wavelengths, while enhancing detection for the shorter ones, as clearly observed in the chirped waveforms of Figure 3.13(a).

For the study of both linear [55, 121] and nonlinear [114, 124] interactions, the confinement of the available spectrum to a short transient is essential. Dispersion compensation of pulses in this spectral range can be difficult due to a relatively small choice of suitable materials. Figure 3.13(c) shows the measured spectral phase of the pulse shown in parts (a) and (b). Also shown is the phase expected due to dispersion through 6 mm of bulk germanium. It is clear that in the longer wavelength part of the spectrum (9-20 μm), germanium can provide suitable compensation for the generated IPDFG pulse [125]. Using this arrangement, we experimentally demonstrated compression of the MIR transient by performing EOS detection after transmitting the pulse through 6 mm of bulk germanium. Figure 3.13(c) shows the measured spectral phase, which agrees well with the numerical calculations. Figure 3.13(d) shows the measured and retrieved field for the compressed pulse,

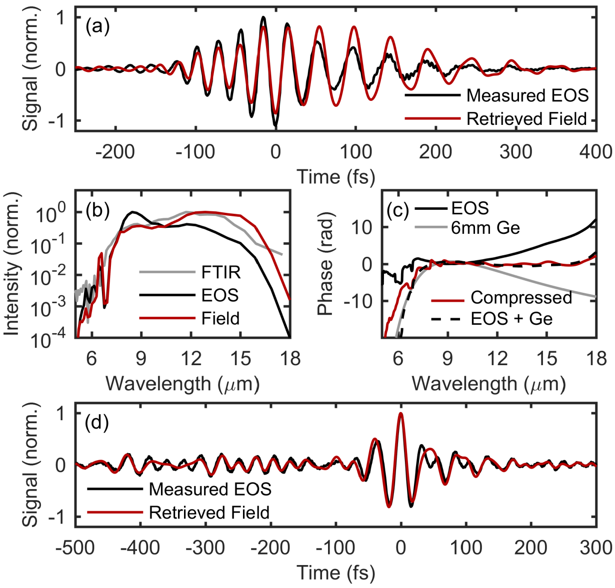

Figure 3.13: (a) Measured EOS trace of MIR transient generated by IPDFG (black) and recovered MIR input field (red). (b) Measured EOS spectrum (black) (Fourier transform of the temporal waveform) compared with the independently measured FTIR spectrum (grey) and the recovered spectrum (red). (c) Spectral phase of the measured EOS pulse (black). Phase due to 6 mm of propagation through bulk germanium (grey). Sum of EOS phase and Ge (black dashed). Measured spectral phase after insertion of bulk Ge in the beam path (red). (d) Measured EOS after compression with bulk Ge (black) and the retrieved field (red) with a 43-fs intensity FWHM.

with an intensity FWHM of 43 fs. This pulse duration is just 1.16 times the fundamental oscillation period of the central carrier field at 11.1 μm. In this case, the compression medium introduces some Fresnel reflection losses to the MIR beam. However, with a Brewster-angle compression plate and minimal power loss, the absolute field strength of the transient could exceed 4 MV/cm. The generation of such field strengths at a >10 MHz repetition rate, combined with the single-cycle duration, make this source ideally suited to multi-dimensional spectroscopy and other pump-probe experiments. Along with high output power, the spectrum of the MIR idler covers a broad bandwidth, from 6 to 18 μm (-30 dB).

Figure 3.14(a) shows the calculated spectral brilliance [117] compared to two other commonly used MIR radiation sources, thermal and synchrotron (BESSY II IRIS beamline) [122]. The brilliance of our coherent MIR source is at least 2 orders of magnitude greater over 7-17 μm and exceeds that of the synchrotron over nearly two octaves (from 5 to 18 μm). The power spectral density of the source is greater than 1 mW/THz across a large part of the spectrum (20-40 THz), while the power per combline value exceeds 1 μW in the 19 to 27.5 THz region, with a peak of 2.2 μW per combline. This value is more than 10 times larger than previously reported 2-μm driven IPDFG sources with a peak value of

<70 nW [46] and <200 nW [47] per combline and over 3 orders of magnitude greater than state-of-the-art 1.5-μm driven MIR combs with 1 nW per combline [91].

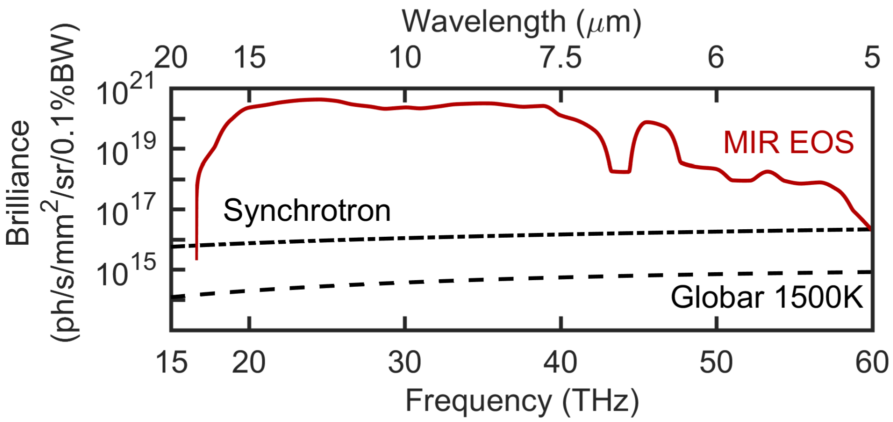

Figure 3.14: Photon brilliance of the MIR spectrum calculated from the measured average power and retrieved EOS spectrum, compared with other common FTIR sources [122].

In conclusion, we have demonstrated a phase-stable, high-power (0.5 W), broad-band MIR source, covering the long-wavelength part of the MIR fingerprint region (550-2000 cm^{-1}). Combined for the first time with a high repetition rate (50 MHz), ultrashort pulse duration (43 fs), and field-resolved EOS detection with high-power, 2-μm pulses, this system presents a flexible, compact, and cost-effective platform for precision measurements across a wide gamut of applications. These results demonstrate the advantage of employing a 2-μm based pump source over 1 μm for IPDFG-based MIR generation, with higher efficiencies and broader phase matching. Even higher average powers and peak field strengths may be possible with further power scaling of the driver, leveraging advances in Tm:fiber CPA [126] or bulk-based nonlinear compression [127]. This may also offer the ability to use thinner generation media, boosting the bandwidth toward multi-octave terahertz spectra and even shorter sub-cycle transients [119] while retaining high output power. The ultrashort MIR pulse train is well suited for background-free time-resolved studies of molecular dynamics, corresponding in the frequency domain to a harmonic frequency comb with a record μW-class power per combline. Finally, we have shown for the first time EOS detection of short MIR transients by means of a 2-μm based sampling pulse, demonstrating favorable phase-matching conditions for a broad MIR band. A high average sampling power meanwhile benefits the efficiency of the frequency up-conversion step in EOS detection [52]. These results establish 2-μm fs technology as a new, viable route toward high-power, high-precision, field-resolved molecular vibrational metrology.

3.2.2 Multi-octave spanning, Watt-level ultrafast mid-infrared source

This section is identical[7] in wording and figures to the paper with the title "Multi-octave spanning, Watt-level ultrafast mid-infrared source" published in Journal of Physics: Photonics, vol. 1, no. 4, p. 044006 in 2019 [128]. As one of the authors[8] together with Thomas Butler I built the setup for the pulse compression, IPDFG and EOS and performed the measurements. I analyzed the FROG data and contributed to the initial drafting of a manuscript. A detailed author contribution is found here[9].

Abstract

We present a source of brilliant mid-infrared radiation, seamlessly covering the wavelength range between 1.33 and 18 μm (7500-555 cm^{-1}) with three channels, employing broadband nonlinear conversion processes driven by the output of a thulium-fiber laser system. The high-average-power femtosecond frontend delivers a 50 MHz train of 250 fs pulses spectrally centered at 1.96 μm. The three parallel channels employ soliton self-compression in a fused-silica fiber, supercontinuum generation in a ZBLAN fiber, and difference-frequency generation in GaSe driven by soliton selfcompressed pulses. The total output enables spectral coverage from 1.33 to 2.4 μm, from 2.4 to 5.2 μm, and from 5.2 to 18 μm with 4.5 W, 0.22 W and 0.5 W, respectively. This spatially coherent source with a footprint of less than 4 m^2 exceeds the brilliance of 3rd-generation synchrotrons by more than three orders of magnitude over 90 % of the bandwidth.

Introduction

Broadband light sources are an important enabling technology for the spectroscopic study of molecular vibrations, helping to classify the chemical composition and conformation of a wide range of materials [3]. By illuminating a sample with broadband radiation, it becomes possible to study large ensembles of molecules in a widely parallel manner [28]. In particular, the infrared molecular fingerprint region, spanning from the near-infrared to the long-wavelength mid-infrared (MIR) (2-20 μm), can be used to probe a huge variety of vibrational molecular modes and overtones [6]. Such molecular resonances can provide new insights in the areas of atmospheric and trace-gas analysis [40], biomedical diagnostics [115, 129], and microscopy [130, 131].

---

[7] only the numbers of the references, figures and tables are changed for consistency throughout the thesis

[8] authors: Thomas Patrick Butler, Nikolai Lilienfein, Jia Xu, Nathalie Nagl, Christina Hofer, Daniel Gerz, Ka Fai Mak, Christian Gaida, Tobias Heuermann, Martin Gebhardt, Jens Limpert, Ferenc Krausz, Ioachim Pupeza

[9] Author contributions: Experimental realization of the self-compression and IPDFG was performed by TPB DG, CH. The ZBLAN experiments were performed by NL, JX with the help of NN. Simulations of the fibers were performed by TPB. The front-end and self-compression scheme came from CG, TH, MG, JL. Analysis was performed by TPB and DG. Initial writing: TPB; Supervision: KM, JL, FK, IP; Review and editing: all authors.

For many applications, such as Fourier-transform infrared spectroscopy (FTIR), thermal radiation sources are most commonly employed for illumination. Such thermal sources rely on blackbody radiation generated by electrically heating a material. While this method is relatively simple in practice, the generated blackbody radiation is both temporally and spatially incoherent. Spatial incoherence reduces the achievable brightness (i.e. a highly spatially confined flux of photons), despite the Watt-level average powers emitted by thermal sources. While greater spatial coherence can be achieved using quantum cascade semiconductor lasers, such lasers typically have a narrow tuning range, limiting their use in parallel detection of multiple species [13]. In comparison to the laboratory workhorse of thermal blackbody sources, synchrotron radiation sources can offer a high flux, ultra-broadband source of photons in the near-infrared and MIR spectral ranges [12]. In a synchrotron source, electrons are accelerated and stored in a large ring structure, generating a continuum of radiation spanning from the XUV to THz frequencies. Synchrotron sources offer a much higher brightness than thermal sources. However, the temporal coherence of such sources means that the output light can only be confined to nano- or picosecond pulse widths. Such pulse widths limit the temporal resolution of dynamical studies, and restrict the investigation of nonlinear phenomena. While such sources can alleviate some of the shortcomings of tabletop thermal sources, and indeed currently enable many state-of-the-art MIR studies [132, 133], the use of a facility scale particle accelerator as a light source makes it unfeasible for many studies and day to day measurements.

In recent years, the development of high-power, ultrafast laser sources has paved the way for a new class of broadband light sources. Temporal confinement of pulses to the sub-picosecond regime enables the exploitation of nonlinear phenomena only possible with high peak power sources. Parallel advances in optical fiber and waveguide design and materials have similarly allowed for increased spatial confinement of the electric field and further increases in peak power. Leveraging effects such as self-phase modulation [93], Raman self-frequency shifting [134], difference frequency generation (DFG) [43], and supercontinuum generation (SCG) [38], it is now possible to cover much of the electromagnetic spectrum using well established laser technology based in the visible and near-infrared. Such laser-based sources have the potential for generating super-octave broadband output spectra with high power and spatial coherence. Crucially, they can also provide the basis for ultrashort, waveform-stabilized pulse synthesizers, which can be exploited for time domain studies [75, 121] and pump-probe experiments [135], or through frequency comb techniques [91, 136]. At the same time, laser-based sources can maintain a small-footprint and low cost when compared with synchrotron sources, a vital component for ensuring the adoption of such technologies in a wide setting.

For the study of molecular vibrations, most of the interesting resonant modes are found in the band between 2 and 20 μm, often referred to as the molecular fingerprint region. The generation of light in this region is often challenging, due to the limited variety of existing laser gain media. In the field of ultrafast oscillators, much work has been done to push the emission toward longer wavelengths. Laser oscillator and amplifier systems have been developed utilizing fiber, bulk, and thin disk architectures based on holmium [34, 137], thulium [35, 36, 138] or chromium [37, 45] doped gain-media. Such advances now mean that it is possible to generate pulses with subpicosecond, Watt-level powers, in the range of 1.9-2.5 μm. Pulses at these wavelengths can offer a good starting point for further nonlinear generation of broadband spectra to cover the entire MIR fingerprint region. In general, this is due to a smaller quantum defect associated with pumping at longer wavelengths, as well as better availability of MIR transparent crystals with higher damage threshold and nonlinear coefficients. Compared with systems pumped in the 1 μm spectral range, longer pump wavelengths can improve the available bandwidth [42] or average power [44]. Here, we describe a laser frontend based on a thulium doped fiber chirped pulse amplifier (TmFCPA). The TmFCPA offers 100 W level output at a 50 MHz repetition rate with a pulse duration of 250 fs. These pulses, spectrally centered at 1.96 μm, offers a stable and reliable driving source for further spectral broadening and nonlinear wavelength shifting techniques.

Nonlinear frequency conversion processes in the MIR region have typically fallen into two major categories; SCG via waveguide confinement, or parametric frequency conversion processes in nonlinear crystals. SCG in photonic crystal fibers (PCF) was first shown in the late 90s as an efficient way to broaden the spectral coverage of an input femtosecond pulse [139]. Since then, SCG has been demonstrated in a wide range of waveguide materials such as silica [90], fluoride glass [140], ZBLAN [141], and silicon nitride [142], as well as different waveguide geometries, including step index fibers, PCF, tapered and planar waveguides. In order to access the longer wavelength fingerprint region, more traditional nonlinear parametric processes can be employed. Light sources in this region have been realized using optical parametric oscillation [41, 97], and DFG [43, 96]. One particular type of DFG process known as intra-pulse DFG (IPDFG) has shown promise as a relatively simple method for waveform-stable MIR generation. Such sources offer tens-of-mW level MIR output powers with a super-octave spectral coverage [42, 45–48, 111].

In this work, we present a broadband source, capable of covering the majority of the molecular fingerprint region, with an output power spectral density on the order of 1 mW/THz. The source is driven by a TmFCPA, detailed in section 2, with three output channels providing parallel spectral broadening. In the 2 μm wavelength region, a silica glass PCF provides a medium for soliton self-compression to the few cycle regime [99]. This channel covers the wavelength region of 1.33-2.4 μm, and is described in section 3. ZBLAN-based step index fibers offer good transmission into the MIR up to 6 μm. Their use to generate a supercontinuum spanning 2.4-5.2 μm is discussed in section 4. Section 5 presents a technique for coverage of the longer wavelength regime, provided by IPDFG of 2 μm driving pulses in a Gallium Selenide crystal (GaSe) [111]. The driving pulses are precompressed to 32 fs pulse duration in another silica PCF before being focused into a GaSe crystal to generate a spectrum spanning 5.2-18 μm. Finally, in section 6, we compare the brightness of the laser-based source to both thermal and synchrotron sources, showing that the demonstrated source can significantly outperform state-of-the-art synchrotron beamlines at a fraction of the footprint and cost.

Thulium doped fiber amplifier

Figure 3.15(a) shows a schematic of the frontend laser used to drive the three-channel spectral broadening. The system is based on a master oscillator power amplifier architecture. A fiber oscillator seeds a fiber-based CPA (Active Fiber SystemsGmbH), whose output is subsequently split to drive the three parallel spectral broadening stages. The seed pulse train is derived from an erbium fiber oscillator operating at 1.5 μm with a repetition rate of 100 MHz (Menlo C-fiber). This commercial Er:fiber oscillator offers a stable (RIN of <0.1 % rms from 1 Hz to 1 MHz) and reliable pulse train, as well as the opportunity to stabilize both the repetition frequency and the carrier envelope offset frequency of the pulse train. While not directly utilized in this work, this capability provides a starting point to ensuring and exploiting the full frequency comb nature of the following spectral broadening stages [80].

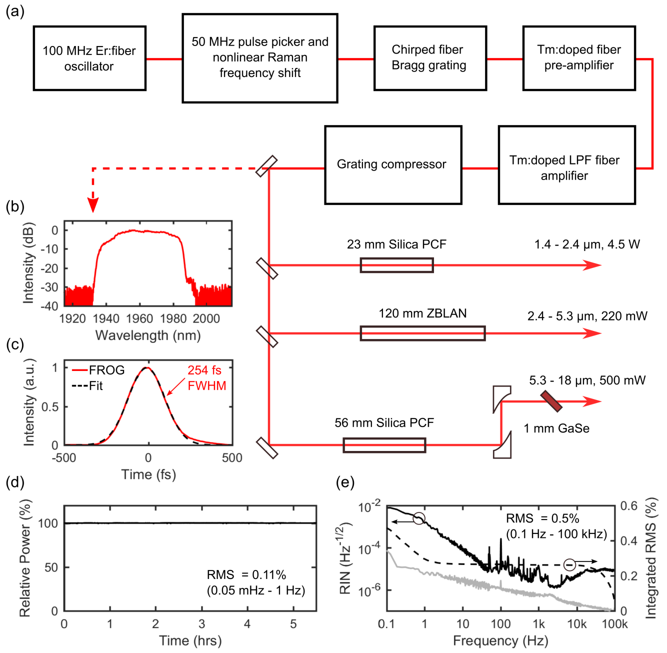

Figure 3.15: (a) Schematic layout of the fiber CPA used to generate a multi-octave infrared spectrum with 3 parallel spectral broadening techniques. (b) Spectrum of the CPA, centered at 1965 nm with more than 50 W output power at 50 MHz. (c) FROG measurement of the CPA temporal intensity envelope (solid line) with 254 fs pulse duration. The dashed line shows a Gaussian least-square fit to the intensity profile. (d) Relative power output of the CPA system measured with a thermal power-meter, showing drift-free output overvmultiple hours. (e) Relative intensity noise of the CPA system (black solid line) in the band 0.1 Hz-100 kHz. The solid grey line shows the background noise of the detector and spectrum analyzer, while the dashed line displays the integrated spectral noise, with a total of 0.5 %.

The output of the erbium oscillator is reduced to 50 MHz using an electro-optic modulator based pulse picker, before being boosted with an erbium-doped fiber amplifier and then wavelength shifted to 2 μm. The input spectrum spans from 1545 to 1625 nm at the -10 dB level. Frequency down-conversion results from a Raman self-frequency shift generated in a nonlinear fiber, providing a seed spectrum (1900-2000 nm) that is overlapping with the gain bandwidth of the thulium-doped amplifier. The wavelength-shifted pulses are stretched using a chirped fiber Bragg grating (CFBG), which has a bandwidth of 50 nm centered at 1965 nm. The pulses are stretched to a duration of approximately 500 ps before being sent to the two-stage amplifier. The pre-amplifier boosts the average power of the pulse train from a few milliwatts to approximately 600 mW.The main amplifier fiber is a 3 m long large pitch photonic crystal fiber (LPF) [102], providing a maximum output power of 100 W. Both thulium-doped amplifier fibers are diode-pumped at a wavelength of 793 nm. The output of the main amplifier is sent to a free-space Treacy-type grating compressor housed in a vacuum chamber to avoid unwanted absorption by atmospheric water vapor and subsequent thermal air fluctuations [101].

At the output of the amplifier, the pulse train power is divided into 3 parallel channels using a series of half-wave plates and thin-film polarizing plates. Figure 3.15(b) shows the output spectrum of the CPA measured at this point using an optical spectrum analyzer. The output spectrum is approximately 50 nm wide at -30 dB from the peak and centered near 1965 nm, as defined by the reflection bandwidth of the CFBG. The compressed output of the amplifier is characterized by a home-built second harmonic generation frequency resolved optical gating (SHG-FROG) instrument. The recovered output temporal pulse envelope is presented in Figure 3.15(c). The pulse is well described by a Gaussian pulse shape, with a full width at half maximum (FWHM) duration of 254 fs. The power stability of the system has been characterized using a slow, thermal power-meter, as well as a fast extended InGaAs photodetector and electronic spectrum analyzer. Figure 3.15(d) shows the power of the source recorded once per second over more than 5 h. The root mean squared (rms) output stability is less than 0.15 %. The relative intensity noise of the pulse train has also been measured over the band 0.1-100 kHz. Figure 3.15(e) shows the relative spectral density of the fast fluctuations, as well as the integrated rms percentage over the same bandwidth, with a total of 0.5 %.

Soliton self-compression in silica PCF

At wavelengths greater than 1.3 μm, silica glass exhibits anomalous dispersion, with a dispersion parameter D (measured in ps/nm/km) >0. In a fiber, both the material as well as the waveguide properties contribute to the overall dispersion of light guided in a mode. In the case of solid-core PCF, the waveguide is formed from a pattern of cylindrical air holes placed in a solid material. Commonly, cylindrical inclusions are placed in a hexagonal lattice, with the waveguide core defined by one or more missing air-holes. Such PCF can provide tight confinement that strengthens the nonlinear effects of the propagating pulse, especially when driven by suitably high pulse energies [90, 139]. By operating in the anomalous dispersion regime, it is possible to engineer a situation in which the dispersion compresses the pulse, while the Kerr nonlinearity broadens the pulse spectrum through self-phase modulation, lowering the Fourier transform-limited pulse duration. By cleaving the fiber to the optimal length, the pulse at the output facet can be self-compressed to a nearly transform limited duration, eliminating the need for additional chirp compensation, e.g. chirped mirrors or prism compressors. Such a system is also very simple to implement practically, with high coupling efficiencies and beam quality routinely achievable.

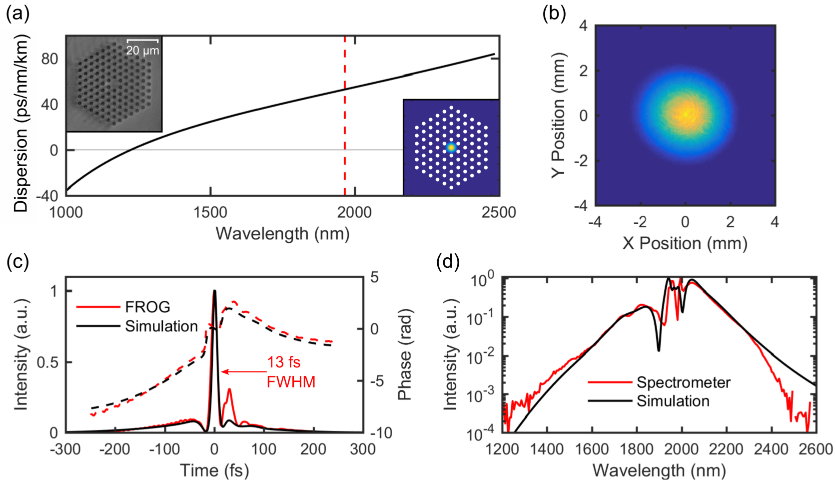

Figure 3.16: (a) Microscope image of the LMA15 PCF facet. (b) Calculated mode profile of the fundamental mode. (c) Dispersion profile of the LMA15 PCF. The dashed line indicates the central wavelength of the input spectrum for driving the self-compression process. (d) Collimated mode profile from the fiber output measured at a distance of 6 m using a 50 mm focal length silver parabolic mirror. (e) FROG measurement of the self-compressed output pulse (red line) compared to the simulated pulse (black). The dashed lines show the temporal phase of the FROG and simulated pulse. (f) Experimentally measured spectrum of the self-compressed source compared with the simulated spectrum.

In order to generate broad spectra near the output wavelength of the amplifier system, a 23 mm long piece of LMA15 PCF (NKTPhotonics) was chosen. For simulation of the spectral broadening and temporal self-compression process in the fiber, its dispersion was first calculated. Using the PCF simulation tool CUDOSMOF [143], the effective refractive index n_{eff} of the fundamental mode was calculated in the wavelength range from 0.5 to 2.5 μm using the multipole method. Due to the relatively large mode-field diameter (MFD), the waveguide contribution to the index is quite small. Once $n_{eff}(\lambda)$ has been calculated, the dispersion parameter is calculated by $D = -1 \times 10^6 \frac{\lambda}{c} \frac{d^2 n_{eff}}{d\lambda^2}$ (ps/nm/km) where λ is the wavelength in meters and c is the speed of light in m/s [144]. The MFD is also determined from the calculated intensity distribution. Figure 3.16(a) shows a light microscope image of the LMA15 fiber facet with 5 layers of hexagonal air-inclusions in a silica matrix. Figure 3.16(b) shows the corresponding geometry of the fiber simulation as well as the intensity distribution of the fundamental mode at the pump wavelength. Figure 3.16(c) presents the calculated dispersion showing the positive value (anomalous dispersion) in the wavelength range from 1226 nm onward. Pulse propagation in the fiber was modelled with the Fiberdesk software tool [145], using the dispersion as well as input pulse parameters of 250 fs FWHM, Gaussian envelope, 84 nJ pulse energy, and MFD of 13.1 μm.

Coupling of the CPA pulses into the PCF was realized by free space coupling using a beam expanding telescope and 30 mm focus length plano-convex lens made from anti-reflection coated suprasil glass. At an incident power of more than 7 W, optimal spectral broadening was observed with an output power of approximately 4.5 W. At this point, the output pulse duration is at a minimum. Increasing the input power past this point generally leads to a collapse of the spectral bandwidth, with further increases leading to fiber damage due to over-compression and critical self-focusing of the beam inside the fiber [99]. The output beam was collimated with a silver off-axis parabola, so as to provide achromatic collimation and reduce unwanted dispersion of the output pulse. The collimated output beam profile is shown in Figure 3.16(d), with a $4.3 \times 4.0\,\mathrm{mm}^2$ $1/e^2$ beam diameter. The temporal profile was measured with SHG-FROG, while the spectrum was measured independently with an extended InGaAs array grating spectrometer (Ocean Optics NIRQUEST-256). The experimentally measured temporal pulse and spectrum are presented in Figures 3.16(e) and (f) respectively. In each case the experimental values are compared with the simulated pulse obtained from the fiber geometry and ideal input pulse parameters as discussed above. The simulation is found to be in good agreement with the measured values, predicting a very similar pulse shape and spectral coverage of the source. The output pulse duration is measured to be 13 fs, with over 40 % of the energy in the main peak (slightly less than the 46 % of the simulated pulse). The spectrum spans from 1.4 to 2.5 μm at the -30 dB level. Some slight drop-off is observed in the long wavelengths (2300 nm onward), attributed to the roll-off of the spectrometer sensitivity as well as excess loss due to the spectrometer coupling fiber, and is not expected when compared to the simulated spectrum.

Supercontinuum generation in step index ZBLAN fiber

ZBLAN fibers show promise for applications in the MIR due to their low attenuation in the 2-5 μm region. Previous work with these fibers has demonstrated SCG and soliton formation as an efficient route to generating broadband MIR spectra using a variety of input pulse wavelengths and durations [146–148]. Here, we generate broad spectra from 2 to 5.2 μm using a ZBLAN fiber driven by 250 fs input pulses. The fiber used was a step index fiber fabricated by FiberLabs Inc. The core diameter of the fiber was nominally 6 μm (specified as ranging from 6 to 6.5 μm in the batch provided by the manufacturer). In order to identify a suitable fiber length and input power, the pulse propagation in the ZBLAN fiber was modelled similarly to the PCF self-compression as discussed in section 2. In this case, the dispersion parameter of the fiber is calculated by solving the unified dispersion equation of the step index fiber. In order to do this, the refractive index of the core and cladding material must be known. The Sellmeier coefficients of the core and cladding regions are listed in Table 3.2. The resulting refractive index values n_{core} and

$n_{cladding}$, combined with the core radius r and the light wavelength λ, define the normalized frequency (or V number), $\nu = 2\pi \frac{r}{\lambda}\sqrt{n_{core}^2 - n_{cladding}^2}$. The V number can be used to solve the unified dispersion equation for the LP01 fundamental mode of the step index fiber [149] at each wavelength, yielding n_eff over the spectral region of interest. The V number is also used to approximate the MFD $MFD = 2r(0.65+1.619\nu^{-1.5}+2.879\nu^{-6}-0.016-1.561\nu^{-7})$, according to the Petermann II definition [150].

	a_0	a_1	a_2	a_3	a_4	a_5
Core:	0.341789	70.20172	0.920628	100.8285	0.305513	9951.441
Cladding:	0.507707	36.01478	0.717316	107.2653	0.243546	9895.962

$$n = \sqrt{1 + \frac{a_0\lambda^2}{\lambda^2 - a_1^2} + \frac{a_2\lambda^2}{\lambda^2 - a_3^2} + \frac{a_4\lambda^2}{\lambda^2 - a_5^2}}$$

Table 3.2: Sellmeier coefficients and formula for estimating the refractive index of the ZBLAN fiber core and cladding regions, as provided by the manufacturer.

Figure 3.17(a) presents the dispersion curve calculated for a 6.4 μm core diameter ZBLAN fiber. In this case, 6.4 μm was chosen to best represent the qualitative broadening behavior observed in the experimental test fiber. The dispersion of the simulated fiber can vary significantly with the core diameter, leading to a shift in the zero-dispersion wavelength, and therefore a change at the pumping wavelength from normal to anomalous dispersion. Combined with the relatively large core size variation that can occur from the drawing of soft ZBLAN glass, it is more difficult to perform quantitative modelling of the exact experimental fiber parameter. However, the qualitative behavior of the simulated supercontinuum process can be instructive in guiding the design of the experiment. Figure 3.17(b) shows the results of a representative simulation using the dispersion of Figure 3.17(a), MFD of 6.65 μm, 20 nJ pulse energy and 250 fs input pulse duration. The ZBLAN material parameters used in the simulation were $f_r = 0.3, \tau_1 = 16.67\,\text{fs}, \tau_2 = 20.23\,\text{fs}$, and $n_2 = 4.7 \times 10^{-20}\,\text{m}^2/\text{W}$, representing the fractional contribution and time constants of the Raman response, as well as the nonlinear index, respectively [148]. The simulation shows the evolution of the spectrum as the pulse propagates along a 20 cm length of fiber. Self-phase modulation effects dominate during the early propagation, broadening the spectrum and introducing spectral modulations.

However, after approximately 10 cm of propagation, the spectrum begins to broaden further. This behavior is due to self-compression of the pulse, leading to an increase in the peak intensity of the pulse and allowing for other nonlinear effects such as soliton fission and Raman self-frequency shift to take over and further broaden the spectrum toward 4.5 μm. This general behavior was observed for multiple different core diameters and input powers, with significant broadening usually occurring after approximately 10 cm of propagation. As a result, several lengths of fiber were tested, with a length of 12 cm being optimal.

Coupling of light into the fiber is achieved by using a 6 mm focal length aspheric lens made from BD2 glass (Thorlabs Inc.). The experimentally measured spectrum is presented in Figure 3.18(a), for a 12 cm long fiber. The output spectrum contains 1.07 W of total

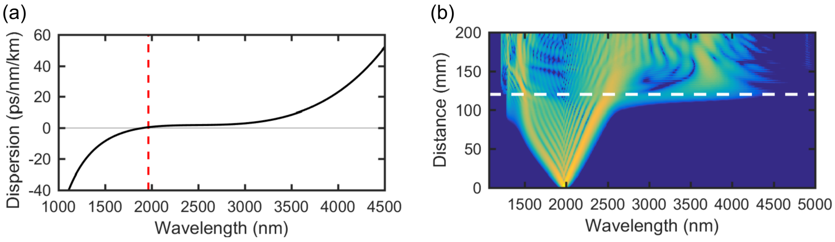

Figure 3.17: (a) Numerically calculated dispersion of the ZBLAN step index fiber with 6.4 μm core diameter. (b) Spectral evolution of a 250 fs input pulse with 1 W of average power over 20 cm propagation.

power. Coated germanium longpass filters were used to select only the wavelengths longer than 2.4 or 3.6 μm. It is found that the spectrum contains over 216 mW of power at wavelengths greater than 2.4 μm, with 51 mW in the range of 3.6 μm and above. Figure 3.18(b) shows the relationship between total launched power and total output power, as well as the measured power behind each of the long pass filters. While in this case a total efficiency of 35 % is reached, this figure can be improved by more suitable design of coupling optic and input mode matching, which should improve the overall efficiency of the MIR generation, as well as reduce thermal heating effects at the input facet. A broadband (2-5 μm) antireflective coated BaF_2 lens was used to collect the light from the fiber output. As expected from a fiber output, the emitted mode is quite clean, with single mode behavior observed. Figure 3.18(c) presents the measured mode profiles of the collimated beam measured with no spectral filtering, as well as behind a 2.4 μm and 3.6 μm longpass filter, confirming that the output was confined to the fiber core even with an octave spanning spectrum. The output power of the fiber was also tracked over the course of an hour to gauge the stability of the source. Figure 3.18(d) shows the measured power over the course of 60 min showing less than 1.3 % rms power fluctuations over this time period. It was observed that after some initial thermalization of the fiber at the input facet, the input coupling and output power remains stable thereafter.

Intra-pulse DFG in GaSe

Parametric frequency downconversion of light from the near-infrared to the MIR and terahertz domain is capable of generating extremely broadband ultrashort pulses [119]. While devices such as optical parametric oscillators and amplifiers can provide high conversion efficiency, practical implementations of such a system often require synchronizing multiple pump and signal beams, while locking their spatial and temporal overlap to ensure a stable nonlinear mixing process [96]. Intra-pulse DFG relies on a single broadband driving pulse, providing both pump and signal photons simultaneously, eliminating the need for tight temporal and spatial overlap control. By phase matching in a suitable nonlinear medium, opposite wings of the broad input spectrum can mix and generate photons in the MIR. Recently IPDFG has been shown to afford conversion efficiencies greater than 1 %

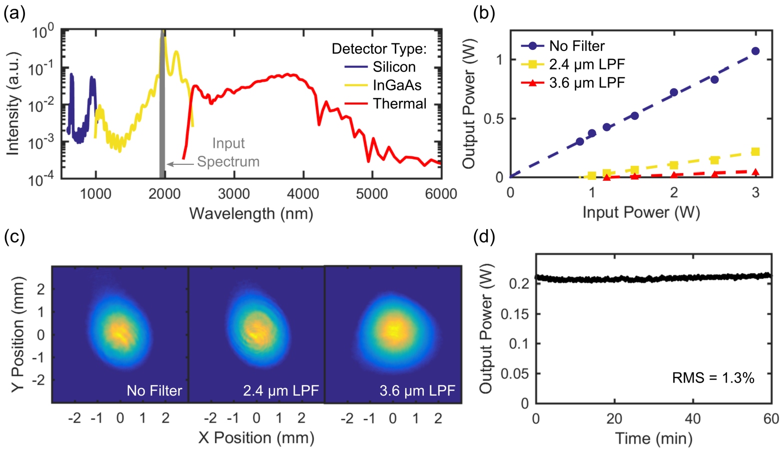

Figure 3.18: (a) Experimentally measured supercontinuum spectrum generated in a ZBLAN fiber. Due to the broad bandwidth of the output spectrum, three spectrometers were used, a silicon array grating spectrometer, an extended InGaAs array grating spectrometer, and an FTIR spectrometer with a thermal detector. (b) Plot of input power versus output power showing a coupling efficiency of 35 %, as well as the power evolution of the MIR components after the onset of supercontinuum broadening. (c) Collimated beam profiles captured 3 m after the fiber output. (d) Power stability of the ZBLAN fiber output in the spectral range of 2.4-5.5 μm over a 1 h period with 1.3 % rms fluctuations.

while maintaining more than one octave of bandwidth [47, 111]. In particular, by driving with a central wavelength of 2 μm it is possible to take advantage of the higher damage threshold and broader phase matching bandwidth provided by crystals such as gallium selenide (GaSe), while exploiting a lower quantum defect [120]. Importantly, a significant advantage of this approach is that because both signal and pump photons are derived from the same beam, the output idler pulse train is intrinsically phase stabilized [44]. Such a waveform-stable output field, with constant phase between the carrier field and the intensity envelop of the pulse, enables straightforward use of field-resolved and frequency comb based techniques for precision spectroscopy.

The IPDFG process relies on a broadband driving spectrum, with the total bandwidth determining the spectral position of the generated MIR idler frequency. To achieve a broad spectral coverage in our system, the 250 fs pulses generated by the thulium fiber amplifier are pre-broadened before IPDFG. Again, self-compression in a micro-structured silica fiber is employed, similar to the process described in section 3. In order to find a compromise between a broad driving spectrum and a high average power, a larger mode area fiber (LPF40) was chosen as the self-compression stage. Figures 3.19(a)–(c) shows a microscope image of the fiber facet with a core diameter of 40 μm along with the calculated mode distribution and fiber dispersion. At a pump input power of approximately 33 W, a broad spectrum is achieved with over 90 % efficiency. Figure 3.19(d) shows the beam profile after collimation with a 100 mm focal length silver parabolic mirror, with a $1/e^2$ beam

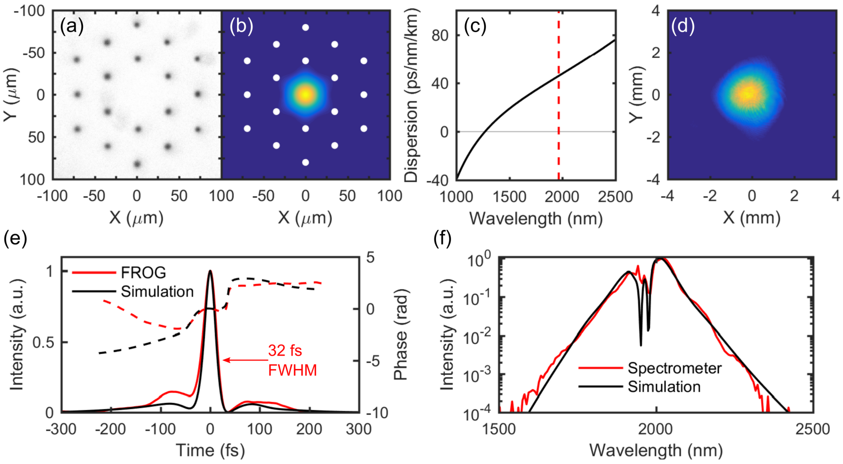

Figure 3.19: (a) Microscope image of the LPF40 PCF facet. (b) Calculated mode profile of the fundamental mode. (c) Dispersion profile of the LPF40 PCF. The dashed line indicates the central wavelength of the input spectrum for driving the self-compression process. (b) Collimated mode profile from the fiber output measured at a distance of 4 m using a 100 mm focal length silver parabolic mirror. (c) FROG reconstruction of the self-compressed output pulse (red line) compared to the simulated pulse (black). The dashed lines show the temporal phase of the FROG and simulated pulse. (d) Experimentally measured spectrum of the self-compressed source compared with the simulated spectrum.

diameter of 3.1 mm. SHG FROG of the pulse reveals a 32 fs pulse with a corresponding -30 dB bandwidth of 1640-2300 nm, as seen in Figures 3.19(e) and (f), with both the temporal envelope and spectrum, respectively, agreeing well with the simulated output. The collimated beam is focused into a 1 mm thick GaSe crystal with a $1/e^2$ focal diameter of approximately 160 μm. After mixing in the nonlinear medium, the driving 2 μm beam is separated from the generated MIR using a gold-coated diffraction grating designed for use as a longpass filter [123]. In this geometry, approximately 500 mW of MIR light is generated at the output crystal face, with an overall efficiency of approximately 2 %.

The IPDFG process can be visualized by examining the spectrum of the driving beam after the GaSe crystal. By changing the orientation of the crystal axis with respect to the input beam polarization, the generation efficiency of the DFG process can be changed. Figure 3.20(a) shows the spectrum with the MIR generation effectively switched on and off. The difference in intensity shown in Figure 3.20(b) illustrates the depletion of the low frequency pump and parametric amplification of the higher frequency signal photons. Considering every possible combination of pump and signal photons, this measurement suggests idler frequencies in the range of 14.5-60 THz, which is seen to agree well with the generated idler spectrum in the inset of Figure 3.20(a).

In order to measure the spectrum of the idler with a higher dynamic range, the MIR field is measured using electro-optic sampling (EOS). The probe pulse used in the EOS detection of the MIR field is the 13 fs long 2 μm pulse from section 3. EOS works through

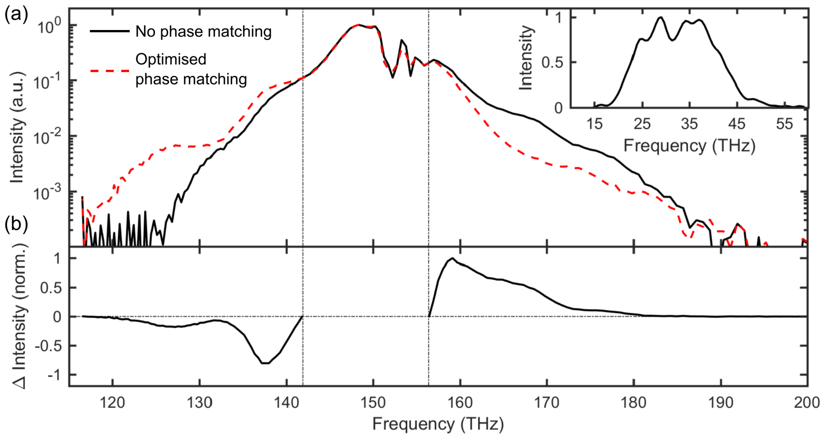

Figure 3.20: (a) Spectrum of the driving 2 μm spectrum measured with (solid) and without (dashed) IPDFG phase matching of the GaSe crystal. (b) Normalized difference in intensity between the 2 lines in (a), showing the depletion and parametric gain of the pump and signal photons in the 120-140 THz region and the 160-180 THz region respectively. The difference in frequency between the pump and signal spectral regions correspond to the idler spectrum shown in the inset of (a), measured with an FTIR spectrometer

the combination of heterodyne detection and a sum-frequency generation of the MIR beam with the time delayed probe pulse, providing a direct time-domain measurement of the idler electric field [52]. Our previous work has shown that the generated MIR pulse train is waveform-stable, with a sub-100 fs duration compressible to a single cycle [111]. Through the Fourier transform of the field, the full spectrum of the MIR pulse can be measured, spanning from approximately 5 to 18 μm (see Figure 3.21).

Conclusions and outlook

Due to the high average power available from the thulium fiber frontend, it is possible to simultaneously operate each of the three generation channels. Figure 3.21(a) presents the output power spectral density (PSD) of each channel plotted on a common frequency axis, covering a frequency band of 16.7-225 THz (1.33-18 μm) at a threshold of 0.1 mW/THz, corresponding to $\log_2(225/16.7) = 3.75$ octaves of total bandwidth, with a median PSD of 3.0 mW/THz (0.09 mW/cm^{-1}). This value is comparable to other multi-channel, high repetition rate MIR supercontinua that have been demonstrated in the 1-10 μm range [42], and is higher than both typical synchrotron [[115], chapter 14] or single-channel waveguide [38] sources.

In order to compare the current performance of this system to other standard broadband infrared sources, we use the spectral brilliance as a figure of merit. The definition of the brightness describes the photon flux of the source (in ph s^{-1}) inside a certain spectral window (usually defined as 0.1 % of the bandwidth at each frequency), as well as the focusability and beam quality of the source (encompassing the focal spot size (mm^2) and divergence (Sr)) [151]. The total brightness of the source is then expressed in units of $[phs^{-1}mm^{-2}sr^{-1}/0.1\%BW]$. Figure 3.21(b) presents the brightness of the three-channel source compared to that of a third-generation synchrotron (DIAMONDB22,UK), as well as the brightness expected from a thermal blackbody source at 1500 K [12]. The laser-based multi-octave source offers a higher brilliance compared to the synchrotron source across its entire bandwidth, with an improvement factor of over 3 orders of magnitude over 92 % of the spectrum. Even at the weakest point, the laser-based source offers over an order of magnitude more brightness in an optical-table-sized footprint than a facility-sized synchrotron beamline.

The availability of a device offering orders of magnitude increased performance at fraction of the cost compared with modern synchrotron light sources opens up new avenues in exploiting broadband light sources for spectroscopic applications. One further important advantage that laser-based sources can offer is the ability lock the carrier envelope offset of the pulse. Considering that the long wavelength DFG spectrum is intrinsically waveform-stable, and both PCF [80] and fluoride fiber [140] broadening should preserve the coherence of the multi-octave output, it is conceivable that such a multi-channel synthesis could produce high-repetition rate sub-cycle transients [152]. For example, the full spectrum in Figure 3.21 supports an 5 fs Fourier transform limited pulse duration at a center frequency of 137 THz (7 fs period).

With such increased spatial and temporal coherence over traditional IR light sources, laser-based supercontinua could in the future become reliable and powerful engines for future FTIR, frequency comb, time and field-resolved studies in a wide range of applications. In this work, we have described a device that has the potential to fill such a role. Based on a thulium-doped fiber amplifier and master oscillator system, the high average power source can generate more than 3 octaves of bandwidth in the MIR spectral region, with a high output power and exceptional brightness. Although utilizing nonlinear spectral broadening techniques, the system is implemented with only optical fibers and a single beam nonlinear crystal stage, leading to a stable output and relatively simple arrangement.

3.3 Intra-pulse difference frequency generation

The molecular fingerprint region spanning the wavelength range from 2 μm to 20 μm, corresponding to the wavenumber region 500-5000 cm^{-1}, is rich in spectroscopic information. In Figure 3.22, absorption lines from gas-phase molecules and a typical condensed-phase biological sample are shown. For spectroscopy of complex samples, a broad spectral coverage of the radiation source is desirable. The focus of this work was on IPDFG because of its inherent waveform stability required in EOS detection, see section 2.2. The system was primarily designed for spectroscopy of liquid biological samples. Typically, between 3.7 μm and 5.5 μm (1800-2700 cm^{-1}), these samples contain no significant spectroscopic information and this region is often referred to as "silent region". The efficient generation of IPDFG wavelengths below 3.7 μm requires a broader spectrum than was available with the PCFs employed here and, thus, the focus in the following discussion is on the generation

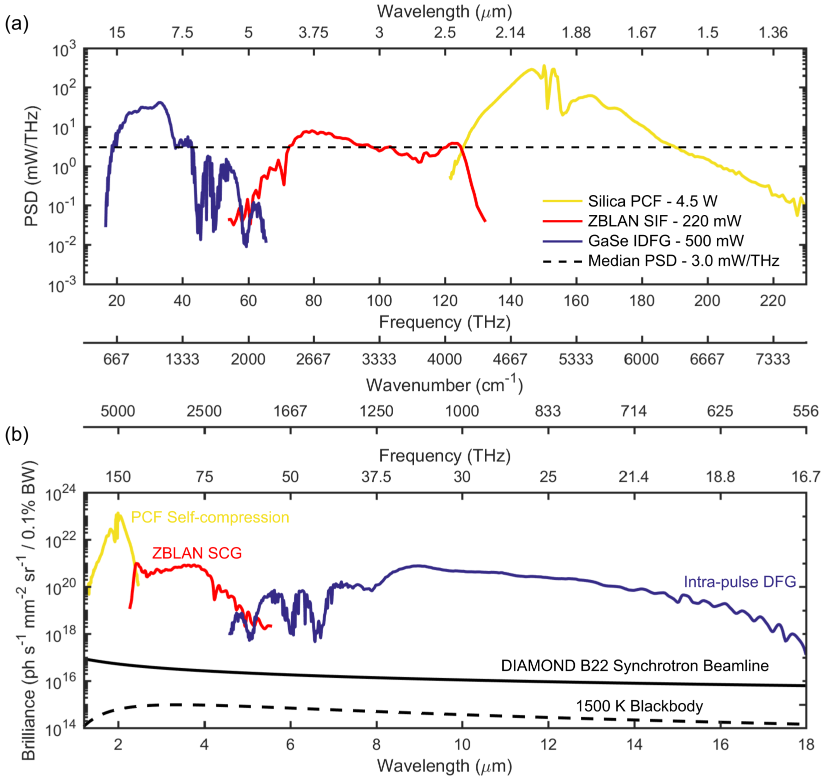

Figure 3.21: (a) Power spectral density of the presented 3-channel source. (b) Calculated brilliance of the laser-based, tabletop source compared with an IR synchrotron beamline facility and a standard 1500 K blackbody source [12]. The ripples in various spectral regions are due to self-phase modulation (PCF), CO_2 absorption at 4.3 μm, water vapor absorption between 5 and 7 μm, as well as some ripples in the spectrum at longer wavelengths, which are attributed to artefacts of the EOS detection process, and are not observed in an FTIR spectral measurement.

of wavelengths in the spectral region of 5.5-20 μm.

3.3.1 Phase matching and nonlinear crystals

The second-order nonlinear process of IPDFG requires a non-centrosymmetric crystal and high peak intensities for high efficiency. With Ti:sapphire laser sources, the photon energy (800 nm corresponds to 1.55 eV) is close to typical bandgaps of non-oxide, birefringent crystals and one-photon or two-photon absorption results in low damage thresholds. Oxide crystals on the other hand have larger bandgaps but are often only transparent up to 5.5 μm. Employing a longer center wavelength (2 μm corresponding to a photon energy of 0.62 eV) for the pulses driving the IPDFG process allows the usage of non-oxide crystals with high intensities. In Table 3.3 several suitable crystals are listed. The parameters are chosen for the mixing process $\frac{1}{9.55\,\mu\text{m}} = \frac{1}{1765\,\text{nm}} - \frac{1}{2165\,\text{m}}$ as the NIR wavelengths lay

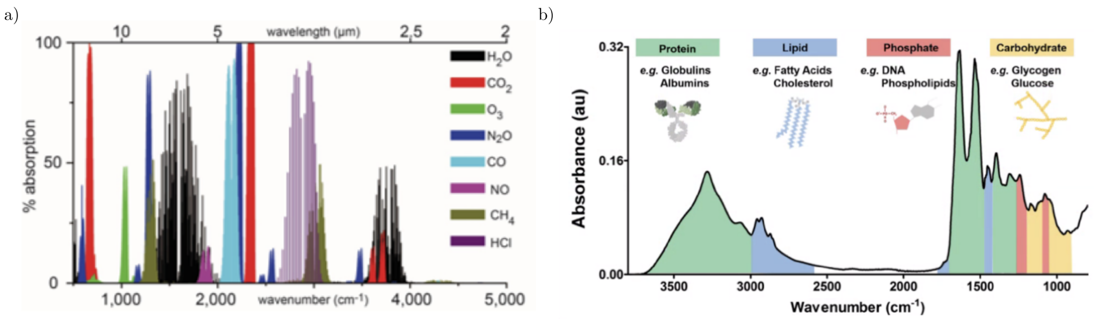

Figure 3.22: Examples of MIR absorption spectra in the molecular fingerprint region. a) Gas phase, taken from [40]. b) Dried serum with absorption bands coarsely assigned to groups of biomolecules, taken from [153].

symmetrically around the central wavelength 1965 nm of the employed pulses. The figure of merit (FM) corresponds to the crystal parameters of DFG and SFG in the non-depletion regime and is calculated by $\frac{d_{eff}^2}{n_1 n_2 n_3}$ (see Equation 2.13). The last column lists the pulse splitting length of the mixing NIR components for a pulse with a duration of 30 fs (see Equation 2.16). Due to the high FM and broad transmission range, gallium selenide (GaSe) has the highest prospects to enable the desired spectral coverage with a high power spectral density.

Crystal	Bandgap [eV]	Transmission [μm]	FM [pm^2/V^2]	ℓ [mm]
GaSe	1.91	0.65-18	158	1
ZGP	1.67	0.74-12	201	0.43
CSP	1.88	0.66-6.5	234	2.25
AGS	2.5	0.5-13	5.3	9
AGSE	1.74	0.71-18	40.6	0.56

Table 3.3: Nonlinear crystals with key characteristics for IPDFG with spectral components 400 nm apart (1765 nm and 2165 nm) for the generation of a MIR beam with a wavelength of 9.55 μm.

3.3.2 IPDFG with gallium selenide

GaSe is a negative uni-axial crystal with a high optical birefringence ($\Delta n \approx 0.3$) and a layered structure. Within the layers, the bonds are strong due to their mainly covalent nature. In contrast, the inter-layer bonds are comparatively weak as they are mainly of the van der Waals type and, thus, layers can easily be separated [154]. Therefore, GaSe cannot be cleaved along crystal orientations other than 001 and the optical axis is always perpendicular to the crystal surface.

For achieving birefringent phase matching in uniaxial crystals, usually the angle θ, which spans between the optical axis and the k-vector of the beam, is adjusted in order to change the extraordinary refractive index, see section 2.1.2. In the case of GaSe, the incident angle onto the crystal needs to be adjusted for the tuning of θ. The difference in refractive index of the mixing components due to polarization and wavelength results in a different strength in refraction and therefore spatial walk-off inside the crystal. For the IPDFG case considered in Table 3.3, the angle between the NIR components is 53 m°, resulting in a spatial walk-off of around 1 μm after 1 mm. Depending on the focus size, this spatial walk-off is negligible. In contrast the pulse splitting length of 1 mm given in the Table 3.3 is limiting the increase in crystal thickness in which relevant gain in the conversion efficiency is expected. A thicker crystal also comes at a trade-off between efficiency and bandwidth, due to imperfect phase matching.

The angle ϕ between the x-axis of the crystal and the plane spanned by the surface normal and the incident beam, affects the effective nonlinear coefficient d_{eff}. When turning φ by 360°, the power of the IPDFG beam has six maxima and minima that reach zero, due to the hexagonal crystal symmetry of GaSe.

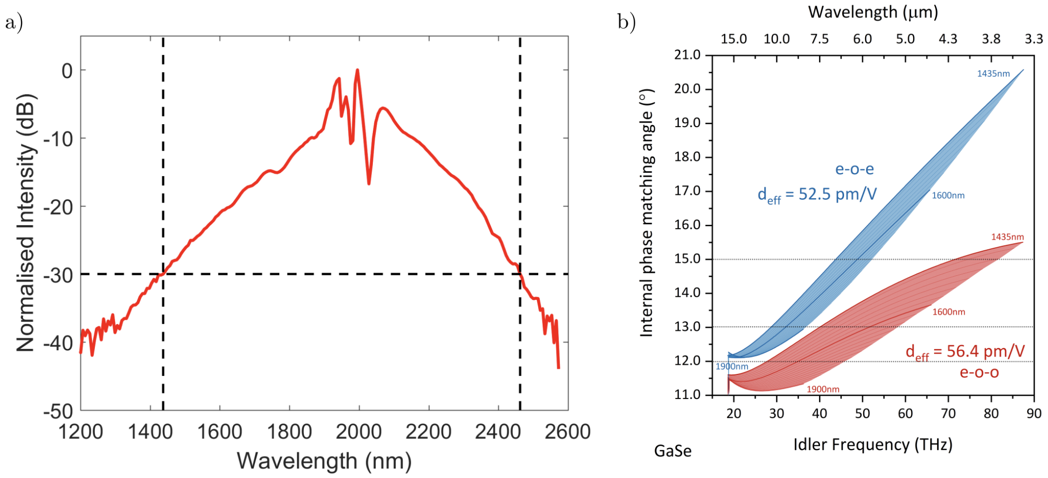

Figure 3.23: Phase matching of a 13-fs long pulse. a) Pulse spectrum with indicated −30 dB level at 1420 nm and 2450 nm. b) Internal crystal angle for perfect phase matching vs the IPDFG wavelength. The areas indicate for type I and type II phase matching existing combinations of the wavelengths within the −30 dB range.

In Figure 3.23 relevant phase matching curves are presented. In a) the spectrum of an SPM-broadened, 13-fs long pulse is shown. In b), for each θ the result of perfect phase matching of wavelengths above the −30 dB level are shown. In GaSe, phase matching of type I and type II can exist at the same internal crystal angle, but yield orthogonal polarizations and different wavelengths. Thus, the polarization allows to distinguish the phase matching type. In Figure 3.24 some IPDFG results are plotted as power spectral density. In red, the results achieved with 13-fs-pulses employing two different crystal thickness and θ angles and measured with an FTIR spectrometer are shown. They span the targeted spectral region but only achieve less than 5 mW average power each. Furthermore, the θ angles of around 13° and 15° for the bright and darker red curves, respectively, allow for both phase matching types, compare Figure 3.23. Indeed, control measurements with a polarizer confirm that the shorter wavelengths belong to the type I and the longer ones to the type II phase matching arm. While this spectral coverage of coherent light is suitable for FTIR measurements, for the polarization dependent EOS detection and its signal strength a single polarization and higher average power would be more favorable. For this purpose the 30-fs-pulses with higher pulse energy from the LPF40 PCF are utilized with a θ angle around 12°.

At $\theta = 12°$, type I phase matching is broadband and type II is suppressed, compare Figure 3.23. Two spectra measured with EOS are shown in blue and are obtained from slightly different fiber lengths and therefore different pulse durations. The dark blue spectrum covers the spectral range of 5.5-18 μm at a power spectral density above 0.1 mW/THz and contains 460 mW average power after the GaSe crystal. A NIR-to-MIR conversion efficiency of 2 % in the crystal was achieved. The dips at 6 μm are 6.7 μm are due to absorption of water vapor and can be avoided by purging the beam path by dry air or generation of a vacuum. The spectral components below 8 μm are not perfectly phase matched by direct IPDFG. One explanation for their generation is a cascaded process where in a first step, the DFG between the generated MIR components and the fundamental beam occurs. In a second step, the large spectral separation between these newly formed spectral components and the fundamental beam allows for the IPDFG process to cover the spectral region between 5.5-8 μm. Such a cascaded process can result in waveform stable pulses and was previously observed in [155, 156].

For the purpose of a higher long-term stability and longevity, a longer fiber was eventually employed, see section 3.4. This resulted in 32-fs-long driving pulses and the light blue spectrum with a total average power of 230 mW after the GaSe crystal. Here, no cascading process was observed and the spectral bandwidth of the direct IPDFG was slightly reduced.

With GaSe, the shorter wavelength range of the desired spectral coverage was not be generated simultaneously with a high power spectral density. This is due to phase matching becoming increasingly more narrowband for shorter DFG wavelengths and due to limited power in the spectral wings that are required for the generation of shorter wavelengths.

In both possible phase matching types IPDFG in GaSe requires perpendicular polarized NIR photons. For this purpose the linear polarization of the pulses was orientated such, that the full spectrum is projected equally onto the ordinary and extraordinary axis of the crystal. This approach comes at the expense of half of the power being in the wrong polarization. Employing a bichromatic waveplate for rotation of half of the spectrum resolves this limitation and has shown to improve the conversion efficiency up to around a factor of 3 [157–159].

Damage threshold

The damage threshold of the nonlinear crystal limits the usable peak intensity of the driving pulse. As a consequence the intensity of the IPDFG beam is limited, as it scales with the square of the peak intensity in the non-depletion regime. Peak intensities at the incident

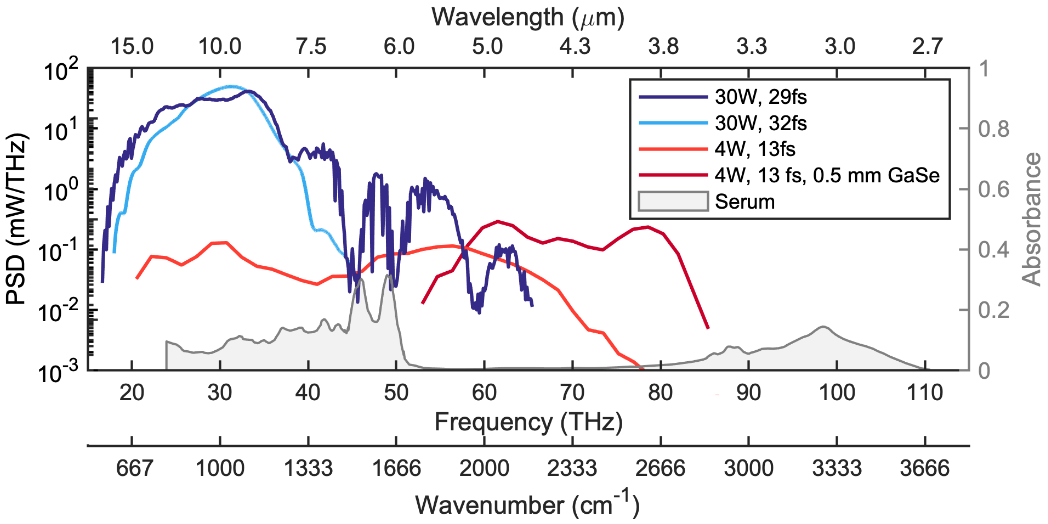

Figure 3.24: MIR spectrum resulting from IPDFG in 1-mm thick GaSe of different pulses and crystal angles. The absorbance of serum is plotted as a reference.

crystal surface without damage reached as high as 25 GW/cm^2 and 75 GW/cm^2 for the 13-fs-pulses and 32-fs-pulses, respectively.

Damaged crystals often exhibited cracks indicating a large thermal stress, as well as craters on the side of the crystal with the incident pulse, see Figure 3.25. The crater is often surrounded by GaSe dust and material is deposited around the holder. One of the likely damage mechanisms is direct three-photon absorption or third harmonic generation with subsequent absorption. Third harmonic generation of photons with a wavelength of 1731 nm is phase matched for $\theta = 12°$ and ordinary polarization. The third harmonic is generated on the extraordinary axis and has a wavelength of 577 nm, where GaSe exhibits an absorption coefficient of 6.9 cm^{-1} (resulting in the absorption of around half of the power after 1 mm propagation) [160]. Furthermore, after the temporal pulse compression in the PCF, visible light was observed, indicating a third harmonic process. It is unclear how this visible co-propagating light impacts the generation of new photons with energy above the bandgap of GaSe via combinations of nonlinear processes such as OPA and SFG.

The experimentally closest case reported in literature is found in [47], with a determined damage threshold of 1.7 TW/cm^2 and the following pulse properties: central wavelength of 1.92 μm, average power of 30 W and a 1/e^2 radius of 190 μm. The origin of this much higher damage threshold with respect to the peak intensity compared to the here observed limits is not yet understood. For test purposes, the same physical crystal used in [47] was tested in the here described setup, yielding no higher damage threshold than 75 GW/cm^2 and thus excluding the crystal quality as the cause for the different damage thresholds. The main differences between the setups lay in the pulse repetition rate (50 MHz vs. 1.25 MHz), which might indicate cumulative effects, and the surrounding gas (vacuum of around 1 mbar vs. dry helium at 1 bar). Helium exhibits the highest thermal conductivity of gases and is as such an effective coolant. In case of a damage mechanism starting from thermal stress this cooling effect is expected to increase the damage threshold.

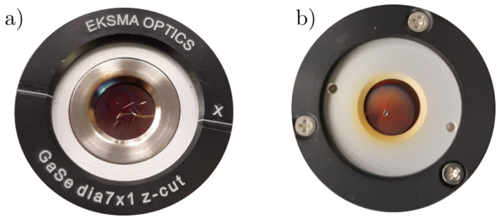

Figure 3.25: Damaged GaSe crystal with a) cracks and b) hole with deposited GaSe.

3.4 Long-term stability

For an experiment it is desirable that the performance of the measurement instrument changes significantly less than the expected change of the observable over the acquisition time. Otherwise the investigated signal can be distorted and overshadowed by noise. The system described here was intended for measurements with typical acquisition times on the scale of a few seconds to several minutes. High reproducibility and reliability are furthermore required for studies involving thousands of samples measured over days, weeks or months. In the following the long-term stability of the presented system is discussed.

3.4.1 Water temperature stabilization

For laser systems emitting average powers in the range from several to hundreds of Watts heating by absorption can often impact the beam pointing stability. In order to compensate this thermal heating, water cooling of optical components, breadboards and chambers via a chiller is often implemented. Here, two chillers were used to stabilize the temperature of the CPA (namely pump diodes, amplifier fiber and breadboard), the mounts of the PCF and every mirror mount with more than 4 W of incident power. The chillers (P208, Termotek) have an internal water circuit that can be stabilized with a PID loop to an accuracy of ±0.1 °C, often limited by the temperature sensor resolution. An additional external water circuit, in the following referred to as "house water", was used to transport excess heat away from the aforementioned chiller. Another source of slow thermal change was the air temperature of the laboratory, which was stabilized to around 21.5 °C.

In Figure 3.26, the initial impact of the chiller output temperature on the average power of the generated MIR radiation can be seen. The output temperature of the chiller changes by 0.05 °C in a sinusoidal manner with a period of around 15 minutes and the MIR power follows this oscillation with a slight delay and with an peak-to-peak amplitude of around 15 %. This high degree of coupling is unwanted and, in the following, the remedies investigated in the frame of this work are discussed.

In order to detect the coupling mechanism, a test with a sudden change in the chiller output temperature by changing the set-point by 0.2 °C was performed. Figure 3.27 shows the observed average power of the MIR beam and the CPA output, as well as the pointing of the CPA. Due to the slow heat transport to the components of the optical system reaching an equilibrium state requires a typical time scale of dozens of minutes. Therefore the impact of the sudden temperature change is not instantaneous, but is detected in the observables time scales of minutes. The MIR power follows a saw tooth pattern and changes by nearly half. Simultaneously, the CPA power changes on a significantly smaller scale, namely by roughly 0.3 %.

More interesting is the occurring beam pointing change of the CPA output in the vertical dimension, which follows the same pattern as the MIR power. This indicates that the input coupling into the PCF can be the leading cause of the strong dependence. The nonlinear self-compression process in the fiber is highly intensity-dependent and relies on free-space coupling into the fundamental mode. Further investigations showed that

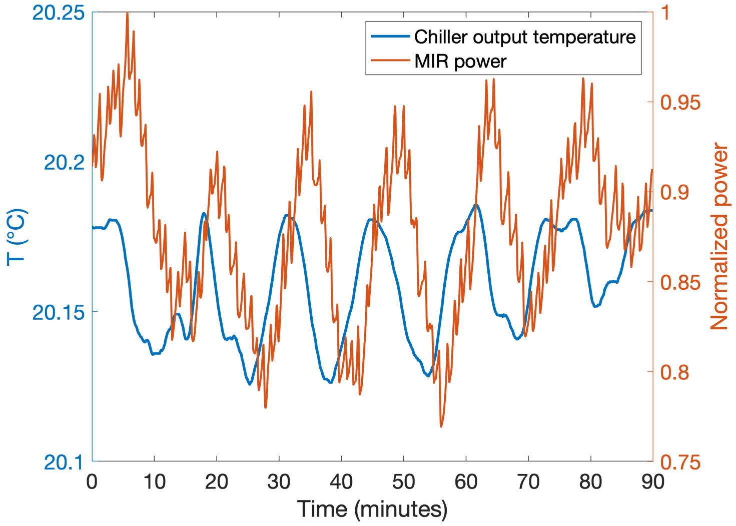

Figure 3.26: Impact of chiller water temperature on MIR power.

the power transmitted through the LPF40 fiber and the spectral bandwidth changes with changing temperature, confirming the drift in the input coupling as the main cause of performance degradation.

There are several possible components that can cause such a beam pointing variation, namely the grating compressor, the breadboard and the holder of the main amplifier fiber. These components are difficult to exchange and to diagnose. An active beam pointing stabilization before the PCFs would be one solution to the beam pointing drifts impacting the compression of the pulses after the CPA. This approach wasn't pursued due to the implementation challenges such as limited space in the vacuum chamber, the need to have for each PCF a separate stabilization setup and the cost efficiency. Furthermore, active stabilization schemes often only shift the noise/drift to another frequency range. Therefore, instead of decreasing the coupling strength or its direct impact due to its difficulty, more focus was given on decreasing the temperature change of the water.

The temperature oscillations stem from the temperature controlled house water, which is kept at around 15 °C with an oscillating PID loop. By optimizing the PID settings, the oscillation amplitude was reduced from 0.5 °C to 0.2 °C for the house water and from 0.15 °C to 0.05 °C for the chiller, respectively. This was already implemented before taking the measurements shown in Figure 3.26 and proved to be an insufficient improvement.

The stabilization loop of the chiller remains inactive as long as the difference of the output temperature to the setpoint is within the accuracy of ±0.1 °C. Therefore, for a thermalized laser, where the required cooling power doesn't change, a more stable house water temperature can result in a better temperature stability of the chiller output.

One passive approach, which was tested, consisted in the implementation of a low-pass frequency filter for temperature changes. For a flow rate of around 4 l/minute and an oscillation period of 15 minutes a 60 l tank contains water from the full temperature

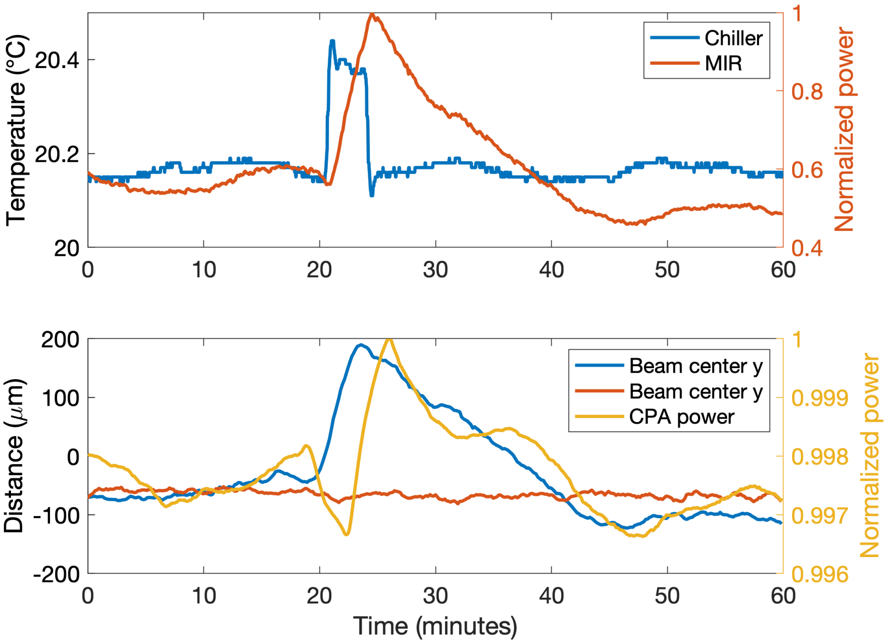

Figure 3.27: Impact test of abrupt change in chiller set point temperature. Top: Chiller output temperature and generated MIR power. Bottom: Beam position of the CPA output in the diagnostic arm after 1.5 m and the corresponding average power.

oscillation and can facilitate averaging. Due to limited convection and heat transfer, an even larger volume would be required for a more efficient averaging. Here, empty beer kegs were used as a reservoir and due to the limited storage space and water pressure, a volume of 40 l was installed. This passive approach led to an amplitude reduction of the temperature change of the house water by a factor of 2.

Another approach is the active stabilization by heating and cooling the house water. For this purpose, one beer keg was wrapped with a electrical heating wire and the temperature before and after the beer keg was tracked, see Figure 3.28. A PID loop acts on the voltage of a computer controlled power supply to adjust the heating power. By choosing appropriate PID values, the house water temperature oscillations can be reduced. Figure 3.27 c) shows that the water temperature change going to the chiller was reduced to 0.02 °C. The noise of the temperature sensor and slow drifts in the flow rate and house water temperature limit the performance. The best setting of the PID values required weekly re-calibration to compensate for these slow drifts.

In Figure 3.27, the optimized stability of the MIR power for a thermalized system is shown. The relative peak-to-peak changes over an hour are reduced to below 0.7 % and exhibit a standard deviation of 0.14 % for frequencies below 1 Hz. The MIR power seems uncorrelated to the house water temperature before the PID loop. Instead, saw-tooth like modulations are visible. These are inversely correlated to the photodiode current of the pulse picker. As described in section 3.1.2, the pulse train from the oscillator was pulse-

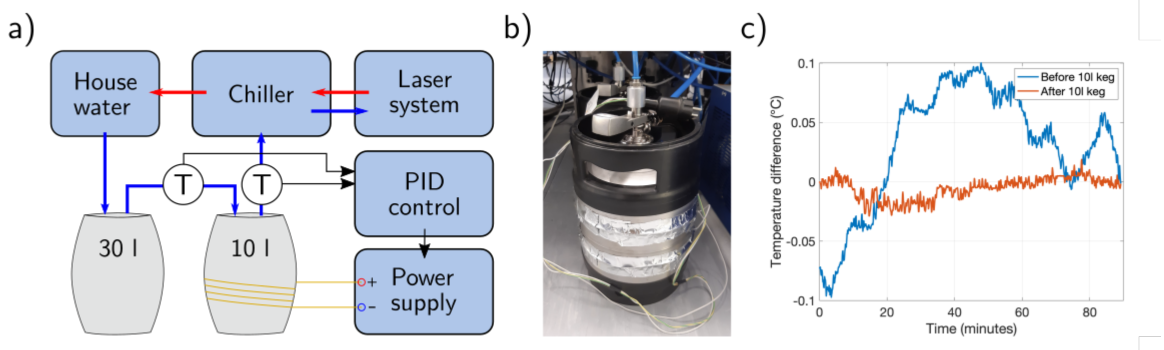

Figure 3.28: Water temperature stabilization with increased water volume and heating control. a) Schematic of the water circuit with kegs and PID loop. b) Picture of 10 l keg with heating wire. c) Performance of the stabilization with the PID loop.

picked before being nonlinearly frequency shifted. The pulse picker suffered from a slow drift that required active stabilization, for which the photocurrent after the pulse picker was used. The frequency shift is highly sensitive to the pulse energy and shape and even small changes can result in changes of the amplitude and phase of the seed pulse going to the CPA. Thus, the compensation of the drift in the pulse picker can lead to changes further down the chain, like the MIR power. A drift compensation with smaller step sizes can reduce the amplitude. In our system, the step size was limited by the hardware of the pulse picker (Pulse Selector IOM150, LaCoSys GmbH). Another version of this device was tested, which allowed to reduce the change of the MIR power below 0.2 %, but increased the PSD in the high-frequency region (>1 kHz).

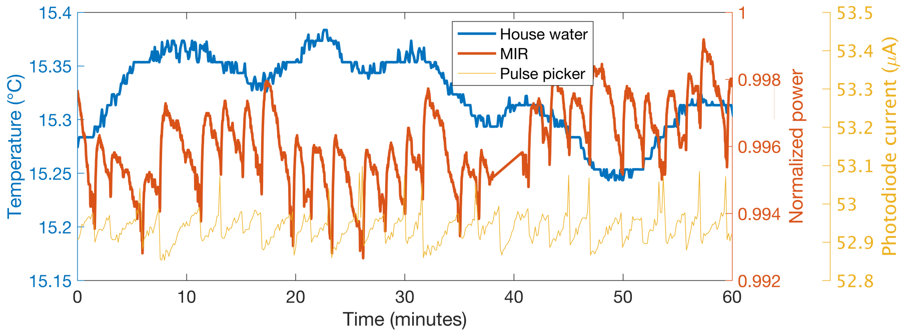

Figure 3.29: MIR power stability with optimized settings resulting in a standard deviation of 0.14 % over one hour.

Another factor beside peak performance is the overall reliability of the system for longer measurement campaigns. Finding the best trade-off between these two factors in the presented system was most challenging for the PCF and the IPDFG crystals. Due to nonlinearities even small changes in the front-end, such as pulse duration, pulse shape, beam profile and pointing, can result in damages. Therefore, a conservative margin from the damage threshold is preferred. For the PCFs, a longer fiber will result in self-compression requiring lower pulse energies and resulting in longer pulse durations and thus reduced peak powers and peak intensities at the end of the PCF. The maximum of the peak intensity at the point of best self-compression also results in a maximum of the generated MIR average power, see Figure 3.30. Operating at this turning point will reduce the impact of drifts and noise before the PCF, thus improving the long-term stability. This turning point also limits the peak intensity at the IPDFG crystal and allows to approach the damage threshold of the crystal with a smaller safety margin.

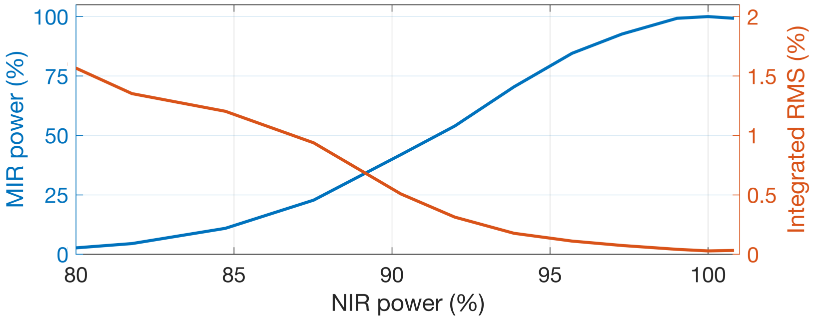

Figure 3.30: MIR change for increasing input power of the NIR pulse into a LPF40 fiber of 64 mm length. Blue: The powers are given in percent of the setting with maximum MIR power (136 mW and 30.45 W). In red the integrated RIN in the frequency range of 1 Hz-102 kHz.

3.4.2 Fiber considerations

In the previous section 3.2.2, the pulse compression with solid-core photonic crystal fibers (PCF) was simulated and demonstrated [128]. For long-term applications the design of the fiber is crucial and in this subsection some light is shed on usage considerations.

The design of the hole pattern in a solid-core PCF allows low-loss guidance of light in a highly-confined single spatial mode [161]. Single-mode operation is achieved by a suitable hole diameter-to-pitch ratio in e.g. a hexagonal hole pattern that is perfectly mode-matched with the single mode while higher-order modes experience losses during propagation [162]. In the solid-core PCF, the transmitted mode is located at the center, where one hole is missing. The light propagates through the solid, which can exhibit a high nonlinear index (fused silica: around $2.2 \times 10^{-20}\,\mathrm{m^2/W}$). Together with a small mode size and an adaptable dispersion, nonlinear effects can be promoted.

The main limitation of a solid core, compared to a hollow-core PCF which is often filled with gas, is the potential damage of the solid. One of the limits is set by catastrophic self-focusing, which occurs by exceeding the critical power (compare Equation 2.21). Fused silica has a critical peak power of 16 MW for linearly and 24 MW for circularly polarized light at a wavelength of 2 μm [99]. The peak power of a Gaussian pulse is roughly 0.94 times the pulse energy divided by the FWHM pulse duration. This peak-power limit thus results in a trade-off between pulse duration and pulse energy. Furthermore, a limited peak power also impacts the achievable shortest pulse duration, as it scales inversely with the square root of the peak power in soliton-compression stages [99, 144]. Another point to consider when choosing a PCF is that the shortest achievable pulse duration is proportional to the mode-field diameter of the fiber [99, 144].

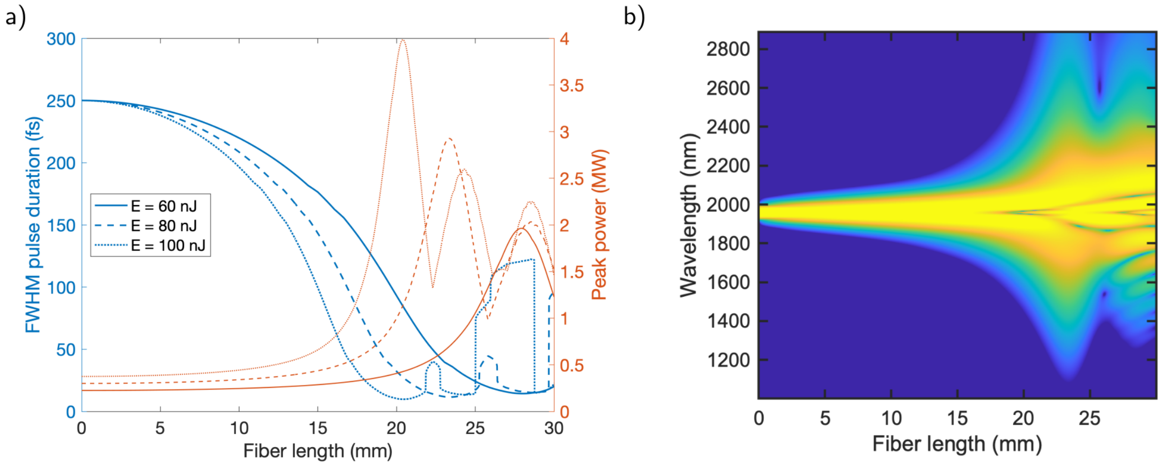

Figure 3.31: Simulated pulse propagation through the LMA15 PCF with mode field diameter of 13.1 μm, for details see section 3.2.2. The initial pulse is a transform-limited Gaussian pulse with a FWHM duration of 250 fs and a center wavelength of 1965 nm. a) Pulse duration and peak power vs. fiber length for 3 different pulse energies. For a 50 MHz repetition rate these energies correspond to 3 W, 4 W and 5 W, respectively. b) Spectral evolution of a pulse with an energy of 80 nJ.

In the case of a given PCF structure and input pulse shape (that is, pulse energy and spectrum with phase) the remaining adjustable parameter is the length of the PCF. In Figure 3.31 the pulse evolution through an LMA15 fiber is simulated (see section 3.2.2 for details on the simulation). For a given input pulse energy, the FWHM pulse duration first decreases until it reaches a minimum, after which it increases until jumps appear. These jumps are indicative of the pulse breaking up into a multi-pulse structure and more pulse energy being distributed into side pulses. The initial decrease of the pulse duration accelerates during the propagation because of SPM being proportional to the temporal derivative of the intensity. At the point of best self-compression the waveguide dispersion, which is dominated by the anomalous dispersion of fused silica, and the nonlinear dispersion by SPM have mostly canceled each other out. Upon further propagation the broad spectrum results in a stronger impact of the waveguide dispersion, resulting in a down-chirped pulse. Thus the highest frequency components precede the pulse and the rising flank of the intensity envelope results in a reduction of these frequencies by SPM (compare Equation 2.20). The same effect happens with the lowest frequency components resulting in an overall spectral narrowing [163]. This spectral narrowing can also be observed in Figure 3.31 b), where the spectrum collapses around 26 mm and increasing modulations appear afterwards.

For increasing pulse energy, the intensity slope has a steeper starting point and the point of best self-compression is reached for a shorter propagation distance. This can also be seen in Figure 3.32 where the pulse duration and the required pulse energy for reaching self-compression is plotted versus the fiber length. The shortest achievable pulse duration is proportional to the fiber length. In contrast, the required pulse energy for reaching the self-compression scales inversely in a nonlinear manner.

These scaling laws indicate that making the fiber as short as possible results in the shortest and most energetic pulse. Unfortunately, as mentioned earlier, this is limited by potential damages of the core material. In Figure 3.31 a) it can be seen that the peak power for a 100-nJ pulse reaches only 5 MW around the self-compression and afterwards decreases with an oscillatory modulation. 5 MW is well below the estimated critical power of 16 MW for linear polarization. Nonetheless, in our experiments damages of the fiber end facet where observed several times. This indicates that a different damage mechanism takes place at the end facet, limiting the achievable pulse duration. This mechanism and its scaling with the relevant pulse and fiber parameters are subject of further investigations that are taking place in our laboratory at the time of writing this thesis.

In the case of a peak-intensity-induced damage mechanism, the self-compression mechanism allows for operation in a safe regime. Let us assume a fiber length where the self-compression can be reached without damaging the fiber. A higher pulse energy than required then results in a pulse compressed inside the fiber. At the end facet the pulse is temporally dispersed and the peak intensity decreased. A lower pulse energy than required cannot fully compress the pulse, thus preventing damage. This turning point of the peak intensity at the end facet with increasing pulse energy also results in desirable lower peak intensity fluctuations at the point of best self-compression in case of a sufficient long fiber [164].

In Figure 3.33 a) a schematic of the setup for such a PCF is shown. One end of the fiber is sealed by a spliced fiber cap. The other end is collapsed by shortly heating the fiber to around its melting point (≈1700 °C). This ensures that the hole structure stays filled with air and can't be contaminated, e.g. with water.

Due to the divergence of the unconfined light in the collapse region the beam diameter at the exit surface is significantly increased, and the peak intensity of the temporally compressed pulse is reduced at the glass-air surface. For example, the LMA15 has an NA of 0.13 and thus propagation through a 1 mm long collapsed region increases the beam diameter from 13.1 μm to 103 μm - resulting in a reduction of the peak intensity by a factor of 62. The fiber cap at the entrance has an anti-reflective coating, which reduces the Fresnel reflection losses (for fused silica around 3.2 %) to well below 1 %. The anti-reflective coating together with the diverging propagation in the collapsed region reduce the amount of light being reflected back into the amplifier, which could lead to unwanted losses. While applying an anti-reflective coating at the fiber end benefits the transmission but the time-properties need to be considered. The broadband spectrum of a short pulse makes the design of an anti-reflective coating more challenging and the material dispersion of a fiber cap elongates the nearly transform-limited pulse duration. The length of the collapsed region is therefore kept to a length of around 1 mm, much thinner than the typically used

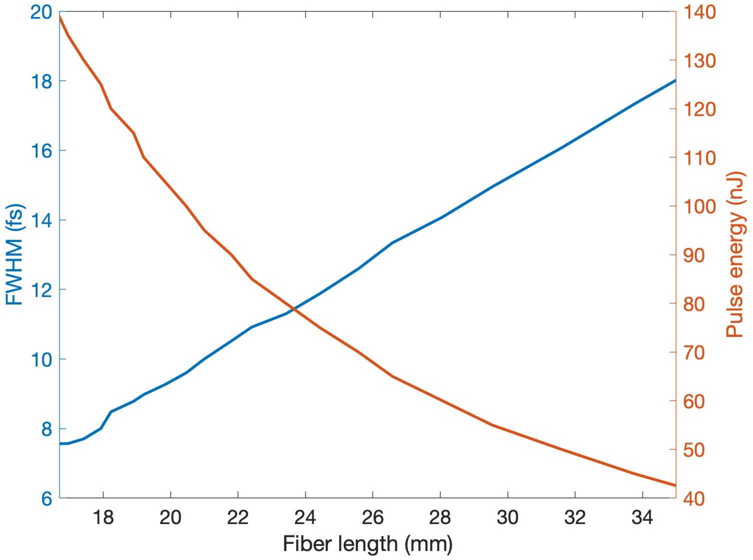

Figure 3.32: Simulation results of the point of best self-compression for different LMA15 PCF lengths and initial Gaussian pulse with a FWHM pulse duration of 250 fs and center wavelength 1965 nm.

fiber cap (≈5 mm). For our application of compressing femtosecond pulses with a center wavelength around 2 μm, substantial heating of the fibers can be observed. Absorption of fused silica, depending on its grade, typically gains significance around 2.2 μm and above. Furthermore, water vapor that might be trapped in the holes of the PCF has absorption bands in the relevant wavelength ranges of 1810-1920 nm and 2500-3300 nm. For example, the tip of a 62-mm long LPF40 fiber reaches temperatures of 115 °C after thermalization in vacuum and broadening to the point of best self-compression with an average power of roughly 30 W. The operation in vacuum (on the order of 0.1 mbar) reduces the convection cooling of air dramatically and the main paths for dissipating the absorbed energy remain (i) thermal radiation and (ii) heat transfer via the small contact area to the fiber mount.

Figure 3.33 b) shows a fiber mount which can be water cooled. Metal clamps softly hold the fiber in place in a thermally robust manner (instead of, e.g., glue that deforms due to heating and can result in beam pointing changes). In order to ensure efficient usage of the water cooling and a low equilibrium temperature, the fiber is thermally contacted with the mount via a vacuum-compatible thermal paste (Heat-Away 641-EV). The fiber material, fused silica, has one of the lowest thermal heat conductivity (1.38 W/m/K) among solids. Thus, a temperature gradient is expected from the hole structure to the edge of the cladding, as well as from the fiber cap to the fiber tip where the broadened spectrum leads to further absorption. The temperature has an impact on the material dispersion of the waveguide [165] and can also, due to thermal expansion, impact the mode field diameter. These two effects have not been considered in the previous simulations and are subject to further investigation.

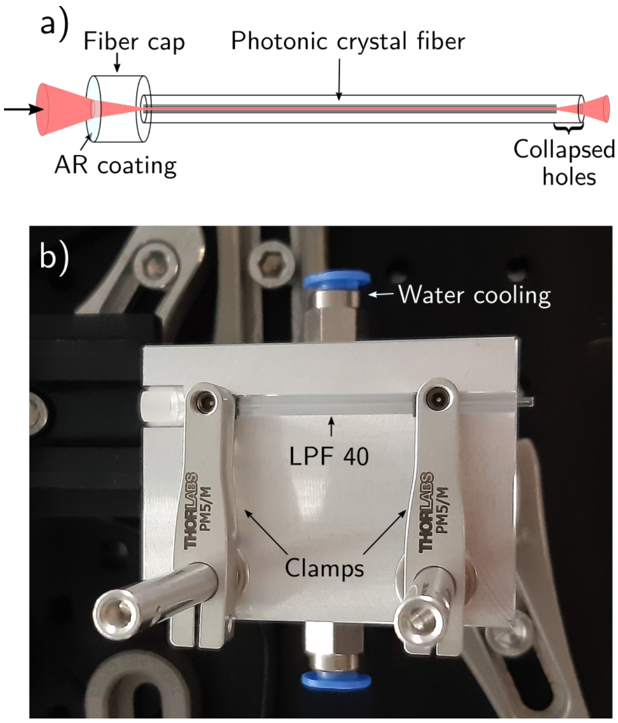

Figure 3.33: PCF integration. a) Schematic of a PCF setup with the intended beam propagation indicated in red. b) Picture of LPF40 fiber (MFD of 40 μm) clamped on a water-cooled mount with a V-groove.

3.5 Dispersion control in the MIR spectral region

For an ultrashort pulse, the spectral phase needs to be as flat as possible in order to approach a bandwidth-limited pulse duration. In the MIR spectral region, materials exhibit high chromatic dispersion, see Figure 3.34, thus making the management of the spectral phase crucial for applications requiring a short pulse duration. The group delay velocity (GDV) of the commonly used transmissive materials is mostly negative above 5 μm, while only silicon and germanium exhibit slightly positive GDV. Above 3 μm, all investigated materials exhibit strongly positive third order dispersion (TOD). The shape of the refractive index and thus, of its derivatives is due to the absorption edges arising at longer wavelengths and the relation between the real and imaginary parts, as specified by the Kramers-Kronig relation. In case material dispersion can only be employed for MIR pulse compression, one strategy is to initially avoid transmissive optics as far as possible. This is because the accumulated TOD cannot be compensated for with more material due to the same sign[111].

There are various techniques to influence the spectral phase of an ultrashort pulse, whereas often the pulse is split into its spectral components and the optical path-length is adjusted before recombination. The highest flexibility in these approaches is given by employing pulse shapers that allow for tailoring the spectral phase even on time scales of milliseconds [166, 167].

For the molecular fingerprint region, several approaches have been developed, e.g., germanium-based acousto-optic modulators [168], deformable mirrors [169] and dispersive filters [170]. With the pulse shaper approach, often a trade-off between the spectral bandwidth and the number of spectral elements arises and the total dispersion that can be adjusted is limited. Furthermore, this active shaping adds a high complexity to the system, and noise in the shaping can lead to degradation of the waveform stability.

Passive approaches include grating and prism compressors, but these are rarely used in the MIR spectral region. On one hand, a large spatial foot-print is required for generating a sufficient long path-length difference between the spectral components, e.g. the compressor used in [31] had a length of 40 cm for compensating a GDD of around 11 ps^2 in a spectral range of 1180-1280 cm^{-1}. On the other hand, the efficiency is limited by possible absorption losses in air and by the performance of used optical components, e.g. grating diffraction efficiency or limited anti-reflection coatings on prisms.

A compact and versatile approach for adjusting the spectral phase are chirped mirrors. They were first developed in the 1990s [171] for femtosecond lasers and were recently extended to the MIR spectral range [172, 173]. A chirped multilayer mirror has a coating with multiple layers made of different refractive index materials and thicknesses. The multiple Fresnel reflections at the interfaces interfere and result in a wavelength-dependent penetration depth in the multilayer structure. Thus, the optical path length can be tailored for different spectral elements. In the visible and near-infrared spectral range, chirped mirrors typically permit reflectivites exceeding 99 % and GDD values of hundreds of fs^2.

For the intended application of field-resolved spectroscopy, the pulse compression is desirable as it allows to temporally separate the pulse from the molecular response. In order to combine and average thousands of measurement, a high waveform stability over the entire measurement time is crucial. Furthermore, as the system is designed to be housed in vacuum chambers, a compact pulse compression is required. For these reasons, besides avoiding unnecessary dispersion, the passive and compact pulse compression approaches of using material dispersion and newly developed dispersive mirrors were employed [55, 111].

To our knowledge, the first broadband chirped mirrors in the molecular fingerprint range are reported in [173] and were designed for pulse compression in the system described in [55]. The author of this thesis performed the practical evaluation of these dispersive mirrors (DM) which is presented in the following. In Figure 3.35 the experimentally determined reflectance and GDD are shown. In the targeted spectral region between 6.5-11.5 μm, the reflectance exceeds 90 % and the GDD ranges between 550 fs^2 and 2100 fs^2. The main contributor to the spectral dispersion is a sample cell made with ZnSe walls, introducing a negative GDD. In the middle panel of Figure 3.35 this strongly quadratic spectral phase is compensated to below 1 rad. This nearly flat phase results in a compression close to the Fourier-limit of the intensity FWHM from 86 fs to 55 fs after 4 reflections. With power losses of less than 35 % this demonstrates an efficient and compact pulse compression in the MIR spectral range for a pulse with a bandwidth close to one octave.

Ideally, these chirped mirrors would be available for the entire spectroscopically interesting molecular fingerprint region. However, this technological advance faces severe

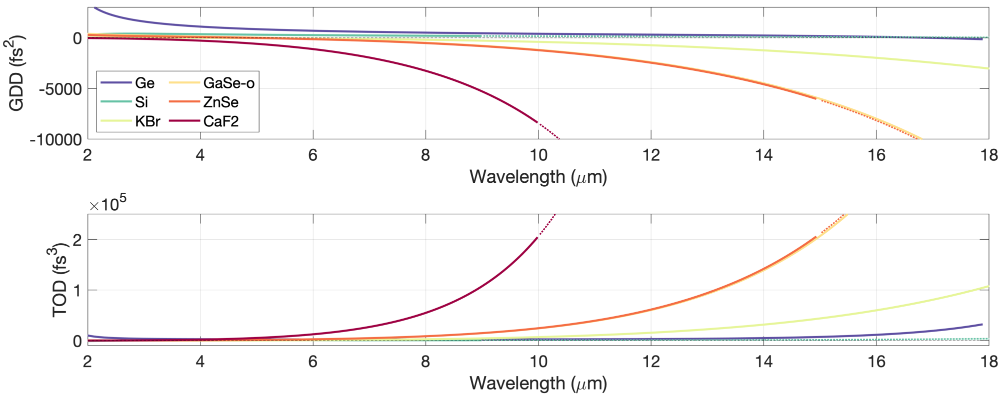

Figure 3.34: Higher order dispersion of different MIR transmissive materials with 1 mm thickness derived from the Sellmeier equations found in [174–178]. Dotted lines indicates the dispersion outside the transmission range of the material. GDD: group delay dispersion, TOD: third order dispersion.

challenges. Chirped mirror designs are subjected to a trade-off between the spectral bandwidth and maximal GDD. The molecular fingerprint region spans several octaves with strong material dispersion. The concept of a field synthesizer, where a pulse is split into several spectral channels in which the phase and amplitude can be manipulated before recombining them, is one possible approach to overcome this limitation [152, 179]. Another challenge is finding suitable material combinations for the multi-layers that offer a high transparency in the longer wavelength (>10 μm) range. The typically-employed thickness of the layers is proportional to the wavelength of the incident light. The coating machines that fabricate these layers are often limited in the amount of material that can be deposited in one coating run. Thus, compared to multilayer designs for the visible or near-infrared spectral regions, the designs for the MIR spectral region need to be relatively simple with a few layers only. Another challenge is delamination of the coating from the substrates due to the surface tension, an issue that becomes more severe the thicker the coating becomes.

In order to avoid unnecessary dispersion upon transmission, reflective instead of transmissive optical components are preferable. In the following section, a new reflective MIR beam splitter is presented, which was developed in the frame of this doctorate.

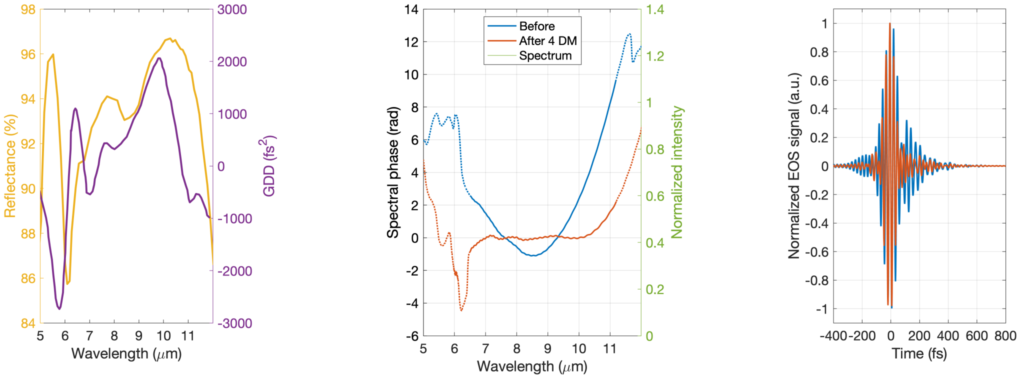

Figure 3.35: Dispersive mirrors (DM) for pulse compression in the MIR spectral range. Left: Measured data of chirped mirrors detailed in [173]. Middle: Spectral phase before and after 4 DM. The dotted lines indicates the spectral range with less than 1 % of the maximum spectral intensity and thus less well retrieved spectral phase. Right: EOS signal in the time domain.

3.5.1 Mid-infrared long-pass filter for high-power applications based on grating diffraction

This section is identical[10] in wording and figures to the paper with the title "Mid-infrared long-pass filter for high-power applications based on grating diffraction" published in Optics Letters, vol. 44, no. 12, p. 2014 in 2019 [123]. As the leading author[11] I simulated the expected filter characteristics, performed the experiments and analysis for the evaluation of the filters and wrote the initial manuscript. A detailed author contribution is found here[12].

Abstract

A gold-coated silicon grating has been developed, enabling efficient spatial separation of broadband mid-infrared (MIR) beams with wavelengths $>5\,\mu$m from collinearly propagating, broadband, high-power light in the near-infrared (NIR) spectral range (centered at $2\,\mu$m). The optic provides spectral filtering at high powers in a thermally robust and chromatic- dispersion-free manner such as that necessary for coherent MIR radiation sources based on parametric frequency downconversion of femtosecond NIR lasers. The suppression of a >20 W average-power, $2\,\mu$m driving pulse train by three orders of

---

[10] only the numbers of the references, figures and tables are changed for consistency throughout the thesis

[11] authors: Daniel Gerz, Wolfgang Schweinberger, Thomas Patrick Butler, Thomas Siefke, Martin Heusinger, Tatiana Amotchkina, Vladimir Pervak, Uwe Zeitner, Ioachim Pupeza

[12] Author contributions: Conceptualization: WS, IP; Design and Manufacturing: TS, MH, UZ, TA, VP; Data curation: DG, WS, TPB; Analysis: DG; Simulation: DG; Writing: DG; Supervision: IP ; Review and editing: all authors.

magnitude, while retaining high reflectivity of the broadband MIR beam, is presented.

Main text

Molecular spectroscopy in the mid-infrared spectral range, particularly in the "molecular fingerprint region" (500-4000 cm^{-1}), is a widely used analytical tool for applications ranging from fundamental science [180] to applied and life sciences [115], environmental monitoring, and quality control [181]. Crucial to the improvement of the sensitivity, specificity, and availability of such techniques is the development of robust, table-top sources of coherent mid-infrared (MIR) radiation. In recent years, the advent of high-power, near-infrared (NIR) femtosecond lasers has provided a way to reach the MIR regime through nonlinear optical methods. In particular, laser systems delivering trains of pulses with durations of a few tens of femtoseconds, multi-10 MHz repetition rates, and several tens of watts of average power are available today, both at 1 [92, 127] and 2 μm [80, 137] central wavelengths. Via parametric frequency downconversion in suitable nonlinear crystals [40], these lasers have recently established a new class of MIR radiation sources [42, 44, 46, 47, 75, 111], combining broad spectral coverage with brilliance values exceeding, even those of third-generation synchrotrons [44, 111], as well as with excellent temporal coherence [121, 182].

In nonlinear sources based on the processes of optical parametric amplification [42] or intrapulse difference frequency generation (IPDFG) [44, 46, 47, 111, 121, 182], a common goal is to generate an isolated MIR idler beam, which can be used as a probing signal in a spectroscopic measurement. Therefore, this requires a method of separating the NIR driving pump/signal beam(s) from the generated MIR light. Typically, a dielectric-coated substrate is used in order to separate the NIR beam while transmitting the MIR wavelengths, with desirable features such as high separation contrast, steep slope, high transmission, and broad blocking range [183, 184]. Employing chirped mirrors additionally allows for tailoring the pulse dispersion [172]. However, the production of these optics in the MIR spectral region remains challenging due to technical issues such as the peeling of layers owing to the internal stress of thick layers and the scarcity of suitable MIR transparent coating materials. In IPDFG, the use of femtosecond driving pulses can also result in relatively short (<100 fs) and broadband idler pulses. In time-resolved applications such as pump-probe or electricfield- resolved spectroscopy [121], the temporal profile of the MIR field is essential and, therefore, any excess temporal broadening due to transmission through dispersive materials is disadvantageous. Furthermore, absorption of the dielectric substrate can limit the MIR bandwidth, as well as lead to thermal issues in the case of absorption of a driving beam of several tens of watts.

To address the challenge of dispersion-free, high-power filtering in parametric downconversion experiments, we have developed a novel diffraction-grating-based optic. The optic has been designed to suppress a nearly octave-wide spectrum centered at 2 μm with a power of a few tens of watts, while retaining as much of the broadband MIR spectrum above 5 μm as possible. In this Letter, we present the design and fabrication of the optic, as well as experimental characterization of the diffraction efficiency and proof-of-principle experiments showing the power scalability up to 40 W and suitability for current parametric

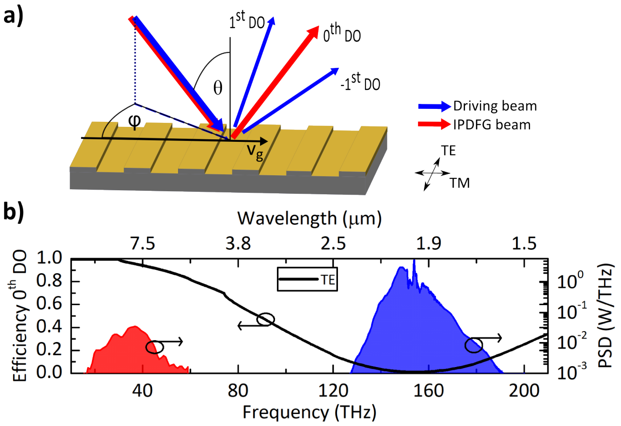

Figure 3.36: Concept of a grating as a long-pass filter. (a) Binary grating diffracts the long wavelength beam mainly into 0th DO, while the short wavelength driving beam is mainly diffracted into higher DOs. θ, incident angle; ν_g , grating vector; TE, transverse-electric polarization; TM, transverse-magnetic polarization (b) Simulated diffraction efficiency into 0th DO for an IPDFG example (IPDFG beam, 0.3 W; driving beam, 23 W) [111].

MIR sources.

A schematic of the operating principle of the long-pass filter is shown in Figure 3.36(a). Two collinearly propagating beams are incident on the gold-coated silicon diffraction grating. The sub-MIR-wavelength reflecting structure efficiently diffracts the shorter wavelength NIR radiation into the 1st diffraction order (DO), while the MIR radiation is reflected specularly, remaining in the 0th DO. Similar approaches were previously employed in infrared monochromators utilizing echelette gratings in order to suppress shorter wavelength stray light [185]. More recently, beam splitting gratings have been used to separate extreme ultraviolet light from the driving NIR beam in high-harmonic generation [186, 187]. The 0th DO corresponds mathematically to a specular reflection and, thus, is dispersionfree. In order to provide good thermal conductivity and facilitate production, the 30 mmx30 mm grating structure was imprinted into a silicon substrate using electron-beam lithography and reactive ion etching [188]. High reflectivity is ensured by coating the grating with a 140 nm gold layer (3 nm of chromium used as an adhesive layer), deposited using an electronbeam- evaporation-based deposition plant (SYRUSpro 710). The grating period of 7 μm leads to a diffraction angle of 16.5° between the 0th and the 1st DO for a wavelength of 2 μm.

Simulations of the diffraction efficiency were carried out using the MATLAB-based grating diffraction calculation tool GD-Calc [189] with the optical constants of thin gold film on SiO_2 found in Ref. [190]. This numerical tool uses a generalized variant of the rigorous coupled-wave diffraction theory. Several geometric parameters are used as inputs to the numerical model. For the light beams, the incident angle θ is defined as the angle between the propagation vector of the light and the normal vector to the grating plane, as shown in Figure 3.36(a). The azimuthal angle φ is the angle between the incoming light vector projected onto the grating plane and the grating vector ν_g , shown in Figure 3.36(a).

A grating depth of 50 %, and grating depth of 600 nm were used. A high truncation order of 160 was chosen for the Fourier series in order to ensure a convergence with an error well below one percent relative diffraction efficiency. Figure 3.36(b) shows a calculated diffraction efficiency curve plotted together with the NIR and MIR spectra from Ref. [111]. The simulated diffraction efficiency shows a >80 % reflection into the 0th DO for wavelengths >5 μm, with a minimum efficiency of 1 % at 1.96 μm, chosen to coincide with the peak of the NIR spectrum.

The fabricated gratings were characterized using a Fouriertransform infrared (FTIR) spectrometer (Bruker, Vertex 70), together with an accessory for near-normal specular reflectance (Pike Technologies, 10Spec). The experimental setup of the FTIR characterization is shown in Figure 3.37(a). A wire-grid polarizer was used to set the polarization of the incident field. Figure 3.37(b) presents the experimentally measured diffraction efficiencies for the TE- and TM-polarizations (θ = 10°; φ =0°, 90°), along with the numerically calculated efficiencies. Excellent agreement is observed between the measured data and numerical model for φ =0°. Small deviations are found in the TM case, with the model predicting some sharp features near 5.8 and 8.3 μm whose spectral position is very sensitive to the grating depth and the width of the ridge. The smoother experimental curve is attributed to fabrication tolerances, as well as the effects of the gold layer deposition. Larger deviations in the shape of the diffraction efficiency are observed in the case of TM-polarization and φ =90°. Better agreement is achieved by setting φ to 93° in the simulations, thus indicating the high dependence of the diffraction efficiency on φ for TM-polarized radiation. For wavelengths longer than 8.5 μm, the reflection of the grating in the 0th DO approaches the reflectivity of a flat gold surface with R>97 % for both polarizations. As expected, for longer MIR wavelengths, the incident electric field is unaffected by the periodic grating structure, with the grating behaving as a plane metallic reflector. The minimum measured efficiency in Figure 3.37(b) is around 0.8 % at 2.1 μm for TE-polarization and 0.1 % at 2.45 μm for TM-polarization, meaning that the suppression of narrowband signals by three orders of magnitude is possible with just a single optic. The 5 % suppression bandwidth is approximately 490 (TE) and 650 m (TM).

In the case of IPDFG setups, a broadband, ultrashort driving pulse is employed. In order to provide suitable extinction across the entire driving spectrum, the minima of the efficiency curve can be tuned by adapting the incident angle on the grating: with increasing incidence angle, the diffraction minima shift to shorter wavelengths. This tuning behavior allows for the use of multiple identical gratings in series in order to cover a larger bandwidth. This concept was demonstrated using a high-power 2 μm femtosecond laser employed in IPDFG experiments [111], as discussed in the following. The driving spectrum had a SI20dB bandwidth of around 500 nm, with an average power of 23 W. Using three gratings with different incident angles, a suppression of more than 30 dB was achieved. Figure 3.38(a) shows the simulated reflectance of up to three gratings for the spectral region of the driving pulse and for three gratings, as well the measured spectrum after the arrangement. The type-1 phase matching in the used IPDFG process leads to orthogonal polarizations of the MIR beam and NIR beam. Figure 3.38(b) shows a transmission of >85 %in the MIR spectral region above 7 μm. Due to the grating setup replacing a dielectric long-pass filter

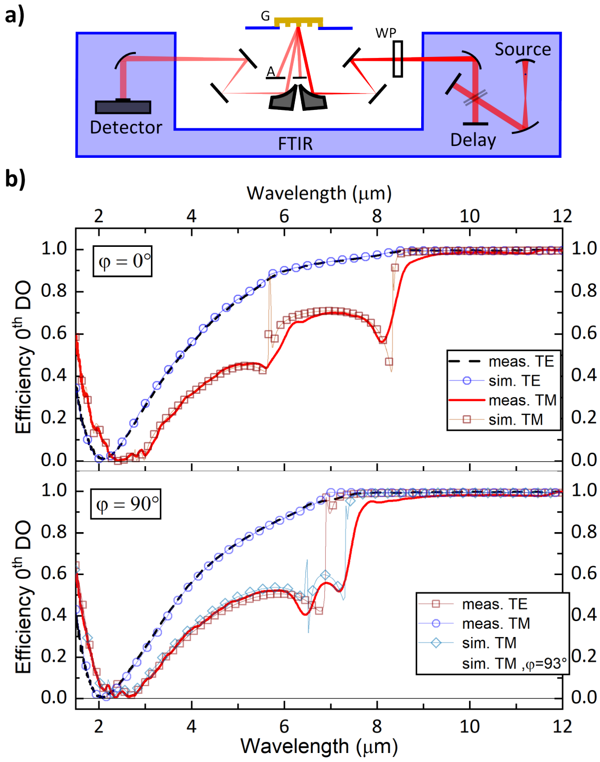

Figure 3.37: Diffraction efficiencies simulated and measured. (a) Commercial FTIR for reflection measurements at 10°, modified with a polarizer and iris for the measurement of only the 0th DO. G, grating; WP, wire grid polarizer; A, aperture. (b) Comparison of measured and simulated diffraction efficiencies into the 0th order. The incident angle is 10°, the grating depth is 0.6 μm, and the grating period 7 μm.

based on a germanium substrate (with which thermal lensing was observed) in the vacuum chamber available for the experiments reported here, the choice of angles was limited. An ideal positioning of the gratings for higher reflectance around 5 μm would lead to a MIR reflectance close to that of three gold mirrors (>92 %) for wavelengths longer than 5.5 μm and to a suppression of the driving pulse by 40 dB, shown in Figures 3.38(c) and 3.38(d), respectively. The use of incident angles close to 45° facilitates integration into common optical setups, while sufficient beam separation is achieved after several centimeters. By operating in an all-reflective regime and using silicon substrates the grating affords good thermal stability.

The power scalability was investigated for average powers up to 40 W(pulse energy: 0.8 μJ, power density: 831 W/cm^2). A schematic of the experimental test setup for one grating is shown in Figure 3.39(a). The laser used was a femtosecond fiber chirped-pulse amplification system, operating at a central wavelength of 1.96 μm, with a pulse width of 250 fs [111]. The experiment was performed in vacuum, which is necessary to avoid absorption of the 2 μm light by ambient water vapor. For testing, the grating was glued to a kinematic mirror mount with thermal adhesive. While in these experiments, the back

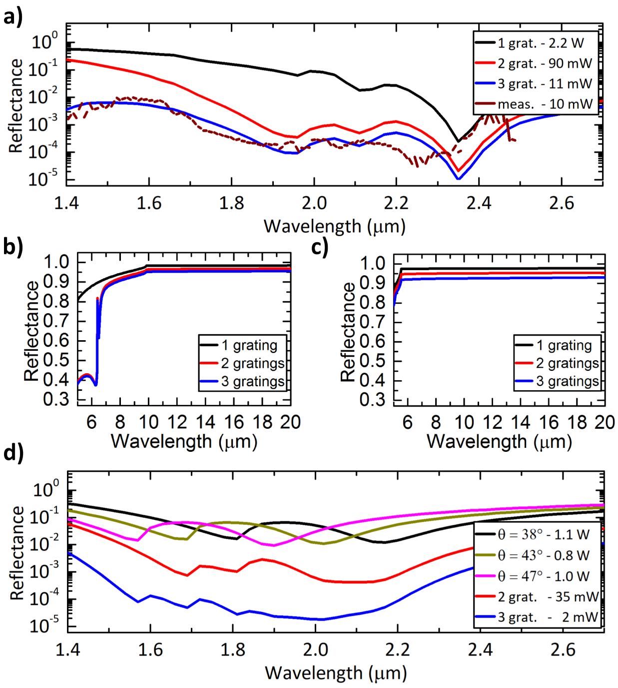

Figure 3.38: Suppression of a broadband 23 W NIR driving pulse and reflectance of MIR for different grating settings. (a) Suppression for three implemented gratings ($\varphi = 90°$; TE-pol; $\theta = 24°$, $52°$ and $\varphi = 0°$; TM-pol; $\theta = 24°$) and measured suppression of the NIR spectrum. (b) MIR reflectance for gratings as in (a) with MIR beam polarization orthogonal to that of the NIR beam. (c) MIR beam reflectance for higher efficiencies at shorter wavelengths ($\varphi = 90°$, TE-pol $\theta = 38°$, $43°$, $47°$). (d) NIR beam suppression by >40 dB with grating configuration as in (c) and TM-polarization. The 0th-order diffraction efficiency minima shift to shorter wavelengths with an increasing incidence angle.

side of the grating was not water-cooled, the reflective geometry of the filter allows efficient water cooling of the entire substrate (which is not possible with transmissive optics). In order to characterize the influence of the residual absorption, the beam profile of the 0th DO off the grating was recorded for increasing incident power. To further differentiate whether changes in the beam profile originate from the grating or the laser, a control experiment with the reflection off a dielectric-coated high-reflectivity NIR mirror and glass wedge was performed. Figure 3.39(b) shows the beam profile reflected from the grating for powers ranging from 1 to 40 W. Figure 3.39(c) presents a vertical linecut through the maximum of the beam profile, along with a Gaussian fit, used to minimize the effect of noise from the two-photon imaging sensor. Figures 3.39(b) and 3.39(c) show no substantial changes with increasing incident power, which would be expected if there was any significant thermal gradient present on the grating surface. This is also underlined in Figure 3.39(d), which shows the measured beam width versus the incident power. Only a minor difference in the beam width betweeen control and sample is seen, thus indicating that the thermal load contribution on the grating is small. In this test, the maximum fluence is $4.2\,\mu\mathrm{J/cm}^2$, well below the typical ablation thresholds of thin gold films (typically in the order of 0.1 J/cm^2 [191]). Therefore, the power scalability is mostly limited by thermal effects, e.g., deformation or melting. At increased power levels (>40 W), these effects could be mitigated by larger spot sizes on the gratings.

In conclusion, we have reported the design, fabrication, and experimental characterization of a high-power-suitable and chromatic-dispersion-free long-pass filter based on a diffractiongrating geometry. The gold-coated silicon gratings are capable of separating high-power, broadband NIR light from a collinearly propagating MIR beam by taking advantage of the differing diffraction efficiency between the short and long wavelength components. The used gratings have been shown to be suitable for idler wavelengths above 5.5 μm, with the reflectivity limited only by the intrinsic gold absorption and, thus, rendering these gratings suitable for a wide range of MIR and THz applications.

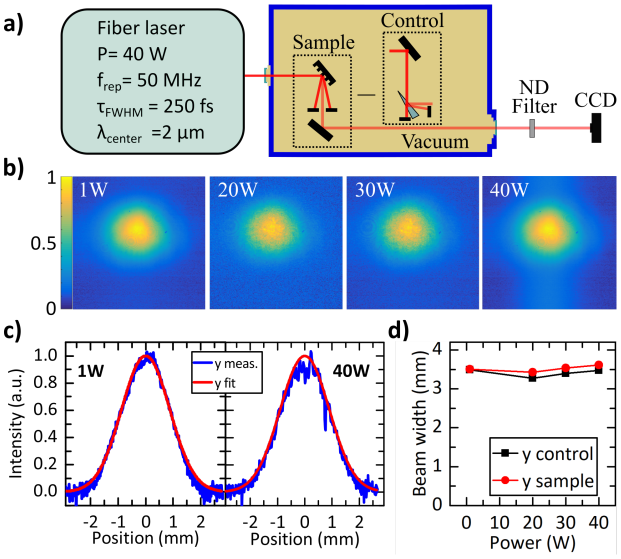

Figure 3.39: Thermal stability measurements. (a) Setup for thermal stability test is in vacuum. The control test uses a dielectric mirror and glass wedge to sample the beam. (b) NIR beam profiles of the grating 0th DO at different powers taken with a silicon CCD, employing two-photon absorption. (c) Linecuts along the y-axis measured and fit with a Gaussian function. (d) $1/e^2$ beam diameter of the y axis Gaussian fit at different powers for the sample and control setup.

Numerical simulations of the grating structure and incident beam geometry have been shown to accurately predict the filter characteristics, allowing the necessary optimization of the grating parameters and placement of the gratings for a tailored blocking range of the driving pulse and a suitable MIR diffraction. Although the slope is not as steep as possibly achievable in multilayer optics, it is sufficient for IPDFG applications with its usually distinct spectrally separated pump and idler wavelength ranges. By using a series of filters, broad bandwidth driving pulses can be suppressed by several orders of magnitude, while simultaneously keeping a high throughput of MIR light and not introducing any additional dispersion to ultrashort MIR pulses. The power scaling of the gratings has been investigated, with no significant thermal effect observed with incident average powers of up to 40 W. Most recently, these optics were successfully applied in the generation of single-cycle transients in the molecular fingerprint region via IPDFG [111], corroborating their suitability for minimizing the dispersion of the MIR beam path in a time-domain experiment. They are likely to find application in experiments with even longer wavelengths such as femtosecond-laser-driven terahertz spectroscopy (see, e.g., [192, 193] and references therein).

Chapter 4

Sensitive electric-field-resolved detection of infrared waves

In the previous chapter a bright source of ultrashort MIR pulses was presented with the focus on the spectral coverage of the molecular fingerprint region, a high average power and a short pulse duration of MIR waveform. In the following section, first the adjustments of the instrument for improving the signal-to-noise ration in the EOS detection are discussed. Followed by the presentation of the achieved detection efficiency of MIR photons. Lastly, FRS spectroscopy of gases with determinations of the limit of detection is presented.

4.1 Experimental prerequisites

In section 3.2.1 the first EOS detection of a MIR waveform derived from a thulium-fiber system was demonstrated. For further improving the spectrometer several changes were performed. The stability and robustness of the instrument is vital for measurements with long acquisitions times and for this purpose several steps presented in section 3.4 were undertaken, such as water temperature stabilization and adequate choice of PCF length and working point. Another important aspect for a spectrometer is its sensitivity and the signal-to-noise ratio of the measurements. This was investigated together with Christina Hofer and details can be taken from her dissertation ([194], chapter 4.7-4.9).

The noise throughout the system can be minimized by the choice of the working points in the chain. This starts with the spectral shift from $1.5\,\mu$m to $2\,\mu$m, where the settings of the pulse picker and the pump current of the amplifier before the HNLF must be carefully chosen to avoid broadband noise in the kilohertz range (see Figure 3.7,b)). The pulse compression scheme with the PCFs exhibits a turning point of the peak intensity and the spectral bandwidth (see Figure 3.31a)). This working point is favorable as it makes the compression robust against noise of the driving pulse and results in lower RIN of the MIR beam (see Figure 3.30).

In the employed balanced detection of EOS the common noise on both photodiodes is suppressed by subtraction, see 2.2. This entails that in case of perfect balancing only uncorrelated noise, like shot-noise or electronic noise remains. In Figure 4.1 the measured PSD and the calculated shot-noise limit (using Equation 2.27) are shown to differ by only a factor of 1.8 above the frequency of 6 kHz. Therefore, detections at frequencies above 6 kHz, e.g. with a lock-in amplifier, help to decouple RIN of the local oscillator from the detected waveform. The experimental balancing has shown to be able to suppress excess noise of the local oscillator by slightly more than two orders of magnitude. This is limited by the quality of the linear polarization of the beam and the chromatic behavior of the employed waveplates and Wollaston prism.

In the heterodyne detection ideally the noise is limited by shot-noise. In this case the SNR stays independent of the local oscillator power because the shot-noise level as well as the signal strength scale with the square-root of the incident power. Thus, the electronic noise, which is independent of the incident power, should remain below the shot-noise level. Higher powers of the local oscillator should also be avoided, as the excess noise scales linear with the incident power and thus rises faster than the shot-noise level for increasing incident powers. In the case of imperfect balancing limiting the suppression a decrease in SNR for high local oscillator powers can occur.

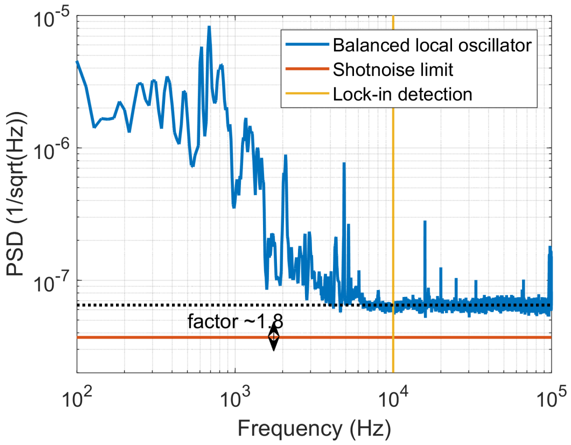

Figure 4.1: Noise limits of the heterodyne detection. The noise of local oscillator after balancing and amplification (blue) is a factor of 1.8 above the expected shot noise limit at the lock-in detection frequency of 10 kHz.

The signal strength of EOS scales linearly with the average power of the MIR in the non-depletion regime and thus higher MIR average power are beneficial for increasing signal strength. As the detection is shifted by the nonlinear process of SFG the conversion efficiency of this process is crucial. For the purpose of increasing the efficiency the ideal thickness of the employed GaSe crystal was searched in a range from 0.13 mm to 1 mm. The SFG power should scale quadratically with the crystal thickness in the non-depletion limit (compare Equation 2.13). Effects like dispersion, resulting in an intensity decrease of the gate pulse, phase matching or walk-offs in the time and frequency domain can significantly reduce the conversion efficiency for thick crystals. For example after a 0.5 mm thick GaSe crystal the temporal walk-off amounts to 75 fs, which is on the duration of the MIR pulse. Another aspect is the spectral bandwidth of the detection, which decreases due to imperfect phase matching in longer crystals. Furthermore, the birefringence of the crystal slightly turns the polarization of the gate pulse and thus increases the difficulty for balancing. The best trade-off between SNR and spectral bandwidth was achieved with a 0.5 mm thick crystal.

The SFG generation efficiency scales linearly with the intensity of each of the interacting beams. These intensities scale quadratically inversely with the focus size and thus the focus size is an important parameter. A tighter focus results in higher intensity, but also a shorter Rayleigh length, a more sensitive alignment and has the risk of exceeding the damage threshold of the crystal. Here, the best trade-off was found to be focusing with an off-axis parabolic mirror with a focal length of 2 ". This resulted in $1/e^2$ diameters of 60 μm and 80 μm and corresponding Rayleigh lengths of 1400 μm and 500 μm, for the NIR and MIR beam respectively.

Another improvement of the SNR stems from replacing the recombiner (previously a polarizer) with a Brewster plate. For the s-polarized and reflected gate pulse this recombination scheme resulted in a reduction of the gate pulse power by a factor of 2. But the dispersion-free reflection allows to control the dispersion of the gate pulse. The gate pulse is slightly pre-chirped by a 1 mm thick fused silica substrate, which results in a slight pulse compression inside the GaSe crystal. In Figure 4.2 the FROG retrieval of the 13.8-fs-long gate pulse is shown. Furthermore, the orientation at Brewster angle has a cleaning effect on the linear polarization, which improves the suppression at the balancing step. These improvements resulted in an intensity dynamic range of more than 14 orders of magnitude for a 1 s measurement time at a resolution of 15 cm^{-1}. In order to demonstrate the linearity in the intensity dynamic range the MIR beam was attenuated step-wise up tol 14.3 OD and the agreement between the expected and measured signal strength confirmed the linearity (compare [194], Figure 4.43).

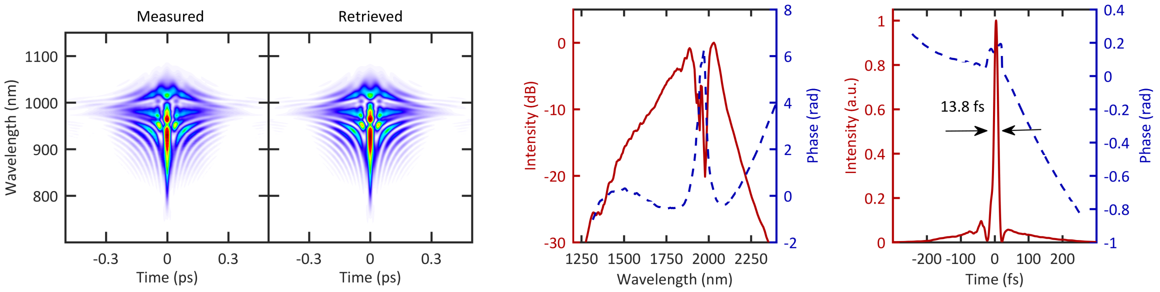

Figure 4.2: FROG of gate pulse used for the sensitive EOS. Form left to right: Measured and retrieved FROG trace, spectrum and time-domain intensity envelope.

4.2 Field-resolved spectroscopy approaching ultimate detection sensitivity

This section is identical in wording and figures to the manuscript with the title "Field-resolved spectroscopy approaching ultimate detection sensitivity" submitted to Nature in 2022 (reference numbers are kept consistent throughout the thesis). As one of the joint first authors[1] of this manuscript, I planned and performed the experiments, as well as analyzed and presented the gas phase spectroscopy part. Together with Christina Hofer and Ioachim Pupeza, I wrote the initial draft of the manuscript. A detailed author contribution is found here[2].

4.2.1 Abstract

Electric-field oscillations are now experimentally accessible in the THz-to-PHz frequency range [49, 50, 87, 119, 179, 195–200]. Their measurement delivers the most comprehensive information content attainable by optical spectroscopy - if performed with high sensitivity. Yet, the trade-off between bandwidth and efficiency associated with the nonlinear mixing necessary for field sampling has so far strongly restricted sensitivity in applications such as field-resolved spectroscopy of molecular vibrations [55, 201]. Here, we demonstrate electric-field sampling of octave-spanning mid-infrared waves in the 18-to-39 THz (600-to-1300 cm^{-1}) spectral region, with amplitudes ranging from the MV/cm level down to a few mV/cm. Employing powerful short-wave mid-infrared gate pulses [111, 202], the field-measurement sensitivity approaches within a factor of 4 the ultimate detection limit of capturing all photons in the temporal gate. This combination of detection sensitivity and dynamic range enables optimum use of newly-emerging high-power waveform-controlled infrared sources [31, 45, 47, 55, 111, 156, 203–205] for molecular spectroscopy. In a proof-of concept experiment, we performed broadband quantitative linear spectroscopy of multiple gases over more than 8 orders of magnitude in concentration, at an interaction length of only 45 cm. Our technique brings fast, label-free, quantitative multivariate detection of volatile organic compounds over the entire known physiologically-relevant molecular landscape [206, 207] within reach.

4.2.2 Main text

Among quantitative multivariate molecular analysis techniques, broadband vibrational spectroscopies [3] uniquely combine several advantages. They require minimal sample

---

[1] authors: Christina Hofer, Daniel Gerz, Lukas Fürst, Maximilian Högner, Thomas Patrick Butler, Martin Gebhardt, Tobias Heuermann, Christian Gaida, Kiran Sankar Maiti, Marinus Huber, Ernst Fill, Jens Limpert, Ferenc Krausz and Ioachim Pupeza

[2] Conceptualization: CH, DG, FK, IP; Data curation: CH, DG; Formal Analysis: CH, DG, LF, MHö; Supervision: JL, FK, IP; Investigation: CH, DG, LF, TB, MG, TH, CG, KM, MHu, EF; Visualization: DG, CH; Methodology: CH, DG, LF, MHö, KM, MHu, EF; Project administration: IP; Writing – original draft: CH, DG, IP; Writing – review and editing: all authors

preparation, and the specific "vibrational fingerprint" signal is acquired via optical interrogation, non-destructively and in a label-free manner. Recent progress in broadband, coherent sources of ultrashort mid-infrared (MIR) pulses is heralding a vast new potential for sensitivity and specificity in vibrational spectroscopy, in particular for molecular gases. On one hand, the bright vibrational fingerprints generated by their Watt-level average powers [31, 45, 47, 55, 111, 156, 203–205] afford the potential of highly-multivariate detection in a matter of minutes (Supplementary Information section I). On the other hand, their temporal coherence enables time-domain electric-field sampling [208]. This has recently proven a power and bandwidth scalability [55, 201] superior to traditional, time-integrating spectroscopies [6, 25, 209, 210], thereby possibly providing a means of optimally detecting vibrational fingerprints.

First quantitative MIR vibrational spectroscopy experiments employing electro-optic sampling (EOS)[49, 50, 195] have achieved the most sensitive broadband infrared spectroscopy of biological systems to date[55], and dual-frequency-comb spectroscopy over the entire molecular fingerprint region [201, 211]. However, while these represent breakthrough results, the photon detection efficiency has stayed well below 1 % (Supplementary Information section II). Furthermore, the range of quantified molecular concentrations has remained below 6 orders of magnitude, for both field-resolved and state-of-the-art time-integrating broadband vibrational spectroscopies [19, 28, 201] (see also Extended Data Table 4.1).

Here, we demonstrate electric-field sampling with photon detection efficiencies of up to 17 %, and an average of 7.5 % throughout the 600-to-1300-cm^{-1} spectral region. This exceeds the previous sensitivity record in the MIR range [55], (Extended Data Table 4.2) by more than one order of magnitude while simultaneously doubling the detection bandwidth. Because the electric-field strength scales with the square root of the number of photons, this implies a field measurement sensitivity close to the ultimate limit of detecting all photons in the interaction time window of the gate pulse with the MIR wave. In a benchmark experiment, we recorded the coherent response of multiple gases contained in a 45-cm-long cell to resonant excitation with broadband, waveform-stable MIR pulses. The linearity of the measured signals for concentrations spanning more than 8 orders of magnitude, from the sub-ppb range to vapor pressure, is confirmed.

High-sensitivity optical-field sampling

Drawing on preliminary experiments [111, 212], we implemented EOS of a 50-MHz-repetition-rate train of few-cycle MIR waveforms, with 1.9-W-average-power, 13.8-fs gate pulses spectrally cantered at 1.95 μm, using GaSe nonlinear crystals (Figure 4.3, Extended Data Figure 4.7, for detailed setup description see Methods). In contrast to EOS configured to simultaneously employ sum- and difference-frequency generation, which requires a thin crystal [118], here we optimized the efficiency of phase-matched upconversion [52] using sum-frequency generation [55, 119, 213]. To this end, both the carrier wavelength and the average power of the gate pulses were increased as compared to the most sensitive EOS implementations to date [55, 118]. The long central wavelength favors increasing the crystal thickness without compromising broadband detection [202]. In addition, the reduced gate-pulse photon energy mitigates multi-photon absorption, allowing for gate-pulse intensities as high as $9 \times 10^{10}\,\mathrm{W/cm^2}$ inside the EOS crystal, maximizing the upconversion efficiency.

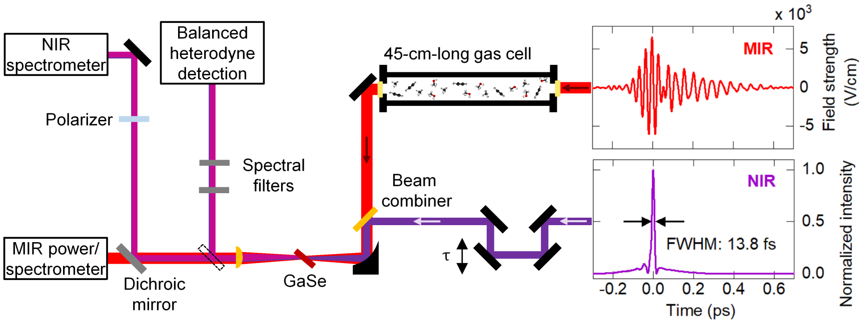

Figure 4.3: Schematic of the experiment. Detailed in Methods and Extended Data Figure 4.7. Measurement of the photon detection efficiency (without the dashed-line-framed mirror and with evacuated sample cell): a train of waveform-stable, few-cycle mid-infrared (MIR) pulses (red waveform) is focused collinearly with the variably-delayed (τ) train of near-infrared (NIR), 13.8-fs full-width-at-half-intensity-maximum (FWHM) gate pulses (purple intensity envelope) onto the EOS crystal (GaSe). The spectrally-integrated MIR average power and the NIR spectrum are recorded as functions of τ. Gas spectroscopy configuration (with the dashed-line-framed mirror and filled cell): MIR pulses excite molecular vibrations in a gas. The resulting coherent field oscillations are sampled electro-optically using the variably-delayed NIR gate pulses and a balanced heterodyne detection setup including spectral filters [214].

Scanning the gate pulse over a delay range of 1.3 ps using a 541-μm-thick GaSe crystal as the EOS interaction medium resulted in the trace shown in black in Figure 4.4A (time-dependent EOS-signal-to-detection-noise ratio, SDNR). The detection noise (inset) is dominated by the gate-pulse shot noise in the balanced detection [69] and was measured for an integration time of 1 s per temporal element, see also Methods). At the delay of maximum absolute power depletion, the fraction of converted MIR photons ($\eta_{\mathrm{conversion}}$) was 22 % (Figure 4.4B). Because only a portion of the MIR wave (Extended Data Figure 4.9) interacts with the gate pulse upon propagation through the crystal ($\eta_{\mathrm{interaction}}$, indicated by shaded area), we estimate a depletion of $\eta_{\mathrm{conversion}}/\eta_{\mathrm{interaction}} = 31\,\%$ within the temporal gate. For this delay, Figure 4.4C shows the generated sum-frequency signal. Its power matches the MIR power depletion in terms of number of photons, thus allowing us to exclude other possible mechanisms of significant MIR depletion. The spectral filters employed to optimize the SDNR [214] have a transmission. Selecting this spectral band for balanced heterodyne detection [52, 55] reduced the fraction of detectable MIR photons from within the temporal gate to $\eta_{\mathrm{total}} \approx 7.5\,\%$. This spectrally-integrated photon detection efficiency is consistent with the value determined from the ratio of the peak SDNR of the EOS trace to that of the MIR photon rate on the EOS crystal (see also Methods).

Figure 4.4D shows the spectrally-resolved detection efficiency (right y-axis) obtained from the EOS spectra (left y-axis), assuming delay-independence of η_{total} (confirmed in Extended Data Figure 4.10, see also Methods). It peaks at 17 % and exceeds 1 % in the 900-to-1270 cm^{-1} range. The measurement noise floor (Figure 4.4A, inset) indicates a minimum measurable field strength of 2.2 mV/cm (dashed line). This limit is calculated for our MIR beam radius of 35 μm at the detection crystal. For comparison, this value is only a factor of 4 above the ultimate limit achievable with an ideal EOS detection capturing all MIR photons within the temporal gate.

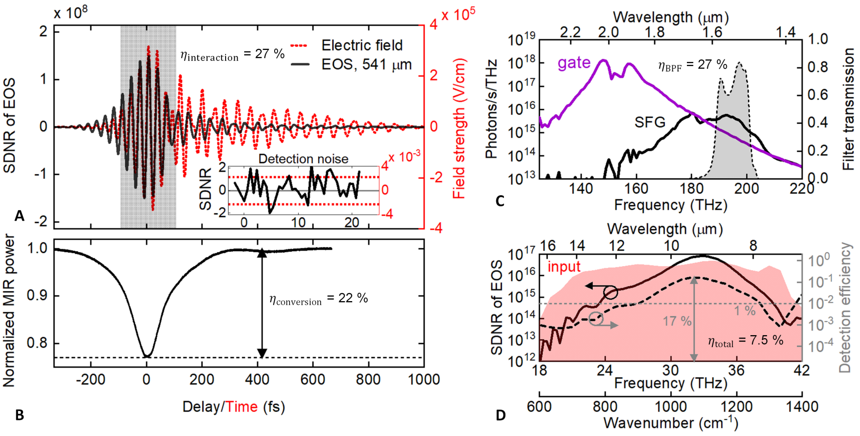

Figure 4.4: Characterisation of EOS detection sensitivity and dynamic range. (A) 1.3-ps-long EOS trace with 2240 data points (temporal elements), EOS-signal-to-detection-noise ratio SDNR (black). Red, dotted on right y-axis: retrieved electric-field at the EOS crystal (see also Methods and Extended Data Figure 4.8). Shaded area: estimated duration of the temporal gate, related by $\eta_{\text{interaction}}$ to the total flux of MIR photons per second. Inset: detection noise measurement (blocked MIR) for 1-s integration time per temporal element. Dotted lines: minimum measurable field strength (at SDNR=1). (B) Spectrally-integrated MIR power measured behind the EOS crystal (see Figure 4.3), using the same time axis as in (A), $\eta_{\text{conversion}}$: MIR to sum-frequency conversion efficiency measured at maximum depletion. (C) Sum-frequency signal (black) between MIR wave and gate pulses (purple, blocked MIR beam), recorded at maximum MIR depletion, and filter transmission (grey area, η_{BPF}). (D) Red area: MIR spectrum impinging on the EOS crystal (at arbitrary logarithmic scale), measured with a Fourier-transform spectrometer. Left y-axis/continuous line: EOS spectral-intensity SDNR obtained from the full scan shown in (A), scales linearly with measurement time[55]. Right y-axis/dashed line: spectrally resolved detection efficiency (independent on measurement time), calculated as the ratio of the EOS spectra and the MIR spectrum (red), normalized to the spectrally-integrated detection efficiency $\eta_{\text{total}} = \eta_{\text{conversion}}/\eta_{\text{interaction}} \times \eta_{\text{BPF}} \times \eta_{\text{Fresnel}}$, which includes Fresnel-reflection losses at the GaSe crystal ($\eta_{\text{Fresnel}} = 0.87$), see also Methods. Grey dashed line indicates 1 % detection efficiency.

The shape and duration of the temporal gate (Extended Data Figure 4.9) and, therefore, the temporal resolution (or, the detection bandwidth), as well as the upconversion efficiency, result from a complex interplay of the experimental parameters [52]. These include crystal thickness and orientation, gate-pulse power, bandwidth and chirp, as well as focusing geometry and spectral filters. In fact, the demonstrated upconversion efficiency, in combination with lower-noise gate pulses would enable a peak detection efficiency exceeding 50 % (see Supplementary Information section III). A more uniform spectral coverage at the expense of a lower detection efficiency was achieved employing a thinner EOS crystal. In this case the spectral range for $\eta_{\text{total}} > 1\,\%$ is nearly doubled (Extended Data Figure 4.11 and Extended Data Table 4.3).

Field-resolved spectroscopy of gases

The instrument response of both crystals is sufficiently broadband for the EOS traces to qualitatively reproduce the temporal evolution of the super-octave electric field (Figure 4.4A, red, Extended Data Figures 4.11,4.12) which reaches MV/cm levels. Under the assumption of a linear instrument response, precise knowledge of the MIR electric field evolution is not necessary for quantitative, linear spectroscopy [55]. To confirm this assumption and to put the detection sensitivity and dynamic range to the test in a spectroscopy experiment, we recorded EOS traces of gas samples.

The 45-cm-long gas cell was first filled with methanol at concentrations between the vapor pressure ($11\,\% = 1.1 \times 10^8$ ppb) and the lower ppb range (Extended Data Figure 4.13). Figure 4.5A shows the envelope of time-domain EOS traces. Empty-cell EOS measurements allow for a quantitative comparison of the molecular response with the HITRAN line-by-line database [73, 79], see also Methods.

The reference measurement (that is, the difference of two empty-cell EOS traces, Figure 4.5A, black dotted line) shows that roughly 3 ps after the excitation maximum, detection-noise-limited sensitivity is approached within a factor of 3. Evaluating the methanol Q-branch signal in the 3-ps-to-9.8-ps time window after subtraction of the separately-measured empty-cell response yields excellent agreement with the HITRAN-based model for concentrations below 1000 ppm (Figure 4.5B). A noise-equivalent limit of detection (LOD) of 0.8 ppb is obtained (Figure 4.5B, brown line). Near vapor pressure, strong modulations of the leading part of the sample response are observed. To ensure that these can be solely attributed to the linear refractive index of the sample, we measured the response of two high concentrations (0.5 % and 11 %) at a 100-times weaker excitation power (Figure 4.5A, left, dashed lines, Extended Data Figures 4.14,4.15). The accordance of the respective sample responses confirms the linearity both of the light-matter interaction and of the instrument response within our measurement accuracy, see also Methods and Extended Data Figure 4.16. Thus, linear detection of methanol vibrations over a range of concentrations spanning 8 orders of magnitude was confirmed (Figure 4.5C).

To showcase the benefit of broadband detection, we investigated a mixture of methanol, acetylene and methane, whose absorption spectra encompass more than one octave in the molecular fingerprint region. The Fourier transformations of time-filtered EOS traces along with corresponding HITRAN-based simulations are shown in Figure 4.6A. The excellent agreement between experiment and model corroborates the ability of our instrument to

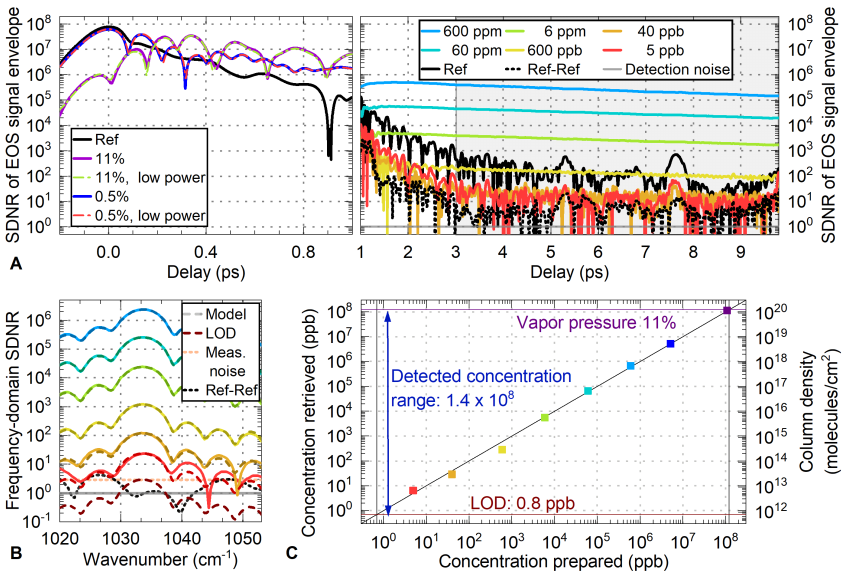

Figure 4.5: Field-resolved spectroscopy of methanol. (A) envelopes of time-domain EOS traces, normalized to the single-scan detection-noise level. Black line: reference waveform (empty gas cell). Left panel: reference and sample response for percent-level concentrations with excitation powers of 19 mW in a 6-mm $1/e^2$-intensity-diameter beam at the sample (12 mW reaching the EOS crystal, solid line) and 100 times lower power (dashed line). Right panel: differences between sample-response and empty-cell reference measurements. Individual 10.6-ps-long traces were acquired in a total measurement time of 80 seconds per trace. (B) solid lines: magnitude of the Fourier transforms of the signals in A, in the 3-ps-to-9.8-ps time window. Dashed lines: HITRAN model. (C) retrieved versus prepared concentration. See Methods for details on sample preparation, signal acquisition, processing, and concentration retrieval.

perform broadband quantitative measurements, and predicts simultaneous LOD values of 0.8 ppb, 0.6 ppb and 40 ppb for methanol, acetylene and methane, respectively.

Conclusions and outlook

In conclusion, we have demonstrated sampling of super-octave long-wave mid-infrared electric fields with sensitivities approaching the ultimate limit set by the detection of all infrared photons within the temporal gate. For our geometry, this implies the ability to measure MIR electric-field strengths in the few-mV/cm range, with detection linearity preserved up to the MV/cm field-strength range. As a direct implication of far-reaching importance, we have demonstrated quantitative, super-octave molecular vibrational spectroscopy of gases, with concentrations spanning 8 orders of magnitude. The limit of detection, evaluated in terms of noise-equivalent absorbance, exceeds that of state-of-the-art broadband infrared vibrational spectroscopies [28, 91, 201, 215] by more than one order of magnitude (Extended Data Table 4.4). The presented instrumentation will yield detectable concen-

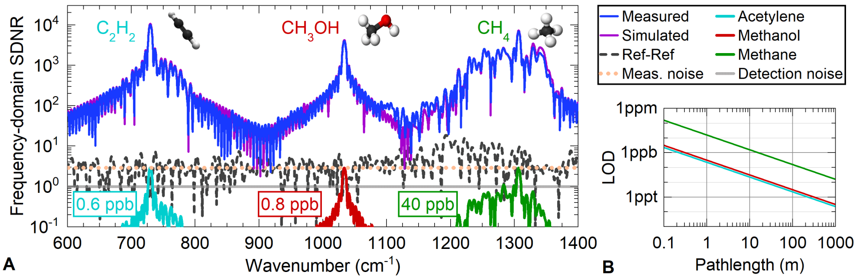

Figure 4.6: Broadband spectroscopy of a mixture of methanol, acetylene and methane. (A) Blue: scaled magnitude of the Fourier-transform of the 3-to-9.8-ps time window after subtracting an empty-cell measurement from the sample response. Purple: sample response simulated using our measured excitation, HITRAN line-by-line data[79] and fit parameters for the concentration of the three gases: 0.9 ppm, 41 ppm and 84.4 ppm for methanol, acetylene and methane, respectively. Black, dashed: magnitude of the Fourier-transform of the difference of two empty-cell EOS measurements. Beige: measurement noise floor obtained from the mean of the black, dashed line. Grey: detection noise. Simulated spectra of the measurement-noise-equivalent LOD concentrations are shown. (B) LOD for methanol, acetylene and methane extrapolated with respect to the interaction length.

trations well into the lower (or even sub-) ppt range by means of path-length elongation (Figure 4.6B) with, e.g., multi-pass cells [28] or enhancement cavities [216, 217].

This new regime of detection sensitivity and dynamic range, together with its power scalability opens new perspectives for ultrafast optical spectroscopy. Quantitative, label-free breath gas analysis with ppt-level sensitivity, used for identifying and monitoring infectious diseases [206] and cancer [218] are prominent examples addressing yet unmet medical needs.

4.2.3 Methods

Description of the experimental setup

The employed instrument is an adapted implementation of the system described in detail in Ref. [111]. The setup is depicted in Extended Data Figure 4.7. The pulsed output of an erbium fiber oscillator (Menlo C-fiber), operating at a wavelength of 1.5 μm and a repetition rate of 100 MHz, is pulse-picked down to 50 MHz, amplified and shifted to 2 μm in a highly nonlinear fiber. A chirped fiber Bragg grating cuts out a spectrum around 1965 nm resulting in stretched pulses with 500 ps pulse duration. This pulse train seeds a two-stage thulium-doped fiber amplifier and delivers, after a free-space grating compressor, near-infrared (NIR) pulses with a full-width-at-half-intensity maximum (FWHM) duration of 250 fs. Starting at the grating compressor, the free-space beam path is enclosed in a vacuum chamber ($<1 \times 10^{-3}$ mbar) to avoid absorption from gases such as water vapor, thus ensuring minimal background from molecules outside the measurement cell. The beam is split in two and the pulses are further compressed in silica photonic crystal fibers.

Sampling pulses for electro-optic sampling (EOS) are nonlinearly self-compressed in a large mode area fiber (LMA15 from NKT Photonics) down to a FWHM duration of 13.8 fs with an average power of 4.5 W. For mid-infrared (MIR) generation, the NIR pulses are compressed down to durations of 32 fs FWHM with 30 W of average power in a large-pitch-fiber (LPF40 fiber). Intra-pulse difference frequency generation (IPDFG) in a 1-mm-thick gallium selenide (GaSe) crystal results in waveform-stable MIR pulses with 250 mW average power and an intensity spectral coverage between 630 cm^{-1} and 1370 cm^{-1} at the -20-dB-level. As compared to the original implementation in Ref.14, here we operate the system at a safe level below its power record. Grating-based long pass filters (LPF) separate the MIR pulses from the pump [123] before the MIR beam is mechanically chopped at a frequency of 10 kHz. The MIR beam passes a home-built, 45-cm-long measurement cell with 1-mm-thick ZnSe windows. A 10-mm-thick germanium substrate compensates the second-order dispersion of ZnSe. A 1-mm-thick ZnSe substrate placed at Brewster angle recombines the sampling pulses (s-polarization, in reflection) and the MIR pulses (p-polarization, in transmission). The sampling beam is transverse-mode-matched to the MIR beam via a reflective telescope. It is variably delayed for EOS measurements with a mechanical stage, whose displacement is tracked with a Michelson interferometer (SmarAct Picoscale). The collinearly propagating beams are focused into a GaSe crystal with average powers of 1.9 W and 12 mW for the sampling and MIR pulses, respectively. The EOS crystal phase-matches p-polarized sum frequency generation (SFG). After a 1500-1600 nm bandpass filter, the NIR beam is split in two orthogonal polarizations by a Wollaston prism, followed by a balanced detector with two InGaAs diodes. By adjusting a quarter-wave plate and a half-wave plate before the Wollaston prism, close to shot-noise-limited detection (factor 1.4) is achieved at the chopping frequency of 10 kHz, with a lock-in amplifier using an integration time of 2.2 ms. This ellipsometer detects the SFG field in a heterodyne fashion.

Electro-optic sampling and detection efficiency

The EOS traces were acquired with an integration time of 2.2 ms per temporal element. For calculation of the detection efficiency via the photon flux, the signal-to-detection-noise ratio (SDNR) is shown for an effective averaging time of 1 s per temporal element. To that end, noise traces were acquired for 1 s, the averages and standard deviation resulting in the noise measurement shown in Figure 4.4A and Extended Data Figure 4.11. Linear scaling of the intensity SDNR with for integration times up to 1600 s was previously shown [55].

To relate the time-domain SDNR to the detection efficiency, we first calculate the MIR photon flux as a function of time (i.e., delay) from the pulse energy and electric field distribution. For the given time-domain instrument response, the photons in the interaction time window at the delay of maximum signal strength are then estimated. The ratio of the SDNR to the photon flux then gives the overall detection efficiency. This includes effects which are not considered by the calculation of MIR depletion and spectral filtering, e.g., spectrally varying phase relations between the sum-frequency and local oscillator components [53], as well as imperfect spatial interference. The result is an estimated overall average detection efficiency of 5.9 %.

The spectrally-resolved detection efficiency in Figure 4.4D is calculated as follows: First, the area under the EOS spectrum is normalized to the overall detection efficiency η_{total}. Then, the ratio of the spectrum to the spectrally-resolved input photon flux (incident power of 12 mW (chopped) with Fresnel losses at the GaSe interface and FTIR spectrum) results in the detection efficiency. This calculation neglects the remaining chirp of the MIR waveform, as it assumes a constant spectral distribution equal to that of the FTIR spectrum (i.e. a Fourier-transform limited MIR field) and, correspondingly, a constant spectrally integrated relative depletion throughout the entire EOS trace.

The MIR focus size was chosen for optimum spatial overlap with the gate beam [219]. For a constant detection efficiency and integration time window, i.e. the same required minimum MIR photon flux per second, the minimum measurable field strength scales as follows: Increasing both the MIR and gate beam foci in the EOS crystal by a factor of 2 (to ensure spatial overlap) halving the minimum measurable field strength. To still achieve the required conversion efficiency, would need the gate pulse power to be increased by a factor of 4.

Gas sample preparation

The gas handling setup is shown in Extended Data Figure 4.13. For the preparation of the gas samples, small amounts of the substance are injected with a gas tight syringe into an evacuated (<0.1 mbar) gas sampling bulb. The gas sampling bulb with the sample gas (acetylene, methane and/or evaporated methanol) is then filled with nitrogen up to atmospheric pressure. Varying amounts of this stock solution are further diluted by injection via gas-tight syringes and septa into a 250-ml syringe filled with nitrogen. Via a three-way valve, the connection to a previously evacuated ($<1 \times 10^{-4}$ mbar) transport gas cell is opened and the atmospheric pressure on the piston leads to the filling of the transport cell. The transport cell is then connected to the measurement cell, which is evacuated ($<1 \times 10^{-2}$ mbar) and located in vacuum. Pressure equalization leads to a sample pressure of 84 mbar and further dilution. For methanol concentrations higher than 1000 ppm, a flask with liquid methanol is directly connected to the evacuated measurement cell. After removing the remaining gas in the flask with a vacuum pump, the liquid methanol evaporates and the pressure in the gas cell increases until reaching the vapor pressure of 110 mbar at 19 °C. For the 0.5 % concentration measurement the pressure was reduced via repeated pressure equalization with an evacuated cell. For ease of comparison, the specified gas concentrations are given with respect to atmospheric pressure. For the gases used here, the signal strengths differ only by 14 % when changing the total pressure from 84 mbar to 1 bar.

The gas cell components were cleaned between measurements by repeated nitrogen purging and evacuation of the gas cells to pressures below 1×10^{-2} mbar for several minutes. Prior to preparing the concentrations below 1 ppm all gas cell components were left over night in an oven at 60 °C to remove remaining adsorbed molecules. However, for prepared methanol concentrations below 10 ppb, measurements revealed slowly increasing concentrations on timescales of minutes. The minimum preparable concentration was thus

5 ppb. This implies the need for more advanced sample preparation for low ppb and ppt concentrations such as constant gas flow setups.

Processing of spectroscopic data

For the gas-phase measurements, ten 10.6-ps-long EOS scans were averaged, each with a measurement time of 8 s. In order to circumvent the dynamic range limitations stemming from the utilized lock-in amplifier (MFLI, Zurich Instruments) and analog-to-digital converter (Picoscale, Smaract), ten additional scans with 100 times higher amplification of the transimpedance amplifier (DLPCA-200, FEMTO) were measured for the weak signals after the main pulse. The two averaged scans were serially stitched together at a time delay where the amplified scan wasn't saturated (typically starting around 1.5 ps). We refer to the result of this procedure as one trace. Thus, the effective measurement time of one trace is 80 s. Stitching can, in principle, be avoided by employing electronics with sufficient bit depths (26-bit) or fast scanning techniques (smaller integration time). In order to show the relevant signal and noise of the time-domain EOS traces, their envelopes presented in Figure 4.5 are frequency-filtered with a cosine-squared filter, suppressing noise outside the spectral region of the excitation (500-1500 cm^{-1}). The traces are scaled to the mean of the detection noise (single trace, MIR blocked). In the following analysis, a reference trace (evacuated gas cell) is subtracted. For further isolation of the molecular signal from the excitation noise [55], a cosine-squared filter is applied in the time domain (3-9.8 ps). After padding the time-domain traces with zeros up to a delay of 100 ps, they are Fourier transformed and the real-valued magnitude is shown, normalized to the detection noise floor derived from a trace with the MIR beam being blocked (that is, the time-domain SDNR).

For quantitative concentration retrieval using a time-filtering approach, a model for the molecular response on the level of the electric field is necessary. To this end, we employ the line-by-line database from HITRAN to calculate the complex attenuation coefficient that includes the effects of temperature and pressure. The HITRAN Application Programming Interface (HAPI) [79] provides for each absorption line i the parameters for a Lorentzian lineshape, namely the line strength (S_i), wavenumber (μ_i) and line width ($\Delta\nu_i$). The resulting attenuation coefficient μ can be used together with the path length d to calculate the transmission $T = \exp(-\mu \cdot d) = 10^{-A}$, where A is the decadic absorbance.

For the calculation of a complex Lorentzian L_c with these parameters, we use the following equation:

$$L_c(\nu, \nu_i, \Delta\nu_i) = \frac{\Delta\nu_i - 1i(\nu - \nu_i)}{\pi((\nu - \nu_i)^2 + \Delta\nu_i^2)}.$$

In order to obtain a real-valued time-domain signal after the Fourier transformation, the complex conjugate of the values at negative frequencies is added. The complex attenuation coefficient is then defined by the sum over all absorption lines, scaled by their line strength:

$$\mu_c(\nu) = \sum_i S_i \times \left(L_c(\nu, \nu_i, \Delta\nu_i) + L_c^*(-\nu, \nu_i, \Delta\nu_i)\right).$$

All relevant processes (sample interaction, EOS instrument response function) scale linearly with the MIR electric field. Therefore, the molecular response can be directly applied to the reference EOS trace to obtain the modelled sample EOS trace:

$$E_{sim}(\nu) = E_{ref}(\nu) \times \exp\left(-\frac{\mu_c(\nu)}{2} \cdot d\right).$$

Note that for small attenuations of the excitation pulse $(\mu_c \nu)/2 \cdot d \ll 1$ the electric field envelope of the molecular response scales linearly with the number of emitters. As a consequence, it also scales linearly with the attenuation coefficient and the concentration, as can be seen in Figure 4.5A and B. This scaling is derived in detail in the supplementary material of [55]. It differs from concentration retrievals based on intensity change such as in conventional FTIR spectroscopy, where the absorbance scales linearly with the concentration.

In the case of methanol and for our experimental settings, the assumption of a small attenuation breaks down for concentrations >1000 ppm, requiring an exact model of the molecular response for quantitative concentration retrievals. Extended Data Figure 4.14 shows the frequency-domain SDNR of the 3-9.8 ps time window together with the modelled spectra for methanol concentrations of 0.5 % and 11 %. For 0.5 %, the agreement is good, while for the higher concentration the model does not reproduce the measured signal, as two additional peaks arise around 960 cm^{-1} and 1080 cm^{-1}.

In order to ensure that we measure only the linear molecular response the measurements were repeated at a hundred times lower MIR power. Differences in the excitation (spectrum and intensity) are corrected using a calculated transfer function $H(\nu) = \mathrm{FT}[E_{ref}(t)]/\mathrm{FT}[E_{ref,low\ power}(t)]$ and applying it to the trace measured at low power: $E_{sample,low\ power,corrected}(t) = \mathrm{IFT}[H(\nu)\mathrm{FT}[E_{sample,low\ power}(t)]]$. The resulting spectra of the time filtered traces are shown as dashed lines in Extended Data Figure 4.14 and are in good agreement with the high-power data, confirming a linear measurement of the refractive index of the sample. These traces can be used as a calibration for the prepared methanol concentration and allows its retrieval in the future.

The reason for the difference of the measured and modelled spectra can be found in the comparison of the absorption spectra derived from the HITRAN database and from a FTIR measurement (PNNL database50), shown in Extended Data Figure 4.15. The Q-, P- and R-branch of the C-O stretch band of methanol are in decent agreement, while outside of the spectral region of 870-1100 cm^{-1} the HITRAN data approaches zero due to an incomplete set of absorption lines in the database. The PNNL data shows additional absorption features and an offset from zero. This difference has only a marginal influence in the case of small attenuations as the signal from the strongest absorption line (Q-branch absorption peak) dominates. For stronger absorbances (>1 AU) the abrupt end of the P and R-branch absorption line series gives rise to the peaks at 960 cm^{-1} and 1080 cm^{-1} in the modelled spectra. Other measured peaks can also be found in the PNNL data, e.g. at 736 cm^{-1}, 779 cm^{-1} or 821 cm^{-1}.

The concentration retrieval using the model described in the previous section can be successfully employed until either the uncertainties of the model or saturation effects start to majorly impact the analysis. In the non-depletion regime, the signal strength scales linearly with the concentration (Extended Data Figure 4.16, red line). In our case, a deviation from linear scaling by 1 % and 10 % occurs at concentrations of 36 ppm and 370 ppm, respectively (Extended Data Figure 4.16, yellow line). The signal increases monotonically up to 3000 ppm and follows a linear behavior over more than 5 orders of magnitude in concentration.

For absorbance measurements, the measurable range can be determined as described in Extended Data Table 4.1. The relative standard deviation δI of the intensity was determined from ten measurements to be 1.9×10^{-3}.

$$A_{max} = -\log_{10}(\delta I) = 2.7\,\mathrm{AU}$$

$$A_{min} = \frac{\sqrt{2}}{\log(10)}\delta I = 1.2 \times 10^{-3}\,\mathrm{AU}$$

The measurable absorbance range spans more than 3 orders of magnitude, corresponding to methanol concentrations between 2.5 ppm and 0.7 %. Combining emission and absorption analysis for one spectral element derived from the same trace, the linear retrievable concentration range spans around 7 orders of magnitude in this spectral element (e.g., from 0.8 ppb to 0.7 % for the spectral element centered at 1033.7 cm^{-1}). However, parallel and linear probing of a multitude of spectral elements, as enabled by broadband spectroscopy, increases the retrievable concentration range by more than one order of magnitude (see, e.g., resonances at 736 cm^{-1}, 779 cm^{-1} or 821 cm^{-1} in Extended Data Figures 4.14,4.15).

4.2.4 Supplementary information

I. Estimation for highly-multivariate detection within minutes

We assume an ideal light source and detection with negligible technical excess noise and detector noise. The detection limits are then set by shot noise. For the absorbance A, its uncertainty δA, the signal-to-noise ratio (SNR) and the photon numbers of the reference measurement, N_{ref} and the sample measurement N, we find:

$$\begin{aligned}
A &= -\log_{10}\left(\frac{N}{N_{ref}}\right) \\
\delta A &= \sqrt{\left(\left|\frac{dA}{dN}\right|\delta N\right)^2 + \left(\left|\frac{dA}{dN_{ref}}\right|\delta N_{ref}\right)^2}, \text{ with } \delta N = \sqrt{N},\ \delta N_{ref} = \sqrt{N_{ref}}, \\
\delta A &= \frac{1}{\ln(10)} \cdot \sqrt{\frac{1}{N} + \frac{1}{N_{ref}}}, \\
SNR = \frac{A}{\delta A} &= -\frac{\ln\left(\frac{N}{N_{ref}}\right)}{\sqrt{\frac{1}{N} + \frac{1}{N_{ref}}}}.
\end{aligned}$$

For large N_{ref} and $N \approx N_{ref}$, that is, for low absorbance, the SNR can be approximated as

$$SNR \approx \frac{1 - \frac{N}{N_{ref}}}{\sqrt{\frac{2}{N_{ref}}}}.$$

For SNR = 1, solving the above equation for N yields:

$$N_{\text{small A}} \approx N_{ref} - \sqrt{2N_{ref}}.$$

For large absorbance, the smallest N, larger than or equal to its standard deviation and yielding SNR>1 is $N_{\text{large A}} = 1$. The measurable range of absorbances A_{range} is then given by

$$A_{range} \approx \frac{-\log_{10}\left(\frac{N_{largeA}}{N_{ref}}\right)}{-\log_{10}\left(\frac{N_{smallA}}{N_{ref}}\right)} = \frac{\ln(N_{ref})}{-\ln\left(1 - \sqrt{\frac{2}{N_{ref}}}\right)}.$$

In accordance with the Beer-Lambert law, the measurable concentration range corresponds to the absorbance range. The number of photons available for a given power P, average time T, wavelength λ, speed of light c and Planck constant h is calculated as: $N_{ref} = \frac{P\lambda}{hc}T$. The molecular fingerprint region is often defined as the spectral range between 2.5 μm and 20 μm (500-4000 cm^{-1}). Doppler-broadened lines of gases at room temperature have widths on the order of 0.001 cm^{-1}, resulting in around 3.5 million meaningful spectral bins. Assuming a laser source with 1 W of average power, a center wavelength of 10 μm and an averaging time of 180 minutes, this results in a measurable concentration range per spectral bin of $> 10^{10}$. It should be noted that (i) the availability of the broadband absorption spectrum of a gaseous molecular species, consisting of a multitude of absorption lines with strongly varying strength [79], normally allows for a quantitative concentration retrieval surpassing the measurable concentration range in a single spectral bin by an order of magnitude or more. Furthermore, (ii) in many practical cases, a lower spectral resolution is sufficient. Both (i) and (ii) indicate the feasibility of quantitative molecular fingerprinting of complex gaseous samples, such as breath, with individual concentrations of 10 orders of magnitude in a total averaging time of a few minutes.

II. Estimation of the detection efficiency in state-of-the-art field-resolved infrared spectroscopy

In Ref. [55], highest detection efficiency was achieved with a 500-μm-thick GaSe EOS crystal, amounting to a spectrally-averaged value of 0.5 % for an EOS measurement in the 970-to-1320-cm^{-1} band (at -30 dB intensity). In Ref.[201], the authors claim a time-domain signal-to-noise ratio of 40, for a detection bandwidth of 50 MHz. With the stated mid-infrared power of 50 μW and central frequency of 39 THz, this corresponds to 4×10^7 photons within the integration time window. Attenuation by $40^2 = 1600$ (to result in a SNR of 1) leads to 24000 photons within the integration time window, and an estimated 8000 photons within the interaction time window (MIR pulse duration: 29 fs, gate pulse duration: 10 fs), corresponding to a photon detection efficiency of 0.013 %.

III. Estimation of the detection efficiency for gate pulses with lower intensity noise

The spectral filter in our experiment was empirically optimized for the best SDNR, while the theoretical optimum cut-off wavelength [214] would be at approximately 1700 nm, enabling transmission of more than 90 % of the generated sum-frequency photons. Increased intensity noise and diode saturation for higher local oscillator power/broader spectral ranges prevents us from balancing to the shot noise limit in such a filtering geometry and thus decreases the SDNR.

4.2.5 Extended data

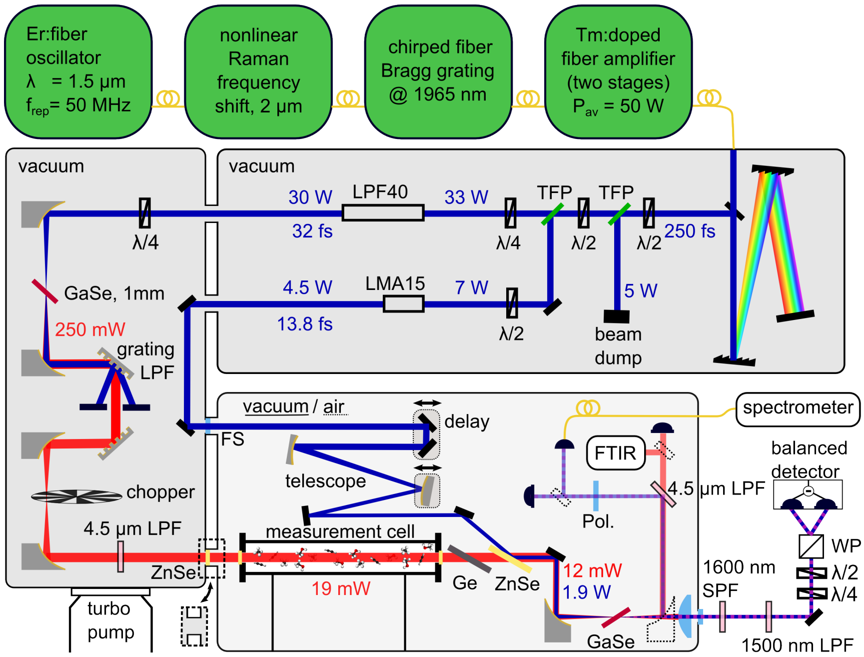

Figure 4.7: Detailed schematic of the optical setup. Er: erbium, Tm: thulium, TFP: thin-film polarizer, LMA15: a large mode area fiber, LPF40: a large-pitch fiber, $\lambda/2$: half-wave plate, $\lambda/4$: quarter-wave plate, GaSe: gallium selenide, LPF: long-pass filter, FS: fused silica, ZnSe: zinc selenide, Ge: germanium, SPF: short-pass filter, WP: Wollaston prism. The detection efficiency measurements were performed with the last chamber in air, with the ZnSe window between the chambers and the parabola after the EOS crystal inserted.

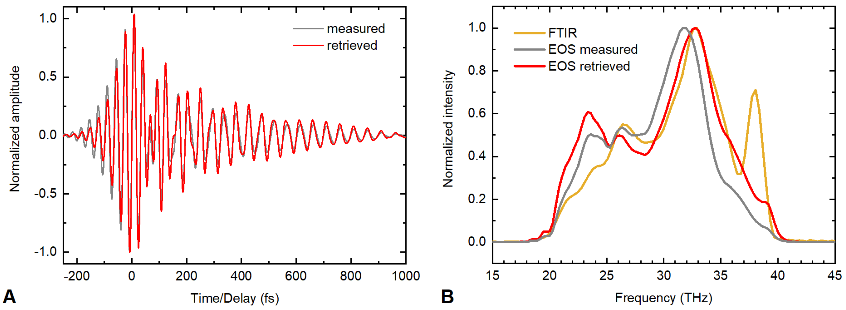

Figure 4.8: Estimated MIR electric field and EOS instrument response function for a 130-μm-thick GaSe crystal, ensuring a broadband spectral response and negligible spatial walk-off. (A) Measured EOS trace (grey), estimated MIR field retrieved using the calculated spectral response (red). (B) Measured (grey) and instrument-response-corrected (red) MIR spectra, as well as MIR spectrum measured with an FTIR spectrometer (orange). The instrument response function was calculated using a one-dimensional model for the EOS detection process, with the gate-pulse intensity envelope shown in Figure 4.3 (purple, from second-harmonic generation frequency-resolved optical gating (FROG) measurement), the crystal geometry as determined from the experimental setup and the measured transmission for the 1500-1600-nm band-pass filter (Figure 4.4C, right). The Fourier transform of the measured trace was then divided by the complex frequency-domain instrument response, yielding the red line in (B). This instrument response function incorporates phase matching, temporal walk-off, the gate-pulse properties and the effects of spectral filtering. It does not include spatial effects and gives no information on the carrier-envelope phase of the MIR waveform [53] (which is irrelevant for the experiments shown here). The waveform shown in Figure 4.3 is obtained from the waveform shown in Figure 4.4A and Extended Data Figure 4.8A (red lines), by numerically correcting for the spectral phase of 3-mm-thick ZnSe and 10-mm-thick Ge.

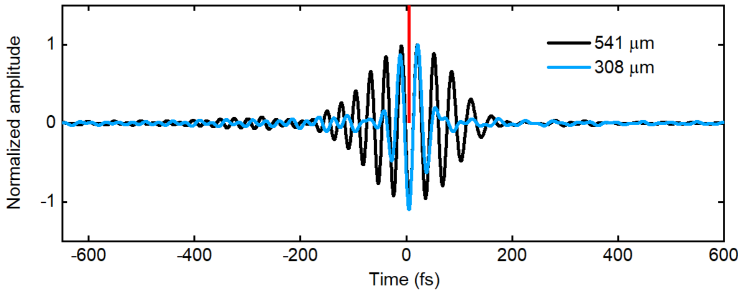

Figure 4.9: Temporal gate functions for the two detection crystal thicknesses, calculated as the Fourier transform of the respective complex spectral instrument response (complex ratio of the Fourier transforms of the incident field (Extended Data Figure 4.8) and the EOS traces (Figure 4.4A)). Multiplication by the complex frequency-domain instrument response corresponds to a convolution of the incident electric field with this (oscillating) time-domain gate function. The red line indicates the Dirac-delta-peak-like temporal response required for the theoretical limit of measuring exactly the electric field.

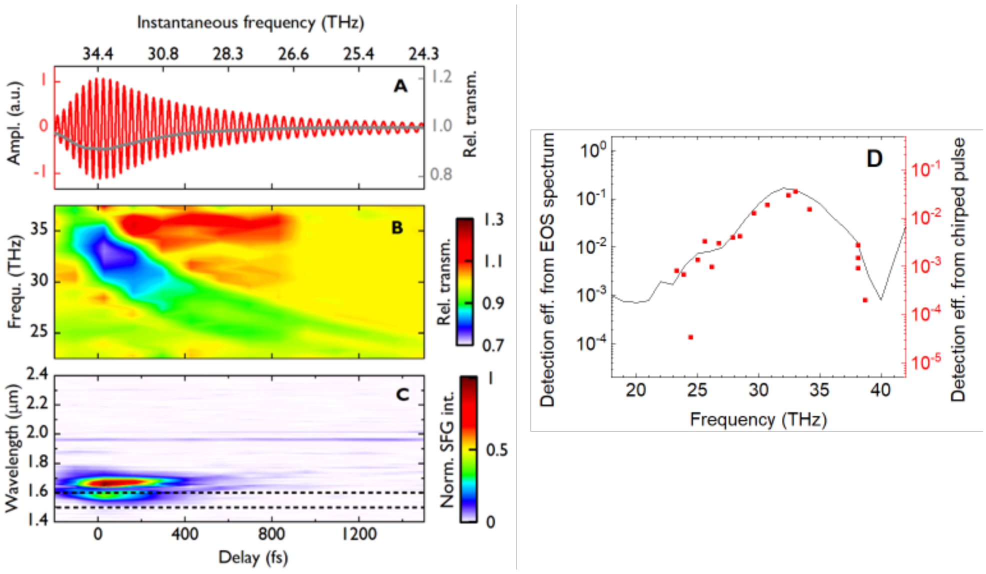

Figure 4.10: Determination of the spectrally-resolved detection efficiency from depletion measurements with a chirped MIR waveform. (A) EOS trace of the chirped MIR waveform (left axis) with instantaneous frequency (top x-axis) and spectrally-integrated power depletion measurement (right axis, grey). (B) Spectrally-resolved MIR depletion, measured with FTIR spectrometer. (C) Generated sum-frequency spectra, dashed lines indicating the spectral filtering region. (D) Frequency-dependent detection efficiency. Grey line, left y-axis: as in Figure 4.4D. Red dots: calculated for the instantaneous frequencies in (A) and with the spectral filter transmission. While the spectral shapes agree well qualitatively, discrepancies in the quantitative values arise from a decreased number of interacting photons, as not all photons of one frequency are located at one delay.

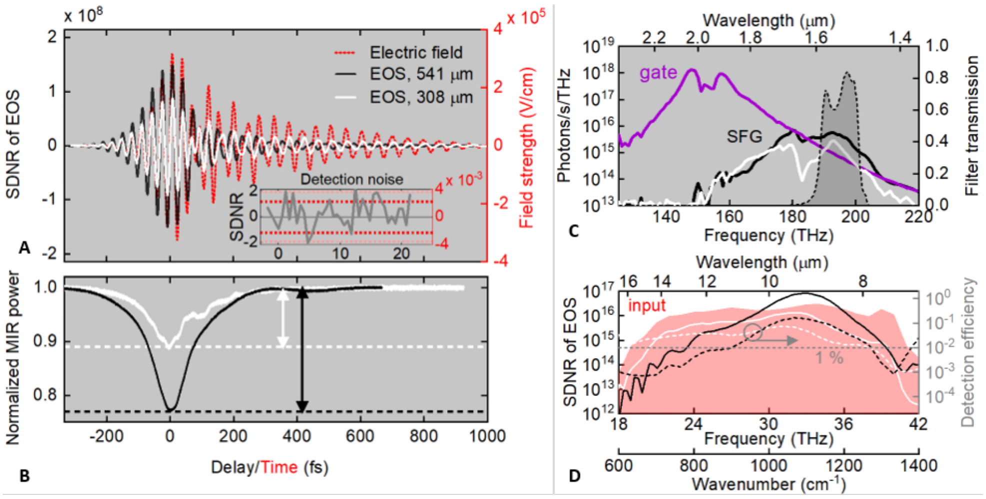

Figure 4.11: Comparison of the detection efficiency for two different detection crystal thicknesses. The black and red lines show the same results as in Figure 4.4 in the various panels. The white lines are the results for a 308-μm-thick GaSe crystal. The corresponding efficiency values are summarized in Extended Data Table 4.3, together with the values for the 541-μm-thick crystal for comparison.

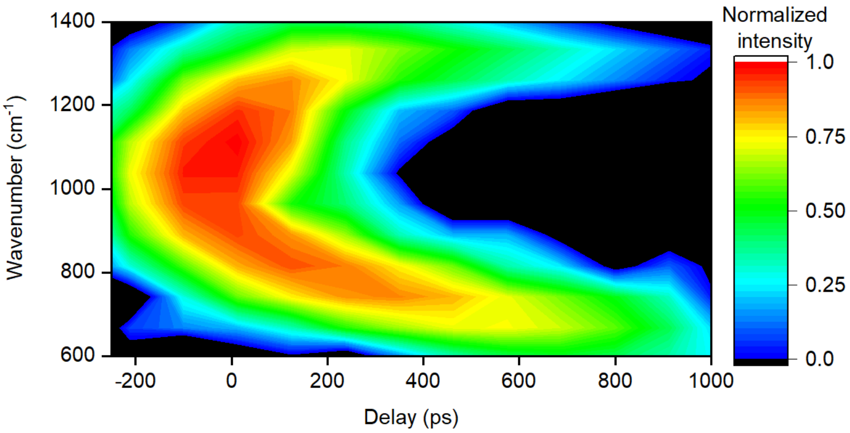

Figure 4.12: Spectrogram of the MIR waveform in Extended Data Figure 4.8A, elucidating the remaining chirp of this waveform. The time-dependent amplitude of the EOS trace results from a combination of the frequency dependent detection efficiency and instantaneous spectrum. It thus decreases towards longer delays in comparison to the MIR waveform (Figure 4.4A), where the chirp is combined with the reduced detection efficiency for longer MIR wavelengths (Figure 4.4D).

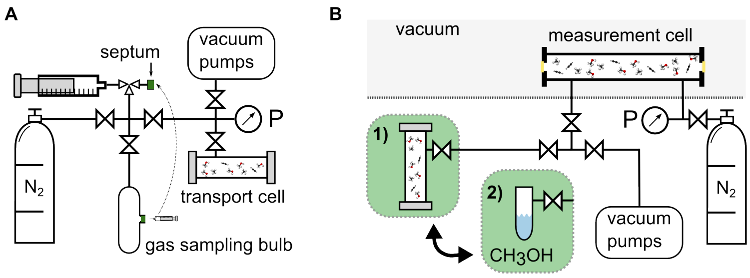

Figure 4.13: Gas handling setup (see also Methods). (A): preparation of low concentrations and gas mixtures in transport cell. (B): loading of measurement cell with 1) transport cell for low concentrations or gas mixtures and 2) high concentrations from evaporation.

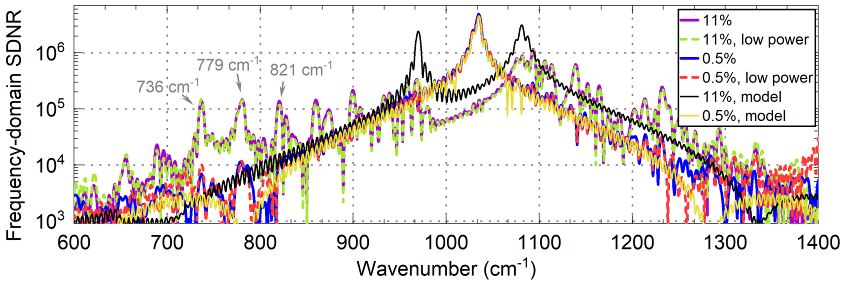

Figure 4.14: Frequency-domain magnitude of the 3-9.8 ps time window of modelled and measured EOS traces of methanol concentrations of 0.5 % and 11 %. Dashed lines: measured with 100 times lower MIR power and corrected using the transfer function $H(\nu)$.

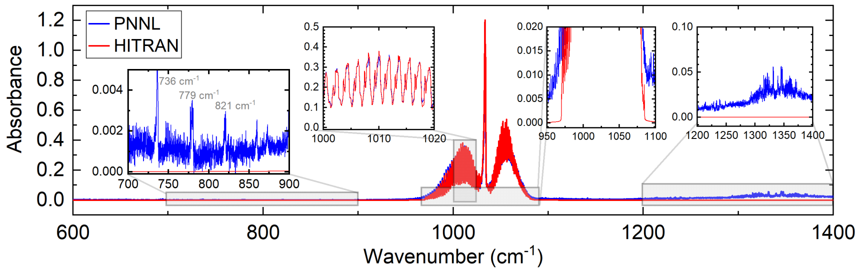

Figure 4.15: Comparison of the methanol absorbance (pressure: 1 atm (1013.25 mbar), path length: 1 m, concentration: 0.1 %, resolution 0.125 cm^{-1}, instrument response: boxcar) evaluated from transmission data in blue (PNNL) [220] and from HAPI based on the HITRAN line-by-line database in red [73]. Insets from left to right: absorbance peaks in PNNL which are absent in HITRAN; excellent agreement for P-branch; HITRAN model absorption line coverage (970-1085 cm^{-1}); broad absorbance feature in PNNL, absent in HITRAN.

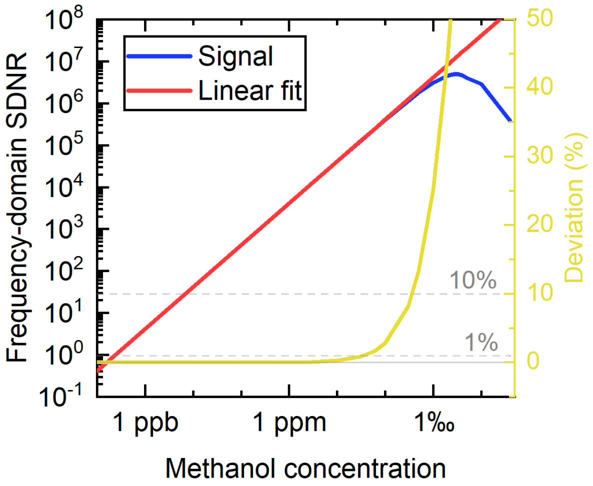

Figure 4.16: Simulated signal strength of the methanol (emission) peak ($1033.7\,\mathrm{cm}^{-1}$) of the Fourier transformed 3-9.8 ps time window. Red: result of linear fit using concentrations below 10 ppb. Yellow: relative deviation of the signal from the linear fit.

	Method	Intensity RMS noise	A_{min} [AU]	A_{max} [AU]	Dynamic range $\left(\frac{A_{max}}{A_{min}}\right)$
Ref.[201]	FRS ASOPS	0.013	8.1×10^{-3}	1.9	2.3×10^{2}
Ref.[28]	Dual comb	1×10^{-3}	6.1×10^{-4}	3	4.9×10^{3}
Ref.[19]	FTIR	1.9×10^{-5}	1.2×10^{-5}	4.7	4.0×10^{5}
Ref.[19]	EC-QCL	4.4×10^{-5}	2.7×10^{-5}	4.4	1.6×10^{5}

Table 4.1: Dynamic range comparison for state-of-the-art broadband vibrational spectroscopies. FRS: field resolved spectroscopy, ASOPS: asynchronous optical sampling. Dual comb: dual comb spectroscopy, FTIR: Fourier-transform infrared spectroscopy, EC-QCL: external-cavity quantum-cascade laser. The minimal absorbance A_{min} is determined in an equivalent manner to the first paragraph of the supplementary text, assuming a noise proportional to the intensity, $A_{min} = \frac{\sqrt{2}}{\log(10)}\delta I$ where δI is the relative standard deviation of intensity or RMS (root-mean-square) noise. The maximum absorbance A_{max} is estimated with the sample transmitted intensity being equal to the noise of the reference intensity: $A_{max} = -\log_{10}(\delta I)$. In Ref.[19] the RMS value of the absorbance is given and thus used as the basis for the calculations.

	T_{in} $[ms]$	SNR for T_{int}	SNR for $T_{int} = 1\,\mathrm{s}$	P_{avg} $[mW]$	f_{rep} $[MHz]$	ν_c $[THz]$	τ_p $[fs]$	w $[\mu m]$	E_{min} $[\frac{mW}{cm}]$	η_{total} $[\%]$
Ref. [55]	2.4 [i]	1.4×10^6 [*ii*]	2.9×10^7	12 [*ii*]	28	34.2	60	35	**26**	**0.5**
Here	1000	1.6×10^8	1.6×10^8	12	50	33	100	35	**2.2**	**7.5**

Table 4.2: State-of-the-art EOS detection efficiency and sensitivity (i.e., minimum measurable field strengths). [*i*] Lock-in time constant of $183\,\mu$s (internal knowledge) with a 6th order filter; the settling time to reach 99 % signal strength was assumed to be the integration time (T_{int}), calculated according to the Zurich Instruments manual. [*ii*] Calculated from Ref.[55] for the 500-μm-thick GaSe crystal, and a chopped average power of 12 mW (internal knowledge). From the attenuation experiment (Extended Data Figure 4.8), the intensity noise floor of a single measurement corresponds to 5×10^{-13}, related to the maximum spectral intensity (in the frequency domain). τ_p : (estimated) FWHM pulse durations, w: $1/e^2$ gate pulse beam radius. The minimum measurable field strength is determined for $SNR = 1$ for an integration time per temporal element of 1 s. Scaling of the SNR with the square-root of the integration time is assumed. In order to include the effect of chopping, the average power was doubled for the field-strength calculation: $E\left[\frac{mW}{cm}\right] = \sqrt{\frac{4 \times P_{avg}[W]}{SNR_{1s} \times f_{rep}[Hz] \times \tau_p[s] \times w^2[cm^2] \times \pi \times c[\frac{m}{s}] \times \epsilon_0[\frac{As}{Vm}]}}$

thickness GaSe $[\mu m]$	$\eta_{\mathrm{conversion}}$ [%]	$\eta_{\mathrm{interaction}}$ [%]	η_{BPF} [%]	η_{Fresnel} [%]	spectrally averaged η_{total} [%]	peak of $\eta_{\mathrm{total}}(\omega)$ [%]	spectral range with > 1 % $\eta_{\mathrm{total}}(\omega)$ $[cm^{-1}]$	E_{min} $[\frac{mW}{cm}]$
308	10	60	25	87	3.7	7.4	600-1300	3.6
541	22	70	27	87	7.5	16.6	900-1270	2.2

Table 4.3: Comparison of the various efficiency values for two different thicknesses of GaSe crystals used as the nonlinear medium in the EOS detection.

Lit.	Method	Spectral coverage $[cm^{-1}]$	Cell length $[m]$	Reso-lution $[cm^{-1}]$	Species	Acq. time $[s]$	LOD $[ppb]$	Min. coloumn density $[molecules/cm^2 Hz^{-1/2}]$	Noise equivalent absorbance $[AU\ Hz^{-1/2}]$	Adj. noise equivalent absorbance $[AU\ Hz^{-1/2}]$
Here	FRS	666-1430	0.45	3.1	CH_3OH C_2H_2 CH_4	80	0.8 0.6 40	8.6×10^{12} 6.3×10^{12} 4.3×10^{14}	2.9×10^{-6} 1.3×10^{-5} 5.8×10^{-5}	8.8×10^{-5} 4.1×10^{-4} 1.8×10^{-3}
Ref. [201]	FRS ASOPS	500-2000	0.15	3.3×10^{-3}	CO_2	1320	10^4	5.8×10^{14}	1	1
Ref. [28]	Dual comb	1820-3250	76	3.8×10^{-3}	CO_2 OCS	720	2 7	3.3×10^{13} 1.1×10^{14}	2.7×10^{-2} 2.7×10^{-2}	2.9×10^{-2} 2.9×10^{-2}
Ref. [91]	Dual comb	830-2500	0.15	3.3×10^{-3}	CH_3OH	100	10^6	1.7×10^{16}	7×10^{-2}	7.2×10^{-2}
Ref. [215]	WMS with EC-QCL	920-1150	2.64	0.1	CH_3OH C_2H_4	10	20 25	4.5×10^{14} 5.6×10^{14}	2×10^{-4} 3×10^{-4}	1×10^{-3} 1.7×10^{-3}

Table 4.4: Comparison of state-of-the-art broadband infrared spectroscopy experiments. FRS: field resolved spectroscopy, ASOPS: asynchronous optical sampling. Dual comb: dual comb spectroscopy, WMS: wavelength modulation spectroscopy, EC-QCL: external-cavity quantum-cascade laser. The limit of detection indicates the sensitivity of the instrument for a given molecular species. The minimum column density per second allows for the comparison under consideration of interaction length and integration time. In order to quantify the instrument performance independent of the environment (pressure, temperature) and absorption cross section, the noise-equivalent absorbance is given in the table. The last column indicates the noise-equivalent absorbance adjusted to a resolution of 3.3×10^{-3} cm^{-1} considering the necessary increase in integration time and assuming statistical averaging. The red values are determined from simulations using HAPI.

Chapter 5

Applications - an Outlook

The first part of this chapter, section 5.1, continues the discussion of FRS in the gas phase from the previous chapter. To start with, the energy transfer of vibrational resonances and the impact of pressure on the molecular response is investigated. Followed by a discussion on some of the experimental challenges that FRS in the gas phase faces. Furthermore, the implementation of an enhancement cavity in the MIR is referred to.

In the end, the application of the FRS instruments for high-throughput flow cytometry experiments is discussed and the first step towards the realization, the implementation of a rapid scan, is presented in section 5.2.

5.1 Gas-phase EOS

5.1.1 Energy transfer and spectral lines

Spectroscopy in the gas phase has a wide variety of applications spanning from environmental sciences and industrial process optimization to biological analytics and medical diagnostics[2, 95, 215, 218]. The gas phase is less dense compared to the liquid and the solid phase resulting in weaker molecular interactions and thus more narrowband absorption lines. The high abundance of these spectroscopically accessible and spectrally isolated absorption lines facilitates the classification of molecular species based on their IR spectra. This allows for high specificity of vibrational spectroscopy even in complex samples [28].

A spectroscopic efficiency can be defined as the ratio of the energy contained in the measured quantity to the energy of the excitation. In FRS the measurement occurs on the level of the electric field and, as derived in section 2.3.2, the filed strength of the molecular response scales linearly with the number of emitters and thus their concentration. The following discussion on the coherent energy transfer of the excitation to the emission of the molecular response is based on the findings for the liquid phase in [221].

The molecular response can be described similar to Equation 2.37 with an approximation for small concentrations ($\tilde{n}(\omega) \approx 1 + \chi(\omega)/2$):

$$\tilde{E}(\omega, z) = \tilde{E}(\omega, 0) \exp\left(-i\tilde{n}(\omega)\frac{\omega}{c}z\right) \approx \tilde{E}(\omega, 0) \exp\left(-i(1 + \chi(\omega)/2)\frac{\omega}{c}z\right) \tag{5.1}$$

$$= \underbrace{\tilde{E}(\omega, 0) \exp\left(-i\frac{\omega}{c}z\right) H_{ref}(\omega)}_{=\tilde{E}_{ref}(\omega)} H_{sam}(\omega). \tag{5.2}$$

Here, $H_{ref}(\omega)$ denotes the transfer function of a reference measurement, e.g. water in a liquid sample and $H_{sam}(\omega)$ is the transfer function for the molecules under investigation. In this approximation $H_{sam}(\omega)$ can be rewritten as:

$$H_{sam}(\omega) = \exp\left(-i\rho_N \alpha \frac{\omega}{c} z\right), \tag{5.3}$$

with the number density ρ_N and the complex polarizability α. The transfer function of the sample can then be obtained by a simple division in the frequency domain $H_{sam}(\omega) = \tilde{E}_{sam}(\omega)/\tilde{E}_{ref}(\omega)$. In the time domain Equation 5.2 corresponds to a convolution:

$$\tilde{E}_{sam}(t) = \tilde{E}_{ref}(t) * H_{sam}(t) = \underbrace{\tilde{E}_{ref}(t) * (H_{sam}(t) - \delta(t))}_{=\tilde{E}_{reem}(t)} + \tilde{E}_{ref}(t). \tag{5.4}$$

In the limit of an ultrashort excitation, namely a delta-pulse, the last term is only nonzero for the infinitesimally short duration of the excitation at $t = 0$. In this case the last term can be associated with the excitation and the first term corresponds to the re-emitted radiation. With the Plancherel theorem and some rearrangements the coherently re-emitted energy can be described by [221]:

$$E_{reem.} = \int \bar{S}_{ref}(\omega) \left|H_{sam}(\omega) - 1\right|^2 d\omega. \tag{5.5}$$

Here, $\bar{S}_{ref}(\omega) \propto \int |\tilde{E}_{sam}(\omega)|^2 d\omega$ denotes the energy spectral density of the excitation. The total energy that remains in the sample E_{final} in form of heat is just the difference between the energies before and after the sample

$$E_{final} = \int \bar{S}_{ref}(\omega) - \bar{S}_{sam}(\omega) d\omega. \tag{5.6}$$

Incoherent processes such as scattering or spontaneous emission of the sample molecules are not considered here, but they can be contained in the reference measurement and thus referencing can reduce their impact.

The coherent energy transfer (CET) can be written as the difference between the instantaneous intensities $I^{inst}_{ref,sam}(t) = c\varepsilon_0 |\tilde{E}_{ref,sam}(t)|^2$:

$$CET(t) = \int\limits_{t_0}^{t} \left(I^{inst}_{ref}(t') - I^{inst}_{sam}(t')\right) dt'. \tag{5.7}$$

In Figure 5.1 the electric field before and after a sample is shown together with the CET and the involved energy levels. After an initial energy deposition by the excitation into the sample concludes, the absorbed energy reaches a maximum E_{max}. Energy is emitted in form of coherent radiation with a sample specific decay time Γ and approaches the final energy level E_{final}, which corresponds to the absorbed energy predicted by the Beer-Lambert law. The difference between E_{max} and E_{final} is the re-emitted energy E_{reemit}. In the right panel of Figure 5.1 the energy ratios relevant for the spectroscopic efficiency are plotted. The concentration is kept constant to ensure the same shape of the absorption spectrum and the interaction length is scanned. For small path lengths the expected scaling with the path length or equivalently the concentration can be seen: linear scaling of the energy deposited into the sample (Beer-Lambert law) and the quadratic scaling of the re-emitted energy in form of the molecular response. For larger absorptions the separation into a term of ultrashort excitation and re-emitted radiation in Equation 5.4 is not possible anymore, because the excitation deviates further from a delta pulse. The significant absorption leads to a strong molecular response and thus an excitation on the same timescale as the molecular response for later parts of the sample. Thus the re-emitted energy $E_{reem.}$ should decrease again for non-negligible absorptions. This behavior can be observed experimentally and with simulations by time filtering and analyzing the response, see Figure 4.16.

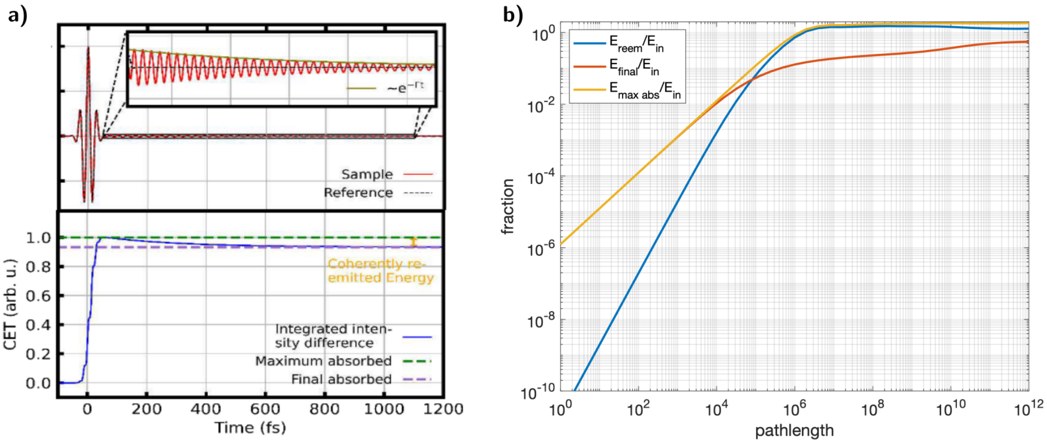

Figure 5.1: Energy transfer of few-cycle excitation a) top: Electric field of reference and methanol sample bottom: time dependent coherent energy transfer (CET), taken from [221]. b) Spectroscopic efficiency for a constant concentration but different path lengths.

In the gas phase the line shape is strongly dependent on external parameters, such as pressure and temperature. The line-by-line data of the high-resolution transmission molecular absorption database (HITRAN) [73] allows to account for different environmental conditions. The Voigt profile was chosen as the simplest line model accounting for Doppler and pressure broadening. Calculation of the complex Voigt profile, which is based on the complex error function, is computational expensive because it must be solved numerically.

Here, the code from [222] is used for its rapid interpolation.

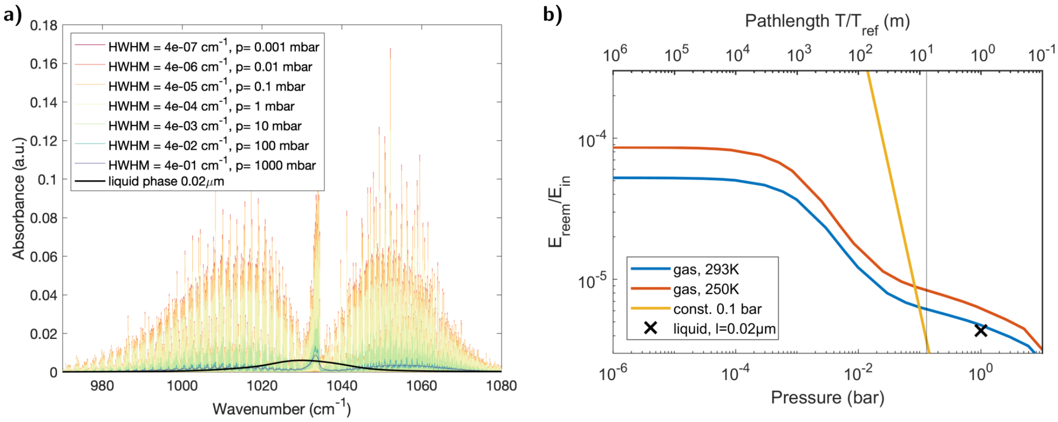

Figure 5.2: Impact of temperature and pressure. a) Calculated absorbance based on the HITRAN line-by-line data for methanol at different partial pressures, but constant number of illuminated methanol molecules. b) Ratio of re-emitted energy fraction for a constant number of molecules in gas and liquid phase in the spectral range 970-1080 cm^{-1}. The vapor pressure of methanol (130 mbar) is indicated by the dashed line. The values above the vapor pressure would require other gas species, such as N_2, to increase the total pressure while the partial pressure of methanol remains below the vapor pressure. The path length would need adjustment to keep the molecule number constant and the gas mix would slightly change the value of α_L. The yellow line indicates the case of a varying number of molecules by increasing the path length at a partial pressure of 100 mbar at a temperature of 293 K

In Figure 5.2 absorption spectra for different pressures of methanol with a constant number of molecules are plotted. It follows from the ideal gas equation $pV = Nk_BT$ that for constant pV/T the volume must be increased. For the same temperature this is achieved by simply increasing the interaction length and for different temperatures this results in a slight shift of the curve in panel b). The absorption spectrum of the liquid phase with the same number of molecules is shown as reference in black. The thickness of the liquid phase ℓ_{equ} can be calculated utilizing the ideal gas equation, the molar mass M and the density ϱ of liquid methanol:

$$\ell_{equ} = CD\frac{M}{N_A\varrho}, \text{ with the coloumn density CD} \tag{5.8}$$

$$CD = \frac{\ell_{gas}p}{k_BT}. \tag{5.9}$$

In the liquid phase, the absorption around the CO stretch of methanol is similar in strength to that of the pressure broadening absorption at 1 bar. The linewidth at the lowest considered pressures is the smallest and is dominated by Doppler broadening, whose HWHM is only depended on the temperature T, the transition wavenumber and the molar mass M

$\alpha_D \propto v_{ij}\sqrt{(T/M)}$. For increasing pressures, the dominant contribution to the line shape is the pressure broadening with its characteristic HWHM $\alpha_L \propto p/T$. For constant temperature, the area under the attenuation coefficient stays constant as the line strength is only dependent on the temperature and the line profiles (Equations 2.30-2.32) are normalized. The ratio of the re-emitted to incident energy increases for the increasingly narrowband line width at lower pressures. This is due to the re-emitted energy scaling quadratically with the absorption coefficient at low absorptions. Surprisingly, the energy transfer of the liquid and gaseous phase at 1 bar for the same number of molecules is comparable.

In Figure 5.3, the simulated amplitude of the sample for fixed molecule number and temperature (293 K) is shown. The smaller HWHM at lower pressures results in a longer decay time ($\alpha_L = 1/(\pi c\Gamma)$, with the decay $\exp(-t\Gamma)$). The resolution of a scan of a field-resolved measurement with delay range T_{range} after the excitation is $dv = 1e-2/(T_{range}c)$, which implies improving resolutions for a longer delay scans. Conversely, this means that one cannot distinguish between differently broadened spectra, when considering only short delays around the excitation, due to the low spectral resolution. And indeed, in the right panel the traces have the same maximum amplitude directly after excitation and only start to differ significantly at delays approaching or surpassing the decay times involved. Therefore, in order to benefit from an increase in E_{reem} a sufficiently long delay scan or resolution of the measurement is required. This is equivalent for the case of time-integrating spectroscopy: For instance, measurements utilizing a monochromator can also benefit from a more narrowband line shape. But only in case of a sufficient resolution a stronger transmission change at the transition wavenumber can be observed.

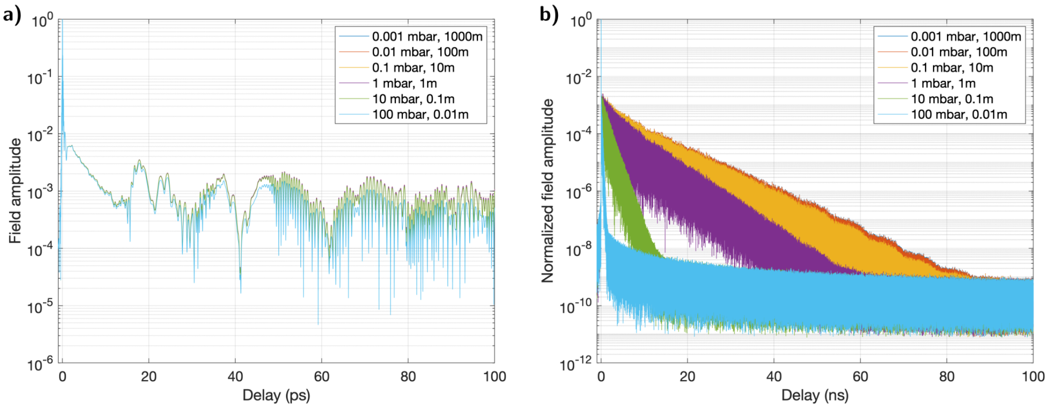

Figure 5.3: Electric field ($\tilde{E}_{sam}(t)$) envelopes of pure methanol samples at room temperature. The pressure and path length is varied such that the number of molecules stays constant. The delay ranges of −1-100 ps and −1-100 ns are shown in a) and b) respectively.

For gas spectroscopic applications the amount of available sample can strongly vary. For small amounts of the sample, the transfer to lower gas pressures increases not only the specificity due to more narrowband, separable absorption lines, but also the measurable re-emitted energy in FRS. For samples available in larger quantities, the interaction length can be adjusted for best spectroscopic efficiency [54]. In Figure 5.2 b) the energy ratio E_{reem}/E_{in} for constant partial pressure is plotted in yellow for different path lengths, highlighting that the path length is a more suitable variable to optimize the ratio due to its quadratic scaling. The ideal measurement conditions are thus highly dependent on the experimental goals and conditions.

5.1.2 Measurement challenges

Integration time and scanning range

The results discussed in chapter (4) show that time filtering of the background-free molecular signal allows for concentration retrievals that are robust against noise of the excitation, in line with the findings in Reference [55]. To further evaluate this performance, consecutive traces with measurement times of 8.3 s and a delay range of 10.6 ps were taken over several minutes and evaluated in analogy to the Allan-Werle plot. The traces where first averaged for a fixed total integration time, and consecutive traces were then subtracted, time-filtered (3-9.8 ps) and Fourier-transformed in order to determine the limit of detection (LOD), compare chapter 4). The LOD is defined as the concentration, where the spectral peak associated with the main absorption line of a Fourier-transformed sample minus reference trace is equal to the average of the spectral amplitude of the reference minus reference measurement.

In a delay window where the EOS signal of the MIR field is far below the noise of the local oscillator of the heterodyne detection, white noise from the local oscillator and the electronics is dominant. In this case, the LOD should average statistically and improve by $T_{av}^{-0.5}$ with the average time T_{av}. This is observed for several measurements of with $T_{av} > 5$ minutes in Figure 5.4. There are two major potential reasons for deviations. On one hand, the balancing of the local oscillator can drift due to slight spectral or pointing changes and thus elevating the noise over time, see the red curve in Figure 5.4. On the other hand, the assumption of a background-free detection becomes insufficient and drifts or noise of the excitation become relevant. Here, the chosen time window exhibits a weak residual signal strength that remains even after the subtraction of two reference traces. Thus even for shorter integration times this time window was not completely background free. Furthermore, it was shown experimentally that for most delays the subtraction of two reference traces reduces the amplitude by two orders of magnitude, thus limiting the delay range where residues of the excitation are negligible. This subtraction is limited by the intensity noise of the system and the timing jitter. The impact of timing jitter on the EOS traces could be reduced by a more accurate determination of the relative arm lengths of the 6 m long interferometer. For example employing interferometric delay tracking allows a delay precision on the level of tens of attoseconds [223].

The choice of the acquisition time of a single trace can significantly change the impact of noise sources on the fidelity of the trace. For instance, acquisition times much shorter than the characteristic time scale of thermal drifts but with the same total acquisition

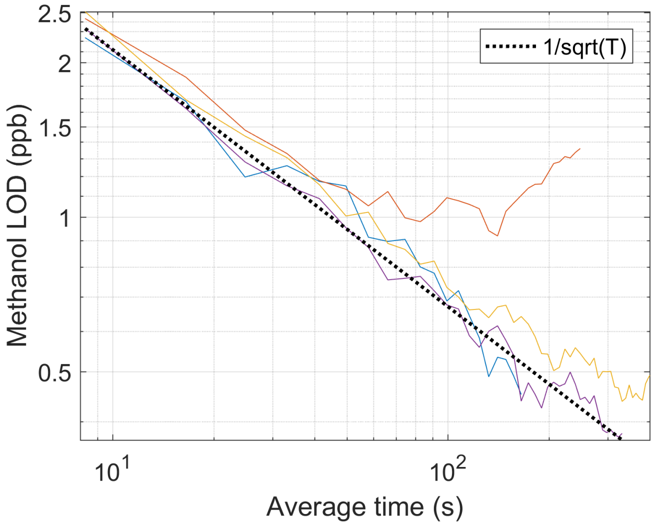

Figure 5.4: LOD of methanol concentration versus total integration time. The 10.6 ps long Individual traces were each taken within 8.3 s with an evacuated sample cell. The LOD was determined after averaging, time filtering 3-9.8 ps, subtraction and Fourier transformation and comparing the noise floor in the frequency domain with a simulated signal strength. In dashed black the expected statistical averaging of white noise is indicated. The shown measurements are taken on separate days.

time yielded smaller distortions due to averaging out of, e.g. intensity changes. In the proof of principle measurements in section 4, a mechanical delay stage with two retroreflectors was used limiting the possible delay range and the scanning speed to 690 ps and 45 mm/s, respectively. The scanning speed is further restricted by the integration time and the reference frequency of the lock-in detection, such that the waveform is recorded with high fidelity. Figure 5.5 shows the results of a scan utilizing the full scan range. A low pressure of 1.23 mbar and a pure methanol sample results in a typical linewidth of around $1 \times 10^{-3}\,\mathrm{cm}^{-1}$. This corresponds to a decay time of around 10 ns and thus the signal decays only marginally over the initial 500 ps. In the spectrogram of the sample measurement in Figure 5.5 b) the typical beating of the absorption branches can be seen. For larger delays, the deviation from equidistant absorption lines results in a smearing out of the beatings. Panels d) and e) show the good agreement of the measured and simulated absorbance at the measurement resolution of $0.06\,\mathrm{cm}^{-1}$. The spectrogram of the reference EOS trace, shown in panel c) reveals strong signal strengths around 11 ps and 25 ps. These stem from multiple reflections in the nonlinear crystals used in EOS and IPDFG, respectively. For background-free detection these multiple reflections pose a challenge. Subtraction of a reference trace from a sample trace can only reduce their strength up to the excitation noise carried by these reflections. These backward reflections carry a copy of the excitation spectrum and appear as an offset in the frequency domain after time-filtering and Fourier transformation. One approach to limit the impact of the reflections is choosing an analysis time window after the main pulse and before the first reflection, compare Figure 4.5. The signal after a MIR pulse reflection includes the molecular response and thus the signal at subsequent delay points is impacted by interference.

In order to avoid backward reflections most transmissive optics where exchanged with wedged versions, where the backward reflections are spatially separated and, thus, not detected. In case of GaSe, this has not yet been possible due to its soft, layered structure. The high dynamic range of EOS spanning more than 7 orders of magnitude makes sufficient attenuation (factor >1000) of the reflections challenging. For phase-matching purposes, the crystals were placed under an angle θ resulting in a small beam displacement. The employed thickness of the IPDFG crystal separates the beams by a few $100\,\mu$m. This spatial separation can be utilized to reduce the amplitude of the reflection by a hard edge, such as a razor blade.

The standard approach for reducing Fresnel reflections is an anti-reflection coating. This approach is not feasible for GaSe, due to weak bonds between layers not being able to endure the surface tension of the coating and peeling off. Instead nanopattering of the surface via an ion beam can reduce the intensity of the reflection by two orders of magnitude [224]. Furthermore, attaching a refractive index matched bulk material, such as diamond, on one crystal side, allows to increase the time separation of the main pulse and the backward reflection[225]. Furthermore, a wedged substrate even results in a spatial separation.

The last approach is to employ a numerically propagated replica of the excitation pulse, which is measured with a high signal-to-noise ratio, and subtract it. For small crystal thicknesses this has shown promising results in another project of the group[1]. In case of thick crystals, the displacement can be on the order of the focus size, which leads to a difficult to model change of the EOS instrument response function in spectral amplitude and phase. So far, no benefit was seen on the here presented data acquired with a $541\,\mu$m tick GaSe crystal.

Sample preparation and FTIR measurements

The preparation of synthetic gas samples with low and accurately controlled concentration is often challenging due to adsorption of molecules on the chamber walls. In static measurements, where the sample remains over the entire measurement time within the gas cell, gas molecules desorb from or diffuse through the cell walls. For synthetic samples, the gases are typically mixed via a flow regulation, and a constant flow through the sample cell reduces the impact of these slow mechanisms, ensuring a constant partial pressure. Here, for the sake of simplicity of our proof-of-principle measurements, we employed the static protocol described in section 4.2.3. In order to test the reproducibility of the sample preparation and retrieval the same methanol samples at ppm concentration level where measured with an FTIR spectrometer before and after every FRS measurement. The methanol concentration was retrieved with the FTIR by using the absorption peak at $1034\,\mathrm{cm}^{-1}$. Accounting

---

[1] M. Trubetskov, personal communication

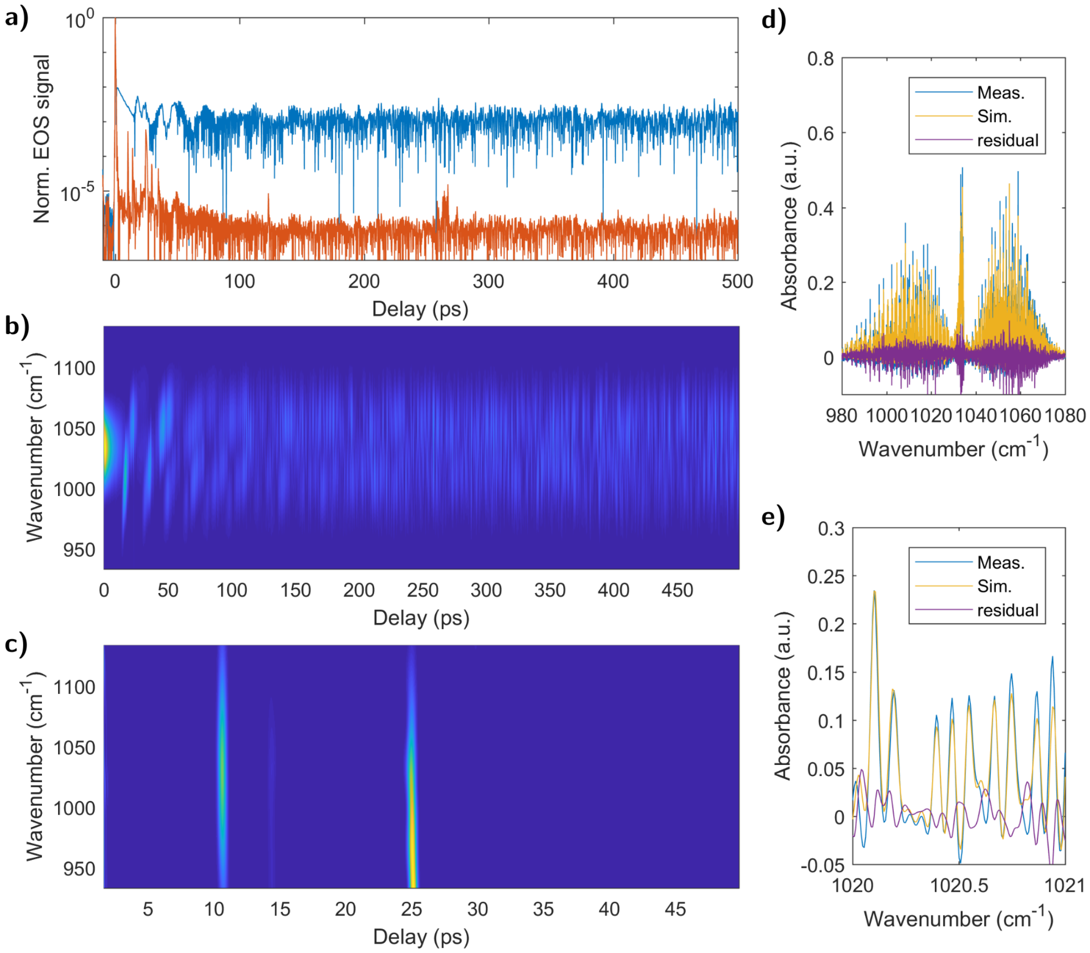

Figure 5.5: Long EOS trace of pure methanol at 1.23 mbar with a 45-cm long sample cell. a) A reference EOS trace in red with an evacuated sample cell (0.1 mbar) and the trace with a methanol sample in blue. b) Spectrogram of the sample trace starting at 0.5 ps after the peak of the excitation. c) Spectrogram of the reference trace between 0.5 ps and 50 ps after the peak of the excitation. d) The measured and simulated absorbance are shown together with the difference of the two, the residual in purple. The 550-ps long EOS trace results in a resolution of 0.06 cm^{-1}. e) Separated absorption lines of the P-branch over 1 cm^{-1}.

for the dilution of the sample occurring in the pressure equalization step (see section 4.2.3), the samples can be prepared with a standard deviation of 11 %[226].

The performance of the available FTIR was also benchmarked for comparison with the FRS detectable concentration range of methanol, see Figure 4.5. The upper limit of retrievable concentration is restricted by saturation effects, where the sample spectrum power at ν_{ij} reaches the noise floor. The lowest retrievable concentration limit is reached, when the standard deviation of the noise floor reaches 100 % of the sample signal strength. The retrievable concentration range using only the fundamental transition of the methanol

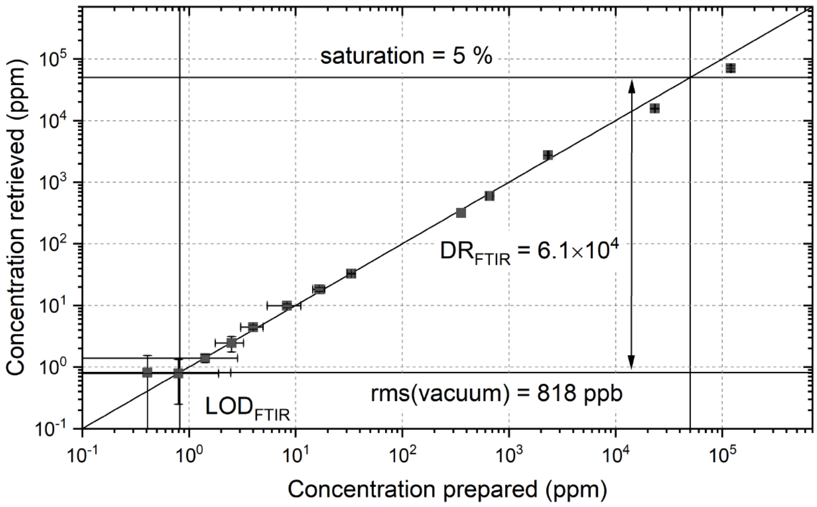

Figure 5.6: Methanol detectable concentration dynamic range with the FTIR (Bruker, Vertex 70) using the CO stretch at 1034 cm^{-1}. The measurements were taken with an integration time of 80 s, a resolution of 4 cm^{-1} and gas cell with 15 cm. The figure is taken from[226][2]

stretch approaches 5 orders of magnitude. This is roughly 2 orders of magnitude smaller than the results obtained with FRS, see section 4.2.3. The thermal source of the FTIR spectrometer covers the entire molecular fingerprint region and, thus, more absorption features can be employed for concentration retrieval. For instance the overtone band of methanol around 2068 cm^{-1} is weaker in absorbance by a factor of 25 compared to the fundamental transition. By including this band in the analysis, the upper limit of retrievable concentration increases by more than one order of magnitude, and thus, also the dynamic range of retrievable methanol concentrations.

5.1.3 Cavity-enhanced field-resolved spectroscopy

Spectroscopy of low density gas samples often benefits in terms of sensitivity, from long interaction lengths, due to the increase in the sample absorbance. The commonly used approach to increase the path length on an optical table is a multi-pass cell, where the beam is folded by multiple mirrors generating intermediate foci in order to control the divergence. Typically, achievable path lengths are on the order of dozens to hundreds of meters and the current research focuses on compact designs, that allow low samples volume [20, 227].

Femtosecond enhancement cavities (fsEC) circulate short pulses that constructively interfere with the input pulses, leading to large enhancements of their electric field. The

---

[2] The measurements were taken by Lukas Fürst in the frame of his MSc thesis, directly supervised by the author of this dissertation.

circulation inside the cavity also effectively increases the interaction length of a MIR pulse with the sample. Furthermore, in contrast to multi-pass cells, the increase of interaction length occurs in the exact same volume. This is crucial for small, localized sample volumes such as in the case of electrospray ionization. While the path length enhancement has been employed for sensitive, linear spectroscopy techniques [216, 228] the field strength enhancement facilitated efficient nonlinear frequency conversion [229, 230]. In order for a fsEC-setup to improve the sensitivity of the here presented field-resolved spectroscopy of gases, a broadband field-enhancement in the MIR spectral range is required. The constructive interference of the circulating pulse and the input pulse requires a temporal overlap and a negligible change of the pulse form and phase after one round trip in the cavity. furthermore, the field and pathlength enhancement is strongly coupled to the cavity losses per round trip. Therefore, dielectric mirrors with high reflectivity (>99.99 %) and a flat spectral phase over a broad spectral range are often used. The absence of these types of broadband mirrors for the MIR spectral range makes the realization of broadband and high finesse fsEC challenging.

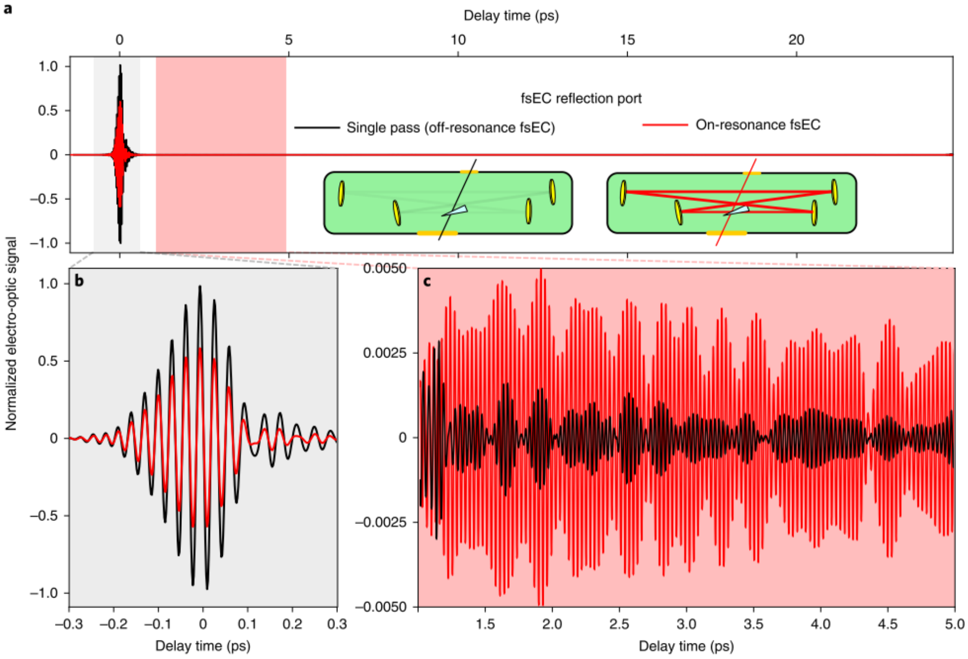

Figure 5.7: Field-resolved detection of the output of the reflection port for the case of on-resonance (red) and off-resonance (black). The panels show the EOS amplitude at different time windows: a) full scan range, b) zoom in on excitation pulse, c) wake of the excitation. The figure is taken from [231].

The following discusses such a fsEC that has been built and characterized by the group led by Ioachim Pupeza based on the previously described front-end and published in [231][3].

---

[3] The author of this dissertation provided help in planning and integrating the experimental setup of the cavity in the instrument described in chapter 4. As well as teaching the usage and its maintenance.

Bare gold mirrors were used as they provide a flat spectral phase and decent reflectivity (around 99 %) over the entire molecular fingerprint region. A thin diamond wedge oriented close to Brewster angle served as the input and output coupler. As the substrate material diamond was chosen due to its large spectral transmission range and low dispersion. Furthermore the wedged configuration allows the separation of the transmission and reflection port.

The repetition rate and the offset frequency of the oscillator can be acted on in order to match the optimum offset frequency (OOF) and the length of the cavity. Due to the IPDFG process the MIR comb has a offset frequency of zero and can't match the OOF of the empty cavity, which stems from the geometric phase and the material dispersion of diamond and gold. By filling the cavity with gas (humid air) the OOF of the cavity was shifted closer to zero in the 8-15 μm spectral range at the cost of a reduction of the enhancement bandwidth to slightly less than one octave. The repetition rate of the laser was scanned to find suitable resonances, where the MIR comb modes overlap with the modes of the cavity. A Hänsch-Couillaud lock on a well chosen resonance from a co-propagating NIR pulse train was used to adjust the repetition rate to the cavity length.

The EOS traces of the reflection port of the cavity are shown for the resonant and off-resonant case in Figure 5.7. The off-resonant case corresponds to the MIR pulses propagating through the 6.5 m long path outside the cavity beam path but inside the chamber filled with 1 ppm methanol, 360 ppm CO_2 and water vapor at 14 % relative humidity. In the on-resonance case (red) the transmitted portion of the input pulse and the output-coupled intracavity pulse overlap in space and time. As a consequence of the input beam being transmitted without a phase change and the reflected part undergoing a π-shift destructive interference occurs. Due to imperfect transverse mode matching and impedance matching the observed attenuation of the main pulse is only 38 % of the amplitude, see Figure 5.7b. The trailing molecular signal generated in the cavity has no temporal overlap and thus experiences no interference. As a result an increase of signal strength in the wake of the excitation is observed, see Figure 5.7c.

The demonstrated fsEC is the first of its kind showing nearly octive-spanning enhancements centered around 10 μm and offers an effective path length of 81 m. Combined with the previously demonstrated EOS performances this allows to estimate the LOD for methanol to be in the lower parts-per-trillion range (12 ppt) within 25 s of averaging time.

5.2 Toward high-throughput flow cytometry

The main advantages of field-resolved spectroscopy lie in the access to the time domain, the signal scaling with the electric field and the high dynamic range. Compared to spectroscopy techniques measuring signals proportional to the intensity, such as the classical FTIR spectrometer, the requirements on the sample thickness for high SNR are more forgiving [54]. In biology the samples are often in a water matrix, which strongly absorbs infrared radiation. Typically very thin ($<10\,\text{um}$) samples or samples close to the surface (e.g. with attenuated total reflection infrared spectroscopy) where previously measured directly with infrared spectroscopy. In recent years the development of QCLs as the source of high power, coherent MIR sources has given new perspectives to vibrational spectroscopy of highly absorbing biological samples [15]. In FRS the favorable scaling and high dynamic range allowed the measurements of living plant leaves and suspended cells in first proof of principle measurements [55].

The identification and sorting of cells finds wide applications in biology and is mainly performed with fluorescence-activated cell sorting (FACS), where the sample is first labeled and then classified via their fluorescent activity in a flow-cytometry setup. This process requires labeling, which can come with significant drawbacks, such as cellular toxicity, photobleaching and time-consuming sample preparation [232]. A label-free approach can circumvent these disadvantages and allow to have a natural functioning cell even after characterization, which can be relevant for example in studies on metabolism or for medical applications. The most often used spectroscopic approach for label-free flow cytometry is Raman spectroscopy, which is based on the inelastic scattering of light by molecular vibrations. Due to the low cross-section of the process high SNR often require long integration times on the order of seconds. Derivatives of coherent Raman techniques such as SRS or CARS have allowed high-throughput (>100 events per second) flow cytometry measurements [233–236]. The demerit of these nonlinear techniques is that their signal is often strongly dependent on the used systems, which renders generalizations of the results challenging. In Figure 5.8 a) Raman spectra of different white blood cells are depicted. The differences in their spectra allow their classification and determination of their ratio occurring in blood. These information can help diagnose infectious diseases. For large heterogeneous samples, such as cells in blood, large numbers of cells are needed for meaningful statistics, rendering Raman spectroscopy on single cells impractical. In panel b) the spectra of a monocyte cell (THP-1) taken with Raman and FRS instruments are depicted. Due to the selection rules vibrational modes of molecules are either Raman or IR active and thus their corresponding spectra contain complimentary information. Furthermore the complexity of the spectra is comparable, implying a similar capability for classification. The large dynamic range of FRS bears the potential for short integration times, while maintaining capabilities for cell classification. In the following a rapid scanning technique, which was implemented on the presented instrument, is detailed.

5.2.1 Fast scan

Rapid scanning of the delay allows to resolve short events in time and can improve the measurement quality, as noise sources much lower in their characteristic frequencies than the scan repetition rate appear to be frozen. For pulsed laser sources the highest sensible acquisition rate is the repetition rate of the source, so that every single pulse yields a new measurement. Such single-shot acquisitions of the waveform are essential for example in the context of Free-Electron Lasers where the high intensities result in irreversible physical and chemical processes. The omission of a scan over several pulses is also beneficial for laser systems with a short-lived waveform stability or low repetition rates. The challenge for single-shot acquisition is to map the delay onto another dimension and retain a sufficient time resolution and scanning range (or in the frequency picture a sufficient bandwidth and resolution). Spatial encoding of the delay has been successfully demonstrated for THz-radiation by employing a non-collinear geometry [237]. Spectral encoding using chirped pulses has historically suffered from a limited time resolution, but recently a new approach has shown promise to resolve this issue [238].

In order to retain the achieved sensitivity of the here developed EOS setup we chose to implement a rapid scan of the delay axis. The previously used mechanical delay stages are often limited in their scan rates by their mass and inertia. Different delay techniques for scanning over distances on the order of millimeters at multi-kHz rates have been established such as acousto-optic delay lines [239] or oscillators with a controlled offset of their repetition rates [240, 241]. Here we employ a Sonotrode that generates a longitudinal standing wave in a rod by applying a sinusoidal voltage on a piezo at a frequency of 19 kHz. This approach was demonstrated for rapid FTIR and FRS measurements in [242, 243] and was implemented and characterized together with Yannick Münzenmaier during his MSc thesis.

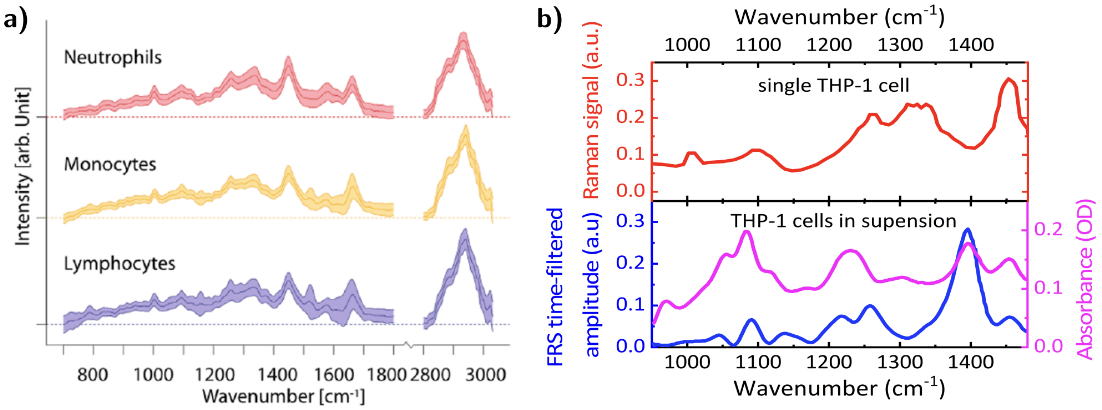

Figure 5.8: Typical Raman and FRS spectra of single white blood cells a) image taken from [234]. b) spectra taken from [55, 244]

The typical displacement of the Sonotrode is on the order of 60-130 μm. The realized scan length can be adjusted by the number of passes over the Sonotrode. Samples in a

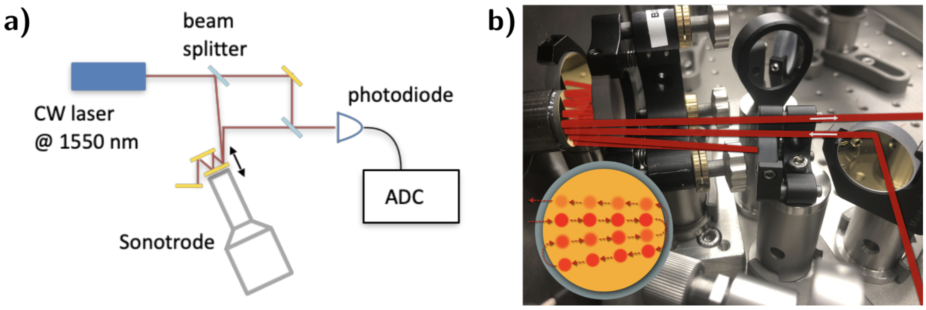

Figure 5.9: Sonotrode setup. a) Schematic of Michelson interferometer. b) Pattern of the gate pulse on the Sonotrode mirror together with experimental realization.

liquid environment have typically their smallest spectral features on the order of 10 cm^{-1}. This corresponds to a scan length of around 1 mm. In order to minimize losses a mirror is glued to the surface of the Sonotrode. The sinusoidal movement of the Sonotrode surface results in a nonlinear delay axis and must be tracked separately. For this purpose a Michelson interferometer is implemented with a CW-light source. In one interferometer arm the Sonotrode setup is included (see Figure 5.9) and the resulting interferogram after recombination allows the reconstruction of the delay. Here each single laser pulse of the 50 MHz pulse train is recorded in order to resolve the waveform under the Niquist-sampling limit. In Figure 5.10 an example of the measured data is shown[4].

5.2.2 Performance

The performance of the fast scan technique can be characterized by analyzing the averaging of consecutive traces. For this purpose the Allan deviation $\sigma_y(\tau)$ is used as a metric. Here, the trace is divided into parts of equal length y_n and the Allan deviation can be calculated with

$$\sigma_y(\tau)^2 = \frac{1}{2}\left\langle (\bar{y}_{n+1} - \bar{y}_n)^2 \right\rangle . \tag{5.10}$$

Where, $\bar{y}_n$ denotes the average value and $\langle .. \rangle$ the expectation operator. In Figure 5.11 the Allan deviation in the time domain and spectral domain is shown together with the expected statistical averaging behavior of $T^{-0.5}$ in the dashed line. Two cases are indicated, where either each individual trace was normalized (orange) or the traces are divided by the mean of the maxima (blue). In orange mostly statistical averaging is observed for more than 100 ms, except for a peak around 3 ms. This peak most likely stems from mechanical vibrations impacting the in-coupling of the photonic crystal fiber and thus the subsequent nonlinear processes and their resulting spectra. This vibrational noise manifests more strongly when each trace is not normalized (blue). In the spectral domain this signifies a SNR of around 350 for an integration time of only around 1 ms.

---

[4] The delay extraction and trace cutting was performed with a modified Labview code written by Alexander Weigel and Patrik Karandušovský

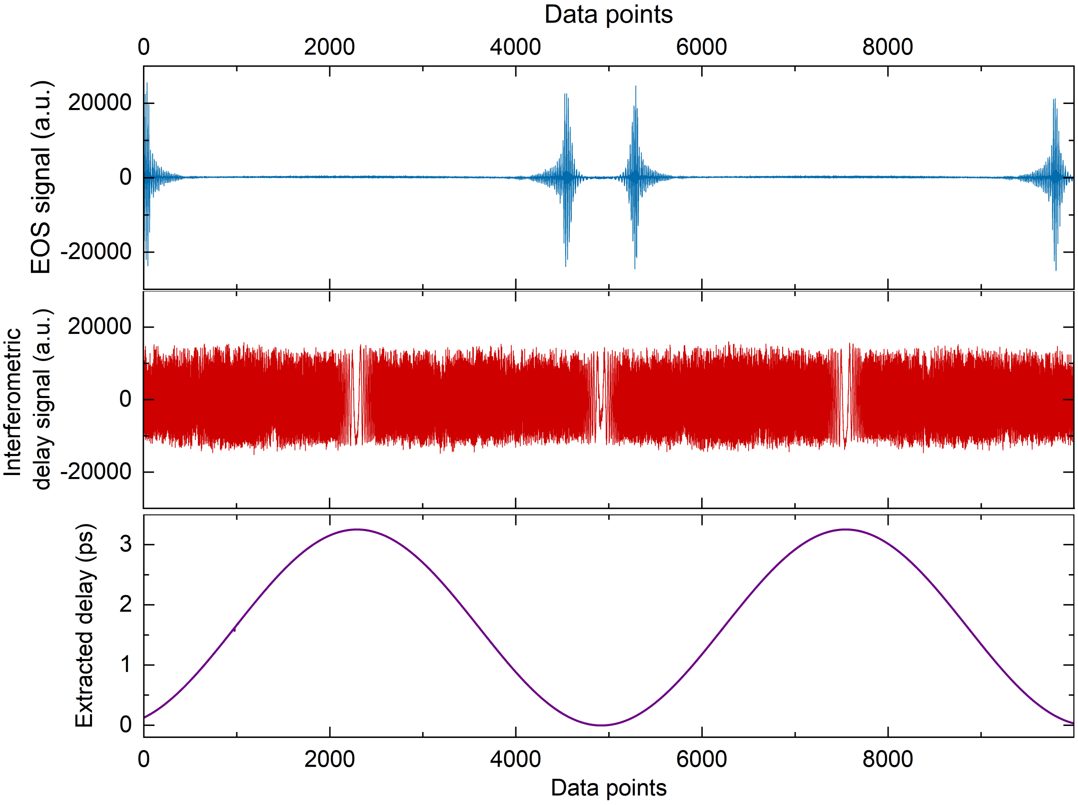

Figure 5.10: Example data recorded with the Sonotrode scan. Top: EOS traces in forward and backward direction. Middle: Interferogram of delay axis. Bottom: Extracted sinusoidal delay.

The relevant intensity dynamic ranges (normalized to blocked MIR beam) are shown in Figure 5.12. In red the result of the slow scan described in the chapter 4 is shown together with the expected curve for statistical averaging for only 1 ms average time. This dashed red line indicates the achievable dynamic range when only a reduced averaging time under statistical averaging is required. The gate pulse power is attenuated due to absorption from the additional dozens of reflections on metal mirrors in the fast scan setup. Additionally the MIR power was weaker, resulting in the blue curves. The dashed blue line is for the same MIR power as the dashed red line, approaching the ideal performance. In order to estimate the performance in a biological application the expected dynamic range is plotted for two different sample thickness. For a measurement time of 1 ms and a sample thickness of 30 μm the expected SNR of the spectral amplitude is above 1000 for a spectral range of over 400 cm^{-1}.

The current implementation of fast scan FRS paves the way to measuring thousands of high-SNR spectra per second. It seems most suitable for the implementation of high-throughput label-free flow cytometry, allowing for classification of cells in large numbers. One application of such a high-throughput system could be the monitoring of the occur-

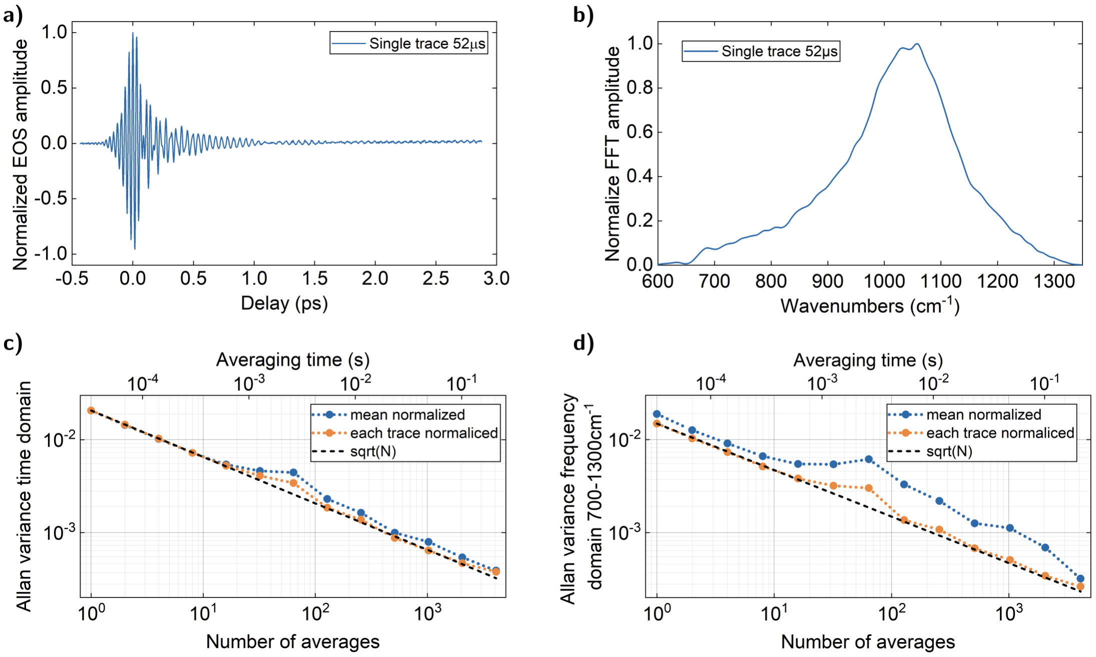

Figure 5.11: Allan deviation in time and frequency domain for scans that average forward and backward traces. a) Time domain signal b) Amplitude of the Fourier transform of a). c) Allan deviation of whole EOS trace in the time domain. d) Allan deviation of the wavenumber window 700-1300 cm^{-1}.

rence of low abundance circulating tumor cells in peripheral blood [245]. Another exciting prospect is the search for new phenotype definitions in conditions such as inflammation, infection or sepsis based on leukocyte activation profiles. Label-free broadband Raman vibrational spectroscopy has recently shown a true potential for this research direction [246]. However, the cross-section of the Raman interactions used in this work has so far limited the throughput to around one cell per second [234], thus severely limiting the applicability to real word settings.

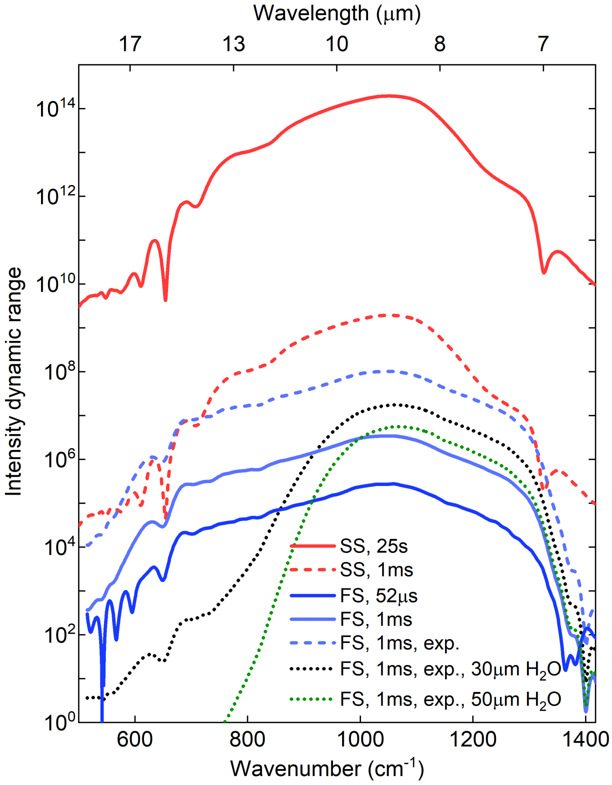

Figure 5.12: Measured intensity dynamic ranges with slow scan (SS) and fast scan (FS) as well as expected performances (dashed lines) for several integration times and a resolution of 10 cm^{-1}.

Bibliography

[1] Philipp E Geyer et al. "Revisiting biomarker discovery by plasma proteomics". In: *Molecular Systems Biology* 13.9 (2017), p. 942. ISSN: 1744-4292. DOI: `10.15252/msb.20156297`.

[2] Jorge Pereira et al. "Breath Analysis as a Potential and Non-Invasive Frontier in Disease Diagnosis: An Overview". In: *Metabolites* 5.1 (Jan. 2015), pp. 3–55. ISSN: 2218-1989. DOI: `10.3390/metabo5010003`.

[3] Wolfgang Demtröder. *Molecular Physics*. Berlin: Wiley-VCH Verlag GmbH, 2005. ISBN: 978-3-527-40566-4.

[4] Andreas Barth and Parvez. I Haris. *Biological and Biomedical Infrared Spectroscopy, Advances in Biomedical Spectroscopy No. v. 2*. Amsterdam: IOS Press, 2011. ISBN: 1875-0656.

[5] Peter Lasch and Janina Kneipp. *Biomedical Vibrational Spectroscopy*. Wiley-Interscience, 2008. ISBN: 978-0-470-22945-3.

[6] Peter R. Griffiths and James A. De Haseth. *Fourier Transform Infrared Spectrometry*. 2nd. Wiley, 2007. ISBN: 978-0-471-19404-0.

[7] Peter Hamm and Martin Zanni. *Concepts and Methods of 2D Infrared Spectroscopy*. Cambridge University Press, 2011. ISBN: 9780511675935.

[8] Matthew J. Baker et al. "Developing and understanding biofluid vibrational spectroscopy: A critical review". In: *Chemical Society Reviews* 45.7 (2016), pp. 1803–1818. ISSN: 14604744. DOI: `10.1039/c5cs00585j`.

[9] Carsten Kötting and Klaus Gerwert. "Proteins in action monitored by time-resolved FTIR spectroscopy". In: *ChemPhysChem* 6.5 (2005), pp. 881–888. ISSN: 14394235. DOI: `10.1002/cphc.200400504`.

[10] A. Rogalski. "History of infrared detectors". In: *Opto-electronics Review* 20.3 (2012), pp. 279–308. ISSN: 18963757. DOI: `10.2478/s11772-012-0037-7`.

[11] James Doherty, Gianfelice Cinque, and Peter Gardner. "Single-cell analysis using Fourier transform infrared microspectroscopy". In: *Applied Spectroscopy Reviews* 52.6 (2017), pp. 560–587. DOI: `10.1080/05704928.2016.1250214`.

[12] Gianfelice Cinque, Mark D. Frogley, and Riccardo Bartolini. "Far-IR/THz spectral characterization of the coherent synchrotron radiation emission at diamond IR beamline B22". In: *Rendiconti Lincei* 22.SUPPL. 1 (2011). ISSN: 20374631. DOI: `10.1007/s12210-011-0149-x`.

[13] Miriam Serena Vitiello et al. "Quantum cascade lasers: 20 years of challenges". In: *Optics Express* 23.4 (2015), p. 5167. ISSN: 1094-4087. DOI: `10.1364/oe.23.005167`.

[14] M. Brandstetter et al. "Direct determination of glucose, lactate and triglycerides in blood serum by a tunable quantum cascade laser-based mid-IR sensor". In: *Applied Physics B: Lasers and Optics* 110.2 (2013), pp. 233–239. ISSN: 09462171. DOI: `10.1007/s00340-012-5080-z`.

[15] Andreas Schwaighofer, Markus Brandstetter, and Bernhard Lendl. "Quantum cascade lasers (QCLs) in biomedical spectroscopy". In: *Chemical Society Reviews* 46.19 (2017), pp. 5903–5924. ISSN: 14604744. DOI: `10.1039/c7cs00403f`.

[16] Christopher K. Akhgar et al. "The Next Generation of IR Spectroscopy: EC-QCL-Based Mid-IR Transmission Spectroscopy of Proteins with Balanced Detection". In: *Analytical Chemistry* 92.14 (2020), pp. 9901–9907. ISSN: 15206882. DOI: `10.1021/acs.analchem.0c01406`.

[17] K. Haase et al. "Advancements in quantum cascade laser-based infrared microscopy of aqueous media". In: *Faraday Discussions* 187 (2016), pp. 119–134. ISSN: 13645498. DOI: `10.1039/c5fd00177c`.

[18] Katharina Haase et al. "Real-time mid-infrared imaging of living microorganisms". In: *Journal of Biophotonics* 9.1-2 (2016), pp. 61–66. ISSN: 18640648. DOI: `10.1002/jbio.201500264`.

[19] Andreas Schwaighofer et al. "Beyond Fourier Transform Infrared Spectroscopy: External Cavity Quantum Cascade Laser-Based Mid-infrared Transmission Spectroscopy of Proteins in the Amide i and Amide II Region". In: *Analytical Chemistry* 90.11 (2018), pp. 7072–7079. ISSN: 15206882. DOI: `10.1021/acs.analchem.8b01632`.

[20] Zhenhui Du et al. "Mid-infrared tunable laser-based broadband fingerprint absorption spectroscopy for trace gas sensing: A review". In: *Applied Sciences (Switzerland)* 9.2 (2019), pp. 1–33. ISSN: 20763417. DOI: `10.3390/app9020338`.

[21] Murad Omar, Juan Aguirre, and Vasilis Ntziachristos. "Optoacoustic mesoscopy for biomedicine". In: *Nature Biomedical Engineering* 3.5 (2019), pp. 354–370. ISSN: 2157-846X. DOI: `10.1038/s41551-019-0377-4`.

[22] Miguel A. Pleitez et al. "Label-free metabolic imaging by mid-infrared optoacoustic microscopy in living cells". In: *Nature Biotechnology* 38.3 (Mar. 2020), pp. 293–296. ISSN: 1087-0156. DOI: `10.1038/s41587-019-0359-9`.

[23] Th Udem, R. Holzwarth, and T. W. Hänsch. "Optical frequency metrology". In: *Nature* 416.6877 (Mar. 2002), pp. 233–237. ISSN: 0028-0836. DOI: `10.1038/416233a`.

[24] Fritz Keilmann, Christoph Gohle, and Ronald Holzwarth. “Time-domain mid-infrared frequency-comb spectrometer”. In: *Optics Letters* 29.13 (July 2004), p. 1542. ISSN: 0146-9592. DOI: `10.1364/OL.29.001542`.

[25] Nathan R. Newbury, Ian Coddington, and William Swann. “Sensitivity of coherent dual-comb spectroscopy”. In: *Optics Express* 18.8 (2010), p. 7929. ISSN: 1094-4087. DOI: `10.1364/oe.18.007929`.

[26] Birgitta Bernhardt et al. “Cavity-enhanced dual-comb spectroscopy”. In: *Nature Photonics* 4.1 (2010), pp. 55–57. ISSN: 17494885. DOI: `10.1038/nphoton.2009.217`.

[27] Abijith S. Kowligy et al. “Infrared electric field sampled frequency comb spectroscopy”. In: *Science Advances* 5.6 (June 2019), eaaw8794. ISSN: 2375-2548. DOI: `10.1126/sciadv.aaw8794`.

[28] A. V. Muraviev et al. “Massively parallel sensing of trace molecules and their isotopologues with broadband subharmonic mid-infrared frequency combs”. In: *Nature Photonics* 12.4 (2018), pp. 209–214. ISSN: 17494893. DOI: `10.1038/s41566-018-0135-2`.

[29] Bachana Lomsadze and Steven T. Cundiff. “Frequency combs enable rapid and high-resolution multidimensional coherent spectroscopy”. In: *Science* 357.6358 (Sept. 2017), pp. 1389–1391. ISSN: 0036-8075. DOI: `10.1126/science.aao1090`.

[30] Johannes Hillbrand et al. “Mode-locked short pulses from an 8 μm wavelength semiconductor laser”. In: *Nature Communications* 11.1 (2020), pp. 1–7. ISSN: 20411723. DOI: `10.1038/s41467-020-19592-1`.

[31] Philipp Täschler et al. “Femtosecond pulses from a mid-infrared quantum cascade laser”. In: *Nature Photonics* 15.12 (2021), pp. 919–924. ISSN: 17494893. DOI: `10.1038/s41566-021-00894-9`.

[32] Gustavo Villares et al. “Dual-comb spectroscopy based on quantum-cascade-laser frequency combs”. In: *Nature Communications* 5 (2014), pp. 1–3. ISSN: 20411723. DOI: `10.1038/ncomms6192`.

[33] Matthew Singleton, Mattias Beck, and Jérôme Faist. “Pulses from a mid-infrared quantum cascade laser frequency comb using an external compressor”. In: *arXiv* 36.6 (2019), pp. 1676–1683. ISSN: 23318422. DOI: `10.1364/josab.36.001676`.

[34] Peng Li et al. “Sub-100 fs passively mode-locked holmium-doped fiber oscillator operating at 206 μm”. In: *Optics Letters* 39.24 (Dec. 2014), p. 6859. ISSN: 0146-9592. DOI: `10.1364/OL.39.006859`.

[35] Jinwei Zhang et al. “High-Power, High-Efficiency Tm:YAG and Ho:YAG Thin-Disk Lasers”. In: *Laser & Photonics Reviews* 12.3 (Mar. 2018), p. 1700273. ISSN: 18638880. DOI: `10.1002/lpor.201700273`.

[36] Fabian Stutzki et al. “152 W average power Tm-doped fiber CPA system”. In: *Optics Letters* 39.16 (Aug. 2014), p. 4671. ISSN: 0146-9592. DOI: `10.1364/OL.39.004671`.

[37] Nathalie Nagl et al. “Directly diode-pumped, Kerr-lens mode-locked, few-cycle Cr:ZnSe oscillator”. In: *Optics Express* 27.17 (Aug. 2019), p. 24445. ISSN: 1094-4087. DOI: `10.1364/OE.27.024445`.

[38] Christian Rosenberg Petersen et al. “Mid-infrared supercontinuum covering the 1.4–13.3 μm molecular fingerprint region using ultra-high NA chalcogenide step-index fibre”. In: *Nature Photonics* 8.11 (Nov. 2014), pp. 830–834. ISSN: 1749-4885. DOI: `10.1038/nphoton.2014.213`.

[39] M. A. Abbas et al. “Fourier transform spectrometer based on high-repetition-rate mid-infrared supercontinuum sources for trace gas detection”. In: *Optics Express* 29.14 (July 2021), p. 22315. ISSN: 1094-4087. DOI: `10.1364/OE.425995`.

[40] Albert Schliesser, Nathalie Picqué, and Theodor W. Hänsch. “Mid-infrared frequency combs”. In: *Nature Photonics* 6.7 (2012), pp. 440–449. ISSN: 17494885. DOI: `10.1038/nphoton.2012.142`.

[41] Viktor Smolski et al. “Half-Watt average power femtosecond source spanning 3–8 µm based on subharmonic generation in GaAs”. In: *Applied Physics B* 124.6 (June 2018), p. 101. ISSN: 0946-2171. DOI: `10.1007/s00340-018-6963-4`.

[42] Marcus Seidel et al. “Multi-watt, multi-octave, mid-infrared femtosecond source”. In: *Science Advances* 4.4 (2018), pp. 1–9. ISSN: 23752548. DOI: `10.1126/sciadv.aaq1526`.

[43] Fritz Keilmann and Sergiu Amarie. “Mid-infrared Frequency Comb Spanning an Octave Based on an Er Fiber Laser and Difference-Frequency Generation”. In: *Journal of Infrared, Millimeter, and Terahertz Waves* 33.5 (May 2012), pp. 479–484. ISSN: 1866-6892. DOI: `10.1007/s10762-012-9894-x`.

[44] I. Pupeza et al. “High-power sub-two-cycle mid-infrared pulses at 100 MHz repetition rate”. In: *Nature Photonics* 9.11 (2015), pp. 721–724. ISSN: 17494893. DOI: `10.1038/nphoton.2015.179`.

[45] Sergey Vasilyev et al. “Super-octave longwave mid-infrared coherent transients produced by optical rectification of few-cycle 2.5-um pulses”. In: *Optica* 6.1 (2019), p. 111. ISSN: 2334-2536. DOI: `10.1364/optica.6.000111`.

[46] Jinwei Zhang et al. “Multi-mW, few-cycle mid-infrared continuum spanning from 500 to 2250 cm-1”. In: *Light: Science and Applications* 7.2 (2018), p. 17180. ISSN: 20477538. DOI: `10.1038/lsa.2017.180`.

[47] Christian Gaida et al. “Watt-scale super-octave mid-infrared intrapulse difference frequency generation”. In: *Light: Science & Applications* 7.1 (Dec. 2018), p. 94. ISSN: 2047-7538. DOI: `10.1038/s41377-018-0099-5`.

[48] Jinwei Zhang et al. “Intra-pulse difference-frequency generation of mid-infrared (2.7–20 μm) by random quasi-phase-matching”. In: *Optics Letters* 44.12 (June 2019), p. 2986. ISSN: 0146-9592. DOI: `10.1364/OL.44.002986`.

[49] Janis A. Valdmanis and G. Mourou. “Subpicosecond Electrooptic Sampling: Principles and Applications”. In: *IEEE Journal of Quantum Electronics* 22.1 (1986), pp. 69–78. ISSN: 15581713. DOI: `10.1109/JQE.1986.1072867`.

[50] Q. Wu and X. C. Zhang. “Free-space electro-optic sampling of terahertz beams”. In: *Applied Physics Letters* 67.1995 (1995), p. 3523. ISSN: 00036951. DOI: `10.1063/1.114909`.

[51] Q Wu and X.-C. Zhang. “Free-space electro-optics sampling of mid-infrared pulses”. In: *Applied Physics Letters* 71.10 (Sept. 1997), pp. 1285–1286. ISSN: 0003-6951. DOI: `10.1063/1.119873`.

[52] G. Gallot and D. Grischkowsky. “Electro-optic detection of terahertz radiation”. In: *Journal of the Optical Society of America B* 16.8 (1999), p. 1204. ISSN: 0740-3224. DOI: `10.1364/josab.16.001204`.

[53] P. Sulzer et al. “Determination of the electric field and its Hilbert transform in femtosecond electro-optic sampling”. In: *Physical Review A* 101.3 (2020), pp. 1–17. ISSN: 24699934. DOI: `10.1103/PhysRevA.101.033821`.

[54] Marinus Huber et al. “Optimum Sample Thickness for Trace Analyte Detection with Field-Resolved Infrared Spectroscopy”. In: *Analytical Chemistry* 92.11 (2020), pp. 7508–7514. ISSN: 15206882. DOI: `10.1021/acs.analchem.9b05744`.

[55] Ioachim Pupeza et al. “Field-resolved infrared spectroscopy of biological systems”. In: *Nature* 577.7788 (2020), pp. 52–59. ISSN: 14764687. DOI: `10.1038/s41586-019-1850-7`.

[56] T. H. Maiman. “Stimulated Optical Radiation in Ruby”. In: *Nature* 187.4736 (Aug. 1960), pp. 493–494. ISSN: 0028-0836. DOI: `10.1038/187493a0`.

[57] H. A. Haus, J. G. Fujimoto, and E. P. Ippen. “Structures for additive pulse mode locking”. In: *Journal of the Optical Society of America B* 8.10 (1991), p. 2068. ISSN: 0740-3224. DOI: `10.1364/josab.8.002068`.

[58] Ursula Keller et al. “Semiconductor saturable absorber mirrors (SESAM’s) for femtosecond to nanosecond pulse generation in solid-state lasers”. In: *IEEE Journal on Selected Topics in Quantum Electronics* 2.3 (1996), pp. 435–451. ISSN: 1077260X. DOI: `10.1109/2944.571743`.

[59] E. P. Ippen. “Principles of passive mode locking”. In: *Applied Physics B Laser and Optics* 58.3 (1994), pp. 159–170. ISSN: 09462171. DOI: `10.1007/BF01081309`.

[60] I. Pinto, A. Sasso, and S. Tosca. “Exact volterra-series computation of nonlinear polarization in optical media”. In: *Il Nuovo Cimento B* 70.1 (1982), pp. 31–38. ISSN: 03693554. DOI: `10.1007/BF02814008`.

[61] R.W. Boyd. *Nonlinear Optics*. 3rd. London: Academic PRess, 2008. ISBN: 9780123694706.

[62] M. Bass, P. A. Franken, and J. F. Ward. “Optical rectification”. In: *Physical Review* 138.2A (1965), pp. 28–31. ISSN: 0031899X. DOI: `10.1103/PhysRev.138.A534`.

[63] J. E. Midwinter and J. Warner. “The effects of phase matching method and of uniaxial crystal symmetry on the polar distribution of second-order non-linear optical polarization”. In: *British Journal of Applied Physics* 16.8 (1965), pp. 1135–1142. ISSN: 05083443. DOI: `10.1088/0508-3443/16/8/312`.

[64] B. C. Stuart et al. “Laser-induced damage in dielectrics with nanosecond to subpicosecond pulses”. In: *Physical Review Letters* 74.12 (1995), pp. 2248–2251. ISSN: 00319007. DOI: `10.1103/PhysRevLett.74.2248`.

[65] Alexander A. Manenkov. “Fundamental mechanisms of laser-induced damage in optical materials: today’s state of understanding and problems”. In: *Optical Engineering* 53.1 (2014), p. 010901. ISSN: 0091-3286. DOI: `10.1117/1.oe.53.1.010901`.

[66] Gintaras Tamošauskas et al. “Transmittance and phase matching of BBO crystal in the 3-5 μm range and its application for the characterization of mid-infrared laser pulses”. In: *Optical Materials Express* 8.6 (2018), p. 1410. ISSN: 21593930. DOI: `10.1364/ome.8.001410`.

[67] C. Manzoni and G. Cerullo. “Design criteria for ultrafast optical parametric amplifiers”. In: *Journal of Optics (United Kingdom)* 18.10 (2016). ISSN: 20408986. DOI: `10.1088/2040-8978/18/10/103501`.

[68] Sang-Gyu Park, Michael R. Melloch, and Andrew M. Weiner. “Comparison of terahertz waveforms measured by electro-optic and photoconductive sampling”. In: *Applied Physics Letters* 73.22 (Nov. 1998), pp. 3184–3186. ISSN: 0003-6951. DOI: `10.1063/1.122712`.

[69] Philip C. D. Hobbs. “Ultrasensitive laser measurements without tears”. In: *Applied Optics* 36.4 (1997), p. 903. ISSN: 0003-6935. DOI: `10.1364/ao.36.000903`.

[70] P. Kwee, B. Willke, and K. Danzmann. “New concepts and results in laser power stabilization”. In: *Applied Physics B: Lasers and Optics* 102.3 (2011), pp. 515–522. ISSN: 09462171. DOI: `10.1007/s00340-011-4399-1`.

[71] Hermann Haken and Hans Christoph Wolf. *Molecular Physics and Elements of Quantum Chemestry.* Second edi. Springer Berlin Heidelberg, 2005. ISBN: 3642074006.

[72] A. Laubereau and W. Kaiser. “Vibrational dynamics of liquids and solids investigated by picosecond light pulses”. In: *Reviews of Modern Physics* 50.3 (1978), pp. 607–665. ISSN: 00346861. DOI: `10.1103/RevModPhys.50.607`.

[73] I.E. Gordon et al. “The HITRAN2020 molecular spectroscopic database”. In: *Journal of Quantitative Spectroscopy and Radiative Transfer* 277 (Jan. 2022), p. 107949. ISSN: 00224073. DOI: `10.1016/j.jqsrt.2021.107949`.

[74] Thomas G. Mayerhöfer and Jürgen Popp. “Beer’s law derived from electromagnetic theory”. In: *Spectrochimica Acta - Part A: Molecular and Biomolecular Spectroscopy* 215.March (2019), pp. 345–347. ISSN: 13861425. DOI: `10.1016/j.saa.2019.02.103`.

[75] A. A. Lanin et al. “Time-domain spectroscopy in the mid-infrared”. In: *Scientific Reports* 4.1 (May 2015), p. 6670. ISSN: 2045-2322. DOI: `10.1038/srep06670`.

[76] Hans U. Stauffer et al. "Broadband, background-free methane absorption in the mid-infrared". In: *Optics Express* 29.13 (2021), p. 21011. ISSN: 10944087. DOI: `10.1364/oe.430315`.

[77] Theresa Buberl et al. "Achromatic interferometric subtraction of optical fields". In: *Optics InfoBase Conference Papers* Part F140-.3 (2019), pp. 2432–2443.

[78] Teemu Tomberg et al. "Background-free broadband absorption spectroscopy based on interferometric suppression with a sign-inverted waveform". In: *Optica* 6.2 (Feb. 2019), p. 147. ISSN: 2334-2536. DOI: `10.1364/OPTICA.6.000147`.

[79] R.V. Kochanov et al. "HITRAN Application Programming Interface (HAPI): A comprehensive approach to working with spectroscopic data". In: *Journal of Quantitative Spectroscopy and Radiative Transfer* 177 (July 2016), pp. 15–30. ISSN: 00224073. DOI: `10.1016/j.jqsrt.2016.03.005`.

[80] C. Gaida et al. "High-power frequency comb at 2 μm wavelength emitted by a Tm-doped fiber laser system". In: *Optics Letters* 43.21 (Nov. 2018), p. 5178. ISSN: 0146-9592. DOI: `10.1364/OL.43.005178`.

[81] Theodor W. Hänsch. "Nobel Lecture: Passion for precision". In: *Reviews of Modern Physics* 78.4 (Nov. 2006), pp. 1297–1309. ISSN: 0034-6861. DOI: `10.1103/RevModPhys.78.1297`.

[82] Scott A. Diddams, Leo Hollberg, and Vela Mbele. "Molecular fingerprinting with the resolved modes of a femtosecond laser frequency comb". In: *Nature* 445.7128 (2007), pp. 627–630. ISSN: 14764687. DOI: `10.1038/nature05524`.

[83] Michael J. Thorpe et al. "Broadband Cavity Ringdown Spectroscopy for Sensitive and Rapid Molecular Detection". In: *Science* 311.5767 (Mar. 2006), pp. 1595–1599. ISSN: 0036-8075. DOI: `10.1126/science.1123921`.

[84] Zenghu Chang and P. Corkum. "Attosecond photon sources: the first decade and beyond [Invited]". In: *Journal of the Optical Society of America B* 27.11 (Nov. 2010), B9. ISSN: 0740-3224. DOI: `10.1364/JOSAB.27.0000B9`.

[85] Scott A. Diddams. "The evolving optical frequency comb [Invited]". In: *Journal of the Optical Society of America B* 27.11 (Nov. 2010), B51. ISSN: 0740-3224. DOI: `10.1364/JOSAB.27.000B51`.

[86] Nathan R. Newbury. "Searching for applications with a fine-tooth comb". In: *Nature Photonics* 5.4 (2011), pp. 186–188. ISSN: 17494885. DOI: `10.1038/nphoton.2011.38`.

[87] Sabine Keiber et al. "Electro-optic sampling of near-infrared waveforms". In: *Nature Photonics* 10.3 (2016), pp. 159–162. ISSN: 17494893. DOI: `10.1038/nphoton.2015.269`.

[88] Florian Tauser, Alfred Leitenstorfer, and Wolfgang Zinth. “Amplified femtosecond pulses from an Er:fiber system: Nonlinear pulse shortening and selfreferencing detection of the carrier-envelope phase evolution”. In: *Optics Express* 11.6 (Mar. 2003), p. 594. ISSN: 1094-4087. DOI: `10.1364/OE.11.000594`.

[89] Andrew Klose et al. “Tunable, stable source of femtosecond pulses near 2 μm via supercontinuum of an Erbium mode-locked laser”. In: *Optics Express* 22.23 (2014), p. 28400. ISSN: 10944087. DOI: `10.1364/oe.22.028400`.

[90] John M. Dudley, Goëry Genty, and Stéphane Coen. “Supercontinuum generation in photonic crystal fiber”. In: *Reviews of Modern Physics* 78.4 (2006), pp. 1135–1184. ISSN: 00346861. DOI: `10.1103/RevModPhys.78.1135`.

[91] Henry Timmers et al. “Molecular fingerprinting with bright, broadband infrared frequency combs”. In: *Optica* 5.6 (June 2018), p. 727. ISSN: 2334-2536. DOI: `10.1364/OPTICA.5.000727`.

[92] T. Saule et al. “Phase-stable, multi-µJ femtosecond pulses from a repetition-rate tunable Ti:Sa-oscillator-seeded Yb-fiber amplifier”. In: *Applied Physics B* 123.1 (Jan. 2017), p. 17. ISSN: 0946-2171. DOI: `10.1007/s00340-016-6611-9`.

[93] O. Pronin et al. “High-power multi-megahertz source of waveform-stabilized few-cycle light”. In: *Nature Communications* 6.1 (Nov. 2015), p. 6988. ISSN: 2041-1723. DOI: `10.1038/ncomms7988`.

[94] Alexandre Parriaux, Kamal Hammani, and Guy Millot. “Two-micron all-fibered dual-comb spectrometer based on electro-optic modulators and wavelength conversion”. In: *Communications Physics* 1.1 (Dec. 2018), p. 17. ISSN: 2399-3650. DOI: `10.1038/s42005-018-0017-4`.

[95] Jane Hodgkinson and Ralph P. Tatam. “Optical gas sensing: A review”. In: *Measurement Science and Technology* 24.1 (2013). ISSN: 13616501. DOI: `10.1088/0957-0233/24/1/012004`.

[96] Kevin F. Lee et al. “Midinfrared frequency comb by difference frequency of erbium and thulium fiber lasers in orientation-patterned gallium phosphide”. In: *Optics Express* 25.15 (2017), p. 17411. ISSN: 10944087. DOI: `10.1364/oe.25.017411`.

[97] Oguzhan Kara et al. “Dual-comb spectroscopy in the spectral fingerprint region using OPGaP optical parametric oscillators”. In: *Optics Express* 25.26 (Dec. 2017), p. 32713. ISSN: 1094-4087. DOI: `10.1364/OE.25.032713`.

[98] H. Pires et al. “Ultrashort pulse generation in the mid-IR”. In: *Progress in Quantum Electronics* 43 (2015), pp. 1–30. ISSN: 00796727. DOI: `10.1016/j.pquantelec.2015.07.001`.

[99] C. Gaida et al. “Self-compression in a solid fiber to 24 MW peak power with few-cycle pulses at 2 μm wavelength”. In: *Optics Letters* 40.22 (2015), p. 5160. ISSN: 0146-9592. DOI: `10.1364/ol.40.005160`.

[100] Florian Adler and Scott A. Diddams. “High-power, hybrid Er:fiber/Tm:fiber frequency comb source in the 2 μm wavelength region”. In: *Optics Letters* 37.9 (May 2012), p. 1400. ISSN: 0146-9592. DOI: `10.1364/OL.37.001400`.

[101] Martin Gebhardt et al. “Impact of atmospheric molecular absorption on the temporal and spatial evolution of ultra-short optical pulses”. In: *Optics Express* 23.11 (2015), p. 13776. ISSN: 1094-4087. DOI: `10.1364/oe.23.013776`.

[102] Jens Limpert et al. “Yb-doped large-pitch fibres: Effective single-mode operation based on higher-order mode delocalisation”. In: *Light: Science and Applications* 1.APRIL (2012), pp. 1–5. ISSN: 20477538. DOI: `10.1038/lsa.2012.8`.

[103] S. V. Chernikov et al. “Soliton pulse compression in dispersion-decreasing fiber”. In: *Optics Letters* 18.7 (1993), p. 476. ISSN: 0146-9592. DOI: `10.1364/ol.18.000476`.

[104] John C. Travers and Michael H. Frosz. *Supercontinuum Generation in Optical Fibers*. Ed. by J. M. Dudley and J. R. Taylor. Cambridge University Press, Apr. 2010. ISBN: 9780521514804. DOI: `10.1017/CBO9780511750465`.

[105] Nathan R Newbury and William C Swann. “Low-noise fiber-laser frequency combs (Invited)”. In: *Journal of the Optical Society of America B* 24.8 (Aug. 2007), p. 1756. ISSN: 0740-3224. DOI: `10.1364/JOSAB.24.001756`.

[106] C.-C. Lee et al. “Stabilization of carrier-envelope phase with MHz bandwidth by an intra-cavity graphene electro-optic modulator”. In: *Lasers, Sources, and Related Photonic Devices*. Vol. 37. 15. Washington, D.C.: OSA, 2012, AM6A.5. ISBN: 978-1-55752-933-6. DOI: `10.1364/ASSP.2012.AM6A.5`.

[107] Hirotoshi Nagata. “Progress and problems in reliability of Ti:LiNbO3 optical intensity modulators”. In: *Optical Engineering* 34.11 (Nov. 1995), p. 3284. ISSN: 0091-3286. DOI: `10.1117/12.212908`.

[108] Jean Paul Salvestrini et al. “Analysis and control of the dc drift in LiNbO3-based Mach-Zehnder modulators”. In: *Journal of Lightwave Technology* 29.10 (2011), pp. 1522–1534. ISSN: 07338724. DOI: `10.1109/JLT.2011.2136322`.

[109] Rick Trebino et al. “Measuring ultrashort laser pulses in the time-frequency domain using frequency-resolved optical gating”. In: *Review of Scientific Instruments* 68.9 (1997), pp. 3277–3295. ISSN: 00346748. DOI: `10.1063/1.1148286`.

[110] Miguel Miranda et al. “Characterization of broadband few-cycle laser pulses with the d-scan technique”. In: *Optics Express* 20.17 (2012), p. 18732. ISSN: 1094-4087. DOI: `10.1364/oe.20.018732`.

[111] T. P. Butler et al. “Watt-scale 50-MHz source of single-cycle waveform-stable pulses in the molecular fingerprint region”. In: *Optics Letters* 44.7 (Apr. 2019), p. 1730. ISSN: 0146-9592. DOI: `10.1364/OL.44.001730`.

[112] Tobias Kampfrath et al. “Strongly coupled optical phonons in the ultrafast dynamics of the electronic energy and current relaxation in graphite”. In: *Physical Review Letters* 95.18 (2005), pp. 26–29. ISSN: 00319007. DOI: `10.1103/PhysRevLett.95.187403`.

[113] R. Huber et al. “How many-particle interactions develop after ultrafast excitation of an electron–hole plasma”. In: *Nature* 414.6861 (Nov. 2001), pp. 286–289. ISSN: 0028-0836. DOI: `10.1038/35104522`.

[114] C. Schmidt et al. “Signatures of transient Wannier-Stark localization in bulk gallium arsenide”. In: *Nature Communications* 9.1 (2018). ISSN: 20411723. DOI: `10.1038/s41467-018-05229-x`.

[115] Andreas Barth and Parvez. I Haris. *Biological and Biomedical Infrared Spectroscopy.* IOS Press, 2009. ISBN: 978-1-60750-457-3.

[116] F. Junginger et al. “Single-cycle multiterahertz transients with peak fields above 10 MV/cm”. In: *Optics Letters* 35.15 (2010), p. 2645. ISSN: 0146-9592. DOI: `10.1364/ol.35.002645`.

[117] Cristian Manzoni et al. “Single-shot detection and direct control of carrier phase drift of midinfrared pulses”. In: *Optics Letters* 35.5 (Mar. 2010), p. 757. ISSN: 0146-9592. DOI: `10.1364/OL.35.000757`.

[118] C. Riek et al. “Direct sampling of electric-field vacuum fluctuations”. In: *Science* 350.6259 (2015), pp. 420–423. ISSN: 10959203. DOI: `10.1126/science.aac9788`.

[119] C. Kübler et al. “Ultrabroadband detection of multi-terahertz field transients with GaSe electro-optic sensors: Approaching the near infrared”. In: *Applied Physics Letters* 85.16 (Oct. 2004), pp. 3360–3362. ISSN: 0003-6951. DOI: `10.1063/1.1808232`.

[120] Valentin Petrov. “Frequency down-conversion of solid-state laser sources to the mid-infrared spectral range using non-oxide nonlinear crystals”. In: *Progress in Quantum Electronics* 42 (2015), pp. 1–106. ISSN: 00796727. DOI: `10.1016/j.pquantelec.2015.04.001`.

[121] Ioachim Pupeza et al. “Field-Resolved Spectroscopy in the Molecular Fingerprint Region”. In: *Conference on Lasers and Electro-Optics (CLEO)/Europe & EQEC.* 2017, p. 1.

[122] Ljiljana Puskar and Ulrich Schade. “The IRIS THz/Infrared Beamline at BESSY II”. In: *Journal of large-scale research facilities JLSRF* 2 (Nov. 2016), A95. ISSN: 2364-091X. DOI: `10.17815/jlsrf-2-95`.

[123] Daniel Gerz et al. “Mid-infrared long-pass filter for high-power applications based on grating diffraction”. In: *Optics Letters* 44.12 (June 2019), p. 3014. ISSN: 0146-9592. DOI: `10.1364/OL.44.003014`.

[124] Matthias Knorr et al. “Phase-locked multi-terahertz electric fields exceeding 13 MV/cm at a 190 kHz repetition rate”. In: *Optics Letters* 42.21 (2017), p. 4367. ISSN: 0146-9592. DOI: `10.1364/ol.42.004367`.

[125] D. Brida et al. “Two-optical-cycle pulses in the mid-infrared from an optical parametric amplifier”. In: *Optics Letters* 33.24 (2008), p. 2901. ISSN: 0146-9592. DOI: `10.1364/ol.33.002901`.

[126] C. Gaida et al. “Ultrafast thulium fiber laser system emitting more than 1 kW of average power”. In: *Optics Letters* 43.23 (2018), p. 5853. ISSN: 0146-9592. DOI: `10.1364/ol.43.005853`.

[127] Kilian Fritsch et al. “All-solid-state multipass spectral broadening to sub-20 fs”. In: *Optics Letters* 43.19 (2018), p. 4643. ISSN: 0146-9592. DOI: `10.1364/ol.43.004643`.

[128] T P Butler et al. “Multi-octave spanning, Watt-level ultrafast mid-infrared source”. In: *Journal of Physics: Photonics* 1.4 (Oct. 2019), p. 044006. ISSN: 2515-7647. DOI: `10.1088/2515-7647/ab4976`.

[129] Zanyar Movasaghi, Shazza Rehman, and Dr. Ihtesham ur Rehman. “Fourier Transform Infrared (FTIR) Spectroscopy of Biological Tissues”. In: *Applied Spectroscopy Reviews* 43.2 (Feb. 2008), pp. 134–179. ISSN: 0570-4928. DOI: `10.1080/05704920701829043`.

[130] G. L. Carr. “Resolution limits for infrared microspectroscopy explored with synchrotron radiation”. In: *Review of Scientific Instruments* 72.3 (2001), pp. 1613–1619. ISSN: 00346748. DOI: `10.1063/1.1347965`.

[131] Sergiu Amarie, Thomas Ganz, and Fritz Keilmann. “Mid-infrared near-field spectroscopy”. In: *Optics Express* 17.24 (Nov. 2009), p. 21794. ISSN: 1094-4087. DOI: `10.1364/OE.17.021794`.

[132] Lisa M. Miller and Paul Dumas. “Chemical imaging of biological tissue with synchrotron infrared light”. In: *Biochimica et Biophysica Acta (BBA) - Biomembranes* 1758.7 (July 2006), pp. 846–857. ISSN: 00052736. DOI: `10.1016/j.bbamem.2006.04.010`.

[133] Luca Quaroni. “Infrared microscopy in the study of cellular biochemistry”. In: *Infrared Physics & Technology* 105 (Mar. 2020), p. 102779. ISSN: 13504495. DOI: `10.1016/j.infrared.2018.11.026`.

[134] Sören Kumkar et al. “Femtosecond coherent seeding of a broadband Tm:fiber amplifier by an Er:fiber system”. In: *Optics Letters* 37.4 (2012), p. 554. ISSN: 0146-9592. DOI: `10.1364/ol.37.000554`.

[135] S. Woutersen, U. Emmerichs, and H. J. Bakker. “Femtosecond Mid-IR Pump-Probe Spectroscopy of Liquid Water: Evidence for a Two-Component Structure”. In: *Science* 278.5338 (Oct. 1997), pp. 658–660. ISSN: 0036-8075. DOI: `10.1126/science.278.5338.658`.

[136] Albert Schliesser et al. “Frequency-comb infrared spectrometer for rapid, remote chemical sensing”. In: *Optics Express* 13.22 (2005), p. 9029. ISSN: 1094-4087. DOI: `10.1364/opex.13.009029`.

[137] Jinwei Zhang, Ka Fai Mak, and Oleg Pronin. “Kerr-Lens Mode-Locked 2-μm Thin-Disk Lasers”. In: *IEEE Journal of Selected Topics in Quantum Electronics* 24.5 (Sept. 2018), pp. 1–11. ISSN: 1077-260X. DOI: `10.1109/JSTQE.2018.2814780`.

[138] Peng Wan, Lih-Mei Yang, and Jian Liu. “High power 2 µm femtosecond fiber laser”. In: *Optics Express* 21.18 (2013), p. 21374. ISSN: 10944087. DOI: `10.1364/oe.21.021374`.

[139] Jinendra K. Ranka, Robert S. Windeler, and Andrew J. Stentz. “Visible continuum generation in air–silica microstructure optical fibers with anomalous dispersion at 800 nm”. In: *Optics Letters* 25.1 (Jan. 2000), p. 25. ISSN: 0146-9592. DOI: `10.1364/OL.25.000025`.

[140] Reza Salem et al. “Mid-infrared supercontinuum generation spanning 1.8 octaves using step-index indium fluoride fiber pumped by a femtosecond fiber laser near 2 µm”. In: *Optics Express* 23.24 (2015), p. 30592. ISSN: 10944087. DOI: `10.1364/oe.23.030592`.

[141] Christian Agger et al. “Supercontinuum generation in ZBLAN fibers—detailed comparison between measurement and simulation”. In: *Journal of the Optical Society of America B* 29.4 (Apr. 2012), p. 635. ISSN: 0740-3224. DOI: `10.1364/JOSAB.29.000635`.

[142] Adrea R. Johnson et al. “Octave-spanning coherent supercontinuum generation in a silicon nitride waveguide”. In: *Optics Letters* 40.21 (Nov. 2015), p. 5117. ISSN: 0146-9592. DOI: `10.1364/OL.40.005117`.

[143] T. P. White et al. “Multipole method for microstructured optical fibers I Formulation: errata”. In: *Journal of the Optical Society of America B* 20.7 (July 2003), p. 1581. ISSN: 0740-3224. DOI: `10.1364/JOSAB.20.001581`.

[144] Govind Agrawal. *Nonlinear Fiber Optics*. 2006. ISBN: 9780123695161. DOI: `10.1016/B978-0-12-369516-1.X5000-6`.

[145] *Fiberdesk (www.fiberdesk.com).*

[146] C. L. Hagen, J. W. Walewski, and S. T. Sanders. “Generation of a continuum extending to the midinfrared by pumping ZBLAN fiber with an ultrafast 1550-nm source”. In: *IEEE Photonics Technology Letters* 18.1 (2006), pp. 91–93. ISSN: 10411135. DOI: `10.1109/LPT.2005.860390`.

[147] Jacek Swiderski, Maria Michalska, and Gwenael Maze. “Mid-IR supercontinuum generation in a ZBLAN fiber pumped by a gain-switched mode-locked Tm-doped fiber laser and amplifier system”. In: *Optics Express* 21.7 (2013), p. 7851. ISSN: 10944087. DOI: `10.1364/oe.21.007851`.

[148] Nathalie Nagl et al. “Efficient femtosecond mid-infrared generation based on a Cr:ZnS oscillator and step-index fluoride fibers”. In: *Optics Letters* 44.10 (2019), p. 2390. ISSN: 0146-9592. DOI: `10.1364/ol.44.002390`.

[149] Katsunari Okamoto. *Fundamentals of Optical Waveguides*. New York: Academic Press, 2006. ISBN: 9780125250962.

[150] C.D. Hussey and F. Martinez. “Approximate analytic forms for the propagation characteristics of single-mode optical fibres”. In: *Electronics Letters* 21.23 (1985), p. 1103. ISSN: 00135194. DOI: `10.1049/el:19850783`.

[151] Pratik Shukla, Jonathan Lawrence, and Yu Zhang. “Understanding laser beam brightness: A review and new prospective in material processing”. In: *Optics and Laser Technology* 75 (2015), pp. 40–51. ISSN: 00303992. DOI: `10.1016/j.optlastec.2015.06.003`.

[152] A. Wirth et al. “Synthesized light transients”. In: *Science* 334.6053 (2011), pp. 195–200. ISSN: 10959203. DOI: `10.1126/science.1210268`.

[153] Ewan Gray et al. “Health economic evaluation of a serum-based blood test for brain tumour diagnosis: exploration of two clinical scenarios”. In: *BMJ Open* 8.5 (May 2018), e017593. ISSN: 2044-6055. DOI: `10.1136/bmjopen-2017-017593`.

[154] K. R. Allakhverdiev et al. “Effective nonlinear GaSe crystal. Optical properties and applications”. In: *Laser Physics* 19.5 (2009), pp. 1092–1104. ISSN: 1054-660X. DOI: `10.1134/s1054660x09050375`.

[155] Alexander Kessel et al. “Generation of multi-octave spanning high-energy pulses by cascaded nonlinear processes in BBO”. In: *Optics Express* 24.5 (2016), p. 5628. ISSN: 1094-4087. DOI: `10.1364/oe.24.005628`.

[156] Philipp Steinleitner et al. “Single-cycle infrared waveform control”. In: *Nature Photonics* 16.7 (2022), pp. 512–518. ISSN: 17494893. DOI: `10.1038/s41566-022-01001-2`.

[157] Q. Bournet et al. “Enhanced intrapulse difference frequency generation in the mid-infrared by a spectrally dependent polarization state”. In: *Optics Letters* 47.2 (2022), p. 261. ISSN: 0146-9592. DOI: `10.1364/ol.444908`.

[158] Neven Ibrakovic et al. “Achromatic dual-waveplate for inline two color high-order harmonic generation”. In: *European Physical Journal D* 72.9 (2018). ISSN: 14346079. DOI: `10.1140/epjd/e2018-80759-9`.

[159] Hanieh Fattahi et al. “Efficient, octave-spanning difference-frequency generation using few-cycle pulses in simple collinear geometry”. In: *Optics Letters* 38.20 (2013), p. 4216. ISSN: 0146-9592. DOI: `10.1364/ol.38.004216`.

[160] K. A. Kokh et al. “Growth and optical properties of solid solution crystals GaSe1-xSx”. In: *Materials Chemistry and Physics* 154 (2015), pp. 152–157. ISSN: 02540584. DOI: `10.1016/j.matchemphys.2015.01.058`.

[161] T A Birks, J C Knight, and P St J Russell. “Endlessly single-mode photonic crystal fiber”. In: *Optics Letters* 22.13 (July 1997), p. 961. ISSN: 0146-9592. DOI: `10.1364/OL.22.000961`.

[162] Philip St.J. Russell. “Photonic-Crystal Fibers”. In: *Journal of Lightwave Technology* 24.12 (Dec. 2006), pp. 4729–4749. ISSN: 0733-8724. DOI: `10.1109/JLT.2006.885258`.

[163] S. A. Planas et al. “Spectral narrowing in the propagation of chirped pulses in single-mode fibers”. In: *Optics Letters* 18.9 (1993), p. 699. ISSN: 0146-9592. DOI: `10.1364/ol.18.000699`.

[164] Fabian Stutzki et al. “Self-protecting nonlinear compression in a solid fiber for long-term stable ultrafast lasers at 2 μm wavelength”. In: *Fiber Lasers XIV: Technology and Systems* 10083.February 2017 (2017), p. 100830D. ISSN: 1996756X. DOI: `10.1117/12.2252662`.

[165] Douglas B. Leviton and Bradley J. Frey. “Temperature-dependent absolute refractive index measurements of synthetic fused silica”. In: *Optomechanical Technologies for Astronomy* 6273.62732 (2006), 62732K. ISSN: 0277786X. DOI: `10.1117/12.672853`.

[166] Andrew M. Weiner. “Ultrafast optical pulse shaping: A tutorial review”. In: *Optics Communications* 284.15 (2011), pp. 3669–3692. ISSN: 00304018. DOI: `10.1016/j.optcom.2011.03.084`.

[167] Antoine Monmayrant, Sébastien Weber, and Béatrice Chatel. “A newcomer’s guide to ultrashort pulse shaping and characterization”. In: *Journal of Physics B: Atomic, Molecular and Optical Physics* 43.10 (2010). ISSN: 09534075. DOI: `10.1088/0953-4075/43/10/103001`.

[168] Sang-Hee Shim et al. “Femtosecond pulse shaping directly in the mid-IR using acousto-optic modulation”. In: *Optics Letters* 31.6 (2006), p. 838. ISSN: 0146-9592. DOI: `10.1364/ol.31.000838`.

[169] A. Cartella et al. “Pulse shaping in the mid-infrared by a deformable mirror”. In: *2013 Conference on Lasers and Electro-Optics Europe and International Quantum Electronics Conference, CLEO/Europe-IQEC 2013* 39.6 (2013), pp. 1485–1488. ISSN: 15394794. DOI: `10.1109/CLEOE-IQEC.2013.6801048`.

[170] Raman Maksimenka et al. “Direct mid-infrared femtosecond pulse shaping with a calomel acousto-optic programmable dispersive filter”. In: *Optics Letters* 35.21 (2010), p. 3565. ISSN: 0146-9592. DOI: `10.1364/ol.35.003565`.

[171] Robert Szipöcs et al. “Chirped multilayer coatings for broadband dispersion control in femtosecond lasers”. In: *Optics Letters* 19.3 (1994), p. 201. ISSN: 0146-9592. DOI: `10.1364/ol.19.000201`.

[172] Florian Habel and Vladimir Pervak. “Dispersive mirror for the mid-infrared spectral range of 9–115 μm”. In: *Applied Optics* 56.4 (2017), p. C71. ISSN: 0003-6935. DOI: `10.1364/ao.56.000c71`.

[173] Tatiana Amotchkina et al. “Broadband dispersive Ge/YbF 3 mirrors for mid-infrared spectral range”. In: *Optics Letters* 44.21 (Nov. 2019), p. 5210. ISSN: 0146-9592. DOI: `10.1364/OL.44.005210`.

[174] John H. Burnett et al. “Refractive index measurements of Ge”. In: *Infrared Sensors, Devices, and Applications VI* 9974.September 2016 (2016), p. 99740X. ISSN: 1996756X. DOI: `10.1117/12.2237978`.

[175] H. H. Moore. “Refractive index of alkaline earth halides and its wavelength and temperature derivatives”. In: *Journal of Physical and Chemical Reference Data* 9.1 (1982), pp. 161–290. ISSN: 15297845. DOI: `10.1063/1.555616`.

[176] David F. Edwards and Ellen Ochoa. “Infrared refractive index of silicon”. In: *Applied Optics* 19.24 (Dec. 1980), p. 4130. ISSN: 0003-6935. DOI: `10.1364/AO.19.004130`.

[177] Berge Tatian. “Fitting refractive-index data with the Sellmeier dispersion formula”. In: *Applied Optics* 23.24 (1984), p. 4477. ISSN: 0003-6935. DOI: `10.1364/ao.23.004477`.

[178] Kiyoshi Kato, Fumihito Tanno, and Nobuhiro Umemura. “Sellmeier and thermo-optic dispersion formulas for GaSe (Revisited)”. In: *Applied Optics* 52.11 (Apr. 2013), p. 2325. ISSN: 1559-128X. DOI: `10.1364/AO.52.002325`.

[179] Enrico Ridente et al. “Electro-optic characterization of synthesized infrared-visible light fields”. In: *Nature Communications* 13.1 (2022). ISSN: 20411723. DOI: `10.1038/s41467-022-28699-6`.

[180] Wolfgang Demtröder. *Molecular Physics: Theoretical Principles and Experimental Methods*. Wiley, 2008.

[181] Julian Haas and Boris Mizaikoff. “Advances in Mid-Infrared Spectroscopy for Chemical Analysis”. In: *Annual Review of Analytical Chemistry* 9.1 (2016), pp. 45–68. ISSN: 19361335. DOI: `10.1146/annurev-anchem-071015-041507`.

[182] A. Kowligy et al. “Direct electric-field sampled infrared spectroscopy from 3 to 25 μm”. In: *Optics InfoBase Conference Papers*. Vol. Part F92-C. Washington, D.C.: OSA, May 2018, JTh5B.6. ISBN: 9781557528209. DOI: `10.1364/CLEO_AT.2018.JTh5B.6`.

[183] G.J. Hawkins et al. “An ultra-wide passband (5–30 μm) filter for FTIR studies of Photosystem II”. In: *Infrared Physics & Technology* 39.5 (Aug. 1998), pp. 297–306. ISSN: 13504495. DOI: `10.1016/S1350-4495(98)00021-8`.

[184] Tatiana Amotchkina et al. “Comparative study of NIR-MIR beamsplitters based on ZnS/YbF3 and Ge/YbF3”. In: *Optics Express* 27.4 (2019), p. 5557. ISSN: 10944087. DOI: `10.1364/oe.27.005557`.

[185] John U. White. “Gratings as broad band filters for the infra-red.” In: *Journal of the Optical Society of America* 37.9 (1947), pp. 713–717. ISSN: 00303941. DOI: `10.1364/JOSA.37.000713`.

[186] D. C. Yost, T. R. Schibli, and Jun Ye. "Efficient output coupling of intracavity high-harmonic generation". In: *Optics Letters* 33.10 (2008), p. 1099. ISSN: 0146-9592. DOI: `10.1364/ol.33.001099`.

[187] Marcus Trost et al. "Structured Mo/Si multilayers for IR-suppression in laser-produced EUV light sources". In: *Optics Express* 21.23 (2013), p. 27852. ISSN: 10944087. DOI: `10.1364/oe.21.027852`.

[188] Uwe D. Zeitner et al. "High performance diffraction gratings made by e-beam lithography". In: *Applied Physics A: Materials Science and Processing* 109.4 (Dec. 2012), pp. 789–796. ISSN: 09478396. DOI: `10.1007/s00339-012-7346-z`.

[189] Kenneth C Johnson. *Grating Diffraction Calculator (GD-Calc)*. 2008.

[190] Arkadiusz Ciesielski et al. "Evidence of germanium segregation in gold thin films". In: *Surface Science* 674 (2018), pp. 73–78. ISSN: 0039-6028. DOI: `10.1016/j.susc.2018.03.020`.

[191] Nicolas Bonod and Jérôme Neauport. "Diffraction gratings: from principles to applications in high-intensity lasers". In: *Advances in Optics and Photonics* 8.1 (Mar. 2016), p. 156. ISSN: 1943-8206. DOI: `10.1364/AOP.8.000156`.

[192] Eiichi Matsubara, Masaya Nagai, and Masaaki Ashida. "Ultrabroadband coherent electric field from far infrared to 200 THz using air plasma induced by 10 fs pulses". In: *Applied Physics Letters* 101.1 (2012). ISSN: 00036951. DOI: `10.1063/1.4732524`.

[193] Jia Xu et al. "Three-octave terahertz pulses from optical rectification of 20 fs, 1 μm, 78 MHz pulses in GaP". In: *Journal of Physics B: Atomic, Molecular and Optical Physics* 51.15 (Aug. 2018), p. 154002. ISSN: 0953-4075. DOI: `10.1088/1361-6455/aacfe7`.

[194] Christina Hofer. "Detection Efficiency and Bandwidth Optimized Electro-Optic Sampling of Mid-Infrared Waves". Dissertation. Ludwig Maximilians university munich, 2021.

[195] A. Leitenstorfer et al. "Detectors and sources for ultrabroadband electro-optic sampling: Experiment and theory". In: *Applied Physics Letters* 74.11 (1999), pp. 1516–1518. ISSN: 00036951. DOI: `10.1063/1.123601`.

[196] Husain Alqattan et al. "Attosecond electronic delay response in dielectric materials". In: *Faraday Discussions* (2022), pp. 317–326. ISSN: 13645498. DOI: `10.1039/d2fd00002d`.

[197] Peter R. Smith, David H. Auston, and Martin C. Nuss. "Subpicosecond Photoconducting Dipole Antennas". In: *IEEE Journal of Quantum Electronics* 24.2 (1988), pp. 255–260. ISSN: 15581713. DOI: `10.1109/3.121`.

[198] Shawn Sederberg et al. "Attosecond optoelectronic field measurement in solids". In: *Nature Communications* 11.1 (2020), pp. 1–8. ISSN: 20411723. DOI: `10.1038/s41467-019-14268-x`.

[199] J. Itatani et al. “Attosecond Streak Camera”. In: *Physical Review Letters* 88.17 (2002), p. 4. ISSN: 10797114. DOI: `10.1103/PhysRevLett.88.173903`.

[200] R. Kienberger et al. “Atomic transient recorder”. In: *Nature* 427.6977 (Feb. 2004), pp. 817–821. ISSN: 0028-0836. DOI: `10.1038/nature02277`.

[201] Abijith S. Kowligy et al. “Infrared electric field sampled frequency comb spectroscopy”. In: *Science Advances* 5.6 (June 2019). ISSN: 2375-2548. DOI: `10.1126/sciadv.aaw8794`.

[202] Christina Hofer et al. “Electro-optic sampling with percent-level detection efficiency”. In: *Optics InfoBase Conference Papers* 3360.2004 (2021), p. 33821.

[203] Ugaitz Elu et al. “Seven-octave high-brightness and carrier-envelope-phase-stable light source”. In: *Nature Photonics* 15.4 (2021), pp. 277–280. ISSN: 17494893. DOI: `10.1038/s41566-020-00735-1`.

[204] Q. Ru et al. “Two-octave-wide (3–12 µm) subharmonic produced in a minimally dispersive optical parametric oscillator cavity”. In: *Optics Letters* 46.4 (Feb. 2021), p. 709. ISSN: 0146-9592. DOI: `10.1364/OL.403910`.

[205] Anthony Catanese et al. “Mid-infrared frequency comb with 6.7 W average power based on difference frequency generation”. In: *Optics Letters* 45.5 (Mar. 2020), p. 1248. ISSN: 0146-9592. DOI: `10.1364/OL.385294`.

[206] Waqar M. Ahmed et al. “Exhaled Volatile Organic Compounds of Infection: A Systematic Review”. In: *ACS Infectious Diseases* 3.10 (2017), pp. 695–710. ISSN: 23738227. DOI: `10.1021/acsinfecdis.7b00088`.

[207] Anton Amann and David Smith. *Volatile Biomarkers*. Elsevier, 2013. ISBN: 9780444626134. DOI: `10.1016/C2012-0-01274-4`.

[208] Alexander Sell et al. “Field-resolved detection of phase-locked infrared transients from a compact Er:fiber system tunable between 55 and 107 THz”. In: *Applied Physics Letters* 93.25 (2008), pp. 1–3. ISSN: 00036951. DOI: `10.1063/1.3040057`.

[209] Aleksandra Foltynowicz et al. “Quantum-noise-limited optical frequency comb spectroscopy”. In: *Physical Review Letters* 107.23 (2011), pp. 1–5. ISSN: 00319007. DOI: `10.1103/PhysRevLett.107.233002`.

[210] Antoni Rogalski. “Next decade in infrared detectors”. In: *Electro-Optical and Infrared Systems: Technology and Applications XIV*. Ed. by David A. Huckridge, Reinhard Ebert, and Helge Bürsing. October 2017. SPIE, Oct. 2017, p. 100. ISBN: 9781510613300. DOI: `10.1117/12.2300779`.

[211] Daniel M.B. Lesko et al. “A six-octave optical frequency comb from a scalable few-cycle erbium fibre laser”. In: *Nature Photonics* 15.4 (2021), pp. 281–286. ISSN: 17494893. DOI: `10.1038/s41566-021-00778-y`.

[212] Christina Hofer et al. “Mid-infrared electric field sampling approaching single-photon sensitivity”. In: *EPJ Web of Conferences* 243 (Oct. 2020). Ed. by P. Helfenstein, p. 16001. ISSN: 2100-014X. DOI: `10.1051/epjconf/202024316001`.

[213] Kai Liu, Jingzhou Xu, and X. C. Zhang. “GaSe crystals for broadband terahertz wave detection”. In: *Applied Physics Letters* 85.6 (2004), pp. 863–865. ISSN: 00036951. DOI: `10.1063/1.1779959`.

[214] Michael Porer, Jean-Michel Ménard, and Rupert Huber. “Shot noise reduced terahertz detection via spectrally postfiltered electro-optic sampling”. In: *Optics Letters* 39.8 (2014), p. 2435. ISSN: 0146-9592. DOI: `10.1364/ol.39.002435`.

[215] M. C. Phillips et al. “In-situ measurement of pyrolysis and combustion gases from biomass burning using swept wavelength external cavity quantum cascade lasers”. In: *Optics Express* 28.6 (2020), p. 8680. ISSN: 1094-4087. DOI: `10.1364/oe.386072`.

[216] G Gagliardi et al. *Cavity-Enhanced Spectroscopy and Sensing.* Vol. 179. 2014. ISBN: 978-3-642-40002-5. DOI: `10.1007/978-3-642-40003-2`.

[217] G. Winkler et al. “Mid-infrared interference coatings with excess optical loss below 10 ppm”. In: *Optica* 8.5 (2021), p. 686. ISSN: 23342536. DOI: `10.1364/optica.405938`.

[218] K. S. Maiti et al. “Towards reliable diagnostics of prostate cancer via breath”. In: *Scientific Reports* 11.1 (2021), pp. 1–11. ISSN: 20452322. DOI: `10.1038/s41598-021-96845-z`.

[219] A. Tomasino et al. “Wideband THz time domain spectroscopy based on optical rectification and electro-optic sampling”. In: *Scientific Reports* 3 (2013), pp. 1–8. ISSN: 20452322. DOI: `10.1038/srep03116`.

[220] Peter Linstrom and Gary Mallard. *NIST Chemistry WebBook, NIST Standard Reference Database 69.* DOI: `10.18434/T4D303`.

[221] Theresa Buberl et al. “Sub-optical-cycle light-matter energy transfer dynamics in molecular vibrational spectroscopy”. In: *Optics InfoBase Conference Papers* (2021). DOI: `10.21203/rs.3.rs-1691869/v1`.

[222] S. M. Abrarov et al. “A Single-Domain Implementation of the Voigt/Complex Error Function by Vectorized Interpolation”. In: *Earth Science Research* 8.2 (2019), p. 52. ISSN: 1927-0542. DOI: `10.5539/esr.v8n2p52`.

[223] Wolfgang Schweinberger et al. “Interferometric delay tracking for low-noise Mach-Zehnder-type scanning measurements”. In: *Optics Express* 27.4 (2019), p. 4789. ISSN: 10944087. DOI: `10.1364/oe.27.004789`.

[224] Matthias Hagner et al. “Ultrabroadband suppression of mid-infrared reflection losses of a layered semiconductor by nanopatterning with a focused ion beam”. In: *Optics Express* 29.21 (2021), p. 33632. ISSN: 10944087. DOI: `10.1364/oe.433703`.

[225] Matthias Knorr et al. “Ultrabroadband etalon-free detection of infrared transients by van-der-Waals contacted sub-10-um GaSe detectors”. In: *Optics Express* 26.15 (2018), p. 19059. ISSN: 1094-4087. DOI: `10.1364/oe.26.019059`.

[226] Lukas Fürst. “Field-Resolved Spectroscopy in the Gas Phase”. Master Thesis. Ludwig-Maximilians-University, 2021.

[227] Manuel Graf, Lukas Emmenegger, and Béla Tuzson. “Compact, circular, and optically stable multipass cell for mobile laser absorption spectroscopy”. In: *Opt. Lett.* 43.11 (June 2018), pp. 2434–2437. DOI: `10.1364/OL.43.002434`.

[228] Thomas K. Allison, Melanie A.R. Reber, and Yuning Chen. “Cavity-enhanced ultrafast spectroscopy: Ultrafast meets ultrasensitive”. In: *Optics InfoBase Conference Papers* 3.3 (2016). DOI: `10.1364/UP.2016.UM3A.5`.

[229] Christoph Gohle et al. “A frequency comb in the extreme ultraviolet”. In: *Nature* 436.7048 (2005), pp. 234–237. ISSN: 00280836. DOI: `10.1038/nature03851`.

[230] Ioachim Pupeza et al. “Extreme-ultraviolet frequency combs for precision metrology and attosecond science”. In: *Nature Photonics* 15.3 (2021), pp. 175–186. ISSN: 17494893. DOI: `10.1038/s41566-020-00741-3`.

[231] Philipp Sulzer et al. “Cavity-enhanced field-resolved spectroscopy”. In: *Nature Photonics* 16.10 (Oct. 2022), pp. 692–697. ISSN: 1749-4885. DOI: `10.1038/s41566-022-01057-0`.

[232] Julien Picot et al. “Flow cytometry: Retrospective, fundamentals and recent instrumentation”. In: *Cytotechnology* 64.2 (2012), pp. 109–130. ISSN: 09209069. DOI: `10.1007/s10616-011-9415-0`.

[233] Chi Zhang et al. “Stimulated Raman scattering flow cytometry for label-free single-particle analysis”. In: *Optica* 4.1 (2017), p. 103. ISSN: 2334-2536. DOI: `10.1364/optica.4.000103`.

[234] Iwan W. Schie et al. “High-Throughput Screening Raman Spectroscopy Platform for Label-Free Cellomics”. In: *Analytical Chemistry* 90.3 (2018), pp. 2023–2030. ISSN: 15206882. DOI: `10.1021/acs.analchem.7b04127`.

[235] Kotaro Hiramatsu et al. “High-throughput label-free molecular fingerprinting flow cytometry”. In: *Science Advances* 5.1 (2019), pp. 1–9. ISSN: 23752548. DOI: `10.1126/sciadv.aau0241`.

[236] Julia Gala De Pablo et al. “High-Throughput Raman Flow Cytometry and beyond”. In: *Accounts of Chemical Research* 54.9 (2021), pp. 2132–2143. ISSN: 15204898. DOI: `10.1021/acs.accounts.1c00001`.

[237] Jie Shan et al. “Single-shot measurement of terahertz electromagnetic pulses by use of electro-optic sampling”. In: *Optics Letters* 25.6 (2000), p. 426. ISSN: 0146-9592. DOI: `10.1364/ol.25.000426`.

[238] Eléonore Roussel et al. “Phase Diversity Electro-optic Sampling: A new approach to single-shot terahertz waveform recording”. In: *Light: Science and Applications* 11.1 (2022). ISSN: 20477538. DOI: `10.1038/s41377-021-00696-2`.

[239] B. Urbanek et al. “Femtosecond terahertz time-domain spectroscopy at 36 kHz scan rate using an acousto-optic delay”. In: *Applied Physics Letters* 108.12 (2016). ISSN: 00036951. DOI: `10.1063/1.4944459`.

[240] Oliver Kliebisch, Dirk C. Heinecke, and Thomas Dekorsy. “Ultrafast time-domain spectroscopy system using 10 GHz asynchronous optical sampling with 100 kHz scan rate”. In: *Optics Express* 24.26 (2016), p. 29930. ISSN: 10944087. DOI: `10.1364/oe.24.029930`.

[241] Stefan Kray et al. “Electronically controlled coherent linear optical sampling for optical coherence tomography”. In: *Optics Express* 18.10 (2010), p. 9976. ISSN: 1094-4087. DOI: `10.1364/oe.18.009976`.

[242] B. Süss, F. Ringleb, and J. Heberle. “New ultrarapid-scanning interferometer for FT-IR spectroscopy with microsecond time-resolution”. In: *Review of Scientific Instruments* 87.6 (2016). ISSN: 10897623. DOI: `10.1063/1.4953658`.

[243] Alexander Weigel et al. “Ultra-rapid electro-optic sampling of octave-spanning mid-infrared waveforms”. In: *Optics Express* 29.13 (June 2021), p. 20747. ISSN: 1094-4087. DOI: `10.1364/OE.423818`.

[244] Natalie Töpfer et al. “Raman spectroscopy reveals LPS-induced changes of biomolecular composition in monocytic THP-1 cells in a label-free manner”. In: *Integrative Biology* 11.3 (2019), pp. 87–98. DOI: `10.1093/intbio/zyz009`.

[245] Jacques J. M. van Dongen et al. “Minimal residual disease diagnostics in acute lymphoblastic leukemia: need for sensitive, fast, and standardized technologies”. In: *Blood* 125.26 (June 2015), pp. 3996–4009. ISSN: 0006-4971. DOI: `10.1182/blood-2015-03-580027`.

[246] Anuradha Ramoji et al. “Leukocyte Activation Profile Assessed by Raman Spectroscopy Helps Diagnosing Infection and Sepsis”. In: *Critical Care Explorations* 3.5 (May 2021), e0394. ISSN: 2639-8028. DOI: `10.1097/CCE.0000000000000394`.

Appendix A - Data Archiving

All experimental raw data and code for analysis utilized in this thesis can be found on the data archive server of the Laboratory for Attosecond Physics at the Max Planck Institute of Quantum Optics:
/afs/rzg/mpq/lap/publication_archive /theses/2022/Gerz, Daniel (PhD).
For each figure a separate folder containing the raw data, code for analysis and a text file with explanations is available.

Acknowledgements

At the end of five exciting years as a PhD student I want to take the opportunity to thank everyone that has contributed to this work and/or has enriched the experience.
First of all, I want to thank my PhD adviser Ferenc for the opportunity to work at Attoworld - a place filled with bright, friendly and interested people with diverse scientific and cultural backgrounds. Ferenc, I found your emphasize on working with a clear goal in mind very inspiring - thank you for sharing your vision of a *Just Cause*.
I want to express my gratitude to my former team members, the BIRD team, and its group leader Mihaela for the insights into the complexity of medical studies.

I had the privilege to be part of the FRM team and I want to especially thank its team leader Ioachim who started and guided the Infrasampler 2.0 project and kept believing in it. Your motivation and great passion for science is infectious. Also, thank you very much for the support during the writing phase.

The project would not have existed and progressed without Jens Limpert and his team members Christian, Tobias and Martin. It was always very reassuring to have your reliable and fast support. Thank you.
I am grateful that from the first day when I arrived at MPQ in Garching I felt like part of the team consisting of Thomas, Julia, Theresa, Jia and Niko. I want to particularly express my gratitude to Thomas for all the long hours spent together to get IS2.0 running and the relaxed train rides home.
Christina, thank you for the great team work and fun we had in the lab. Getting the best performance out of the system required your help as the EOS expert.
I want to thank Wolfgang for sharing his broad knowledge in discussions on all Infrasamplers and helping me to understand the maze of wires in the scanning software. Maxi supported me with simulations and theoretical questions. Theresa was a cheerful and helpful colleague. Alex was a great support for the implementation of the Sonotrdoe setup and always had valuable suggestions. The support and experience of Ernst and Kiran in the gas phase experiments were essential. Naturally, in order to run the experiments and to have an easier time in analyzing the data, functional software is required and I want to thank Wolfgang, Patrik, Alex and Michael for their support.
Thank you Marinus for the many discussions on noise, biological measurements and life in general. I want to thank Ali, Stephan, Tobias, Philip, Hadil and many more for the help and the fun times in and outside the lab.
I also want to thank the Master students Julia, Lukas, Anka, Yannick, Holger and Flo for

exciting and fun times at IS2.0. I learned a lot when we progressed together and I tried to teach you how IS2.0 can be used.

The cavity team with Lukas, Philipp, Anka, Lucy, Ernst and Maxi enriched the liveliness around the optical table and during break times. Thank you.

I want to thank Shane and Sanchi for the comfortable atmosphere in the office.

For all the great lunch breaks and lively discussion, I want to thank Nathalie, Sebastian, Markus, Ka Fai, Philipp, Jinwei, Qing, Aleksander, Shizhen, Maciej, Lucy, Christina, Abhijit, Arun, Dionysios, Matthias and all members of the CMF team and the former AG HFS.

Furthermore, I am grateful to every member of the Krausz group for their supportiveness and the interesting discussions. It was a pleasure to work in such a great atmosphere with you.

Such a huge team cannot function without a good administration and I am thankful to Klaus, Nils, Katharina, Martin and Kerstin for making it work like clockwork. Naturally, the technical team is equally important, so that the facilities and experiments run smoothly and I'm grateful for your support Florian, Hans and Frank.

I want to thank the graduate schools MPSP and IMPRS-APS for providing platforms for personal growth and networking in the world of photonics.

Finally, I want to appreciate the continuous support from my family. I want to especially thank my fianée Alexandra for her patience which was really needed during the writing phase.